Evolution of the modern human brain pp. 124 & 165

Rapid injection molding of glass pp. 126 & 182

Urgent actions to redress inequities in science p. 133

Science

$15
9 APRIL 2021
sciencemag.org

AAAS

MAGNETARS

How hypermagnetized neutron stars power cosmic explosions p. 120

The heart of the matter.

The NEBNext® Ultra™ II workflow lies at the heart of NEB's portfolio for next gen sequencing library preparation. With specially formulated master mixes and simplified workflows, high quality libraries can be generated with low inputs and reduced hands-on time.

As sequencing technologies improve and applications expand, the need for compatibility with ever-decreasing input amounts and sub-optimal sample quality grows. Scientists must balance reliability and performance with faster turnaround, higher throughput and automation compatibility.

NEBNext Ultra II modules and kits for Illumina® are the perfect combination of reagents, optimized formulations and simplified workflows, enabling you to create DNA or RNA libraries of highest quality and yield, even when starting from extremely low input amounts.

The Ultra II workflow is central to many of our NEBNext products, including:

- Ultra II DNA & FS DNA Library Prep
- Enzymatic Methyl-seq
- Ultra II RNA & Directional RNA Library Prep
- Single Cell/Low Input RNA Library Prep
- Module products for each step in the workflow

The Ultra II workflow is available in convenient kit formats or as separate modules – it is easily scalable and automated on a range of liquid handling instruments.

End Repair/ dA-Tailing	Adaptor Ligation	Clean Up/ Size Selection	PCR Enrichment	Clean Up
Module NEB #E7546	Module NEB #E7595	Component of NEB #E7103	Module NEB #M0544	Component of NEB #E7103
NEBNext Ultra II DNA Library Prep Kit for Illumina (NEB #E7645)				
NEBNext Ultra II Library Prep with Sample Purification Beads (NEB #E7103)				

The NEBNext Ultra II workflow has been cited in thousands of publications, as well as a growing number of preprints and protocols related to COVID-19. Citation information and extensive performance data for each product is available on neb.com.

To learn more about why NEBNext is the choice for you, visit **NEBNext.com**.

One or more of these products are covered by patents, trademarks and/or copyrights owned or controlled by New England Biolabs, Inc. For more information, please email us at gbd@neb.com. The use of these products may require you to obtain additional third party intellectual property rights for certain applications.
Illumina® is a registered trademark of Illumina, Inc.
© Copyright 2020, New England Biolabs, Inc.; all rights reserved.

NEW ENGLAND BioLabs® Inc.

be INSPIRED
drive DISCOVERY
stay GENUINE

CONTENTS

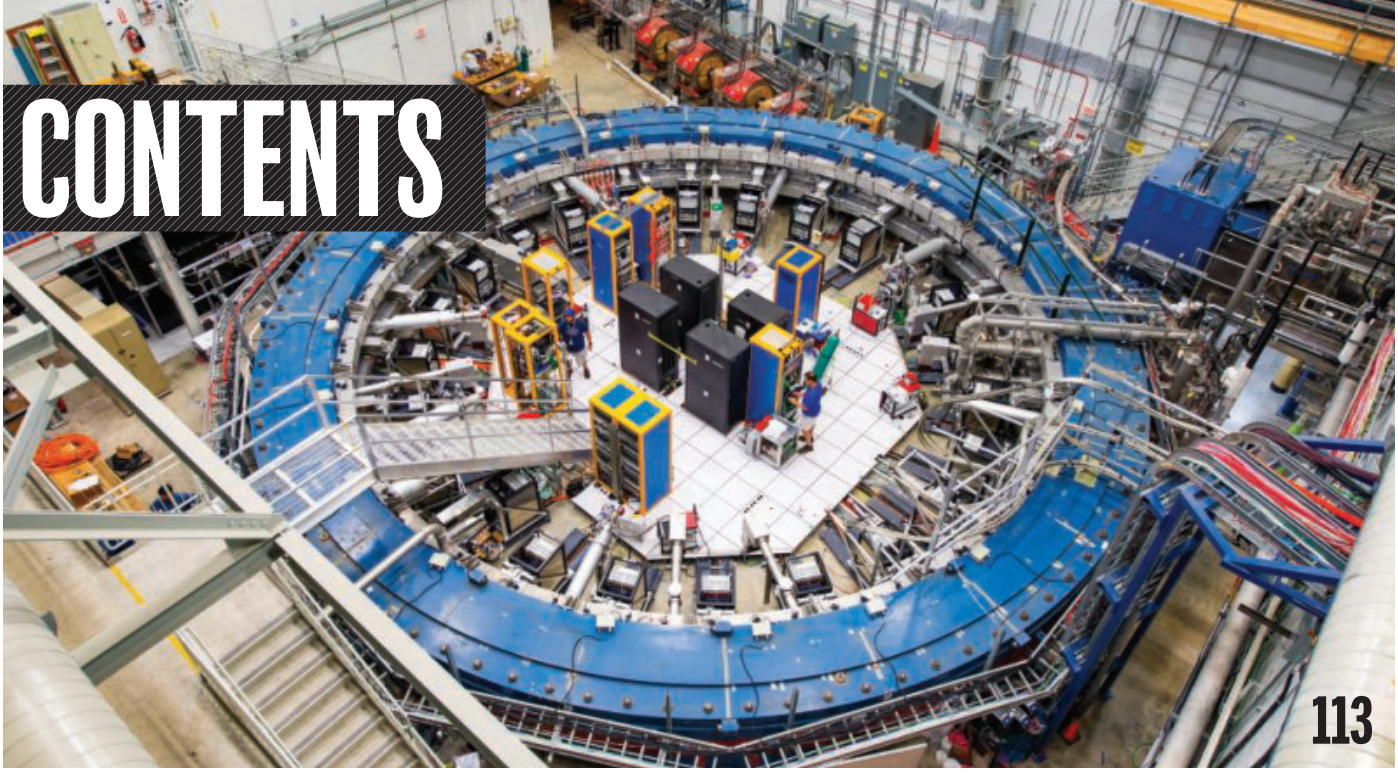

113

9 APRIL 2021 • VOLUME 372 • ISSUE 6538

NEWS

IN BRIEF

110 News at a glance

IN DEPTH

112 Biden, Congress roll out big plans to expand NSF
President and lawmakers push proposals to add technology directorate and boost budget *By J. Mervis*

113 For a change, a hint of new physics does not fade away
Reprise of storied experiment confirms muon's extra magnetism
By A. Cho

115 When modern humans met Neanderthals
Ancient genomes from first moderns in Europe tell stories of diverse origins, ancient trysts *By A. Gibbons*

116 Latest Russian vaccine comes with a big dose of mystery
Vaccine trial participants call for review after unusual private study found they have no virus-blocking antibodies
By O. Dobrovidova

117 Top German psychologist found to have fabricated data
University investigation finds anxiety expert pressured whistleblowers *By H. Boytchev*

FEATURES

120 A star is torn
Nature's most magnetic objects, ripped apart in starquakes, can unleash powerful flashes of light *By J. Sokol*
PODCAST

INSIGHTS

PERSPECTIVES

124 The enigmatic origins of the human brain
Evolutionary history of the human brain appears more complex than thought
By A. Beaudet
RESEARCH ARTICLE p. 165

124 & 165

126 Preshaping clear glass at low temperatures
Pelletized glass-forming composites enable rapid injection molding and facile binder recovery *By R. Dylla-Spears*
REPORT p. 182

127 Epigenetic nucleotides enhance therapy
Targeting sanitation of epigenetic nucleotides synergizes with cancer treatment
By S. Kriaucionis
RESEARCH ARTICLE p. 156

128 The push and pull of DNA methylation
The control of DNA methylation guides cell-fate decisions in development and disease *By T. Gu and M. A. Goodell*
RESEARCH ARTICLE p. 146

130 Recruiting T cells in cancer immunotherapy
T cell dynamics reveal that immunotherapy responses may rely on peripheral T cells
By K. E. Yost et al.

132 Limits on superconductivity in flatland
Experiments explore a new superconducting regime in layered quantum materials
By M. Randeria
REPORT p. 190

POLICY FORUM

133 Concrete steps to diversify the scientific workforce
Any barrier to entry weakens science and its societal impact
By S. Tilghman et al.

CREDITS: (PHOTO) REIDAR HAHN/FERMILAB; (IMAGE) M. PONCE DE LEÓN AND CH. ZOLLIKOFER/UNIVERSITY OF ZURICH

NOMIS & Science
YOUNG EXPLORER AWARD

Research at the intersection of the social and life sciences

Unconventional. Interdisciplinary. Bold.

The newly launched **NOMIS & *Science* Young Explorer Award** recognizes bold, early-career researchers with an M.D., Ph.D., or M.D./Ph.D. who ask fundamental questions at the intersection of the social and life sciences. It is awarded to scientists who conduct research with an enthusiasm that catalyzes cross-disciplinary collaboration and who take risks to creatively address relevant and exciting questions.

Award winners will receive a cash prize of up to $15,000, and their essay submissions will be published in *Science*. They will also be invited to share their ideas with leading scientists in their respective fields at an award ceremony and to present their research to the NOMIS Board of Directors for potential future funding.

Apply by May 15, 2021
at www.sciencemag.org/nomis

Science
AAAS

NOMIS
FOUNDATION
Creating the Spark

BOOKS *ET AL.*

136 Rethinking Alexander Graham Bell's legacy
A new biography confronts the inventor's complicated relationship with the Deaf community
By J. Trussell

137 Refracted reality
A social scientist probes social media–induced polarization
By J. Golbeck

LETTERS

138 Prevent bottom trawling in southern Brazil
By L. G. Cardoso et al.

139 Assess before changing Brazil's shipping policy
By L. R. Forti et al.

139 Northeast Brazil's imperiled Cerrado
By C. H. L. Silva Junior et al.

140 Technical Comment abstracts

140 Errata

RESEARCH

IN BRIEF

141 From *Science* and other journals

REVIEW

144 Medicine
Epigenetics, fragmentomics, and topology of cell-free DNA in liquid biopsies
Y. M. D. Lo et al.
REVIEW SUMMARY; FOR FULL TEXT: DOI.ORG/10.1126/SCIENCE.AAW3616

RESEARCH ARTICLES

145 Imaging development
Imaging cell lineage with a synthetic digital recording system *K.-H. K. Chow* et al.
RESEARCH ARTICLE SUMMARY; FOR FULL TEXT: DOI.ORG/10.1126/SCIENCE.ABB3099

146 Epigenetics
QSER1 protects DNA methylation valleys from de novo methylation *G. Dixon* et al.
RESEARCH ARTICLE SUMMARY; FOR FULL TEXT: DOI.ORG/10.1126/SCIENCE.ABD0875
PERSPECTIVE p. 128

147 Structural biology
Structure and dynamics of the CGRP receptor in apo and peptide-bound forms
T. M. Josephs et al.
RESEARCH ARTICLE SUMMARY; FOR FULL TEXT: DOI.ORG/10.1126/SCIENCE.ABF7258

148 Photoenzymes
Mechanism and dynamics of fatty acid photodecarboxylase *D. Sorigué* et al.
RESEARCH ARTICLE SUMMARY; FOR FULL TEXT: DOI.ORG/10.1126/SCIENCE.ABD5687

149 Coronavirus
Estimated transmissibility and impact of SARS-CoV-2 lineage B.1.1.7 in England
N. G. Davies et al.
RESEARCH ARTICLE SUMMARY; FOR FULL TEXT: DOI.ORG/10.1126/SCIENCE.ABG3055

150 Neuroevolution
Bilateral visual projections exist in non-teleost bony fish and predate the emergence of tetrapods *R. J. Vigouroux* et al.
VIDEO

156 Cancer
Targeting the nucleotide salvage factor DNPH1 sensitizes *BRCA*-deficient cells to PARP inhibitors *K. Fugger* et al.
PERSPECTIVE p. 127

165 Human evolution
The primitive brain of early *Homo*
M. S. Ponce de León et al.
PERSPECTIVE P. 124; PODCAST

171 Plant science
Pollen PCP-B peptides unlock a stigma peptide–receptor kinase gating mechanism for pollination *C. Liu* et al.

REPORTS

175 Organic chemistry
Boron insertion into alkyl ether bonds via zinc/nickel tandem catalysis *H. Lyu* et al.

182 Glass
High-throughput injection molding of transparent fused silica glass
M. Mader et al.
PERSPECTIVE p. 126

187 Time-domain astronomy
Enhanced x-ray emission coinciding with giant radio pulses from the Crab Pulsar
T. Enoto et al.

190 Materials science
Gate-controlled BCS-BEC crossover in a two-dimensional superconductor
Y. Nakagawa et al.
PERSPECTIVE p. 132

195 Nanomaterials
Seeded 2D epitaxy of large-area single-crystal films of the van der Waals semiconductor 2H $MoTe_2$
X. Xu et al.

201 Regeneration
Krüppel-like factor 1 is a core cardiomyogenic trigger in zebrafish
M. Ogawa et al.

DEPARTMENTS

109 Editorial
The story behind COVID-19 vaccines
By Anthony S. Fauci

210 Working Life
A risk worth taking *By Virginia Zarulli*

ON THE COVER

In this artist's conception, plasma erupts from a magnetar, a neutron star with a magnetic field a trillion times stronger than that of a refrigerator magnet. Starquakes in the crust unleash the plasma, which escapes near the poles. The plasma generates a beam of gamma rays, which astronomers can detect on Earth. A handful of these gamma ray flares are confirming this picture of magnetar behavior and suggest that the objects may be relatively common. See page 120. *Image: NASA's Goddard Space Flight Center/Chris Smith (USRA/GESTAR)*

Science Staff 106
New Products 206
Science Careers 207

SCIENCE (ISSN 0036-8075) is published weekly on Friday, except last week in December, by the American Association for the Advancement of Science, 1200 New York Avenue, NW, Washington, DC 20005. Periodicals mail postage (publication No. 484460) paid at Washington, DC, and additional mailing offices. Copyright © 2021 by the American Association for the Advancement of Science. The title SCIENCE is a registered trademark of the AAAS. Domestic individual membership, including subscription (12 months): $165 ($74 allocated to subscription). Domestic institutional subscription (51 issues): $2148; Foreign postage extra: Air assist delivery: $98. First class, airmail, student, and emeritus rates on request. Canadian rates with GST available upon request, GST #125488122. Publications Mail Agreement Number 1069624. **Printed in the U.S.A.**
Change of address: Allow 4 weeks, giving old and new addresses and 8-digit account number. **Postmaster:** Send change of address to AAAS, P.O. Box 96178, Washington, DC 20090–6178. **Single-copy sales:** $15 each plus shipping and handling available from backissues.sciencemag.org; bulk rate on request. **Authorization to reproduce** material for internal or personal use under circumstances not falling within the fair use provisions of the Copyright Act can be obtained through the Copyright Clearance Center (CCC), www.copyright.com. The identification code for *Science* is 0036-8075. *Science* is indexed in the *Reader's Guide to Periodical Literature* and in several specialized indexes.

PHOTO: OCTAVIO CAMPOS SALLES/ALAMY STOCK PHOTO

Science AAAS

Editor-in-Chief Holden Thorp, hthorp@aaas.org

Executive Editor Monica M. Bradford

Editors, Research Valda Vinson, Jake S. Yeston **Editor, Insights** Lisa D. Chong

DEPUTY EDITORS Julia Fahrenkamp-Uppenbrink (UK), Stella M. Hurtley (UK), Phillip D. Szuromi, Sacha Vignieri **SR. EDITORIAL FELLOW** Andrew M. Sugden (UK) **SR. EDITORS** Gemma Alderton (UK), Caroline Ash (UK), Brent Grocholski, Pamela J. Hines, Di Jiang, Marc S. Lavine (Canada), Yevgeniya Nusinovich, Ian S. Osborne (UK), Beverly A. Purnell, L. Bryan Ray, H. Jesse Smith, Keith T. Smith (UK), Jelena Stajic, Peter Stern (UK), Valerie B. Thompson, Brad Wible, Laura M. Zahn **ASSOCIATE EDITORS** Michael A. Funk, Priscilla N. Kelly, Tage S. Rai, Seth Thomas Scanlon (UK), Yury V. Suleymanov **LETTERS EDITOR** Jennifer Sills **LEAD CONTENT PRODUCTION EDITORS** Harry Jach, Lauren Kmec **CONTENT PRODUCTION EDITORS** Amelia Beyna, Jeffrey E. Cook, Chris Filiatreau, Julia Katris, Nida Masiulis, Suzanne M. White **SR. EDITORIAL COORDINATORS** Carolyn Kyle, Beverly Shields **EDITORIAL COORDINATORS** Aneera Dobbins, Joi S. Granger, Jeffrey Hearn, Lisa Johnson, Maryrose Madrid, Ope Martins, Shannon McMahon, Jerry Richardson, Hilary Stewart (UK), Alana Warnke, Alice Whaley (UK), Anita Wynn **PUBLICATIONS ASSISTANTS** Jeremy Dow, Alexander Kief, Ronmel Navas, Brian White **EXECUTIVE ASSISTANT** Jessica Slater **ASI DIRECTOR, OPERATIONS** Janet Clements (UK) **ASI SR. OFFICE ADMINISTRATOR** Jessica Waldock (UK)

News Editor Tim Appenzeller

NEWS MANAGING EDITOR John Travis **INTERNATIONAL EDITOR** Martin Enserink **DEPUTY NEWS EDITORS** Elizabeth Culotta, Lila Guterman, David Grimm, Eric Hand (Europe), David Malakoff **SR. CORRESPONDENTS** Daniel Clery (UK), Jon Cohen, Jeffrey Mervis, Elizabeth Pennisi **ASSOCIATE EDITORS** Jeffrey Brainard, Catherine Matacic **NEWS REPORTERS** Adrian Cho, Jennifer Couzin-Frankel, Jocelyn Kaiser, Kelly Servick, Robert F. Service, Erik Stokstad, Paul Voosen, Meredith Wadman **INTERNS** Lucy Hicks, Cathleen O'Grady **CONTRIBUTING CORRESPONDENTS** Warren Cornwall, Andrew Curry (Berlin), Ann Gibbons, Sam Kean, Eli Kintisch, Kai Kupferschmidt (Berlin), Andrew Lawler, Mitch Leslie, Eliot Marshall, Virginia Morell, Dennis Normile (Shanghai), Elisabeth Pain (Careers), Charles Piller, Michael Price, Tania Rabesandratana (Barcelona), Joshua Sokol, Emily Underwood, Gretchen Vogel (Berlin), Lizzie Wade (Mexico City) **CAREERS** Donisha Adams, Rachel Bernstein (Editor), Katie Langin (Associate Editor) **COPY EDITORS** Julia Cole (Senior Copy Editor), Cyra Master (Copy Chief) **ADMINISTRATIVE SUPPORT** Meagan Weiland

Creative Director Beth Rakouskas

DESIGN MANAGING EDITOR Marcy Atarod **GRAPHICS MANAGING EDITOR** Alberto Cuadra **PHOTOGRAPHY MANAGING EDITOR** William Douthitt **WEB CONTENT STRATEGY MANAGER** Kara Estelle-Powers **DESIGN EDITOR** Chrystal Smith **DESIGNER** Christina Aycock **GRAPHICS EDITOR** Nirja Desai **INTERACTIVE GRAPHICS EDITOR** Kelly Franklin **SENIOR SCIENTIFIC ILLUSTRATORS** Valerie Altounian, Chris Bickel **SCIENTIFIC ILLUSTRATOR** Alice Kitterman **SENIOR GRAPHICS SPECIALISTS** Holly Bishop, Nathalie Cary **SENIOR PHOTO EDITOR** Emily Petersen **PHOTO EDITOR** Kaitlyn Dolan **WEB DESIGNER** Jennie Pajerowski

Chief Executive Officer and Executive Publisher Sudip Parikh

Publisher, Science Family of Journals Bill Moran

DIRECTOR, BUSINESS SYSTEMS AND FINANCIAL ANALYSIS Randy Yi **DIRECTOR, BUSINESS OPERATIONS & ANALYSIS** Eric Knott **DIRECTOR OF ANALYTICS** Enrique Gonzales **MANAGER, BUSINESS OPERATIONS** Jessica Tierney **SENIOR BUSINESS ANALYST** Cory Lipman, Meron Kebede **FINANCIAL ANALYST** Alexander Lee **ADVERTISING SYSTEM ADMINISTRATOR** Tina Burks **SENIOR SALES COORDINATOR** Shirley Young **DIGITAL/PRINT STRATEGY MANAGER** Jason Hillman **QUALITY TECHNICAL MANAGER** Marcus Spiegler **ASSISTANT MANAGER DIGITAL/PRINT** Rebecca Doshi **SENIOR CONTENT SPECIALISTS** Steve Forrester, Jacob Hedrick, Antoinette Hodal, Lori Murphy **PRODUCTION SPECIALIST** Kristin Wowk **DIGITAL PRODUCTION MANAGER** Lisa Stanford **CONTENT SPECIALIST** Kimberley Oster **ADVERTISING PRODUCTION OPERATIONS MANAGER** Deborah Tompkins **DESIGNER, CUSTOM PUBLISHING** Jeremy Huntsinger **SR. TRAFFIC ASSOCIATE** Christine Hall **SPECIAL PROJECTS ASSOCIATE** Sarah Dhere

ASSOCIATE DIRECTOR, BUSINESS DEVELOPMENT Justin Sawyers **GLOBAL MARKETING MANAGER** Allison Pritchard **DIGITAL MARKETING MANAGER** Aimee Aponte **JOURNALS MARKETING MANAGER** Shawana Arnold **MARKETING ASSOCIATES** Tori Velasquez, Mike Romano, Ashley Hylton **DIGITAL MARKETING SPECIALIST** Asleigh Rojanavongse **SENIOR DESIGNER** Kim Huynh

DIRECTOR AND SENIOR EDITOR, CUSTOM PUBLISHING Sean Sanders **ASSISTANT EDITOR, CUSTOM PUBLISHING** Jackie Oberst

DIRECTOR, PRODUCT & PUBLISHING DEVELOPMENT Chris Reid **DIRECTOR, BUSINESS STRATEGY AND PORTFOLIO MANAGEMENT** Sarah Whalen **ASSOCIATE DIRECTOR, PRODUCT MANAGMENT** Kris Bishop **PRODUCT DEVELOPMENT MANAGER** Scott Chernoff **PUBLISHING TECHNOLOGY MANAGER** Michael Di Natale **SR. PRODUCT ASSOCIATE** Robert Koepke **SPJ ASSOCIATE** Samantha Bruno Fuller

DIRECTOR, INSTITUTIONAL LICENSING Iquo Edim **ASSOCIATE DIRECTOR, RESEARCH & DEVELOPMENT** Elisabeth Leonard **MARKETING MANAGER** Kess Knight **SENIOR INSTITUTIONAL LICENSING MANAGER** Ryan Rexroth **INSTITUTIONAL LICENSING MANAGER** Marco Castellan **MANAGER, AGENT RELATIONS & CUSTOMER SUCCESS** Judy Lillibridge **SENIOR OPERATIONS ANALYST** Lana Guz **FULFILLMENT COORDINATOR** Melody Stringer **SALES COORDINATOR** Josh Haverlock

DIRECTOR, GLOBAL SALES Tracy Holmes **US EAST COAST AND MID WEST SALES** Stephanie O'Connor **US WEST COAST SALES** Lynne Stickrod **US SALES MANAGER, SCIENCE CAREERS** Claudia Paulsen-Young **US SALES REP, SCIENCE CAREERS** Tracy Anderson **ASSOCIATE DIRECTOR, ROW** Roger Goncalves **SALES REP, ROW** Sarah Lelarge **SALES ADMIN ASSISTANT, ROW** Bryony Cousins **DIRECTOR OF GLOBAL COLLABORATION AND ACADEMIC PUBLISHING RELATIONS, ASIA** Xiaoying Chu **ASSOCIATE DIRECTOR, INTERNATIONAL COLLABORATION** Grace Yao **SALES MANAGER** Danny Zhao **MARKETING MANAGER** Kilo Lan **ASCA CORPORATION, JAPAN** Kaoru Sasaki (Tokyo), Miyuki Tani (Osaka) **COLLABORATION/CUSTOM PUBLICATIONS/JAPAN** Adarsh Sandhu

DIRECTOR, COPYRIGHT, LICENSING AND SPECIAL PROJECTS Emilie David **RIGHTS AND LICENSING COORDINATOR** Jessica Adams **RIGHTS AND PERMISSIONS ASSOCIATE** Elizabeth Sandler **CONTRACTS AND LICENSING ASSOCIATE** Lili Catlett

MAIN HEADQUARTERS
Science/AAAS
1200 New York Ave. NW
Washington, DC 20005

SCIENCE INTERNATIONAL
Clarendon House
Clarendon Road
Cambridge, CB2 8FH, UK

SCIENCE CHINA
Room 1004, Culture Square
No. 59 Zhongguancun St.
Haidian District, Beijing, 100872

SCIENCE JAPAN
ASCA Corporation
Sibaura TY Bldg. 4F, 1-14-5
Shibaura Minato-ku
Tokyo, 108-0073 Japan

EDITORIAL
science_editors@aaas.org

NEWS
science_news@aaas.org

INFORMATION FOR AUTHORS
sciencemag.org/authors/science-information-authors

REPRINTS AND PERMISSIONS
sciencemag.org/help/reprints-and-permissions

MEDIA CONTACTS
scipak@aaas.org

MULTIMEDIA CONTACTS
SciencePodcast@aaas.org
ScienceVideo@aaas.org

INSTITUTIONAL SALES AND SITE LICENSES
sciencemag.org/librarian

PRODUCT ADVERTISING & CUSTOM PUBLISHING
advertising.sciencemag.org/products-services
science_advertising@aaas.org

CLASSIFIED ADVERTISING
advertising.sciencemag.org/science-careers
advertise@sciencecareers.org

JOB POSTING CUSTOMER SERVICE
employers.sciencecareers.org
support@sciencecareers.org

MEMBERSHIP AND INDIVIDUAL SUBSCRIPTIONS
sciencemag.org/subscriptions

MEMBER BENEFITS
aaas.org/membercentral

AAAS BOARD OF DIRECTORS
CHAIR Steven Chu
PRESIDENT Claire M. Fraser
PRESIDENT-ELECT Susan G. Amara
TREASURER Carolyn N. Ainslie
CHIEF EXECUTIVE OFFICER
Sudip Parikh
BOARD Cynthia M. Beall
Rosina M. Bierbaum
Ann Bostrom
Stephen P.A. Fodor
S. James Gates, Jr.
Laura H. Greene
Kaye Husbands Fealing
Maria M. Klawe
Robert B. Millard
Alondra Nelson
William D. Provine

Science serves as a forum for discussion of important issues related to the advancement of science by publishing material on which a consensus has been reached as well as including the presentation of minority or conflicting points of view. Accordingly, all articles published in *Science*—including editorials, news and comment, and book reviews—are signed and reflect the individual views of the authors and not official points of view adopted by AAAS or the institutions with which the authors are affiliated.

BOARD OF REVIEWING EDITORS (Statistics board members indicated with **(S)**)

Takuzo Aida, *U. of Tokyo*
Leslie Aiello, *Wenner-Gren Foundation*
Deji Akinwande, *UT Austin*
Judith Allen, *U. of Manchester*
Marcella Alsan, *Harvard U.*
Sebastian Amigorena, *Institut Curie*
James Analytis, *UC Berkeley*
Trevor Archer, *NIEHS, NIH*
Paola Arlotta, *Harvard U.*
David Awschalom, *U. of Chicago*
Clare Baker, *U. of Cambridge*
Delia Baldassarri, *NYU*
Nenad Ban, *ETH Zürich*
Franz Bauer, *Pontificia U. Católica de Chile*
Ray H. Baughman, *UT Dallas*
Carlo Beenakker, *Leiden U.*
Yasmine Belkaid, *NIAID, NIH*
Philip Benfey, *Duke U.*
Kiros T. Berhane, *Columbia U.*
Bradley Bernstein, *Mass. General Hospital*
Joseph J. Berry, *NREL*
Alessandra Biffi, *Harvard Med.*
Chris Bowler, *École Normale Supérieure*
Ian Boyd, *U. of St. Andrews*
Emily Brodsky, *UC Santa Cruz*
Ron Brookmeyer, *UCLA* **(S)**
Christian Büchel, *UKE Hamburg*
Dennis Burton, *Scripps Res.*
Carter Tribley Butts, *UC Irvine*
György Buzsáki, *NYU School of Med.*
Mariana Byndloss, *Vanderbilt U. Med. Ctr*
Annmarie Carlton, *UC Irvine*
Nick Chater, *U. of Warwick*
Ling-Ling Chen, *SIBCB, CAS*
M. Keith Chen, *UCLA*
Zhijian Chen, *UT Southwestern Med. Ctr.*
Ib Chorkendorff, *Denmark TU*
Ibrahim Cissé, *Caltech*
James J. Collins, *MIT*
Robert Cook-Deegan, *Arizona State U.*
Virginia Cornish *Columbia U.*
Carolyn Coyne, *U. of Pitt.*
Roberta Croce, *VU Amsterdam*
Ismaila Dabo, *Penn State U.*
Jeff L. Dangl, *UNC*
Chiara Daraio, *Caltech*
Nicolas Dauphas, *U. of Chicago*
Christian Davenport, *U. of Michigan*
Frans de Waal, *Emory U.*
Claude Desplan, *NYU*
Sandra Díaz, *U. Nacional de Córdoba*
Ulrike Diebold, *TU Wien*
Stefanie Dimmeler, *Goethe-U. Frankfurt*
Hong Ding, *Inst. of Physics, CAS*
Dennis Discher, *UPenn*
Jennifer A. Doudna, *UC Berkeley*
Ruth Drdla-Schutting, *Med. U. Vienna*
Raissa M. D'Souza, *UC Davis*
Bruce Dunn, *UCLA*
William Dunphy, *Caltech*
Scott Edwards, *Harvard U.*
Todd Ehlers, *U. of Tübingen*
Jennifer Elisseeff, *Johns Hopkins U.*
Andrea Encalada, *U. San Francisco de Quito*
Nader Engheta, *U. of Penn.*
Karen Ersche, *U. of Cambridge*
Beate Escher, *UFZ & U. of Tübingen*
Barry Everitt, *U. of Cambridge*
Vanessa Ezenwa, *U. of Georgia*
Michael Feuer, *GWU*
Toren Finkel, *U. of Pitt. Med. Ctr.*
Gwenn Flowers, *Simon Fraser U.*
Peter Fratzl, *Max Planck Inst. Potsdam*
Elaine Fuchs, *Rockefeller U.*
Jay Gallagher, *U. of Wisconsin*
Daniel Geschwind, *UCLA*
Ramon Gonzalez, *U. of South Florida*
Sandra González-Bailón, *UPenn*
Elizabeth Grove, *U. of Chicago*
Nicolas Gruber, *ETH Zürich*
Hua Guo, *U. of New Mexico*
Taekjip Ha, *Johns Hopkins U.*
Sharon Hammes-Schiffer, *Yale U.*
Wolf-Dietrich Hardt, *ETH Zürich*
Louise Harra, *U. Coll. London*
Jian He, *Clemson U.*
Carl-Philipp Heisenberg, *IST Austria*
Ykä Helariutta, *U. of Cambridge*
Janet G. Hering, *Eawag*
Heather Hickman, *NIAID, NIH*
Hans Hilgenkamp, *U. of Twente*
Kai-Uwe Hinrichs, *U. of Bremen*
Deirdre Hollingsworth, *U. of Oxford*
Randall Hulet, *Rice U.*
Auke Ijspeert, *EPFL*
Akiko Iwasaki, *Yale U.*
Stephen Jackson, *USGS & U. of Arizona*
Erich Jarvis, *Rockefeller U.*
Peter Jonas, *IST Austria*
Matt Kaeberlein, *U. of Wash.*
William Kaelin Jr., *Dana-Farber Cancer Inst.*
Daniel Kammen, *UC Berkeley*
Kisuk Kang, *Seoul Nat. U.*
V. Narry Kim, *Seoul Nat. U.*
Robert Kingston, *Harvard Med.*
Nancy Knowlton, *Smithsonian Institution*
Etienne Koechlin, *École Normale Supérieure*
Alex L. Kolodkin, *Johns Hopkins U.*
Julija Krupic, *U. of Cambridge*
Gabriel Lander, *Scripps Res.* **(S)**
Mitchell A. Lazar, *UPenn*
Wendell Lim, *UCSF*
Luis Liz-Marzán, *CIC biomaGUNE*
Omar Lizardo, *UCLA*
Jonathan Losos, *Wash. U. in St. Louis*
Ke Lu, *Inst. of Metal Res., CAS*
Christian Lüscher, *U. of Geneva*
Jean Lynch-Stieglitz, *Georgia Inst. of Tech.*
David Lyons, *U. of Edinburgh*
Fabienne Mackay, *QIMR Berghofer*
Anne Magurran, *U. of St. Andrews*
Asifa Majid, *U. of York*
Oscar Marín, *King's Coll. London*
Charles Marshall, *UC Berkeley*
Christopher Marx, *U. of Idaho*
David Masopust, *U. of Minnesota*
Geraldine Masson, *CNRS*
Jason Matheny, *Georgetown U.*
Heidi McBride, *McGill U.*
C. Robertson McClung, *Dartmouth*
Rodrigo Medellín, *U. Nacional Autónoma de México*
Jane Memmott, *U. of Bristol*
C. Jessica Metcalf, *Princeton U.*
Baoxia Mi, *UC Berkeley*
Tom Misteli, *NCI, NIH*
Alison Motsinger-Reif, *NIEHS, NIH* **(S)**
Danielle Navarro, *U. of New South Wales*
Nicholas Navin, *MD Anderson*
Daniel Nettle, *Newcastle U.*
Daniel Neumark, *UC Berkeley*
Beatriz Noheda, *U. of Groningen*
Helga Nowotny, *Vienna Sci., Res. & Tech. Fund*
Rachel O'Reilly, *U. of Birmingham*
Pilar Ossorio, *U. of Wisconsin*
Andrew Oswald, *U. of Warwick*
Isabella Pagano, *Istituto Nazionale di Astrofisica*
Elizabeth Levy Paluck, *Princeton U.*
Jane Parker, *Max Planck Inst. Cologne*
Giovanni Parmigiani, *Dana-Farber Cancer Inst.* **(S)**
Daniel Pauly, *U. of British Columbia*
Samuel Pfaff, *Salk Inst.*
Julie Pfeiffer, *UT Southwestern Med. Ctr.*
Philip Phillips, *UIUC*
Matthieu Piel, *Institut Curie*
Kathrin Plath, *UCLA*
Martin Plenio, *Ulm U.*
Katherine Pollard, *UCSF*
Elvira Poloczanska, *Alfred-Wegener-Inst.*
Julia Pongratz, *Ludwig Maximilians U.*
Philippe Poulin, *CNRS*
Jonathan Pritchard, *Stanford U.*
Lei Stanley Qi, *Stanford U.*
Trevor Robbins, *U. of Cambridge*
Joeri Rogelj, *Imperial Coll. London*
Amy Rosenzweig, *Northwestern U.*
Mike Ryan, *UT Austin*
Miquel Salmeron, *Lawrence Berkeley Nat. Lab*
Nitin Samarth, *Penn State U.*
Erica Ollmann Saphire, *La Jolla Inst.*
Joachim Saur, *U. zu Köln*
Alexander Schier, *Harvard U.*
Wolfram Schlenker, *Columbia U.*
Susannah Scott, *UC Santa Barbara*
Anuj Shah, *U. of Chicago*
Vladimir Shalaev, *Purdue U.*
Jie Shan, *Cornell U.*
Beth Shapiro, *UC Santa Cruz*
Jay Shendure, *U. of Wash.*
Steve Sherwood, *U. of New South Wales*
Brian Shoichet, *UCSF*
Robert Siliciano, *JHU School of Med.*
Lucia Sivilotti, *U. Coll. London*
Alison Smith, *John Innes Centre*
Richard Smith, *UNC* **(S)**
Mark Smyth, *QIMR Berghofer*
John Speakman, *U. of Aberdeen*
Tara Spires-Jones, *U. of Edinburgh*
Allan C. Spradling, *Carnegie Institution for Sci.*
V. S. Subrahmanian, *Dartmouth*
Ira Tabas, *Columbia U.*
Eriko Takano, *U. of Manchester*
Patrick Tan, *Duke-NUS Med. School*
Sarah Teichmann, *Wellcome Sanger Inst.*
Rocio Titiunik, *Princeton U.*
Shubha Tole, *Tata Inst. of Fundamental Res.*
Kimani Toussaint, *Brown U.*
Wim van der Putten, *Netherlands Inst. of Ecology*
Reinhilde Veugelers, *KU Leuven*
Bert Vogelstein, *Johns Hopkins U.*
David Wallach, *Weizmann Inst.*
Jane-Ling Wang, *UC Davis* **(S)**
Jessica Ware, *Amer. Mus. of Natural Hist.*
David Waxman, *Fudan U.*
Chris Wikle, *U. of Missouri* **(S)**
Terrie Williams, *UC Santa Cruz*
Ian A. Wilson, *Scripps Res.* **(S)**
Yu Xie, *Princeton U.*
Jan Zaanen, *Leiden U.*
Kenneth Zaret, *UPenn School of Med.*
Bing Zhu, *Inst. of Biophysics, CAS*
Xiaowei Zhuang, *Harvard U.*
Maria Zuber, *MIT*

Gordon Research Conferences

Innovation by Inorganic Chemistry

Tuesday, April 20, 2021
11:00AM — 1:00PM ET

SPEAKERS:

Dr. Harry Gray,
California Institute of Technology

Dr. Richard Eisenberg,
University of Rochester

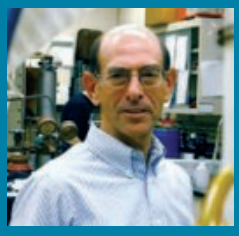

MODERATOR:

Dr. Kara Bren,
University of Rochester

Join us virtually for presentations by and discussions between Dr. Harry Gray and Dr. Richard Eisenberg who will discuss the role GRCs played in the great advances in inorganic chemistry during their careers.

Our virtual initiative, GRC Connects, provides scientific communities with short and informative opportunities to connect and collaborate with their GRC colleagues until we can resume in-person conferences, furthering GRC's commitment to find new and creative ways to advance the frontiers of science.

This free event is open to all members of the scientific community and scientists of all career stages are encouraged to attend.

"GRCs really bring chemists in a specific field or working on a particular research challenge together in substantial ways. GRC greatly helped develop a sense of community in our field."

— Dr. Richard Eisenberg

Visit www.grc.org today to register for this free Connects event and one of the 17 GRCs and GRSs scheduled to take place, in person, in October and November in New England and California. We look forward to connecting with and seeing you soon!

RECENT PHD IN CELL AND MOLECULAR BIOLOGY?

Gain international recognition, win 30,000 USD, and have your thesis essay published in Science.

The Science & SciLifeLab Prize for Young Scientists is a global prize aimed at rewarding scientists at an early stage of their careers, awarded in four categories.

Research in this category includes cellular and molecular processes at levels ranging from single molecule to single cell to tissue and organ systems

Entrants for the 2021 prize must have received their PhD after January 1, 2019.

APPLY FOR THE *SCIENCE* & SCILIFELAB PRIZE FOR YOUNG SCIENTISTS

APPLY BEFORE JULY 15, 2021

SCIENCEPRIZE.SCILIFELAB.SE

Science & SciLifeLab PRIZE For Young Scientists

Science AAAS

SciLifeLab

Knut och Alice Wallenbergs Stiftelse

EDITORIAL

The story behind COVID-19 vaccines

Amid the staggering amount of suffering and death during this historic pandemic of COVID-19, a remarkable success story stands out. The development of several highly efficacious vaccines against a previously unknown viral pathogen, severe acute respiratory syndrome coronavirus 2 (SARS-CoV-2), in less than 1 year from the identification of the virus is unprecedented in the history of vaccinology. A frequently asked question is how such an extraordinary accomplishment could have been realized in such a short time frame, when timelines for other vaccines are measured in years if not decades. In fact, concern about this truncated timeline has contributed in part to the hesitancy in accepting these vaccines. What is not fully appreciated is that the starting point of the timeline for SARS-CoV-2 vaccines was not 10 January 2020, when the Chinese published the genetic sequence of the virus. Rather, it began decades earlier, out of the spotlight.

Two activities predate the successful COVID-19 vaccines: the utilization of highly adaptable vaccine platforms such as RNA (among others) and the adaptation of structural biology tools to design agents (immunogens) that powerfully stimulate the immune system. The RNA approach evolved over several years owing to the ingenuity of individual scientists, including Drew Weissman and Katalin Karikó, and the concentrated efforts of several biotech and pharmaceutical companies.

The discovery of an immunogen adaptable to the multiple platforms (messenger RNA and others) used for COVID-19 vaccines resulted from collaboration across different scientific subspecialities. At the Vaccine Research Center (VRC) of the U.S. National Institute of Allergy and Infectious Diseases, a group led by Peter Kwong had for several years used tools of structure-based vaccine design to determine the optimal structural conformation of a trimeric protein on the surface of the virus (the envelope protein) that allows HIV to bind to cells and ultimately trigger the production of antibodies that neutralize many HIV viral strains. Although this sophisticated approach has not yet led to a successful HIV vaccine, it caught the attention of another VRC investigator, Barney Graham, who was interested in generating a vaccine for respiratory syncytial virus (RSV). Graham joined Jason McLellan (of Kwong's team) to adapt a structure-based approach to an RSV vaccine. They identified the prefusion conformation of the viral spike protein as highly immunogenic and created mutations to stabilize that conformation for successful use as an immunogen. This was a huge step toward the creation of a successful RSV vaccine.

VRC researchers and colleagues then built on the RSV advances. Graham's team, including Kizzmekia Corbett, and collaborators in the laboratories of McLellan and Andrew Ward adopted this approach of mutational stabilization of prefusion proteins in their work on the spike protein of the coronaviruses that cause Middle East respiratory syndrome (MERS) and severe acute respiratory syndrome (SARS). So, when the genetic sequence of the SARS-CoV-2 became available, Graham's team lost no time in joining their long-time collaborators at Moderna to develop an RNA vaccine using a stabilized, prefusion spike protein as the immunogen. Pfizer and BioNTech, where Karikó was working, also used the RNA platform that she and Weissman had perfected and the immunogen designed by Graham to develop an RNA vaccine. Additional companies also used Graham's immunogen in other vaccine platforms that had been evolving for years, to make SARS-CoV-2 vaccines.

> "When the stories...of this pandemic are written, it is important that this history not be forgotten..."

SARS-CoV-2 vaccines based on the new immunogen rapidly moved to clinical trials. Several of these vaccines were tested in phase 3 efficacy trials at a time when the level of community spread of SARS-CoV-2 was extremely high, allowing vaccine efficacy endpoints of greater than 90% to be reached in a timely fashion. The speed and efficiency with which these highly efficacious vaccines were developed and their potential for saving millions of lives are due to an extraordinary multidisciplinary effort involving basic, preclinical, and clinical science that had been under way—out of the spotlight—for decades before the unfolding of the COVID-19 pandemic. When the stories and recounting of this pandemic are written, it is important that this history not be forgotten, as we are reminded once again of the societal value of a sustained and robust support of our scientific enterprise.

–Anthony S. Fauci

PHOTO: NATIONAL INSTITUTE OF ALLERGY AND INFECTIOUS DISEASES

Anthony S. Fauci is director of the National Institute of Allergy and Infectious Diseases, National Institutes of Health, Bethesda, MD, USA. afauci@niaid.nih.gov

10.1126/science.abi8397

NEWS

> "I'm calling it a cicada-palooza."
>
> **Entomologist Mike Raupp** of the University of Maryland, College Park, in *Forbes*, on the massive emergence of cicadas expected this summer in the eastern United States.

IN BRIEF

Edited by **Jeffrey Brainard**

PUBLIC HEALTH

Pfizer shots work in younger teens

COVID-19 vaccines for younger teens may be coming soon: The companies Pfizer and BioNTech announced last week their shot provided powerful protection in 12- to 15-year-olds. In a randomized controlled trial with 2260 participants from that age group, the more than 1100 who received the vaccine showed high levels of protective antibodies—surpassing levels previously recorded in 16- and 25-year-olds—and no COVID-19 cases, the manufacturers said in a press release. No serious safety issues were reported, although data from the trial have yet to be published. The Pfizer-BioNTech vaccine is currently the only one authorized in the United States for 16- and 17-year-olds. The companies now plan to seek authorization for their vaccine in the younger age group, which doctors and scientists say is critical to taming the pandemic. Pfizer and BioNTech recently began another trial in even younger children, 6 months to 11 years old.

Fusion reactor reaches milestone

ENERGY | Fusion energy startup TAE Technologies announced this week that its latest fusion device has achieved high temperatures and long reaction durations—putting the well-financed company on a clear path to a larger machine that could generate net energy, it says. Fusion researchers aim to heat ionized gases so that atomic nuclei fuse together, releasing more energy than the heating consumes. Traditional approaches confine the gas with powerful magnets or crush it with lasers, but TAE's machine creates a spinning "smoke ring" of gas, which generates its own confining magnetic field, and boosts its spin with particle beams. The latest, 30-meter-long machine, dubbed Norman, after TAE co-founder Norman Rostoker, heated gas to more than 50 million degrees Celsius for 30 milliseconds—eight times hotter and 10 times longer than the company's previous machines, TAE said. Hydrogen isotopes fuse at 100 million degrees Celsius, but TAE needs to reach much higher temperatures of 1 billion degrees Celsius because it plans to fuel its machine with regular hydrogen and boron, which are easier to obtain. The company has raised $880 million from investors.

FDA OKs cheap home virus tests

DIAGNOSTICS | The U.S. Food and Drug Administration (FDA) last week authorized two inexpensive, rapid COVID-19 tests to be sold over the counter, allowing people to test themselves. Their widespread availability is expected to help schools and offices reopen safely; testing multiple times per week has been shown to catch asymptomatic carriers and limit the spread of SARS-CoV-2. The tests, Abbott Laboratories's BinaxNOW and Quidel's QuickVue At-Home, detect antigens—proteins unique to the virus—in a nasal swab and can return results in as little as 10 minutes. They are typically less accurate than polymerase chain reaction tests, which must be processed in a laboratory, at greater cost and delay. The Abbott test is expected to cost $25 and the Quidel test $20. FDA had previously authorized both tests but required a doctor's prescription.

Want citations? Drop the jargon

PUBLISHING | Scientists who want other researchers to cite their work should steer clear of discipline-specific jargon in the title and abstract, a study suggests. It measured the use of jargon in about 20,000 published papers about cave science, a field the authors say they chose to examine because it is multidisciplinary and "particularly prone to terminological specialization." The most highly cited papers didn't use any jargon in the title and kept jargon to less than 2% of the text in the abstract. Jargon-heavy papers weren't cited as much—a finding that held up regardless of whether the analysis was restricted to papers published in cave-specific journals, the authors report this week in the *Proceedings of the Royal Society B*.

Microbiome beats malnutrition

POVERTY | A nutritional supplement that fosters healthy gut bacteria has been shown to help young children in Bangladesh grow normally after being severely malnourished. About 120 toddlers received a standard supplement or the experimental one, called Microbiota-Directed Complementary Food, made of locally sourced food that nurtures certain gut microbes. The children receiving it had a greater increase in blood proteins and other components indicative of

Workers measure the growth of a 7-month-old girl at a refugee camp in Bangladesh.

PHOTO: TOM PILSTON/PANOS PICTURES/REDUX

PHYSIOLOGY

Vibrant world of fish larvae unveiled

At long last, the vibrant colors and odd physiques of larval fishes have come into view. The tiny larvae are often mangled in nets; intact specimens' colors are bleached by preservative. But fish scientists at the Smithsonian Institution's National Museum of Natural History and Ocean Research Explorations teamed up with recreational scuba divers in Kona, Hawaii, to devise a different technique. During night dives, they lit, photographed, and gently captured larvae from 76 species that had risen in the water column at night to feed. The method captures their blue hues and bright white, yellow, and orange spots, and unusual appendages likely useful for these ocean drifters during development, the researchers reported last week in *Ichthyology & Herpetology*. They used DNA to identify the specimens, including the deep-sea tripod fish (*Bathymicrops*, shown alive— top, about 2 centimeters long—and preserved). The authors called the collection a first, and they hope more divers will be recruited to help expand it.

PHOTOS: (TOP TO BOTTOM) JEFFREY W. MILISEN; AI NONAKA

restored growth, and had twice the recorded growth rate, as measured by a weight-to-length score, as the others, the researchers reported this week in *The New England Journal of Medicine*. The improved growth rate continued after treatment was stopped.

Geoengineering test delayed

CLIMATE CHANGE | Following the advice of an advisory board, Harvard University researchers last week postponed the first flight in a controversial study of how light-blocking particles, released in the stratosphere, could diminish global warming. The trial of the Stratospheric Controlled Perturbation Experiment's steerable balloon, planned for launch in June from Kiruna, Sweden, would not have released any particles. Nevertheless, the project's plan to eventually deploy up to 2 kilograms of calcium carbonate—chalk dust, essentially—has met fierce opposition from Swedish environmental groups. The team will now ask the Swedish public for feedback, which will likely delay the first flight until 2022 and could move it to a new location.

EPA to remake advisory panels

ENVIRONMENTAL POLICY | The Biden administration is overhauling two key science advisory boards at the U.S. Environmental Protection Agency (EPA), responding to concerns that the Trump administration had stacked the panels with industry-friendly experts. EPA Administrator Michael Regan last week announced he was dismissing all 44 members of the top-level Science Advisory Board and all seven members of the Clean Air Scientific Advisory Committee. Regan said a "reset" was needed to "reverse deficiencies" and restore trust in the panels, which in recent years have been embroiled in fierce controversies over setting safe levels of human exposure to air pollution and toxic chemicals. EPA is now accepting nominations for the panels through 3 May.

Gender gap in MIT corporate ties

GENDER EQUITY | The Massachusetts Institute of Technology (MIT) this week reported striking differences between the rates at which female and male professors have founded companies in biotechnology and related fields or served on their boards. Of more than 1000 company launches and invitations to serve on boards between 2000 and 2018, female faculty members in seven science and engineering departments accounted for 9% although they represent 22% of the 337 faculty surveyed. Women in the biology department, where they were 24% of the faculty, were especially under-represented: Men founded 55 companies and women only two. The authors estimated that if women had founded companies at the same rate as their male peers, 40 more biotechnology firms would exist today. In response, MIT faculty and venture capitalists are collaborating on a new project to boost women's representation in biotech. The study was written by MIT President Emeritus Susan Hockfield, MIT physician-engineer and biotech entrepreneur Sangeeta Bhatia, and MIT emeritus biologist Nancy Hopkins, who led a groundbreaking 1999 report that documented discrimination against MIT female faculty members.

President Joe Biden wants to bolster the National Science Foundation as part of his massive infrastructure plan, which he outlined last week in Pittsburgh.

U.S. SCIENCE POLICY

Biden, Congress roll out big plans to expand NSF

President and lawmakers push proposals to add technology directorate and boost budget

By **Jeffrey Mervis**

The idea of massively expanding the budget and mission of the National Science Foundation (NSF) to help the United States out-innovate China is gaining political momentum in Washington, D.C.

In Congress, Senate Majority Leader Chuck Schumer (D–NY) is preparing to introduce a revised version of bipartisan legislation that would create a technology directorate at NSF and boost its funding by $100 billion. The changes address fears voiced by academic leaders that the new unit might disrupt the agency's culture and dilute NSF's ability to support basic research at universities.

On 31 March, President Joe Biden lined up behind the concept, including both the new directorate and a $50 billion bump for NSF in his $2.3 trillion proposal to upgrade the nation's aging infrastructure. And late last month, Representative Eddie Bernice Johnson (D–TX), chair of the science committee of the U.S. House of Representatives, also backed both a new directorate and a larger NSF budget as part of a bill reauthorizing programs at the agency, which currently has an $8.5 billion budget.

Congress is expected to begin hashing out the legislative details as early as next week. And Biden's vocal support for revamping NSF makes it more likely that something will happen. "I'd say that things are coming together amazingly well," one university lobbyist says. "It was a big win to get the president's support."

Media coverage of Biden's infrastructure plan has focused on rebuilding roads, bridges, mass transit, and housing. But in his Pittsburgh speech to labor union members, Biden also asked Congress to spend $180 billion on "technologies for the future."

That investment would include $35 billion for several agencies to combat climate change, as well as to create an Advanced Research Projects Agency-Climate (ARPA-C) to commercialize promising technologies. The plan also calls for a $40 billion upgrade to the nation's federal and academic research facilities, with one-half of the money going to the nation's more than 100 historically Black colleges and universities. The plan, Biden said, represents "the biggest increase in our federal nondefense research and development spending on record."

For many academic researchers, however, the most compelling news was Biden's support for beefing up NSF, the nation's second largest research funding agency after the National Institutes of Health.

The size of any NSF budget increase, including how much would go to the new directorate, is still very much up in the air. Schumer's original bill, introduced in May 2020, would have allocated $100 billion to the new directorate over 5 years, including $35 billion in each of the last 2 years. But the latest version, circulated last week, would instead give the money to NSF as a whole, with the new directorate receiving "not less than $2 billion a year."

The House bill proposes more modest growth for NSF, roughly doubling its overall budget to $18 billion by 2026. The directorate would be launched with $1 billion and grow to $5 billion over 5 years.

Biden's proposal appears to fall somewhere between the two bills. A fact sheet

New money, expanded mission

The Endless Frontier Act would authorize $100 billion over 5 years for the National Science Foundation (NSF). An undefined amount of the money would go to establishing a new technology directorate, which would apportion its spending across several areas.

Academic research centers on 10 key technologies	35%
Student support	15%
Existing NSF programs	15%
Grants to states with little NSF funding	12%
Technology testbed and fabrication facilities	10%
Help grantees commercialize discoveries	5%
Unspecified	8%

CREDITS: (PHOTO) JIM WATSON/AFP/GETTY IMAGES; (DATA) U.S. SENATE

accompanying his speech asks legislators "to invest $50 billion in NSF, creating a technology directorate that will collaborate with and build on existing programs across the government." It does not specify a budget timeline, although many of Biden's infrastructure spending plans are spread over 8 years. A White House aide says the new directorate would get most of the proposed $50 billion, which would supplement whatever Congress appropriates for NSF in the annual budget process.

Whatever the amount, proponents of the new directorate say it is needed to counter aggressive technology investments by China and other economic competitors. Schumer's bill, The Endless Frontier Act (EFA), is named after an influential 1945 report to then-President Franklin Roosevelt that led to the creation of NSF. And the bill praises NSF's 70-year history of funding research that has fueled U.S. economic growth and national security. But proponents say what it takes to do that has changed over the years, and that the bill is the right response to the current challenges facing the country.

"Just doing more of the same will not get us where we need to be," Massachusetts Institute of Technology President L. Rafael Reif wrote last year in one of many pieces advocating for the EFA legislation. The new technology directorate belongs at NSF, he adds, "precisely because it has been so successful. … It will give NSF a different way of approaching problems; to some extent, a different way of selecting and managing projects."

However, some academic leaders worry that an additional mission could hamper NSF. Under the original Senate bill, the new directorate would have quickly become several times larger than the combined size of NSF's seven existing research directorates. They also fretted about language suggesting it would operate in a more freewheeling fashion, akin to the vaunted Defense Advanced Research Projects Agency, where program managers rely heavily on their own judgment in making awards and can terminate projects abruptly if grantees fail to meet interim milestones. Critics also took issue with Schumer's plan to give the directorate its own deputy director—a higher rank than those leading the existing directorates—and a board of advisers that could set policies on what and whom to fund.

That structure "would promote a collision of cultures within the NSF," warned a group of prominent researchers and academic leaders that included Nobel laureates David Baltimore and Harold Varmus. In a February letter, the scientists also urged Schumer to avoid a steep budget ramp-up and instead move at a pace "commensurate with the long-term nature of scientific work."

Last month, seven former NSF directors met with Schumer's aides after writing him a letter that expressed support for the EFA, but also suggested giving NSF greater flexibility. "We are confident that NSF can meet the goals of this proposed legislation and deliver the expected outcomes if given sufficient resources and discretion in implementation," they wrote without mentioning the new directorate by name.

Schumer appears to have taken the advice to heart. The revised Senate bill, which could be introduced as soon as next week, makes the management structure of the new directorate identical to the rest of NSF's. It neither provides a timetable for the directorate's growth nor mandates its final size. Schumer also dropped the idea of changing NSF's name to the National Science and Technology Foundation, a nod to scientists who were worried that he wanted to dismantle the agency they know and love.

The new bill is also considerably larger. It retains a proposed $100 billion for NSF and $10 billion for a network of regional technology hubs to be created and run by the Department of Commerce. But it adds $10 billion to expand two manufacturing programs run by the department's National Institute of Standards and Technology. It also gives the department an additional $70 billion to stand up a program to strengthen and protect supply chains needed to support technologies critical to U.S. economic and national security.

Despite the emerging consensus on the need to revamp and expand NSF's mission, many hurdles remain. The House and Senate bills only authorize spending levels, with appropriations panels having the final say. That's why proponents are eager to see what Biden requests for NSF in his first budget to the Democratic-controlled Congress, expected in the next month. That proposed budget could also answer another big question for researchers: where the new ARPA-C entity would be housed and how it would operate.

How to pay for the massive boost for NSF—and for the trillions of dollars of other infrastructure investments Biden desires—remains a sticking point. Republicans and some moderate Democrats have vowed to fight Biden's proposal to raise the money by rolling back some of the corporate tax cuts enacted under former President Donald Trump. And if Congress rejects Biden's infrastructure plan, it's hard to imagine legislators approving a massive increase for NSF. ■

PARTICLE PHYSICS

For a change, a hint of new physics does not fade away

Reprise of storied experiment confirms muon's extra magnetism

By **Adrian Cho**

A potential chink in physicists' understanding of fundamental particles and forces now looks more real. New measurements confirm a fleeting subatomic particle called the muon may be ever so slightly more magnetic than theory predicts, a team of more than 200 physicists reported this week. That small anomaly—just 2.5 parts in 1 billion—is a welcome threat to particle physicists' prevailing theory, the standard model, which has long explained pretty much everything they've seen at atom smashers and left them pining for something new to puzzle over.

"Since the 1970s we've been looking for a crack in the standard model," says Alexey Petrov, a theorist at Wayne State University. "This may be it." But Sally Dawson, a theorist at Brookhaven National Laboratory, notes the result is still not definitive. "It does nothing for our understanding of physics other than to say we have to wait a little longer to see if it is real."

Persistent anomaly

Two measurements find the same excess magnetism in the muon, perhaps a hint of unknown new particles.

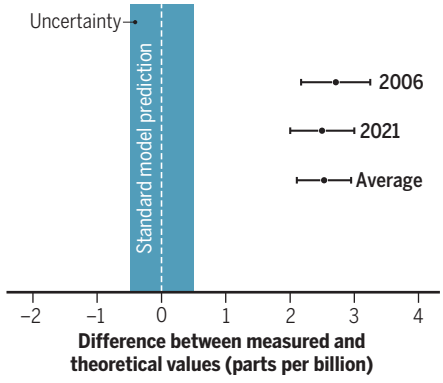

CREDITS: (GRAPHIC) V. ALTOUNIAN/SCIENCE; (DATA) B. ABI ET AL., PHYS. REV. LETT. 126, 141801 (2021)

Muons twirl as they circulate in this ring-shaped accelerator at Fermilab, like race cars perpetually spinning out.

PHOTO: REIDAR HAHN/FERMILAB

For decades, physicists have measured the magnetism of the muon, a heavier, unstable cousin of the electron, which behaves like a tiny bar magnet. They put muons in a vertical magnetic field that makes them twirl horizontally like little compass needles. The frequency at which the muons twirl reveals how magnetic they are, which in principle can point to new particles, even ones too massive to be blasted into existence at an atom smasher like Europe's Large Hadron Collider.

That's because, thanks to quantum uncertainty, the muon sits amid a haze of other particles and antiparticles flitting in and out of existence. These "virtual" particles can't be observed directly, but they can affect the muon's properties. Quantum mechanics and Albert Einstein's theory of special relativity predict the muon should have a certain basic magnetism. Familiar standard model particles flitting about the muon increase that magnetism by about 0.1%. And unknown particles lurking in the vacuum could add another, unpredictable increment of change.

In 2001, researchers with the Muon g-2 experiment, then at Brookhaven, reported that the muon was a touch more magnetic than the standard model predicts. The discrepancy was only about 2.5 times the combined theoretical and experimental uncertainties. That's nowhere near physicists' standard for claiming a discovery: five times the total uncertainty. But it was a tantalizing hint of new particles just beyond their grasp.

So in 2013, researchers hauled the experiment to Fermi National Accelerator Laboratory (Fermilab) in Illinois, where they could get purer beams of muons. By the time the revamped experiment started to take data in 2018, the standard model predictions of the muon's magnetism had improved and the difference between the experimental results and theory had risen to 3.7 times the total uncertainty.

Now, the g-2 team has released the first result from the revamped experiment, using 1 year's worth of data. And the new result agrees almost exactly with the old one, the team announced at a symposium at Fermilab on 7 April. The concordance shows the old result was neither a statistical fluke nor the product of some undetected flaw in the experiment, says Chris Polly, a Fermilab physicist and co-spokesperson for the g-2 team. "Because I was a graduate student on the Brookhaven experiment, it was certainly an overwhelming sense of relief for me," he says.

Together, the new and old results widen the disagreement with the standard model prediction to 4.2 times the experimental and theoretical errors. That's still not quite enough to claim a definite discovery. But in a field in which similar hints of new physics come and go, the magnetism of the muon has remained an almost singular puzzle, says Graham Kribs, a theorist at the University of Oregon. "There's nothing else that's really sort of standing out for which the entire community is like, 'Remember, we also have to deal with this.'"

The entire g-2 team shared a moment of truth when, on 25 February, the experimenters first revealed the new result to themselves. The experiment involves measuring the rate at which the muons twirl to exquisite precision. And to keep themselves from subconsciously steering the measurement to a value they'd prefer, experimenters relied on a clock ticking at a secret frequency known to only two people, both outside the collaboration. Only at the very end of the analysis did they open the envelopes containing the secret frequency—on a Zoom meeting because of COVID-19 restrictions. "Definitely there was this atmosphere of extreme tension," says Hannah Binney, a graduate student and team member from the University of Washington, Seattle. Within seconds, she says, researchers used the secret frequency to figure out that the new result matched the old one.

The immediate responses to the new result will likely be twofold, Petrov says. First, with the experimental value confirmed, physicists will likely question the theoretical estimate anew. Starting in 2017, more than 130 theorists met in a series of workshops to hammer out a consensus value for the standard model prediction, which they published in November 2020. But Petrov says the calculation is a complicated "hodgepodge" that employs a variety of methods—including extrapolating from collider results—to account for different types of standard model particles flitting in and out of the vacuum. Theorists will now redouble their efforts to validate the consensus value and to develop computational methods that would enable them to calculate it from first principles, Petrov says.

And, of course, others will begin to concoct new theories that would go beyond the standard model and explain the muon's extra magnetism. "This is going to be a field day for theorists," Petrov predicts. Their musings may be a tad premature, as g-2 experimenters are still taking data and hope to reduce the experimental uncertainty by 75% within a few years. So the discrepancy could still fade. But, on the chance that the muon is really signaling the presence of something new, many theorists will be eager to start. ■

HUMAN EVOLUTION

When modern humans met Neanderthals

Ancient genomes from first moderns in Europe tell stories of diverse origins, ancient trysts

By **Ann Gibbons**

The four-story labyrinth of galleries in Bulgaria's Bacho Kiro cave has long been a magnet for all sorts of humans. Neanderthals came first, more than 50,000 years ago, and left their characteristic Mousterian stone tools among the stalagmites. Next came modern humans in at least two waves; the first littered the cave floor with beads and stone blades stained with ochre, about 45,000 years ago. Another group settled in about 36,000 years ago with even more sophisticated artifacts.

Now, a new ancient DNA study shows the first group of modern humans at Bacho Kiro carried a recent legacy from Neanderthals: Those people's ancestors had interbred with our extinct cousins as recently as six generations, or 160 to 180 years, previously.

However, another study out this week, of what may be the oldest modern human in Europe, shows the first wave of moderns had diverse Neanderthal legacies. The genome of a dark-skinned, brown-haired, brown-eyed woman from Zlatý kůň cave in the Czech Republic included only 3% Neanderthal DNA, which likely came from a long-ago tryst in the Middle East, not from recent contact, the study suggests.

Taken together, these genomic snapshots offer a glimpse into the identities of the mysterious modern humans who first set foot in Europe and their relationship to Neanderthals, who vanished about 40,000 years ago.

This skull from Zlatý kůň cave near Prague belonged to the earliest known modern human in Europe.

"You're talking about multiple waves of modern humans," says paleoanthropologist Chris Stringer of the Natural History Museum in London. "Some groups mixed with Neanderthals, and some didn't. Some are related to later humans and some are not."

The new revelations fill out the story of these ancient encounters, says Mateja Hajdinjak, a postdoc at the Max Planck Institute for Evolutionary Anthropology (MPI) and an author of the Bacho Kiro study. "For the first time, we're getting ancient DNA from multiple early modern humans that tells us so much about their interactions with some of the very last Neanderthals in Europe," she says.

After modern humans trekked out of Africa 60,000 to 80,000 years ago, they interbred at least once with Neanderthals, most likely in the Middle East about 50,000 years ago, previous ancient DNA research has shown. Those studies include analyses of two early modern humans from Eurasia: a 45,000-year-old thigh bone of a man from Ust'-Ishim in Siberia, and the jawbone of a young man from Peştera cu Oase cave in Romania, dated to between 37,000 and 42,000 years ago. The Oase man inherited as much as 6.4% of his DNA from a recent Neanderthal ancestor. But he lived at least 5000 years after modern humans had arrived in Europe. This week's studies offer a genetic glimpse of an earlier time, when modern humans first ventured into Neanderthal territory.

Hajdinjak and MPI paleogeneticist Svante Pääbo analyzed genomes from Bacho Kiro, where last year researchers used a new protein-based method to show that bone fragments in a middle layer of cave sediments came from modern humans (*Science*, 15 May 2020, p. 697). In the new study, the researchers sequenced genomes from a molar and bone fragments from that middle layer and directly dated them to 42,580 to 45,930 years ago. They also sequenced DNA from bone found in a younger layer and dated it to 35,000 years ago. Remains from both layers were modern humans, but from different populations, they report in *Nature* this week.

The genomes show the three oldest modern humans at Bacho Kiro were distantly related to a 40,000-year-old partial skeleton from Tianyuan in China, as well as to other ancient and living East Asians and Native Americans. That suggests they all descended from an early population that once spread across Eurasia, but whose descendants in Europe seem to have died out. The lineage survived in Asia, later giving rise to people who migrated to America.

Those modern humans had also inherited 3% to 3.8% of their DNA from Neanderthal ancestors. The chunks of Neanderthal DNA were long, which suggested they arose from mixing only six generations earlier, because with each new generation, recombination breaks stretches of DNA in shorter fragments. That mating must have been differ-

Modern humans on the move

Findings from new sites (red) add to the handful of ancient DNA studies of the mysterious modern humans who first ventured into Eurasia and the Neanderthal homeland (blue).

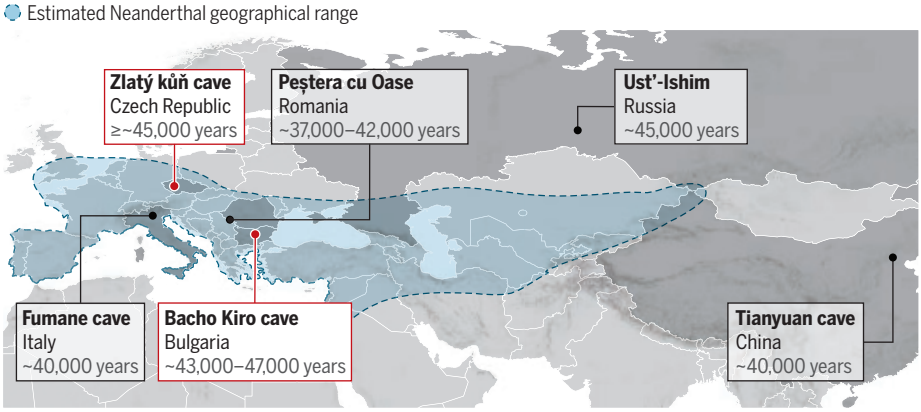

CREDITS: (PHOTO) MAREK JANTAČ; (MAP) K. FRANKLIN/*SCIENCE*; (DATA) PRÜFER *ET AL.*, *NATURE ECOLOGY & EVOLUTION*, DOI: 10.1038/S41559-021-01443-X (2021) HAJDINJAK *ET AL.*, *NATURE*, DOI: 10.1038/S41586-021-03335-3 (2021)

ent from the one that gave the younger Oase man his larger Neanderthal legacy. This "suggests that such mixing was common," Hajdinjak says.

Genomic analysis of the female skull found in Zlatý kůň cave (which means golden horse in Czech), near Prague, tells a different story, according to a paper this week in *Nature Ecology & Evolution* by a team led by paleogeneticists Johannes Krause and Kay Prüfer of MPI. The woman's Neanderthal DNA likely came from the first known interbreeding, between Neanderthals and the ancestors of all living Eurasians, as modern humans expanded out of Africa and moved into Eurasia, Krause says.

Researchers hadn't been able to directly date the Czech skull, which was discovered in the 1950s, because bovine glue used to repair it contaminated the bones. So Krause and Prüfer turned to a clever dating method that uses the ancestral mating with Neanderthals as a time marker. The chunks of Neanderthal DNA in the genome from the Zlatý kůň skull suggest the woman was born 60 to 80 generations (roughly 2000 years) after her ancestors mated with Neanderthals, they conclude. The 45,000-year-old Siberian male inherited his shorter Neanderthal DNA chunks about 85 to 100 generations after that same encounter. That suggests the Czech female lived before the Siberian male and could be as old as 47,000 years—the oldest known modern in Europe, Krause says.

The authors make a "compelling" case that the woman lived at least 45,000 years ago, says population geneticist John Novembre of the University of Chicago.

Krause's team also found that unlike the Bacho Kiro individuals, the Zlatý kůň skull was no more closely related to ancient Asians than to Europeans. This suggests she came from an ancient population that had not yet differentiated genetically into Asians and Europeans, Krause says.

The differences in how often modern humans mated with Neanderthals could reflect the small population sizes of each group at the time, Novembre suggests. And Zlatý kůň is located in what was perhaps the northern edge of Neanderthal territory, whereas Bulgaria's Balkan Mountains were a known refuge for Neanderthals as modern humans pushed into Europe.

The new data show that all of the modern human lineages vanished by the advent of the last ice age, which reached its peak about 20,000 years ago. After the ice melted, other modern humans from Eurasia repopulated the continent. "Multiple groups headed out [to Eurasia], but it seems like only a fraction of these early modern humans left progeny," Novembre says. ■

In March, Russian Prime Minister Mikhail Mishustin (center) visited the institute that developed EpiVacCorona.

PHOTO: SPUTNIK PHOTO AGENCY/REUTERS

COVID-19

Latest Russian vaccine comes with a big dose of mystery

Vaccine trial participants call for review after unusual private study found they have no virus-blocking antibodies

By **Olga Dobrovidova**

When the Kremlin last month said Russian President Vladimir Putin had received the first dose of a homegrown COVID-19 vaccine, a guessing game began. Had he gotten Sputnik V, which Russia had given emergency use authorization—a world first—in August 2020 after testing in just 79 patients? Or had Putin been given another COVID-19 vaccine that Russia had sanctioned with much less fanfare—and with equally sparse evidence that it works?

Putin and state officials wouldn't say, but Russia's second COVID-19 vaccine, known as EpiVacCorona and first authorized in October 2020, has begun to emerge from the shadow of Sputnik V, bringing controversy of its own. Developed by VECTOR, the famed State Research Center of Virology and Biotechnology that once studied bioweapons and now is one of two global repositories of the eradicated smallpox virus, the vaccine is key to the country's plans to combat the pandemic. Russia began to offer it to small numbers of people last year, plans to administer 1.5 million doses per month by this summer, and aims for a bigger national campaign.

Only in late March did VECTOR publish any clinical data on EpiVacCorona, which consists mainly of multiple protein bits, or peptides, from the pandemic coronavirus. The paper, in an obscure Russian journal, described safety tests in 14 people, and a phase 2, placebo-controlled trial in 86 people. The authors reported no safety issues and said volunteers who received vaccine produced antibodies that block SARS-CoV-2's infectivity. But VECTOR has not reported evidence that the vaccine actually protects people from COVID-19.

Two unusual letters from some of the trial participants to the Russian health minister, the first in January calling for the phase 2 trial to be publicly unblinded and the second in March asking for a review of the vaccine, have added to the doubts. The volunteers use commercial assays to look for virus-neutralizing antibodies and say they found none. They note that VECTOR used a special test system for the antibodies that is not public. "The very fact of the publication of this paper is a convincing argument for an independent review" of the vaccine, says Russian entrepreneur Andrey Krynicki, a trial participant who organized the open letters.

Officials at VECTOR, which is under the authority of the Russian government agency in charge of pandemic response, defend the initial clinical studies and note a phase 3 efficacy trial in more than

3000 people is underway in Russia.

Many COVID-19 vaccines generate an immune response to SARS-CoV-2's spike, the protein the virus uses to latch onto and fuse with cells. EpiVacCorona consists of three synthetic fragments of spike, attached to a carrier protein, which itself is composed of synthetic fragments of the virus nucleocapsid protein, known as N. One peptide is designed to create antibodies to the spike's receptor-binding domain, the part that hooks onto a human cell protein. The other spike peptides are meant to elicit antibodies that prevent the virus from getting into the cell. The N peptides may generate still other protective responses. VECTOR officials say the vaccine ultimately provides "three lines of defense."

The innovative peptide approach, which VECTOR also uses for an Ebola vaccine, intrigues some outside scientists. But no peptide-based vaccines have been licensed to date by the United States, Europe, or the World Health Organization (WHO). "There are several in clinical trials. This means we don't have definitive evidence they are effective, but they do look promising," says Sarah Caddy of the Cambridge Institute for Therapeutic Immunology and Infectious Disease.

Caddy adds that peptide selection is "crucial" for this type of vaccine. But Olga Matveeva, a Russian biologist who now works at a U.S. biotech and has tracked the development of EpiVacCorona, is not convinced VECTOR has chosen the best ones. "Unfortunately, last spring, when the vaccine developers at VECTOR were selecting their peptides, there was little information available on the virus and the most appropriate spike protein fragments that should be recognized by the immune system and launch an effective antiviral attack," she says.

VECTOR has said the chosen peptides differ little between SARS-CoV-2 strains, to help protect against new variants, and that they were extensively tested in animals. Preclinical study results are under review at a scientific journal, the center says.

Russians could use another COVID-19 vaccine to supplement Sputnik V, which despite initial uncertainties appears to be highly effective and has been authorized for use in nearly 60 countries. Although cases are not obviously surging in Russia, unlike in Europe, it has had nearly 100,000 COVID-19 deaths, by some estimates. Vaccine manufacturing is not Russia's strong suit, however; most of the 500 million doses of Sputnik V planned for this year will reportedly be made in India.

EpiVacCorona is easier to produce than Sputnik V, which consists of adenoviruses genetically engineered to make spike protein. It could boost a national vaccination campaign, if it clearly protects against COVID-19 and is embraced by Russians. There is significant vaccine hesitancy in the country, which stems in part from an overall distrust of the government and medical research it promotes. Participants in Sputnik V's early trials, for example, used the popular Telegram messaging app to trade information about side effects and results from commercial antibody tests widely available in Russia.

EpiVacCorona trial participants were also wary. Some recruited Alexander Chepurnov, a former head of infectious diseases at VECTOR who now works at another Russian medical institute, to run their ministudy that looked in vain for neutralizing antibodies. Chepurnov declined to talk to *Science*, citing "too much politics in science today."

In a written statement, VECTOR Deputy Director Tatyana Nepomnyashchikh said the center is satisfied with the phase 1 and 2 trials, although the results are preliminary, with final data due in May. "We have also tested the sera of people vaccinated with EpiVacCorona for neutralizing activity, and it has been shown to work against both the reference strain and the British variant. We are confident in this result," Nepomnyashchikh said. She said the antibody validation test, developed by VECTOR specifically for this vaccine, is available in every Russian region where EpiVacCorona is distributed.

Svetlana Zavidova, who heads the Association of Clinical Trials Organizations in Moscow, praised the groundbreaking "citizen science" effort of volunteers, but cautioned against overinterpreting their limited results. And she doubts the protest letters will prompt an independent review.

VECTOR has not applied for an emergency use listing for EpiVacCorona from WHO or other stringent regulatory agencies, but says it will. "More than 60 private and government entities" have expressed interest in the vaccine, Nepomnyashchikh's statement notes. For now, VECTOR says, its priority is supplying Russian domestic demand.

Russia also has a third authorized COVID-19 vaccine, consisting of inactivated coronavirus, and little is also known about its efficacy. Zavidova laments that the practice of COVID-19 vaccine authorization and rollout before phase 3 trial results has largely gone mainstream in Russia, a concern she and her organization raised last year before the Sputnik V endorsement. "We've essentially crossed and burned that bridge," Zavidova concludes. ■

Science's COVID-19 reporting is supported by the Heising-Simons Foundation.

Olga Dobrovidova, a science journalist in Moscow, currently works at Skoltech, a private university not involved in the development of COVID-19 vaccines.

SCIENTIFIC MISCONDUCT

Top German psychologist found to have fabricated data

University investigation finds anxiety expert pressured whistleblowers

By **Hristio Boytchev**

Hans-Ulrich Wittchen, one of Germany's top psychologists and an expert in treating anxiety and phobias, is not shy about promoting himself. His email signature says he is a "highly cited researcher," and with good reason. He has almost 1000 articles to his name, according to the Web of Science, and has racked up nearly 70,000 citations. He is an editor of Germany's diagnostic and statistical manual of mental disorders—the bible of clinical psychology—and until 2017, he led a psychology research institute at the Dresden University of Technology (TU Dresden).

Yet his reputation is under fire after an investigation into one of his studies found evidence of manipulation—and elaborate efforts to cover up the misdeed. The investigation report, turned over to TU Dresden in February and obtained by *Science*, also shows Wittchen intimidated whistleblowers and pressured senior TU Dresden staff. The Federal Joint Committee (G-BA), a public health organization, is suing the company it paid to do the study. And the Dresden public prosecutor's office is now investigating criminal charges related to the study.

Wittchen was one of the top epidemiologists of psychiatry, and TU Dresden "has benefited greatly from him," says Jürgen Margraf, a psychologist at Ruhr University, Bochum, who has collaborated with Wittchen. "If the commission's findings turn out to be true, they are very disturbing for the entire field, and that would also have an impact on TU Dresden." Thomas Pollmächer, director of the mental health center at Ingolstadt Hospital, says the allegations are "startling." He worries about other possible irregularities in Wittchen's extensive publication record.

"Some time bombs may be ticking," he says.

The study in question was a €2.4 million survey of staffing levels and quality at nearly 100 German psychiatric facilities. Working for TU Dresden's Association for Knowledge and Technology Transfer (GWT), Wittchen was the principal investigator of the effort, which aimed to examine workloads at the clinics and inform government regulations.

But in February 2019, German media reported allegations, stemming from whistleblowers close to the survey project, that study data had been fabricated. The university launched a formal investigation, led by law professor Hans-Heinrich Trute.

After 2 years of work, the commission, in its final report, has found that only 73 of 93 psychiatric clinics were actually surveyed. For the others, the report says, Wittchen instructed researchers to copy data from one clinic and apply them to another. "The violations were intentional, not negligent," the report says. "Wittchen wanted to appear more successful than he was."

German psychologist Hans-Ulrich Wittchen is accused of fabricating data in a survey of psychiatry clinics.

Wittchen told *Science* he would not answer detailed questions "because they are the issue of legal proceedings." But he denies any wrongdoing and says the study in question was "scientifically correct."

The investigation report also shows how Wittchen sought to avoid repercussions. In April 2019, he sent an email to Hans Müller-Steinhagen, president of TU Dresden at the time, warning him to "stay out of the project" and stop the investigation, because otherwise there would be a "national political earthquake." "I would like to warn you … once again personally and confidentially that you are taking an extreme risk here," Wittchen wrote in the email.

The two whistleblowers, junior members of GWT, faced pressure, too, according to emails obtained by *Science*. Wittchen asked GWT's director to consider dismissing the whistleblowers—in order to save money. In another document, he accused them of being responsible for the study irregularities. "I will … defend myself with all legal means against this mess," he wrote to a group of survey researchers that included the whistleblowers. According to the commission report, Wittchen even gave the two whistleblowers a prewritten letter to sign, in which they would retract all accusations and apologize.

Investigators found indications that Wittchen manipulated documents to cover his tracks, including presentation slides, emails, and possibly even signatures. He has "shown a willingness to mislead the investigation from the beginning by means of deception and manipulation," the report says. "If these observations were true, they would be within the realm of criminal sanctions."

For his part, Wittchen says the problems with the survey were an innocent mistake. In a 70-page denial included in the investigation report, he claims the duplicated data in the survey were statistically correct and simply not explained properly.

Although the report focused on the alleged scientific misconduct, it also includes hints of possible corruption. It notes allegations that Wittchen employed his daughter in the project for about 2 years—although the other staff never saw her doing any work on it. Wittchen's daughter declined to comment on the allegations.

The commission finds fault with TU Dresden and GWT for not sufficiently protecting the whistleblowers, who remained subordinate to Wittchen during the investigation. When one of the whistleblowers asked GWT for a job reference, the request ended up with Wittchen, who gave him a poor reference.

The commission also criticizes Katja Beesdo-Baum, a behavioral epidemiologist at TU Dresden and longtime colleague of Wittchen's who was deputy head of the survey project. A few days after the allegations became public in February 2019, Beesdo-Baum called an extraordinary meeting of the institute. There, employees were reminded of their duty to maintain secrecy, says a professor who was present at the time, according to the report. The employees "had the feeling of being muzzled," he says. Beesdo-Baum says the commission did not accuse her of misconduct and that her role in the affair will be discussed internally.

Wittchen gave up his professorship at TU Dresden in 2017 when he reached an age limit. In 2017, Ludwig Maximilian University of Munich hired him as a visiting professor, but a spokesperson says it suspended Wittchen's contract this month, after learning of the allegations. Last month, the university deleted the 2017 press release announcing its hiring of Wittchen.

In a statement, the German Psychological Society says it considers the allegations in the report so "very grave" that it has convened a court of honor that could revoke Wittchen's membership. GWT issued a statement saying that in its 25 years of existence, across thousands of studies, it has never encountered "comparable irregularities."

Meanwhile, a TU Dresden spokesperson says the university is investigating additional allegations of corruption. It is evaluating possible sanctions against Wittchen and expects to make a decision in mid-April, at the earliest. The Dresden public prosecutor's office has also launched a criminal investigation. The office says that for "tactical reasons" it is not disclosing details of the investigation but that it will "take some time." ■

Hristio Boytchev is a journalist in Berlin.
This story was produced in a collaboration with BuzzFeed News Germany.

PHOTO: MITTENZWEI KARL/PICTURE-ALLIANCE/*BERLINER ZEITUNG*

eppendorf & Science

PRIZE FOR NEUROBIOLOGY

2020 Winner
Christopher Zimmerman, Ph.D.
Princeton Neuroscience Institute
For research on thirst and drinking behavior

Application Deadline
June 15, 2021

Now It's Your Turn!

Eppendorf & Science Prize for Neurobiology
The annual Eppendorf & Science Prize for Neurobiology is an international prize which honors young scientists for their outstanding contributions to neurobiological research based on methods of molecular and cell biology. The winner and finalists are selected by a committee of independent scientists, chaired by *Science*'s Senior Editor, Dr. Peter Stern. If you are 35 years of age or younger and doing great research, now is the time to apply for this prize.

As the Grand Prize Winner, you could be next to receive
> Prize money of US$25,000
> Publication of your work in *Science*
> Full support to attend the Prize Ceremony held in conjunction with the Annual Meeting of the Society for Neuroscience in the USA
> 10-year AAAS membership and online subscription to *Science*
> Complimentary products worth US$1,000 from Eppendorf
> An invitation to visit Eppendorf in Hamburg, Germany

It's easy to apply! Write a 1,000-word essay and tell the world about your work. Learn more at:

eppendorf.com/prize

eppendorf Science AAAS

AAAS® and Science® are registered trademarks of the American Association for the Advancement of Science, USA. Eppendorf® and the Eppendorf Brand Design are registered trademarks of Eppendorf AG, Germany. All rights reserved, including graphics and images. Copyright © 2021 by Eppendorf AG. Photography: Sameer A. Khan.

A STAR IS TORN

Nature's most magnetic objects, ripped apart in starquakes, can unleash powerful flashes of light

By **Joshua Sokol**

On 15 April 2020, a wave of gamma rays, nature's most powerful kind of light, washed across the Solar System like a storm front. First contact came above Mars, where photons at energies comparable to the radiation from a nuclear bomb peppered a Russian particle detector on NASA's Mars Odyssey probe. Six minutes later, the burst of light lit up a solar wind probe between the Sun and Earth. Five seconds after that, the signal splashed into specialized detectors on Earth's surface.

Gamma ray bursts are not so unusual. Space-based observatories pick one up every day or two; roughly two-thirds of them, lasting tens or hundreds of seconds, hail from massive stars exploding in supernovae. Brief bursts of less than 2 seconds make up the rest, and are thought to arise from the cataclysmic collision of two neutron stars, the smoldering ruins left at the heart of a supernova. But when astrophysicists noticed that the 15 April event fluttered in brightness over microseconds, curiously fast variation, they began to think the mystery source was something else altogether.

The explosion was also uncommonly close. By triangulating the signal's arrival times at the different detectors, astronomers traced it to Sculptor, a neighboring galaxy. All the evidence was pointing to a legendary but elusive type of event: a giant flare erupting from a magnetar—a neutron star with an outlandishly intense magnetic field.

The outburst, dissected in a series of studies released in January, arrived just as magnetars were becoming a go-to solution for theoretical astrophysicists looking for the engines of unexplained celestial explosions, from odd gamma ray flashes to potent eruptions of radio waves. "Originally this was a very obscure subject," says astronomer Chryssa Kouveliotou of George Washington University. "But right now people

IMAGE: NASA'S GODDARD SPACE FLIGHT CENTER/CHRIS SMITH/USRA/GESTAR

Plasma bursts from a magnetar starquake in this artist's conception, an eruption that can create a gamma ray flare.

involve magnetars in almost everything."

Forged in supernovae, magnetars are imbued with magnetic fields a trillion times clingier than refrigerator magnets, strong enough to split x-ray photons and stretch normal atoms into oblong shapes. When those fields tangle and snap, the star can vent vast amounts of energy, enough to launch a burst of radiation across the universe.

Yet actual data on magnetar flares remain sparse. Three earlier magnetar explosions in and near the Milky Way unleashed flashes so bright they swamped detectors and even sent some spacecraft into "safe mode," preventing astronomers from studying anything but the explosions' aftermath in any detail. Candidates from distant galaxies were too faint to confirm.

Scientists have patiently waited for a rare convulsion to strike some unlucky magnetar in just the right place: close, but not too close. Then the Sculptor flare rolled in. The event is providing clues to long-standing questions about how common magnetars might be in the wider universe and how they might power giant flare explosions. "It's just like earthquakes in LA, where you're sitting there and they're rumbling all the time at a pretty low level," says Matthew Baring, an astrophysicist at Rice University. "Then you get the 'big one.' Well, the giant flare [in Sculptor] is the 'big one.'"

THE VERY FIRST giant flare arrived with a bang some 4 decades ago, before anyone had even conceived of a magnetar. In the Cold War of the late 1960s, U.S. surveillance satellites had stumbled onto a surprising fact: Gamma ray flashes emanated not only from nuclear tests below, but also from deep space above. By the 1970s, after these gamma ray bursts were declassified, astrophysicists on both sides of the Iron Curtain tried to identify their cosmic sources.

Triangulating the gamma signals back to their origin required wrangling detectors not just across interplanetary distances, but also geopolitical chasms. By the late 1970s, the West had missions such as Helios around the Sun and Pioneer at Venus; the Soviets had, among others, the twin Venera probes patrolling the inner Solar System after dropping Venus landers. Kevin Hurley, a U.S. astronomer working in France, started a clearinghouse for probe data that allowed researchers at Los Alamos National Laboratory, NASA, and in Moscow to pool information using him as a middleman, forming what would come to be called the InterPlanetary Network. "There wasn't a lot of collaboration at the time," Hurley says, "but there was no formal interdiction not to do it."

Ordinary gamma ray bursts kept drizzling in. Then came 5 March 1979. A split-second pulse of gamma rays 100 times brighter than any gamma ray burst yet seen blazed across the Soviet and U.S. spacecraft. The signal's staggered arrival times indicated it came from the Large Magellanic Cloud, a satellite galaxy in the suburbs of the Milky Way. Suspiciously, the galaxy contained a known supernova remnant, which presumably held a neutron star at its heart. Aftershocks of the burst persisted for a few minutes, repeating every 8 seconds, as if the gamma rays were beaming from a specific spot on a compact, spinning object. Years afterward, a team in St. Petersburg discovered fainter x-ray bursts coming from the same part of the sky, a suggestion that the mystery source continued to simmer.

Astronomers already knew neutron stars were extreme objects, capable of extreme outbursts. When the core of a star implodes during a supernova, gravity trash compacts about one Sun's worth of mass into a 20-kilometer-wide orb. Only the quantum repulsion between neutrons staves off a final collapse into a black hole. The implosion also concentrates the pre-existing star's magnetic field, amplifying it by up to 10 billion times. Those fields power pulsars, which sweep a radio beam past Earth at regular intervals as they spin.

But to get a gamma ray burst like the one in 1979 required an even more magnetic object. In 1992, U.S. astrophysicists Chris Thompson and Robert Duncan (and Bohdan Paczyński in Poland, nearly simultaneously) conjured up a way to do it. They considered the first 10 seconds or so of a baby neutron star's life after its birth in a supernova. The star would be so hot its guts would be molten. For a subset of neutron stars, that fluid would churn enough to set in motion something similar to the roiling dynamos that power magnetic fields inside Earth or the Sun. That dynamo would boost and lock in magnetic fields 1000 times stronger still than on other neutron stars. "These things are so crazy," says Oliver Roberts, an astrophysicist with the Universities Space Research Association. "If you put a magnetar halfway between the Moon and the Earth, it would strip all our credit cards and wipe all our hard disks."

At the time, magnetars were still hypothetical. One way to show they were real was to test a prediction based on the laws of electromagnetism. Magnetars' intense fields should act as a powerful brake on their spin, so that magnetars born rotating every few milliseconds would, in just a few thousand years, slow down to once every few seconds—like the apparent 8-second spin of the 1979 source. Kouveliotou, then at NASA, set out to document this slowing in real time by training an x-ray telescope on a suspected Milky Way magnetar for 3 years. In 1998, she found it did, in fact, slow, by about one-hundredth of 1 second—proof that Duncan and Thompson's theoretical beastie existed in the wild. She included the two theorists on the discovery paper. "They were more than exhilarated," she says. "They were ionized."

From the start, Duncan and Thompson also realized giant fields could crank out giant flares, a scenario theorists continued to elaborate on after Milky Way magnet-

How magnetars erupt

Theorists conjured up magnetars 30 years ago to explain a handful of puzzling x-ray and gamma ray observations. A 2020 flare from a nearby galaxy has shed light on how magnetars generate the bursts—and also suggests these extreme objects are common in the universe. *Graphic by* **Chris Bickel**

Core collapse

During a neutron star's supernova birth, a massive star collapses to a dense cinder the size of a city, concentrating magnetic fields.

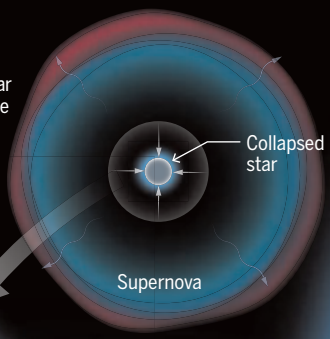

Churning birth

For some neutron stars, the churn of its liquid interior seconds after its birth combines with the spin to drive a dynamo that further boosts fields.

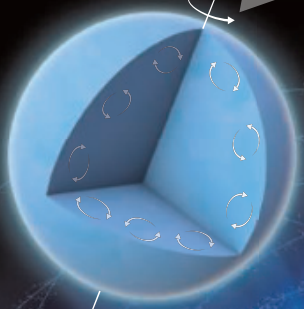

Plasma release

Magnetic field lines

Starquake

Bursts of light

The gamma ray bursts pack 100 years of the Sun's energy into a fraction of a second.

Photon beaming

Electrons and positrons in the plasma knock into emitted photons, raising their energy. The plasma's motion also focuses them into a laserlike beam.

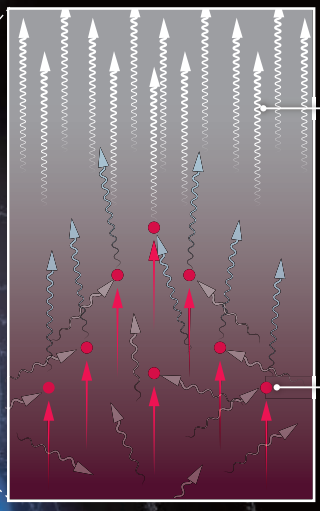

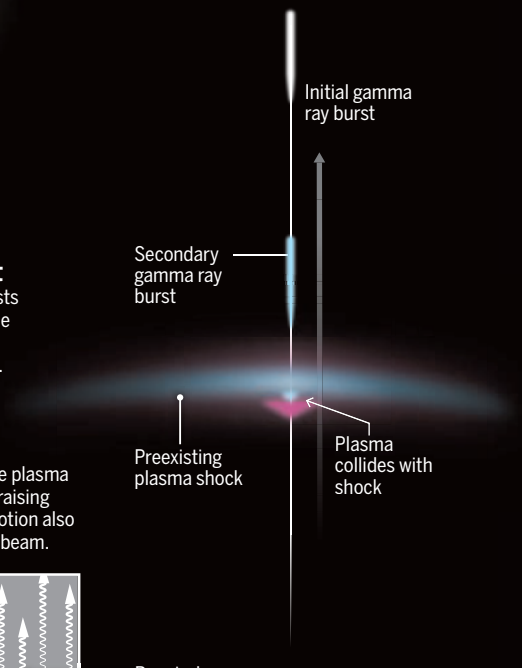

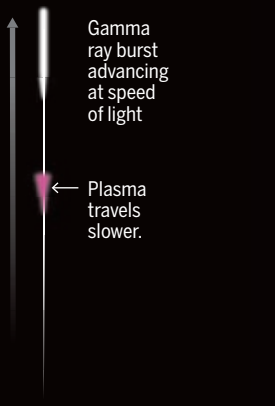

Stress fracture

Grinding layers and magnetic stresses build up to a surface-rupturing starquake. A plasma fireball bursts forth, rocketing out along open field lines near the magnetar's poles.

- **Inner core** (unknown, ultradense matter)
- **Outer core** (neutron-rich liquid)
- **Inner crust** (neutrons, electrons, heavier nuclei)
- **Outer crust** (nuclei and electrons)

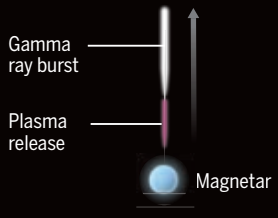

Second light

The plasma burst, traveling near the speed of light, trails the initial gamma ray flare. When the plasma collides with a distant layer of material, where the magnetar's wind hits interstellar space, it generates another gamma ray flare, which strikes Earth seconds after the first.

Field of extremes

Magnetar fields, thought to be the strongest in nature, are so powerful that they can split x-ray photons and stretch atoms into oblong shapes.

Earth
0.00005 tesla

Sunspot
0.4 tesla

High-strength MRI
10 tesla

Neutron star
100 million tesla

Magnetar
100 billion tesla

ars sent two more searingly bright gamma ray bursts crashing into Earth in 1998 and 2004. After its turbulent start, the top few meters of a magnetar would cool enough—still millions of degrees kelvin—to freeze into a crystal lattice of neutrons, electrons, and atomic nuclei. Crackling with electric currents and threaded by magnetic field lines, the crust would shiver and sometimes develop small cracks that would vent puffs of plasma into the magnetized atmosphere around the star itself. That plasma would emit pulsing x-ray storms like those the St. Petersburg team observed.

But beneath the crust, greater stresses might build up. Onionlike layers at different depths are thought to rotate at different rates, which would cause magnetic fields to grind against each other at the layer boundaries, exerting massive forces on the crust. And occasionally, maybe once per century or maybe only once ever, that strained surface might undergo a sudden snap: a starquake that would rearrange as big a fraction of a neutron star's surface, Thompson says, as an earthquake swapping California and New York.

By tearing open large swaths of crust near the magnetar's poles, where its magnetic field lines splay out into space, a large quake could instantaneously disgorge vast volumes of plasma, sending electrons and positrons rocketing into space at relativistic speeds, approaching that of light. A tight, short-lived beam of photons would emerge from that plasma like a headlight, boosted to higher energies and focused into a beam by the plasma's motion. Electrons in the plasma would collide with the photons, nudging them up to gamma ray strength. If beams like that ever swept across Earth, well—they might just explain these misfit gamma ray bursts.

WHEN THE APRIL 2020 giant flare hit after a 16-year drought, observers could finally check at least some of this scenario with today's cutting-edge instruments. The InterPlanetary Network, still cycling space probes in and out, clinched the burst's origin in the Sculptor galaxy. The distance allowed Hurley and his collaborators to calculate the intrinsic strength of the giant flare, which packed 100,000 years of the Sun's shine into a few milliseconds.

As the burst flickered, a detector on NASA's Fermi probe caught gamma ray photons several times more energetic than any measured in a giant flare before, and showed they arrived at the brightest moments, as expected from a plasma moving at speeds high enough to both beam light and boost photon energies.

That, in turn, confirmed the picture of an explosion near the magnetar poles—the only place where magnetic field lines would allow plasma to escape so quickly. Yet another instrument, also on Fermi, caught a few gamma rays at even higher energies starting 19 seconds after the main event. They suggest that some of the ejected plasma, after generating its initial beam of gamma rays, continued on and collided with a distant layer of gas surrounding the star, provoking a powerful afterburst (see graphic, p. 122).

For Eric Burns, an astronomer at Louisiana State University, Baton Rouge, the flare offered a chance to search for similar events in the gamma ray back catalog. Astronomers had suggested a handful of other bursts might have been giant flares from nearby galaxies like Andromeda. But when the coordinates of a burst overlap with a nearby galaxy, it's never clear whether the event actually happened in that galaxy or somewhere more distant along the same line of sight. Many astronomers presumed these bursts were standard-issue short bursts, likely from the collision of neutron stars, seen at greater distances.

A giant flare in 1979 came from N49, a supernova remnant thought to harbor a magnetar.

PHOTO: HUBBLE HERITAGE TEAM/STSCI/AURA; Y. CHU/UIUC *ET AL.*; NASA

Burns searched for very short bursts that overlapped with recent maps of nearby star-forming galaxies—the ones most likely to make magnetars. He found three more old bursts that really did seem to come from Milky Way neighbors. That brings the total count of likely magnetar giant flares in the neighborhood of the Milky Way to seven. Based on that rate, Burns calculated, giant flares should occur across the universe several times more often than all types of supernovae combined and maybe 1000 times more often than other exotic transients like neutron star mergers. But giant flares in the distant universe are too faint to see, and they concentrate most of their energy into a small number of very high-energy photons. "These things are incredibly common," he says. "It turns out they are just harder to detect."

If Burns's rates hold up, they suggest supernovae often do give birth to neutron stars with supercharged magnetic fields. Furthermore, the rates imply that at least several percent of previously observed short gamma ray bursts are actually masquerading giant flares, too. And finally, they suggest there are enough erupting magnetars to power the mysterious fast radio bursts observed from more distant parts of space, a case bolstered by a second watershed magnetar event, also in April 2020: the first detection of a faint fast radiolike signal from a known Milky Way magnetar undergoing a small outburst (*Science*, 12 June, p. 1171).

"It's sort of a running joke, that you can explain everything with a magnetar," says Brian Metzger, an astrophysicist at the Flatiron Institute. "But what's nice is it does seem like these different things are coming together now."

With the Sculptor giant flare as a template, astronomers want to collect a larger statistical sample of flaring magnetars from other galaxies. Burns is digging into more archival data to do that, and hopes gamma observatories like StarBurst, an upcoming smallsat mission, will be sensitive enough to higher energy gamma rays to distinguish giant flares from the more common bursts. Another Milky Way flash, whenever it comes, might help, too; its initial rise would still swamp sensitive gamma detectors, but today's gravitational wave detectors might be able to pick up ripples in spacetime from the starquake itself, offering more clues to what actually happens on the surface of the star.

For now, though, astronomers are stuck with some basic questions—like whether a magnetar that has launched one giant flare has enough magnetic energy left to muster another—which could take centuries to answer. "Not in my lifetime," Hurley says. "I've become a lot more patient since I started working on the InterPlanetary Network."

Hurley is still wrangling gamma ray sensors across the Solar System—and space agencies. NASA committees are less enthused about funding the project, he says, now that the world has higher tech gamma observatories like Fermi and Swift, leaving its future in doubt. But Europe's BepiColombo probe, en route to Mercury, will soon be the 33rd mission to participate, and NASA's Psyche mission to an asteroid, slated to launch next year, will follow. Their gamma detectors will be ready, attuned to the off chance of another big, rare shot in the dark. ■

ANTHROPOLOGY

The enigmatic origins of the human brain

Evolutionary history of the human brain appears more complex than thought

By **Amélie Beaudet**[1,2,3]

Tracking the emergence of humanlike cerebral features in the hominin fossil record could provide evidence of the timing and process of brain changes and offer a glimpse into the behavior of our ancestors and relatives. Because brain tissues rarely fossilize, changes in brain size, shape, and organization are gleaned from brain endocasts (replicas of the inner surface of the braincase) (*1*). After his observations of brain imprints preserved in fossil cranial specimens from Olduvai (Tanzania) (*2*), paleoanthropologist Phillip V. Tobias stated that "hominid evolution attained a new level of organization…with the emergence of the genus *Homo*." There have since been debates on whether humanlike brain organization emerged concomitantly with the appearance of the genus *Homo*. On page 165 of this issue, Ponce de León *et al.* (*3*) challenge this view by suggesting that *Homo* in Dmanisi (foothills of the Georgian Caucasus) 1.85 to 1.77 million years (Ma) ago showed a primitive organization of the brain.

Reconstructing the chronology and mode of hominin brain evolution requires a good knowledge of subtle changes in brain areas. In this respect, the inferior part of the frontal lobe, where Broca's cap is located, has been the focus of thorough investigations and intense discussions (*4*). In addition to its use as a critical landmark for brain reorganization, Broca's cap plays a fundamental role in language production and comprehension, the evolution of which is an equally intriguing topic. The Broca's cap of extant humans differs structurally from that of our closest living relatives, the chimpanzees and bonobos. Chimpanzees and bonobos have one distinct furrow in that region called the fronto-orbital sulcus. This is absent in humans, who instead have two vertical furrows. In human evolutionary studies, it is assumed that the chimpanzee and bonobo brains more closely approximate the primitive condition for the hominin brain. Within this context, the "single-furrow condition" is interpreted as representing the ancestral condition.

Despite crucial recent discoveries of germane specimens and ground-breaking computer-assisted revision of the fossil record (*5*, *6*), little is known about the brain of early *Homo*. This unfortunate situation can be partially explained by the scarcity of complete or at least partial fossil crania from that time period. For example, the putative earliest human remains from Ledi-Geraru (Ethiopia), dated to 2.8 Ma, do not preserve

[1]Department of Archaeology, University of Cambridge, Cambridge, UK. [2]School of Geography, Archaeology and Environmental Studies, University of the Witwatersrand, Johannesburg, South Africa. [3]Institut Català de Paleontologia Miquel Crusafont, Universitat Autònoma de Barcelona, Barcelona, Spain. Email: aab88@cam.ac.uk

IMAGE: M. PONCE DE LEÓN AND CH. ZOLLIKOFER/UNIVERSITY OF ZURICH

Virtual fillings of the braincases of early *Homo* from Dmanisi, Georgia, are shown in turquoise. Their structures provide new insights into human brain evolution 1.8 million years ago.

the braincase (*7*). The early *Homo* specimens for which there are an exploitable amount of endocast data (description of the organization of the cerebral areas) are from African and Asian localities that are geologically relatively young (less than 1.8 Ma) (*8*, *9*), leaving a gap of about 1 Ma in our knowledge of human brain evolution. In terms of frontal organization, this 1 Ma break in the usable fossil record is crucial. Early hominins that wandered in Africa before 2.8 Ma show a relatively primitive organization of this region (*4*), whereas imprints on later human endocasts indicate a derived human condition (*5*). In this case, the hypothesis of a derived organization emerging at the same time as the earliest humans could not be discounted.

Through their comprehensive study of the notable assemblage from Dmanisi and their revision of the African and Asian fossil material, Ponce de León *et al.* cast new understanding on the cerebral organization of early *Homo* in general, and *Homo erectus* (*sensu lato*) in particular, challenging the idea of the emergence of a fully derived human brain at the time of the earliest representatives of the genus *Homo*. The hominin fossil-bearing site of Dmanisi is exceptional for its geographical (Europe) and chronological (1.85 to 1.77 Ma) contexts (*10*). As such, fossiliferous deposits of this locality document one of the earliest dispersals of *Homo* out of Africa. By combining various methods of high-resolution imaging (including synchrotron radiation) and three-dimensional modeling techniques (including geometric morphometrics), the authors demonstrate that the endocast of *H. erectus* at about 1.8 Ma reflects a primitive organization of the frontal lobes, whereas later *H. erectus* specimens in Southeast Asia and Africa show a derived condition (see the figure). Accordingly, the authors suggest that the humanlike frontal lobe organization emerged after the genus *Homo* and the earliest dispersals out of Africa.

The question that will need to be addressed next deals with the nature of the underlying evolutionary processes. What kind of selection pressure may have been responsible for the reorganization of the frontal lobes? This question has tremendous functional and behavioral implications because, apart from language, it has been demonstrated that the Broca's cap was also certainly involved in toolmaking (*11*). The other possibility, which probably deserves more attention, is that there was no selection at all, and changes that affected the Broca's cap were a by-product of the reorganization of other areas of the brain, and that, ultimately, the emergence of language was the result of an exaptation (previously existing anatomical features co-opted for a new use) (*12*). In that respect, the description of the brain imprints of the endocasts of earlier *Homo* specimens, such as the braincase recently found at Drimolen (South Africa) (*13*), and future discoveries of new specimens from that time period will be essential to understanding the evolutionary context of these brain changes. ■

An evolutionary scenario for the hominin frontal lobes

The evolutionary scenario is based on the evidence of brain changes preserved in the fossil record and investigated by Ponce de León *et al*. Dark gray curves indicate the position of the frontal sulci.

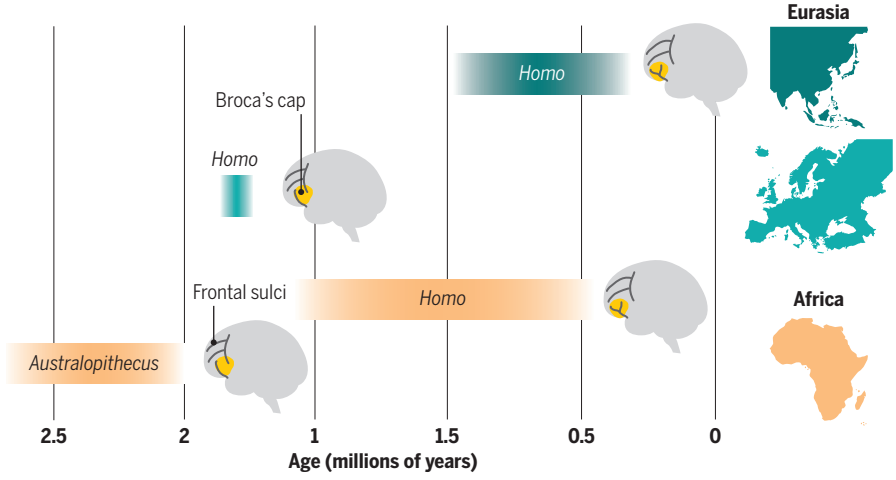

GRAPHIC: N. DESAI/*SCIENCE*

REFERENCES AND NOTES

1. C. P. E. Zollikofer, M. S. Ponce de León, *Evol. Anthropol.* **165**, 20 (2013).
2. P. V. Tobias, *J. Hum. Evol.* **16**, 741 (1987).
3. M. S. Ponce de León *et al.*, *Science* **372**, 165 (2021).
4. D. Falk, *Front. Hum. Neurosci.* **8**, 134 (2014).
5. R. L. Holloway *et al.*, *Proc. Natl. Acad. Sci. U.S.A.* **115**, 5738 (2018).
6. P. Gunz *et al.*, *Sci. Adv.* **6**, eaaz4729 (2020).
7. B. Villmoare *et al.*, *Science* **347**, 1352 (2015).
8. D. Falk, *Science* **221**, 1072 (1983).
9. R. L. Holloway, D. Broadfield, M. Yuan, *Brain Endocasts—The Paleoneurological Evidence*, vol. 3 of The Human Fossil Record, G. T. Schwartz, I. Tattersall, Eds. (Wiley, 2004).
10. L. Gabunia *et al.*, *Science* **288**, 1019 (2000).
11. D. Stout, T. Chaminade, *Philos. Trans. R. Soc. London Ser. B* **367**, 75 (2012).
12. I. Tattersall, *Sci. Am.* **285**, 56 (2001).
13. A. I. R. Herries *et al.*, *Science* **368**, eaaw7293 (2020).

10.1126/science.abi4661

MATERIALS SCIENCE

Preshaping clear glass at low temperatures

Pelletized glass-forming composites enable rapid injection molding and facile binder recovery

By **Rebecca Dylla-Spears**

Advances in available glass chemistries and glass processing methods have accompanied and enabled some of the biggest technology revolutions, from the development and mass production of light bulbs to low-loss fiber optics and durable smartphone touchscreens. An emerging generation of low-temperature processing technologies aims to continue this important trend and make a broader array of glass components mass producible. On page 182 of this issue, Mader *et al.* (*1*) describe one such innovation in glass processing—the use of low-temperature injection molding to preshape silica particle–filled composites that can later be transformed into transparent fused silica glass objects.

Traditionally, transparent glass objects are manufactured in high volume from molten or softened glass, which is floated, drawn, blown, cast, or blow-molded to a desired shape (see the figure, top). The glass composition and processing technique dictate the working temperature, which is usually quite high (near 1000°C) and often restricts the choice of compatible equipment or limits the choice of glass composition. Because geometry-specific capital investment is required for production, drastic or frequent component design changes or small batches may be cost prohibitive. Alternatively, transparent glass components can also be shaped at ambient temperature from solid glass by a series of subtractive processes, including cutting or multiple stages of grinding, followed by slower processing steps, such as polishing or etching. This approach is somewhat less amenable to mass production, and certain geometries containing tool-inaccessible regions cannot be fabricated in this way.

Several emerging glass-shaping technologies aim to reduce the required manufacturing temperatures and still provide access to a broader range of glass compositions and component geometries (see the figure). These approaches use a three-step process. First, a desired shape is preformed at low temperature from a glass-forming, organic-inorganic composite. Next, the preform is dried, and organic materials used to bind particles are removed. Finally, the preform is heated (sintered) well below the glass-melting temperature to densify to transparent glass. Although the second and third steps do occur at increased temperatures, only standard, geometry-agnostic driers and furnaces are required.

This strategy builds on the well-studied sol-gel approach to forming monolithic glass, where silica network–forming chemical solutions are poured into molds, slowly dried, and condensed into dense glass without melting (*2*). In a departure from the sol-gel process, these new technologies use solvents, cross-linkers, and polymers to formulate organic-inorganic composites tuned for compatibility with a particular shaping process, with formats ranging from photocurable liquids to shear-thickening pastes to solids. The composite inorganic loadings are also typically higher than those in the pure sol-gel approach, which drastically reduces shrinkage in comparison.

A host of glass-forming composites and low-temperature shaping technologies for the production of transparent glass have been introduced during the past 4 years, each offering its own benefit (see the figure, bottom). For example, a solid nanocomposite material, called Glassomer, can be shaped at ambient temperature by conventional machining tools like lathes and can also be nanotextured, molded, and roll-to-roll processed in sheets before being converted to fused silica glass (*3*). Further, an additive manufacturing method called direct ink writing has been used to extrude filaments of nanocomposite pastes into pre-

Turning down the temperature

Glass objects such as bottles are usually manufactured by methods such as blow molding of molten glass. Emerging low-temperature techniques that start with organic-inorganic composites may allow glass to be produced economically in previously unrealizable formats.

Blow molding
Molten glass is forced into molds to create desired shapes.

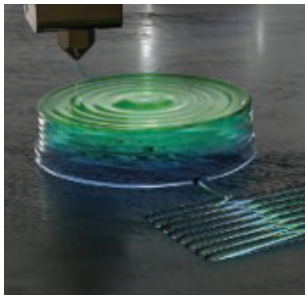

Direct ink writing
Filaments of nanocomposite pastes are shaped into complex preform structures that can include tailored composition.

Stereolithography printing
Nanocomposite liquid resins are photocured in a layer-by-layer process to create complex structures.

Injection molding
Mader *et al*. used injection molding to form pelletized glass-forming composites into functional glass components.

PHOTOS: (CLOCKWISE FROM TOP) SVIATLANA LAZARENKA/ISTOCK.COM; JACOB LONG AND BRIAN CHAVEZ/LAWRENCE LIVERMORE NATIONAL LABORATORY; PANGEAPICS/ISTOCK.COM; NORDRODEN/ISTOCK.COM

Lawrence Livermore National Laboratory, Livermore, CA, USA. Email: dyllaspears1@llnl.gov

form structures ranging from monoliths to meshes to open vessels (*4*). Multiple glass-forming compositions can be mixed inline to create spatial composition variation, such as gradient refractive index glass lenses (*5*). Stereolithography printing—a layer-by-layer additive manufacturing route by which photocurable nanocomposite liquid resins are selectively patterned by exposure to light—can produce transparent glass components that have complex and hierarchical structures with the potential for fine-scale individual features (*6*–*9*).

Most recently, Mader *et al.* have demonstrated the use of pelletized glass-forming composites that are compatible with conventional, low-temperature injection molding—a process used in the high-volume manufacture of polymeric components. Offering an important advance toward sustainable manufacturing, much of the debinding occurs in water rather than at increased temperatures, and the polymers used in the composite can be reclaimed and reused. Fused silica glass items, including tubes, beakers, and microlens arrays, were produced with this composite and existing injection molding equipment at speeds of up to 5 s per piece, without any postprocessing after sintering.

These approaches could make glass available in new formats as well as more cost-competitive with plastic for applications requiring thermal stability, environmental resistance, or improved light transmission. Distributed manufacturing may become a more viable option because processing is done at low temperatures with less-specialized equipment. Additive manufacturing allows changes in component shape through programming rather than retooling for small-volume manufacture and rapid prototyping of glass components. Immediate applications in high-volume optics, lighting, and packaging will drive continued development in low-temperature processing. The combination of methods that enable tunable glass composition and hierarchical microstructures could find use in microfluidics and catalysis. ■

REFERENCES AND NOTES

1. M. Mader *et al.*, *Science* **372**, 182 (2021).
2. L. L. Hench, J. K. West, *Chem. Rev.* **90**, 33 (1990).
3. F. Kotz *et al.*, *Adv. Mater.* **30**, 1707100 (2018).
4. D. T. Nguyen *et al.*, *Adv. Mater.* **29**, 1701181 (2017).
5. R. Dylla-Spears *et al.*, *Sci. Adv.* **6**, eabc7429 (2020).
6. F. Kotz *et al.*, *Nature* **544**, 337 (2017).
7. I. Cooperstein, E. Shukrun, O. Press, A. Kamyshny, S. Magdassi, *ACS Appl. Mater. Interfaces* **10**, 18879 (2018).
8. R. Arita *et al.*, *Commun. Mater.* **1**, 30 (2020).
9. D. G. Moore, L. Barbera, K. Masania, A. R. Studart, *Nat. Mater.* **19**, 212 (2020).

ACKNOWLEDGMENTS

This work was performed under the auspices of the US Department of Energy by Lawrence Livermore National Laboratory under contract no. DE-AC52-07NA27344.

10.1126/science.abg7657

CANCER

Epigenetic nucleotides enhance therapy

Targeting sanitation of epigenetic nucleotides synergizes with cancer treatment

By **Skirmantas Kriaucionis**

Targeted cancer therapy often relies on inhibiting beneficial adaptations of tumor cells. For example, inhibiting complementary or compensatory mechanisms can push cells over the edge of survival. An example of this kind of intervention, which is used in the clinic, is inhibition of poly(adenosine diphosphate–ribose) polymerase (PARP) for treatment of tumors with compromised DNA repair by the homologous recombination pathway (mutated *BRCA1* or *BRCA2* genes). Despite overall beneficial response to treatment with PARP inhibitors (PARPi), resistance is still a formidable problem. Although the search for PARPi sensitizers has been extensively explored, new combinations to improve responses are needed. On page 156 of this issue, Fugger *et al.* (*1*) found that interference with nucleotide metabolism potentiates the efficacy of PARPi in homologous recombination–compromised cancer cells. This discovery opens several promising avenues to enhance PARPi efficacy and could even hold promise for overcoming acquired resistance.

Although the lifetime risk of developing breast cancer in women is 13%, carrying a germline mutation in *BRCA1* or *BRCA2* genes increases this risk to ~70% (*2*). Moreover, mutations in these genes have been linked to increased risk of ovarian cancer and, more recently, prostate, colorectal, stomach, pancreatic, and other cancers. The primary function of the BRCA proteins is the repair of double-stranded DNA breaks by high-fidelity mechanisms using homologous recombination. Defects in homologous recombination lead to genomic instability and gross chromosomal rearrangements, which are typically observed in tumors and cell lines with compromised *BRCA1* or *BRCA2*. The identification of PARP involvement in DNA repair and development of PARPi, which both inhibit and trap PARP on DNA, led to observations that *BRCA1*- and *BRCA2*-deficient cells are hypersensitive to PARPi (*3*, *4*). Several PARPi were approved for treatment of ovarian and breast cancer, achieving a milestone especially in the treatment of ovarian cancer.

Fugger *et al.* undertook a genome-wide loss-of-function screen in haploid human leukemia cells to identify genes that cause resistance or increased sensitivity to the PARPi olaparib. Two genes involved in nucleotide metabolism, 2′-deoxynucleoside 5-monophosphate N-glycosidase (*DNPH1*) and inosine triphosphatase (*ITPA*), enhanced olaparib cytotoxicity. DNPH1 cleaves glycosidic bonds in deoxynucleotide monophosphates (MPs), releasing sugar monophosphate and nucleobase (*5*), whereas ITPA hydrolyzes inosine triphosphate (ITP), resulting in inosine MP (*6*). The substrates of DNPH1 were thought to be canonical nucleotide MPs. Examination of DNA composition in *DNPH1*-deficient cells identified accumulation of 5-hydroxymethyl-uracil base (hmU) in the DNA, suggesting that the free nucleotide 5-hydroxymethyl-deoxyuridine MP (hmdUMP) could be the best substrate of DNPH1. Fugger *et al.* also noticed that exposure to the nucleotide 5-hydroxymethyl-deoxycytidine (hmdC) has a similar synergy with PARPi. In this case, enzymatic deamination converts hmdCMP into hmdUMP in the nucleotide pool, which in turn potentiates activity of PARPi (see the figure). Previous work demonstrated that hmdC is not efficiently phosphorylated but is instead deaminated, ending up in DNA as hmdU (*7*).

Fugger *et al.* propose that the source of hmdU in nucleotide pools could be the epigenetic DNA base hmC. hmC is a product of ten-eleven translocation (TET) enzymes, which are involved in the oxidation of 5-methylcytosine at CpG sites in the DNA (*8*). hmC is not actively removed from DNA; however, it can be further oxidized by TET enzymes, resulting in engagement of base excision DNA repair pathway mediated demethylation (*9*). This could release hmdCMPs into the nucleotide pool. Alternatively, off-target activity of TET enzymes on thymine bases was reported to generate hmU in the DNA directly (*10*). Repair of hmU DNA base could also contribute to hmdUMP in the nucleotide pool.

How does accumulation of hmU in the DNA cause lethality in combination with PARPi? Fugger *et al.* show that uracil DNA

Ludwig Institute for Cancer Research, University of Oxford, Oxford, UK. E-mail: skirmantas.kriaucionis@ludwig.ox.ac.uk

glycosylase 1 (SMUG1), which removes hmU from DNA, generates abasic sites, which cause replication fork collapse that induce double-stranded DNA breaks and thereby provide additional sites for PARP trapping and enhance efficacy of PARPi. Other mechanisms that generate abasic sites should also synergize with PARPi. Indeed, it is likely that inhibiting other noncanonical nucleotide hydrolases, such as MutT homolog 1 (MTH1) and MTH2, might synergize with PARPi.

The discovery of hmdUMP as the preferred substrate for DNPH1 assigns a previously unknown nucleotide "sanitizer" role to this enzyme. Nucleotide "sanitation" involves the removal of potentially damaging, noncanonical nucleotide triphosphate variants from the nucleotide pool. In contrast to DNA, the nucleotide pool has higher susceptibility to damage because of more accessible reactive groups. Moreover, there is a flux of damaged bases and nucleosides from DNA repair and the extracellular space. To limit the availability of noncanonical nucleotides to DNA polymerases, cells have a broad group of enzymes consisting of Nudix hydrolases (with 24 characterized members), deoxyuridine triphosphatase (dUTPase), inosine triphosphatases (ITPases), and SAM domain and HD domain–containing protein 1 (SAMHD1) (*11*).

Future translational work should focus on developing DNPH1 inhibitors into drugs. It will also be interesting to explore inhibition of ITPA as a strategy to potentiate PARPi. Deletion of ITPA produced a higher increase of inosine in the genome than the amount of hmU accumulation observed after ablation of DNPH1, suggesting that ITPA inhibition might be even more effective in synergizing with PARPi. It will also be essential to use in vivo tumor models because maintaining similar efficacy while transitioning from cell lines to actual tumors is often complicated. Elucidation of the impact of DNPH1 or ITPA inhibition in normal cells will help to determine whether off-target effects are likely.

It will be important to know whether tumors have higher pools of hmdUMP or dITP, which could make them more susceptible to treatment with appropriate inhibitors. Multiple reports documented depleted hmC in DNA of cancer cells when compared with normal tissue. However, the interpretation of this observation in inferring hmdU abundance in the nucleotide pool is not straightforward because it may reflect either lower production of hmC by TET enzymes or enhanced removal of this base from DNA. ■

Exploiting nucleotide sanitation

Removal of hmdUMP from the nucleotide pool

5-hydroxymethyl-cytosine (hmC) in DNA is released as the free nucleotide 5-hydroxymethyl-deoxycytidine monophosphate (hmdCMP). This is deaminated by deoxycytidylate deaminase (DCTD) to 5-hydroxymethyl deoxyuridine monophosphate (hmdUMP) and cleaved by 2′-deoxynucleoside 5-phosphate N-hydrolase 1 (DNPH1), resulting in its removal from the nucleotide pool.

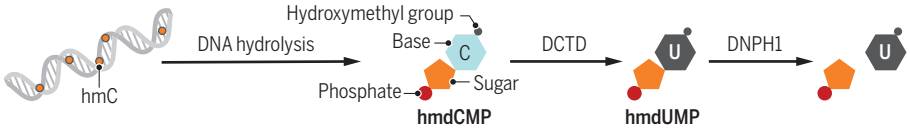

Opportunity for the therapy

Administration of hmdU nucleoside and/or DNPH1 inhibitor leads to accumulation of hmdUMP in nucleotide pools, where it can be incorporated into DNA. This leads to 5-hydroxymethyluracil (hmU) in DNA and repair by uracil DNA glycosylase 1 (SMUG1), which generates abasic sites that can cause replication fork collapse and double-stranded DNA breaks that require poly(adenosine diphosphate–ribose) polymerase (PARP) for repair. Inhibition of DNPH1 thereby enhances sensitivity to PARP inhibition.

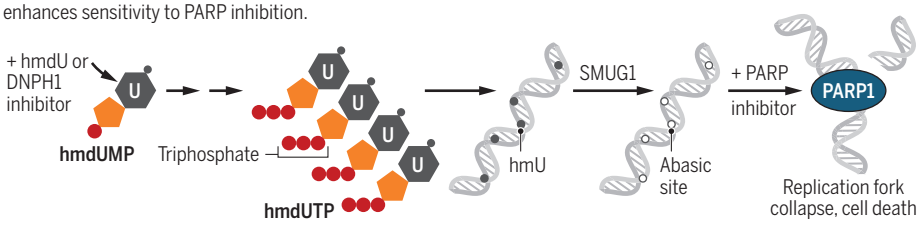

REFERENCES AND NOTES

1. K. Fugger *et al.*, *Science* **372**, 156 (2021).
2. K. B. Kuchenbaecker *et al.*, *JAMA* **317**, 2402 (2017).
3. H. Farmer *et al.*, *Nature* **434**, 917 (2005).
4. H. E. Bryant *et al.*, *Nature* **434**, 913 (2005).
5. Y. K. Ghiorghi *et al.*, *J. Biol. Chem.* **282**, 8150 (2007).
6. S. Lin *et al.*, *J. Biol. Chem.* **276**, 18695 (2001).
7. M. Zauri *et al.*, *Nature* **524**, 114 (2015).
8. M. Tahiliani *et al.*, *Science* **324**, 930 (2009).
9. T. Pfaffeneder *et al.*, *Nat. Chem. Biol.* **10**, 574 (2014).
10. Y.-F. He *et al.*, *Science* **333**, 1303 (2011).
11. S. G. Rudd *et al.*, *DNA Repair* (Amst.) **44**, 193 (2016).

ACKNOWLEDGMENTS

S.K. is supported by the Ludwig Institute for Cancer Research. S.K. also acknowledges funding from the Biotechnology and Biological Sciences Research Council (BB/M001873/1) and the Conrad N. Hilton Foundation.

10.1126/science.abh3188

EPIGENETICS

The push and pull of DNA methylation

The control of DNA methylation guides cell-fate decisions in development and disease

By **Tianpeng Gu** *and* **Margaret A. Goodell**

DNA methylation is an important covalent modification of mammalian genomic DNA that represses transcription. Genomic DNA is mostly maintained with high amounts of methylation, but some regions such as CpG islands are nearly perpetually unmethylated. Recently, large valleys or canyons of unmethylated DNA were discovered throughout the mammalian genome (*1*, *2*). Most are associated with conserved developmental regulators, such as homeobox genes, and are thought to be actively regulated. The size of these canyons is maintained by a push and pull interplay between DNA methyltransferases (DNMTs) and ten-eleven translocation (TET) dioxygenases that oxidize 5-methylcytosine, which leads to demethylation (*2*). On page 146 of this issue, Dixon *et al.* (*3*) identify QSER1 (glutamine and serine–rich protein 1) as part of the "push" protection mechanism that restricts DNA methylation. They show that QSER1 cooperates with TET1 by antagonizing chromatin binding of DNMT3A and DNMT3B, thus helping to retain the developmental potential of stem cells.

Chromatin binding of DNMT3A and DNMT3B, and hence their activity in establishing de novo DNA methylation, is directed by multiple factors, including nucleosomes (*4*), histone modifications (*5*, *6*), and specific interacting partners. For example, DNMT3A is recruited to intergenic regions through dimethylated lysine 36 of histone 3 (H3K36me2), whereas DNMT3B shows enhanced binding to gene bodies of actively transcribed genes in a trimethylated H3K36 (H3K36me3)–dependent manner. Although the mechanism is still unclear, the long DNMT3A1 iso-

Department of Molecular and Cellular Biology, Baylor College of Medicine, Houston, TX, USA.
Email: tianpeng.gu@bcm.edu; goodell@bcm.edu

GRAPHIC: KELLIE HOLOSKI/*SCIENCE*

Regulating DNA methylation canyons

QSER1 (glutamine and serine–rich protein 1) and TET1 (ten-eleven translocation 1) protect DNA methylation canyons from hypermethylation by antagonizing DNA methyltransferase 3A (DNMT3A) and DNMT3B binding and safeguard the developmental potential of stem cells.

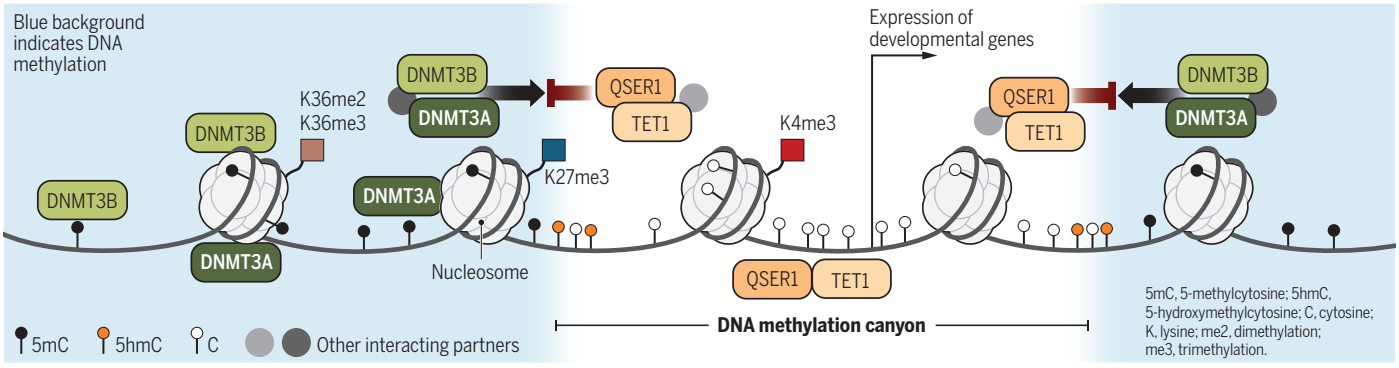

form is enriched at regions flanking CpG islands ("shores") at bivalent promoters bearing both the transcription-activating H3K4me3 and the transcription-repressive H3K27me3 histone modifications (*7*, *8*).

Although such histone modifications appear to guide the activity of DNMTs, additional features are used to actively oppose DNA methylation at CpG islands and canyons. TET proteins in particular have been shown to safeguard bivalent promoters against hypermethylation in human and mouse embryonic stem cells (*8*, *9*). The finding of QSER1 through a clever CRISPR screen to identify unknown regulators of DNA methylation by Dixon *et al.* was consistent with previous data indicating that it is a TET1 binding partner (*10*). They demonstrated that the two proteins are mutually dependent on each other for chromatin binding and that they compete for DNA binding with DNMT3A and DNMT3B at canyons (see the figure). Notably, in human embryonic stem cells lacking *QSER1* and *TET1*, many promoter regions became hypermethylated and showed decreased transcription; the stem cells were less able to differentiate into pancreatic progenitors, underscoring the in vivo biological importance of QSER1-TET1–regulated DNA methylation for stem cell function.

Growing evidence, including the work by Dixon *et al.*, suggests that tightly regulated regional DNA methylation around bivalent promoters is critical for cell-fate decisions. Enrichment of 5-hydroxymethylcytosine, a key intermediate of TET-mediated DNA demethylation at the shores of canyons, signals the greatest methylation turnover at these regions during stem cell self-renewal and differentiation (*2*). Any gene mutations that disrupt the balance of DNA methylation and demethylation at such regulatory regions could be pathogenic. Gain-of-function DNMT3A mutations in the PWWP (Pro-Trp-Trp-Pro) domain cause human growth failure and DNA hypermethylation at canyons associated with the histone modifying Polycomb-repressive complexes in corresponding mouse models (*11*, *12*). Mutations of DNA methylation regulators, including loss-of-function mutations of *DNMT3A* and *TET2* and gain-of-function mutations of *isocitrate dehydrogenase 1* (*IDH1*) and *IDH2*, are frequently found in hematological malignancies, highlighting an essential role for stable DNA methylation status at focal regions in maintaining hematopoietic homeostasis. Moreover, in different cancer types, DNA hypermethylation within the promoters of tumor-suppressor genes occurs concomitantly with global DNA hypomethylation; both are thought to contribute to cancer cell transformation, underscoring the importance of maintaining balance in DNA methylation.

"The discovery of QSER1 [glutamine and serine–rich protein 1] offers a new facet to the push and pull regulation of DNA methylation."

The study of Dixon *et al.* validates QSER1 as a regulator for DNA methylation; nevertheless, some important questions remain unanswered. There are three TET proteins with distinct expression patterns across various cell types. It is unknown whether QSER1 interacts with TET2 and TET3, if any such interactions even exist in somatic tissues, or whether there are distinct mechanisms that serve with (or instead of) QSER1 to keep canyons hypomethylated in different contexts. Animal models in which *QSER1* is ablated will reveal the extent to which QSER1 is essential and will further illustrate the regulatory function of QSER1 during embryogenesis and development. Given the involvement of TET proteins in DNA demethylation, future research should focus on the coordinated function of QSER1 and TETs in epigenetic reprogramming in early embryos and establishing genomic imprinting in primordial germ cells. The maintenance of DNA methylation at canyons in somatic stem cells is also involved in three-dimensional chromatin architecture (*13*); it will be interesting to establish whether QSER1 has a role. There are limited data available on genetic alterations of *QSER1* in patients. Considering the dysregulation of DNA methylation in multiple diseases, it is likely that mutations in *QSER1* will be identified. Future investigation should integrate QSER1 in the regulatory network to achieve a better understanding for bivalent genes associated with cell differentiation and developmental transitions.

DNA methylation and demethylation are balanced through DNMT3 and TET proteins both competing and cooperating in synchrony with histone modifications; the mechanisms through which expression of developmental genes are regulated remain poorly understood (*14*, *15*). The discovery of QSER1 offers a new facet to the push and pull regulation of DNA methylation. ■

GRAPHIC: KELLIE HOLOSKI/*SCIENCE*

REFERENCES AND NOTES

1. W. Xie *et al.*, *Cell* **153**, 1134 (2013).
2. M. Jeong *et al.*, *Nat. Genet.* **46**, 17 (2014).
3. G. Dixon *et al.*, *Science* **372**, eabd0875 (2021).
4. T. H. Xu *et al.*, *Nature* **586**, 151 (2020).
5. T. Baubec *et al.*, *Nature* **520**, 243 (2015).
6. D. N. Weinberg *et al.*, *Nature* **573**, 281 (2019).
7. M. Manzo *et al.*, *EMBO J.* **36**, 3421 (2017).
8. T. Gu *et al.*, *Genome Biol.* **19**, 88 (2018).
9. N. Verma *et al.*, *Nat. Genet.* **50**, 83 (2018).
10. Y. Costa *et al.*, *Nature* **495**, 370 (2013).
11. P. Heyn *et al.*, *Nat. Genet.* **51**, 96 (2019).
12. G. Sendžikaitė, C. W. Hanna, K. R. Stewart-Morgan, E. Ivanova, G. Kelsey, *Nat. Commun.* **10**, 1884 (2019).
13. X. Zhang *et al.*, *Mol. Cell* **78**, 506 (2020).
14. H. Wu *et al.*, *Science* **329**, 444 (2010).
15. D. Douillet *et al.*, *Nat. Genet.* **52**, 615 (2020).

ACKNOWLEDGMENTS

The Goodell lab is supported by grants from the National Institute of Diabetes and Digestive and Kidney Diseases, the National Cancer Institute, the National Institute on Aging, and the Edward P. Evans Foundation.

10.1126/science.abh3187

IMMUNOTHERAPY

Recruiting T cells in cancer immunotherapy

T cell dynamics reveal that immunotherapy responses may rely on peripheral T cells

By **Kathryn E. Yost[1], Howard Y. Chang[1,2], Ansuman T. Satpathy[3]**

Immunotherapies that enhance the ability of the immune system to target cancer cells have proven effective in a variety of tumor types, yet clinical responses vary across patients and cancers. The most effective immunotherapies to date are immune checkpoint blocking antibodies, which target inhibitory surface receptors expressed by T cells, particularly programmed cell death 1 (PD-1). One of the few robust correlates of clinical response to PD-1 blockade is the presence of tumor-infiltrating T lymphocytes (TILs) prior to treatment, with immune-infiltrated tumors achieving better responses than "immune-desert" tumors (*1*). Therefore, it has been widely assumed that PD-1 blockade reinvigorates preexisting cells within the tumor microenvironment (TME). However, recent studies of T cell dynamics suggest that the T cell response to immune checkpoint blockade (ICB) may originate outside the tumor and rely on peripheral T cell recruitment. This has important implications for patient selection, predictive biomarkers, and design of combination treatment regimens.

The site of ICB activity has historically been predicted from the expression pattern of the target inhibitory receptor and its ligand. The first immune checkpoint inhibitor that was approved for cancer targeted the cytotoxic T lymphocyte-associated protein 4 (CTLA-4) receptor, which is primarily expressed by $CD4^+$ effector T cells and regulatory T cells (T_{regs}). Given that the CTLA-4 ligand, B7, is not expressed on malignant cells but rather on antigen-presenting cells (APCs) in the lymph node, CTLA-4 blockade was predicted to act on a lymph node–resident population of $CD4^+$ T cells, which is subsequently recruited to the tumor. Indeed, studies in mouse models and patients have demonstrated that CTLA-4 blockade induces expansion of a subset of tumor-infiltrating $CD4^+$ T cells expressing inducible T cell costimulator (ICOS), and increased $ICOS^+CD4^+$ T cell frequency following CTLA-4 blockade correlates with clinical response (*2*). Given its expression, CTLA-4 blockade has also been hypothesized to deplete intratumoral T_{regs}; however, this has not been consistently observed in patients (*2*).

Several monoclonal antibodies targeting PD-1 have since been approved for the treatment of multiple cancer types. PD-1 is expressed by several subsets of activated $CD8^+$ and $CD4^+$ T cells and is highly expressed on exhausted $CD8^+$ T cells that show diminished cytotoxic responses to antigens (*2*, *3*). Moreover, the ligand for PD-1, PD-L1, is expressed by malignant cells as well as APCs, and high PD-L1 expression within the tumor can correlate with clinical efficacy (*1*). These data suggest that in contrast to CTLA-4 blockade, PD-1 blockade may act primarily on tumor-resident T cells. The reinvigoration of T cells in the TME, particularly exhausted T cells, was further supported by studies in mouse models of cancer and chronic viral infection, which demonstrated that PD-1 blockade could induce proliferation and effector properties in chronically stimulated T cells (*3*).

However, it has been difficult to reconcile this singular paradigm of PD-1 action on tumor-resident T cells with observations that suggest a systemic immune response. For example, T cell proliferation and activation are prevalent within the tumor-draining lymph node (TDLN) and peripheral blood following PD-1 blockade in mouse tumor models (*4*). PD-L1 blockade within the TDLN promotes tumor rejection similar to that induced by systemic therapy, and the inhibition of T cell migration prior to PD-1 blockade abrogates tumor rejection, suggesting that the TDLN may act as a reservoir of PD-1 and PD-L1 blockade–responsive, tumor-reactive T cells (*4*, *5*). Moreover, tumor regression following PD-1 blockade in mouse models is dependent on interactions between APC-derived B7 and the T cell costimulatory receptor CD28, which occur in the lymph node (*3*). In particular, recent studies highlighted the importance of PD-L1 expression on classical dendritic cells (cDCs), suggesting that PD-1 blockade may act at the level of cDC-dependent T cell priming and activation (*5*, *6*). Further profiling of human T cell responses to PD-1 blockade in melanoma patients revealed increased T cell proliferation in the peripheral blood compared with the TME, suggesting that T cells may be activated peripherally and then recruited to the tumor (*7*).

A systemic antitumor immune response to PD-1 blockade is further supported by synchronous regression of multiple metastatic lesions after treatment (*8*). Similar to the abscopal effect, which is characterized by distant responses to site-specific tumor radiotherapy (*9*), uniform patterns of response among individual metastases suggest that peripheral immune cells may play an important role in the clinical response to ICB (*8*). Genomic profiling has also demonstrated that T cell exhaustion is epigenetically fixed, suggesting that PD-1 blockade may be unable to rescue exhausted TILs (*3*).

A productive immune response following ICB results in the clonal expansion of tumor-specific T cells, which can be tracked across different tissues and time points by profiling T cell receptor (TCR) sequences. TCR sequencing allows for preexisting T cell clones to be distinguished from newly activated T cells recruited from distant tissues. Early efforts to profile TCR dynamics in patients receiving anti-CTLA-4 therapy revealed a broadening of the peripheral T cell tumor-reactive TCR repertoire, supporting the idea that CTLA-4 blockade may lower the threshold of the strength of TCR signaling that is required for activation (*2*).

Tracking of peripheral T cell clones using TCR sequencing before and after ICB demonstrated that melanoma patients with a clinical response to therapy have significantly more clonal expansion and T cell turnover following therapy compared with nonresponders (*10*, *11*). However, whether peripherally activated T cells traffic to the tumor remained unclear. Profiling of phenotypic and clonal T cell dynamics in site-matched human basal and squamous cell carcinomas before and after PD-1 blockade revealed that $CD8^+$ T cells with an exhausted phenotype are more clonally expanded relative to other TILs and also expressed surface markers characteristic of tumor-reactive T cells (*12*). Clonal expansion of exhausted T cells in response to therapy was predominantly derived from T cell clones that were not detected in the tumor prior to therapy, and this effect was specific to exhausted T cells. Notably, most preexisting intratumoral T cell clones could be found in the tumor after therapy but did not clon-

[1]Center for Personal Dynamic Regulomes, Stanford University School of Medicine, Stanford, CA, USA. [2]Howard Hughes Medical Institute, Stanford University School of Medicine, Stanford, CA, USA. [3]Department of Pathology, Stanford University School of Medicine, Stanford, CA, USA. Email: howchang@stanford.edu; satpathy@stanford.edu

The cancer-immunity cycle of immune checkpoint blockade response

Immune checkpoint blockade with anti–programmed cell death 1 (anti–PD-1) therapy blocks inhibitory signaling on T cells. The immune response to PD-1 blockade relies on invigoration of tumor-extrinsic T cells during T cell priming and activation within the tumor-draining lymph node (TDLN). Activated T cells traffic to the tumor where they kill cancer cells and release antigens that are presented to T cells by dendritic cells in the TDLN, linking tumor-resident and tumor-extrinsic immune responses.

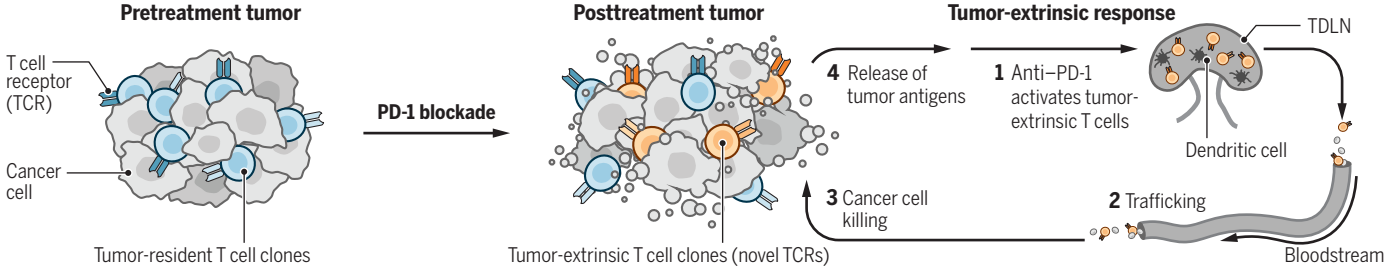

ally expand, and preexisting exhausted T cell clones did not adopt a nonexhausted phenotype following treatment (*12*). This suggests that preexisting exhausted TILs may have limited reinvigoration potential and that clonal replacement of TILs from tumor-extrinsic sources is a major aspect of ICB responses.

Additional support for this role of tumor-extrinsic T cells comes from two studies tracking T cell clones in tumor, normal adjacent tissue, and peripheral blood. In lung, endometrial, colorectal, and renal cancers, expanded T cell clones within the tumor were commonly shared with adjacent normal tissue and peripheral blood (*13*). TIL clones with an exhausted phenotype were less likely to be detected in peripheral blood, suggesting that replenishment of TILs with peripheral T cells may provide a source of nonexhausted TILs. Furthermore, deep TCR profiling during neoadjuvant PD-1 blockade (prior to surgical resection) demonstrated that T cell clones that expanded in the peripheral blood following treatment were enriched within the tumor of responding patients, suggesting that expansion and subsequent infiltration of peripheral T cells may be associated with clinical response (*14*).

Together, these studies support a model of tumor-extrinsic T cell responses to PD-1 blockade (see the figure). Interactions between PD-L1$^+$ cDCs and T cells in the TDLN are a compelling target for PD-1 blockade (*5*, *6*). After priming and activation, T cells can circulate in the peripheral blood and traffic to the primary tumor site, as well as metastases. Upon cancer cell killing, the release of tumor antigens and their subsequent presentation by migratory DCs in the TDLN provide a link between the tumor-extrinsic T cell response and the cancer-immunity cycle (*1*). It is important to note that the tumor-extrinsic T cell response to PD-1 blockade and the reactivation of preexisting TILs are not mutually exclusive and may represent complementary or synergistic mechanisms of response.

Despite these advances, many questions remain. Although T cell clones that respond to PD-1 blockade can be found in the peripheral blood and TDLN, several possibilities regarding their precise site of activation are possible: clonal T cell priming and expansion in the TDLN and/or tertiary lymphoid sites followed by recruitment to the tumor; activation and expansion of a recently primed or unexpanded pool of progenitor T cells (such as stem cell memory or progenitor exhausted cells) within the TME and/or TDLN; or a combination of these possibilities, whereby activation of tumor-resident T cells accelerates recruitment of peripheral T cells to the TME through chemokine secretion or cDC activation. Given that most T cell proliferation in the peripheral blood occurs within 1 week of anti–PD-1 therapy and is largely diminished by 3 weeks (*7*, *11*), what is the timing of clonal replacement? Does clonal T cell recruitment and expansion within the tumor follow the same kinetics? Chemical inhibition of T cell migration can abrogate tumor regression following ICB in some mouse models, but these results vary according to dosage and timing, indicating that such factors can influence therapeutic outcomes (*4*, *15*).

Another area of active investigation concerns how peripheral T cell dynamics are influenced by tumor-intrinsic factors, such as tumor site and mutational heterogeneity. Skin and lung cancers have been most extensively profiled and have high amounts of immune infiltration. Comparisons between metastatic sites suggested that tumors in more immunosuppressive tissue microenvironments (such as the liver) are the least responsive to PD-1 blockade, but how tumor location influences T cell dynamics during therapy remains unclear (*8*). Because clonal neoantigen burden is also associated with clinical response to ICB, and TILs reactive to clonal neoantigens are present prior to treatment (*1*), how do clonal antigens escape immune surveillance before ICB, and what is the relationship between tumor evolution and T cell dynamics? Distinguishing general immunological effects of PD-1 blockade from antitumor immune responses will require studies pairing TIL clonotypes to their target antigens to determine how T cell phenotypes and clonal dynamics are influenced by antigen specificity.

Thus, it is possible that preexisting TILs represent a correlate, rather than a cause, of clinical responses in immune-infiltrated tumors. Namely, intratumoral immune infiltration may simply reflect TME properties such as mutational load, immunogenicity, and/or tumor site that promote continued surveillance by tumor-extrinsic T cells. Future investigations into the origins and mechanisms of response to ICB should help to identify prognostic factors underlying clinical efficacy and will facilitate the rational design of effective treatment combinations to improve responses. In particular, the combination of ICB with immune-modulating agents that amplify peripheral T cell recruitment, such as immunostimulatory agonist antibodies and cytokine-based immunotherapies, may expand the utility of ICB to a wider patient population. ■

GRAPHIC: C. BICKEL/*SCIENCE*

REFERENCES AND NOTES

1. D. S. Chen, I. Mellman, *Nature* **541**, 321 (2017).
2. S. C. Wei, C. R. Duffy, J. P. Allison, *Cancer Discov.* **8**, 1069 (2018).
3. L. M. McLane, M. S. Abdel-Hakeem, E. J. Wherry, *Annu. Rev. Immunol.* **37**, 457 (2019).
4. M. H. Spitzer *et al.*, *Cell* **168**, 487 (2017).
5. F. Dammeijer *et al.*, *Cancer Cell* **38**, 685 (2020).
6. S. A. Oh *et al.*, *Nat. Can.* **1**, 681 (2020).
7. A. C. Huang *et al.*, *Nat. Med.* **25**, 454 (2019).
8. J. C. Osorio *et al.*, *J. Clin. Oncol.* **37**, 3546 (2019).
9. L. Hammerich *et al.*, *Nat. Med.* **25**, 814 (2019).
10. B. P. Fairfax *et al.*, *Nat. Med.* **26**, 193 (2020).
11. S. Valpione *et al.*, *Nat. Can.* **1**, 210 (2020).
12. K. E. Yost *et al.*, *Nat. Med.* **25**, 1251 (2019).
13. T. D. Wu *et al.*, *Nature* **579**, 274 (2020).
14. J. Zhang *et al.*, *Clin. Cancer Res.* **26**, 1327 (2020).
15. S. L. Topalian, J. M. Taube, D. M. Pardoll, *Science* **367**, eaax0182 (2020).

ACKNOWLEDGMENTS

A.T.S. is a scientific founder of Immunai. H.Y.C. is a cofounder of Accent Therapeutics, Boundless Bio and an adviser to 10x Genomics, Arsenal Biosciences, and Spring Discovery.

10.1126/science.abd1329

PHYSICS

Limits on superconductivity in flatland

Experiments explore a new superconducting regime in layered quantum materials

By **Mohit Randeria**

The superconducting state, with dissipation-less electrical current flow, has long been a source of fascination, with implications for fundamental questions like spontaneous symmetry breaking and the Higgs phenomena, as well as for applications ranging from magnets for magnetic resonance imaging machines to hardware for quantum computers. In the classic Bardeen-Cooper-Schrieffer (BCS) theory, electrons in a metal form pairs at a transition temperature (T_c) below which the system is superconducting. The low T_c of BCS superconductors is related to the small fraction of electrons that have their quantum states modified by pairing. One route to exploring a higher T_c is to find quantum materials in which a larger fraction of the electrons get involved in superconductivity. On page 190 of this issue, Nakagawa *et al.* (*1*) report experiments on superconductors in a new regime, where they come close to achieving the theoretically predicted T_c limit (*2*) in two dimensions (2D).

Progress in understanding superconductivity beyond the BCS paradigm has been spurred in part by ultracold Fermi gases (*3*). Though seemingly different, the theoretical description of pairing is essentially the same for neutral Fermi atoms or charged electrons. States below the Fermi energy (E_F) in a noninteracting Fermi system are occupied, whereas those above E_F are empty. BCS showed that a weak attraction between particles leads to the formation of pairs whose radius (ξ_0) is exponentially large compared to the interparticle spacing ($1/k_F$, the inverse Fermi wave vector). In the BCS limit, pairing and superconductivity occur at the same T_c, which is exponentially small compared to the temperature (T_F) corresponding to E_F. With increasing attraction, the pair size decreases, and a Bose-Einstein condensate (BEC) of tightly bound pairs forms in the extreme limit with $\xi_0 << 1/k_F$. This BCS-to-BEC crossover (*4*) has been realized in Fermi gases, where the interaction between atoms can be precisely controlled (*3*).

There is, however, no general way for tuning the interaction between electrons in a quantum material—hence the difficulty of observing a crossover in the solid state. Although it suffices to tune the attraction relative to E_F, controlling E_F in a metal is not easy either. Nakagawa *et al.* address this by doping the layered material ZrNCl with Li^+ intercalation. Using ionic liquid gating, the authors varied the electron density by two orders of magnitude, tuned E_F, and made a compelling case for driving the system to the BCS-BEC crossover regime.

The authors measured the electron density, and thus k_F, using the Hall effect and probed superconducting properties, including the pair size ξ_0 (estimated from upper critical field measurements) and energy gap Δ (obtained from tunneling spectroscopy). The authors also presented clear evidence from tunneling for a pseudogap arising from preformed pairing that onsets at a temperature T^* well above the superconducting T_c, a characteristic feature of the BCS-BEC crossover (*4*) (see the figure).

THE BCS-BEC crossover in 2D

The crossover regime from the BCS to BEC in a 2D Fermi gas has a T_c close to the theoretical limit ($T_c \leq T_F/8$ for parabolic dispersion). The ratio of interparticle distance ($1/k_F$) to pair size ($\xi 0$) grows with increasing attraction between fermions. Pairs form below T^* and superconductivity occurs below T_c.

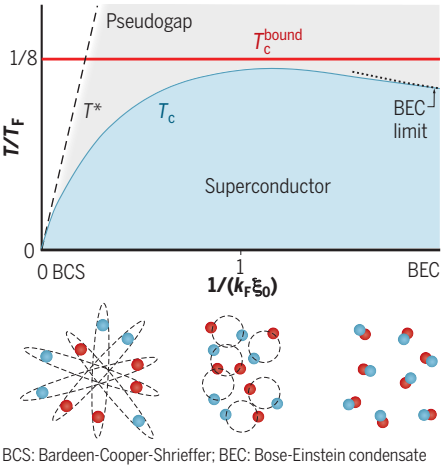

BCS: Bardeen-Cooper-Shrieffer; BEC: Bose-Einstein condensate

Exact upper bounds (*2*) on T_c were recently derived on the basis of general considerations for the Berezenskii-Kosterlitz-Thouless phase transition in 2D. For parabolic dispersion, $T_c \leq T_F/8$. From the known behavior of T_c in the BCS and BEC limits in 2D, the maximum T_c should be attained in the crossover regime and be close to the $T_F/8$ bound. Nakagawa *et al.* show that their samples are in a 2D regime, the dispersion is parabolic, and, notably, their T_c comes close to saturating the 2D bound.

The general 2D bounds (*2*) on T_c are also relevant for several exciting materials such as monolayer FeSe (*5*), magic-angle twisted bilayer (*6*), and trilayer graphene (*7*). These are all multiband superconductors with more complex electronic structure than the parabolic band of Li: ZrNCl, which makes comparison with theory less straightforward.

It should be emphasized that there are no known absolute limits to the superconducting T_c. Room-temperature superconductivity was observed (*8*) in carbonaceous sulfur hydride at high pressures, and T_c may be ~10^9 K in neutron stars. However, T_c in these systems is much smaller than T_F. The highest known T_c/T_F ratio is around 0.22 in the 3D BCS-BEC crossover (*4*) in ultracold Fermi gases. This value is higher than the 3D BEC result, which is known not to be an upper bound on T_c. Even though experiments suggest that there could be a limit on T_c/T_F, establishing such a bound in 3D remains an open theoretical question (*2*).

The experiments of Nakagawa *et al.* raise many other questions, such as the microscopic pairing mechanism that leads to T_c as high as 20 K in a 2D material with an electron density as low as 10^{20} per cubic centimeter. Determining why ZrNCl can be doped into a strongly interacting BCS-BEC crossover regime is also of clear importance. The authors' discovery opens the door to a fascinating new world of strongly interacting superconductivity in 2D materials. ■

Department of Physics, The Ohio State University, Columbus, OH 43220, USA. Email: randeria.1@osu.edu

REFERENCES AND NOTES

1. Y. Nakagawa *et al.*, *Science* **372**, 190 (2021).
2. T. Hazra, N. Verma, M. Randeria, *Phys. Rev. X* **9**, 031049 (2019).
3. W. Ketterle, M. W. Zwierlein, *Riv. Nuovo Cim.* **31**, 247 (2008).
4. M. Randeria, E. Taylor, *Annu. Rev. Condens. Matter Phys.* **5**, 209 (2014).
5. D. Huang, J. E. Hoffman, *Annu. Rev. Condens. Matter Phys.* **8**, 311 (2017).
6. Y. Cao *et al.*, *Nature* **556**, 80 (2018).
7. J. M. Park *et al.*, *Nature* **590**, 249 (2021).
8. E. Snider *et al.*, *Nature* **586**, 373 (2020).

ACKNOWLEDGMENTS

M.R. acknowledges support from NSF Materials Research Science and Engineering Center grant DMR-2011876.

10.1126/science.abg1752

GRAPHIC: N. CARY/*SCIENCE* BASED ON M. RANDERIA

POLICY FORUM

DIVERSITY IN SCIENCE

Concrete steps to diversify the scientific workforce

Any barrier to entry weakens science and its societal impact

By **Shirley Tilghman[1], Bruce Alberts[2], Daniel Colón-Ramos[3], Kafui Dzirasa[4], Judith Kimble[5], Harold Varmus[6]**

The recent events that precipitated the resurgence of the Black Lives Matter movement and the disproportionately devastating impact of COVID-19 on many communities of color are stark reminders of the pernicious effects of systemic racism on all aspects of our society, including science, medicine, and public health. The lack of diversity in the scientific and health professions—a long-standing manifestation of racism—can no longer be ignored, excused, or attributed to uncontrollable factors. We write at this moment of reckoning to explain what is lost by a lack of diversity; to describe some promising efforts to achieve it; and to propose urgent, larger-scale actions that political and institutional leaders, educators, and scientists can take to redress the inequities that pervade our professions.

THE IMPORTANCE OF DIVERSITY IN SCIENCE

African American, Latinx, and Indigenous peoples have historically been underrepresented in the research enterprise, with their proportions declining as they progress from undergraduate to graduate school to faculty positions (see the figure, top). The glacial pace of the increase in the percentage of minority PhDs over the past two decades, if extrapolated, suggests that it will take many more decades for the workforce to reflect the makeup of the US population (see the figure, bottom). To wait so long for an equitable outcome should be unacceptable to us all.

Some who defend the status quo claim that a lack of diversity does not compromise the quality of science or the likelihood of making discoveries that improve human well-being. We strongly disagree. Why? First, because any barrier to entry into STEM (science, technology, engineering, mathematics) fields weakens science and carries unacceptable opportunity costs. By limiting the pool from which future scientists are drawn, the full range of talent is reduced, and progress is slowed.

Second, when science is more inclusive, the range of questions asked will broaden, as happened when women began to enter the biomedical profession in larger numbers in the 1970s and 1980s (*1*). As an example, a more diverse group of geneticists might have prevented the large human genetic databases from becoming so highly skewed toward European ancestry genomes, limiting their power to identify genetic determinants of disease in other groups (*2*).

Third, barriers to the inclusion of specific demographic groups limit the potential impact of science on society. Today, the reluctance of minority communities to participate in clinical trials for COVID-19 vaccines or even to receive vaccines that have been rigorously tested and approved (*3*) reflects an understandable skepticism of medical authority that arose from historic injustices toward African American and Hispanic communities. For scientific advances to be widely accepted throughout an increasingly diverse US population, both the composition and leadership of our scientific and medical communities must become much more representative.

Last, the US census projects that by 2045, no single group, as defined by the US government, will hold a majority (*4*). In 2018, only 50% of the population under 18 years of age was white—with 25% Hispanic, 14% African American, and 5% Asian American—and the white proportion continues to drop every year. As Congress has recognized, the US will be unable to compete in the global arena in the future if it fails to draw talent from its diverse citizenry.

The tendency to prefer and to value people most like oneself is a deeply held human trait, one that needs conscious monitoring to overcome. Scientists are not singularly resistant to the phenomenon of implicit or unconscious bias, which can affect all aspects of professional life: hiring, evaluation, promotion, citation practices, and grant funding (*5*). For example, data suggest that African American grant applicants for funding from the National Institutes of Health (NIH) face racial bias in the awarding of grants (*6*), with African American applicants receiving grant review priority scores that were 10 percentile points lower than scores for white or Asian American applicants, substantially reducing their chances to receive funding. Despite the efforts of the NIH leadership to understand these findings, the discrepancy has never been fully explained, and the difference in success rates (the "funding gap") has never been closed.

The NIH recently announced a new initiative, UNITE, a multipronged effort to end structural racism and its consequences at the NIH, including inequities in evaluations of grant applications (*7*). A commitment of this kind is a first and laudable step to making meaningful progress.

LEARNING FROM SUCCESSES

In an attempt to rationalize the lack of diversity in the scientific workforce, some have argued that science is a meritocracy, and that the absence of diverse voices, although unfortunate, largely reflects the limited diversity of the pipeline of trainees. This passive view—delegating the problem to a metaphorical pipeline outside of our control—ignores actions that the scientific community can take to address systemic racism and its consequences.

During the past few decades, several programs have aimed to increase the inclusion of minorities in science. Although well-meaning, many of these have been either ineffective or not conducted at a scale adequate to substantially change national percentages. We urgently need more and bolder efforts. Fortunately, we can now build on some recent programs that have had notable success in training minority scientists who are now pursuing productive careers in research. These programs appear to have three key features: reducing the sense of isolation by using cohorts to create communities, making strong institutional and individual commitments to mentoring, and removing barriers to research careers by providing full financial support during training.

For example, since 1993, hundreds of undergraduates from the University of Maryland Baltimore County's (UMBC) Meyerhoff Scholars Program have gone on to receive MDs and PhDs in STEM fields (*8*). The program relies heavily on a cohort model, in which Meyerhoff scholars form a community that provides mutual support

[1]Princeton University, Princeton, NJ, USA. [2]University of California, San Francisco, CA, USA. [3]Yale University, New Haven, CT, USA. [4]Duke University Medical Center, Durham, NC, USA. [5]University of Wisconsin, Madison, WI, USA. [6]Weill Cornell Medicine, New York, NY, USA.
Email: smt@princeton.edu

and encouragement; students receive intensive personal advising and counseling by UMBC faculty; and they enjoy access to laboratory opportunities, starting in their freshman year. The program is now being replicated, with promising outcomes, at a number of other research universities (*8*).

Another successful model is the Specialized Training and Advanced Research (STAR) program at the University of California, Los Angeles (*9*). This program attracts physicians nearing the end of their clinical training to study for a PhD in a variety of research fields. Although not designed as a minority-serving program, it has capitalized on medical schools having been more successful than graduate programs in attracting minority students. By removing financial burdens that often discourage medical trainees from considering substantial engagement in laboratory research, and by building a strong sense of community that counters the isolation that minority students often experience in the sciences, the program has been successful in directing physicians into research.

Another approach that universities have successfully used to diversify their faculty is cluster hiring, in which searches are designed to attract a group of faculty of color over a short period of time. This approach exploits features of the cohort model, including building a community that provides mutual support, encouragement, and peer mentoring. Recognizing the effectiveness of such approaches, in January 2020 the NIH announced the $241 million Faculty Institutional Recruitment for Sustainable Transformation (FIRST) initiative. The FIRST program has allowed approximately a dozen universities and medical schools to expand their faculty in emerging areas of research, with a requirement that every person hired must have a track record of working to promote an inclusive culture in science (*10*).

One should not underestimate the role that money plays in the choices that students make to become scientists. The pay gap between whites and African American, Latinx, and Indigenous people, coupled with long-standing and often unwritten discriminatory policies, has prevented generations of minority Americans from accruing appreciable property and other forms of wealth (*11*). Without the security that such family assets provide, it is much more difficult to embark on PhD or MD training that may not lead to an attractive salary for many years—often while carrying substantial student debt.

Race and ethnicity in the biomedical research workforce

(Top) Demographics by career stage in 2016. The red line denotes the proportion of the specified race and ethnicity in the US population in 2016. (Bottom) Growth in Black and Hispanic PhD recipients over time. The dashed line indicates a linear best-fit trendline. Data are from (*15*).

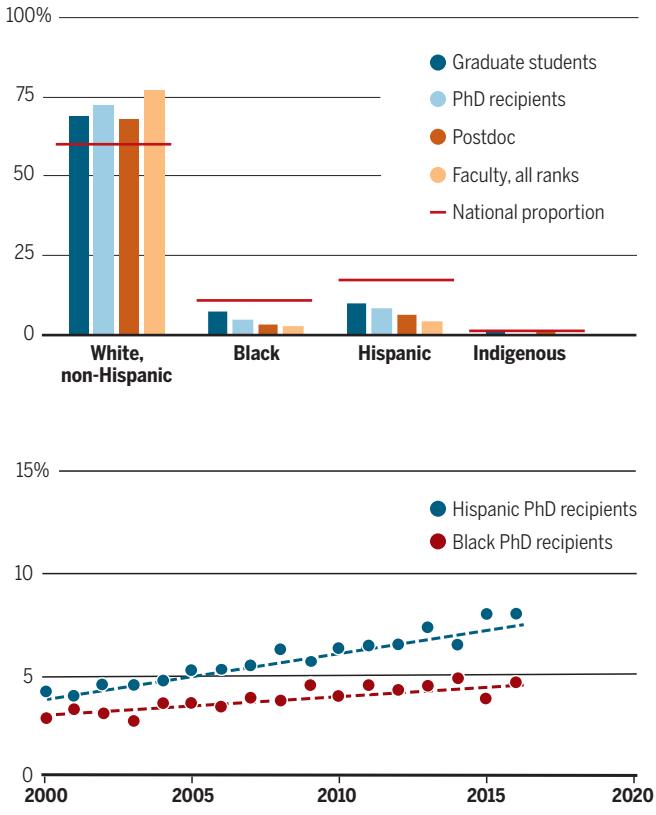

RECOMMENDATIONS

We recommend three approaches to redress this situation: a major federal initiative to diversify the scientific and engineering workforce, a reshaping of institutional culture to welcome underrepresented minorities into STEM research, and grant-funding policies that immediately address current inequities.

A coordinated federal program to diversify the scientific workforce

President Biden has strongly signaled his intention to seek remedies for past racial injustice in this country. At the same time, he has forcefully declared his commitment to scientific solutions to the nation's problems, and he has elevated the role of the White House Office of Science and Technology Policy (OSTP) by seeking to place its director, nominee Eric Lander, in his Cabinet, an unprecedented action. We call on President Biden to take an even bolder step in support of both equity and science by proposing legislation that would establish and fund a broad interagency National Science and Engineering Diversity Initiative (NSEDI). And we call on Congress to pass such a bill once submitted for consideration.

We recommend that OSTP, reporting directly to the President, organize a programmatic planning process for NSEDI, establish a long-range national strategic plan for diversifying the scientific workforce, and coordinate the distribution of funds to the relevant federal agencies to carry out these plans. A comprehensive effort for diversifying the STEM workforce will require actions that affect and provide support for all components of the scientific enterprise: K-12, college, and graduate education; professional training programs; employment in the public and private sectors; and research grants in many fields. Therefore, NSEDI will need to be developed in conjunction with all of the federal science agencies that participate in the National Science and Technology Council, as well as with the Small Business Administration and the Department of Education. Although it is premature to estimate NSEDI's budget until extensive planning has been undertaken, it seems prudent to expect, on the basis of examples of the anticipated activities (see the box), that an effective program will require an annual new Congressional appropriation of at least 10 billion dollars for several years—a substantial sum but only about 2% of national spending (public and private) on research and development and less than 8% of the federal government science budget.

To ensure that NSEDI's programs are working appropriately, Congress should require that an external advisory board be established that develops evidence-based measures to evaluate NSEDI's projects, recommends changes in its portfolio and budget, and reports regularly on the diversity of the nation's scientific workforce.

Reshaping institutional policies

As important as federal funding will be, there are also steps that academic institutions must take to effect an enduring change in the culture of science. The

GRAPHIC: H. BISHOP/*SCIENCE* BASED ON S. TILGHMAN *ET AL.*

Possible programs to diversify the workforce

- A competitive grants program to fund elementary and high schools that compete successfully to develop new and inclusive science education programs
- Full scholarships for students entering undergraduate programs designed to encourage the participation of minorities in STEM fields
- Full stipends and tuition for minority students in graduate programs that are designed to attract and retain underrepresented minorities
- Salaries and tuition for graduates of health professional schools who seek additional research training through programs that resemble the STAR program
- Grants to early-stage investigators from minority groups, supported by allocations to the NIH Director's Common Fund and by similar mechanisms at other science agencies
- Programs that build research infrastructure in minority-serving institutions
- Programs and grants to promote entrepreneurship for individuals from underrepresented racial and ethnic groups within the biomedical research and development sector

criteria for hiring and promotion of all scientists—from junior faculty to senior administrators—should include evidence of a commitment to diversity, equity, and inclusion. Institutions should also take steps to diminish the "minority tax" that is imposed on faculty of color engaged in diversity efforts by ensuring that such programs are led, at least jointly, by nonminority faculty. Moreover, offices and programs established to enhance the careers of minority scientists should be empowered with clear reporting structures to leadership, as well as with administrative and financial support.

Colleges, universities, and research institutions should take steps to educate faculty, students, and staff about the history of racism in the United States and provide training for those who serve as mentors and advisers for minority scientists at all career stages. For example, the Center for Improvement of Mentored Experience in Research at the University of Wisconsin–Madison designs training modules that are used by many institutions across the country (https://cimerproject.org). Mentors need not be sought solely within a single laboratory, department, or institution but can be found within the national mentoring networks being generated by scientific and engineering societies.

Experimental approaches for bringing about change in the culture of science should be encouraged, and the impact of programs designed to expand the participation of minority scientists should be regularly assessed to identify the most successful strategies.

NIH policies to redress structural racism

Our first two recommendations are directed to the broad scientific enterprise irrespective of field. Their adoption will take time, and their full impact will not be felt for many years. As biomedical scientists driven by the "fierce urgency of now," we propose three immediate steps that our major source of funding, the NIH, could take that do not require either Congressional action or a culture change in academia.

1. **Address financial barriers faced by minority scientists**
   The NIH Research Supplements to Promote Diversity in Health-Related Research is a targeted mechanism that allocates extramural funds to support scientists from diverse backgrounds before establishing an independent research program (*12*). We recommend that these grant supplements be paired with a student loan repayment program to reduce the financial burdens of advanced education and training. This would repay up to $50,000 annually of qualified educational debt for minority PhD and MD students. In addition, the application process and evaluation criteria for these Research Supplements should be standardized across NIH institutes, and the length of support should be increased to at least 3 years to enable adequate time for securing individual grant funding.

2. **Close the gap in NIH funding of grants for minority scientists**
   The funding gap for African American scientists has been estimated by one of us to be equivalent to about 25 research project grants and 25 smaller exploratory grants per year (*13*). We recommend that the NIH director establish, through the Common Fund, a Demonstration Project (DP) designed to eliminate the gap within 5 years. Eligibility should be similar to the requirements for other DPs and follow the guidelines for the NIH Research Supplements to Promote Diversity in Health-Related Research.

3. **Expand funding for businesses that employ minority scientists**
   Currently, 4.8% of the NIH research project grant budget is directed toward small businesses through the Small Business Innovation Research (SBIR) and Small Business Technology Transfer (STTR) programs ($1.1 billion annually). In 2019, only 3.5% of these SBIR/STTR grants were awarded to principal investigators from minority groups (*14*). We recommend that the OSTP establish a goal of at least 5% for minority participation in the NIH SBIR/STTR programs.

REPRISE

We propose ambitious, concrete steps for political and institutional leaders, educators, and scientists to take in the immediate future. But we acknowledge that even a successful implementation of these policy recommendations will fall short unless society addresses the broader issues of racism that produce the inequities in the first place. ■

REFERENCES AND NOTES

1. J. Stone, V. W. Pinn, J. Rudick, M. Lawrence, M. Carlyn, *J. Womens Health* (Larchmt.) **15**, 234 (2006).
2. A. C. Need, D. B. Goldstein, *Trends Genet.* **25**, 489 (2009).
3. B. Farmer, "COVID vaccine trials move at warp speed, but recruiting Black volunteers takes time," *Kaiser Health News*, 2020; https://khn.org/news/covid-vaccine-trials-move-at-warp-speed-but-recruiting-black-volunteers-takes-time/.
4. S. L. Colby, J. M. Ortman, "Current population reports," P25-1143 (US Census Bureau, 2014).
5. K. Dutt, "How implicit bias and lack of diversity undermine science," *Scientific American,* 2018; https://blogs.scientificamerican.com/voices/how-implicit-bias-and-lack-of-diversity-undermine-science/.
6. D. K. Ginther *et al*., *Science* **333**, 1015 (2011).
7. M. Lauer, "NIH stands against structural racism in biomedical research," Open Mike, 2021; https://nexus.od.nih.gov/all/2021/03/01/nih-stands-against-structural-racism-in-biomedical-research.
8. M. R. Sto. Domingo *et al*., *Science* **364**, 335 (2019).
9. UCLA STAR program, https://medschool.ucla.edu/star.
10. J. Mervis, *Science* (2020). 10.1126/science.abb1082
11. E. Patten, "Racial, gender wage gaps persist in US despite some progress," Pew Research Center, 2016; www.pewresearch.org/fact-tank/2016/07/01/racial-gender-wage-gaps-persist-in-u-s-despite-some-progress.
12. National Institutes of Health, "Research supplements to promote diversity in health-related research," PA-20-222 (NIH, 2020); https://grants.nih.gov/grants/guide/pa-files/PA-20-222.html.
13. K. Dzirasa, *Cell* **183**, 576 (2020).
14. National Institutes of Health, NIH SBIR/STTR award data (NIH, 2020); https://sbir.nih.gov/statistics.
15. National Center for Science and Engineering Statistics, "Women, minorities, and persons with disabilities in science and engineering: 2019," National Science Foundation, 2019; https://ncses.nsf.gov/pubs/nsf19304.

ACKNOWLEDGMENTS

We are deeply grateful to F. Hrabowski, H. Valantine, O. Ajijola, A. Diaz Vazquez, Y. Fortis Santiago, G. Guerrero-Medina, B. Jones Marlin, K. Milligan-Myhre, C. C. Pinnix, and P. Silveyra for speaking to us about their experiences in bringing diversity and inclusion to biomedical science. The authors also thank C. Pickett for help preparing the manuscript and the members of the Rescuing Biomedical Research Steering Committee for helpful discussions.

10.1126/science.abf9679

BOOKS *et al.*

SCIENCE LIVES

Rethinking Alexander Graham Bell's legacy

A new biography confronts the inventor's complicated relationship with the Deaf community

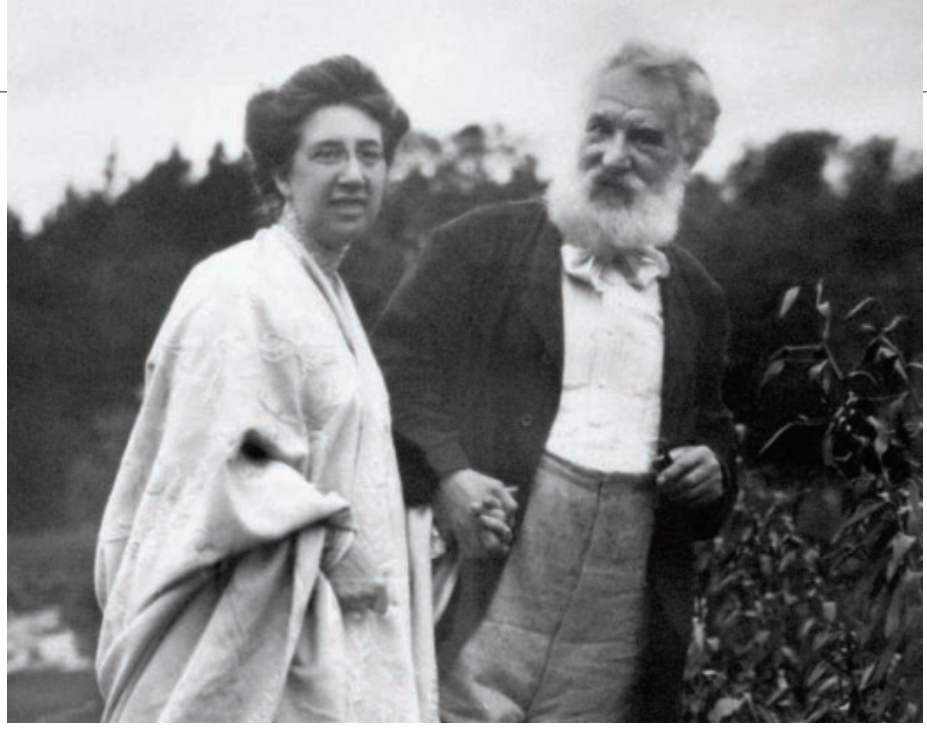

Bell (right) holds hands with his wife, Mabel, who lost her hearing to scarlet fever at the age of five.

PHOTO: WIKIMEDIA COMMONS

By **Jessica Trussell**

Alexander Graham Bell is well known as the inventor of the telephone. He is lesser known for his role in promoting audism, or prejudice against deaf and hard of hearing (DHH) people. Yet both endeavors have had lasting impacts on humanity. In *The Invention of Miracles*, Katie Booth revisits Bell's legacy, exploring his creative genius and his misguided efforts to eradicate Deaf culture (*1*).

Bell, known to his family as Aleck, was born into a family immersed in the communication strategies of the deaf. His mother, Eliza Grace Bell (née Symonds), an accomplished pianist who was deafened after she acquired language and speech, taught Aleck British Sign Language. His father, Alexander Melville Bell, created a phonetic alphabet called Visible Speech, designed to aid the deaf by illustrating the proper position of the lips, tongue, and throat in various language sounds. Following the family's lead, as teenagers, Aleck and his brother Melville built an automaton that could simulate human speech.

As the Bell family began promoting Visible Speech to potential investors, Alexander encouraged Aleck, approaching adulthood, to pursue elocution over invention. An educator named Susanna Hull became aware of the system and wondered whether it could be used to teach DHH children to speak. Working with Hull's DHH students, in 1868, Aleck succeeded in teaching the children to speak using the system. Oral schools for the deaf and well-off families began to seek out Aleck's expertise, fueling his passion for teaching. He would eventually become a professor of vocal physiology and elocution.

Meanwhile, Bell's interest in creating a machine that would faithfully transmit sound and speech endured. Yet even as the invention that would ultimately become the telephone progressed, he viewed the technology as a mere means to an end. "The telegraph, the telephone—they were fulfilling," writes Booth, "but Aleck's idea was for them to serve his larger goal, to give him time to devote to reforming deaf education."

During this period, Bell married Mabel Hubbard, a former student who lost her hearing as a child, and together they started a family. But defending his various patents frequently took him away from his family and from his work with the deaf.

In 1883, Bell established a school for the deaf in Washington, DC. Even as many in the Deaf community began to advocate signed language over oralism, Bell and the school remained committed to teaching DHH students to speak aloud and to read lips. Soon, however, he began to realize that oralism privileged learning how to speak over learning other sorts of information. He closed his school and began to rethink his beliefs about the DHH population.

The isolation of the deaf meant that DHH individuals were more likely to marry one another. Having observed that unions in which both partners were deaf had a higher likelihood of producing deaf offspring and fearing that the deaf would eventually outnumber the hearing, Bell began to encourage DHH people not to intermarry. His new stance was embraced by eugenicists, who eventually succeeded in passing a law in the United States that made it illegal for DHH people to marry one another. Bell did not support the law, and he attempted to align himself with other leaders in deaf education who opposed it, but he would nonetheless come to be perceived as the movement's leader.

In the waning years of his life, Bell distanced himself from deaf education. However, his curriculum would go on to become the predominant method for educating DHH children for many years to come. Today, many DHH people who work diligently to preserve the Deaf community's language, culture, and institutions blame Bell for the generation of DHH children whose education emphasized speaking over true learning.

The Invention of Miracles
Katie Booth
Simon and Schuster, 2021. 416 pp.

At the end of the book, Booth discloses that Bell died signing into his wife's hand. She reminds readers that Bell—who feared the intergenerational perpetuation of deafness—married a DHH woman and had children with her. Booth summarizes this central tension that defined Bell's life using Mabel's words: "You are very tender and gentle to the deaf children," she once wrote to him, "but their interest to you lies in their being deaf, not in their humanity." ■

REFERENCES AND NOTES

1. Deaf with a capital D is used to denote deaf and hard of hearing people who are culturally deaf. Deaf with a lowercase d is used to denote people who have a hearing loss but do not consider themselves part of the Deaf culture.

10.1126/science.abg8248

The reviewer is at the National Technical Institute for the Deaf, Rochester Institute of Technology, Rochester, NY 14623, USA. Email: jwtnmp@rit.edu

Refracted reality

A social scientist probes social media–induced polarization

Breaking the Social Media Prism: How to Make Our Platforms Less Polarizing
Chris Bail
Princeton University Press, 2021. 240 pp.

By **Jennifer Golbeck**

The media writ large, and social media in particular, have a lot to answer for with regard to the polarization currently plaguing society. But the influence of so-called "echo chambers" on ideology is much more complicated than it first appears. In *Breaking the Social Media Prism: How to Make Our Platforms Less Polarizing*, computational social scientist Chris Bail has done the hard work of breaking down ideological polarization, misinformation, and the impact that other people's content has on our social media experience.

The book brings the reader through a carefully constructed set of experiments, featuring bots, secret pairings between people on opposite ends of the political spectrum, and insightful personal stories, designed to identify promising interventions that might repair our fractured politics, as well as those that probably are not worth the effort of implementing. Bail does a masterful job weaving together insights drawn from people's backgrounds, politics, and online reactions to help readers understand how individuals across the ideological spectrum experience social media platforms. The experiments answer many of the questions a curious reader may wonder about, often with surprising results.

The people and data science in this book are compelling enough to stand on their own, but Bail has also done excellent work making the book immediately relevant. It speaks directly to the present moment, with stories about Trump-style politics, the lead-up to the 2020 US election, the COVID-19 pandemic, and ongoing international political issues. The reader never feels as though she has strayed into the theoretical because all of the book's context comes directly from these strange times.

Bail argues that the structure of social media is designed to amplify extreme voices and make moderates nearly invisible, shifting the discourse. Algorithms then push the more extreme discourse to like-minded users. But is this design responsible for our polarization? If we were exposed to more diverse views, would we all shift back toward the middle?

Bail's careful research suggests that is not the case. Through compelling personal profiles of a left-leaning moderate and a strong Trump supporter who participated in a long-term experiment to evaluate such an intervention, he shows that exposure to content from the other side of the ideological spectrum actually pushed the subjects further toward their existing positions: The liberal-leaning moderate adopted more left-wing ideas and embraced Democratic policy positions more strongly, and the Trump supporter ramped up her attacks on liberals.

Bail argues that platforms make it easy to misread the social environment. Rather than reflecting a world full of mostly well-meaning, moderate people, they twist reality, refracting our view (hence the eponymous "prism") and distorting our understanding of ourselves and others. He further argues that people have a natural desire to experiment with their self-presentation and to receive feedback that helps hone and refine their self-expression and identity. Social media platforms satisfy this desire, providing immediate reward—or punishment—in the form of likes, shares, and comments. Together, these factors can refine and polarize our perception of ourselves without us even knowing that it is happening.

Social media also magnifies extremists, making political polarization appear worse than it really is. However, this perception makes people, especially moderates, less likely to engage and thus less likely to be seen. The appearance of polarization feeds itself.

The book culminates in an experiment around a simulated redesign of a social media platform that brings anonymous users together in direct conversation. The result of chatting one-on-one with someone from the other side of the ideological divide? People became considerably less polarized. Bail hopes that this suggests that there are platform changes that can be made to make people more moderate. His experiments are solid, and I believe his results, although as a social media researcher, I am not quite as optimistic as he is about the success this would have at scale. (That said, I hope he is right.)

Breaking the Social Media Prism answers important questions about the origins of our current political environment and suggests how existing platforms and reward systems might be redesigned to make things better. Bail's scientific conclusions are refreshing in a space dominated by informed speculation, and the book offers hope that data-driven solutions can bring us back from the brink. ■

IMAGE: ADAPTED FROM ISTOCK.COM/ERHUI1979 BY C. AYCOCK/*SCIENCE*

The reviewer is at the Social Intelligence Lab, University of Maryland, College Park, MD 20742, USA. Email: golbeck@cs.umd.edu

10.1126/science.abg8045

LETTERS

The nets used by Brazil's fishing trawlers can harm the marine ecosystem.

Edited by **Jennifer Sills**

Prevent bottom trawling in southern Brazil

Bottom trawling, a method of fishing in which nets are dragged across the ocean floor, leads to the death of an estimated 4.2 million tons per year of non-target species worldwide (*1*), decreases revenue by disrupting the growth of juvenile fishes (*2*, *3*), threatens ocean ecosystems worldwide (*4*), and increases aqueous CO_2 emissions by disturbing the seafloor (*5*). The coastal shallow waters of the Rio Grande do Sul state in southern Brazil, an ecological hotspot for megafauna and fish feeding, spawning, and nursing, have deteriorated due to extensive fishing. To protect and reconstruct their former fishery productivity, scientific evidence should be valued over the industry's immediate interests, and bottom trawling should not be allowed in this ecosystem.

Extreme overfishing (*6*, *7*) and the chronic inefficiency of federal fisheries management pushed local fishers in Rio Grande do Sul to lead the push for the 2018 approval of the Sustainable Fisheries State Policy Act (Rio Grande do Sul State Law 15,223/2018), which banned all motor-powered bottom trawling up to 12 miles from the state's 570 km of marine coast. Decades of scientific evidence indicated that the ban would have sustainable ecosystem benefits and ensure continued revenues for small-scale and industrial fisheries (*6*–*8*). For the same reasons, trawling bans have been established in other countries (*9*). However, the law was questioned in Brazil's Federal Supreme Court in 2019 after the neighboring state Santa Catarina's industrial fishing sector claimed economic losses. The dean minister maintained the law (*10*), but in December 2020, his successor suspended it (*11*).

Efficient and effective fisheries management is essential to the food security of the more than one million people along the 8000-km Brazilian coastline for whom fishing is a way of life and primary source of income (*12*). The new minister's decision led to uncertainty about the state's right to legislate on this issue, which could be an enormous setback in ecological and fisheries restoration. We urge the Supreme Court to formally recognize rights of states in Brazil to legislate in their coastal waters. Only then will local and other coastal fisheries be able to choose a sustainable path forward.

Luís Gustavo Cardoso[1]*, Manuel Haimovici[1], Patrízia Raggi Abdallah[2], Eduardo Resende Secchi[1], Paul Gerhard Kinas[3]

[1]Instituto de Oceanografia, Universidade Federal do Rio Grande, Rio Grande, RS, Brazil. [2]Instituto de Economia, Universidade Federal do Rio Grande, Rio Grande, RS, Brazil. [3]Instituto de Matemática, Estatística e Física, Universidade Federal do Rio Grande, Rio Grande, RS, Brazil.
*Corresponding author.
Email: cardosolg15@gmail.com

REFERENCES AND NOTES

1. M. A. P. Roda *et al*., "A third assessment of global marine fisheries discards," Food and Agriculture Organization of the United Nations (FAO Fisheries and Aquaculture Technical Paper, 633, 2019).
2. A. Jensen, R. Reider, W. Kovalak, *N. Am. J. Fish. Manag*. **8**, 191 (1988).
3. U. R. Sumaila, *Game Theory and Fisheries* (Routledge, London, 2013).
4. J. G. Hiddink *et al*., *Proc. Natl. Acad. Sci*. **114**, 8301 (2017).
5. E. Sala *et al*., *Nature* 10.1038/s41586-021-03371-z (2021).
6. M. Haimovici, L. G. Cardoso, *Mar. Biol. Res*. **13**, 135 (2017).
7. L. G. Cardoso, M. Haimovici, P. R. Abdallah, L. F. C. Dumont, "Efeitos para o setor pesqueiro do deslocamento do arrasto de fundo para além da 12 milhas náuticas na costa do Rio Grande do Sul" (Tech. Rep. 1, BRA-0142- 2017, Universidade Federal do Rio Grande, 2018); https://demersais.furg.br/images/Cardoso_et_al_2018_Efeitos_para_o_setor_pesqueiro_do_deslocamento_do_arrasto_de_fundo_para_alm_da_12_milhas_nuticas_na_costa_do_Rio_Grande_do_Sul.pdf [in Portuguese].
8. Instituto Chico Mendes de Conservação da Biodiversidade/Ministério do Meio Ambiente, "Livro Vermelho da Fauna Brasileira Ameaçada de Extinção," VI – Peixes (ed. 1, Brasília, 2018) [in Portuguese].
9. T. L. Loh, Z. Jaafar, *Aquatic Conserv. Mar. Freshw. Ecosyst*. **25**, 581 (2015).
10. C. Mello, "Medida cautelar na ação direta de inconstitucionalidade 6.218 Rio Grande do Sul" (2019); www.stf.jus.br/arquivo/cms/noticiaNoticiaStf/anexo/ADI6218cautelar.pdf [in Portuguese].
11. N. Marques, "Ag.Reg. na medida cautelar na ação direta de inconstitucionalidade 6.218 Rio Grande do Sul" (2020); www.conjur.com.br/dl/nunes-marques-autoriza-pesca-arrasto.pdf [in Portuguese].
12. J. Dias Neto, "O uso da biodiversidade aquática no Brasil: uma avaliação com foco na pesca" (Instituto Brasileiro do Meio Ambiente, Brasília, BR, 2015) [in Portuguese].

10.1126/science.abh0279

PHOTO: OCTAVIO CAMPOS SALLES/ALAMY STOCK PHOTO

Assess before changing Brazil's shipping policy

In September 2020, the Brazilian Infrastructure Ministry announced a plan to incentivize additional ship traffic by increasing transport rights for ships, creating new routes between ports, and reducing the cost of transporting containers (*1*). Although more ships may help the local economy and streamline cargo transport, the Ministry has not evaluated the potential ecological impacts of increasing cargo ship traffic among ports by an estimated 40% by 2022 (*1*). Ship traffic is associated with greenhouse gases (*2*), oil spills (*3*), and noise pollution (*4*). Policies likely to increase ship traffic should not be implemented before an independent environmental assessment has been conducted.

The current ship traffic has already led to loss of livelihoods for Brazil's people and degradation of its ecosystems. Residents of the Brazilian coast, particularly fishers, are still recovering from the 2019 oil spill (*5*, *6*). Underwater noise pollution by cargo ship traffic disrupts the behavior and populations of marine animals (*7*, *8*), increasing the risks to endangered species (*9*, *10*). Ships are also potential vectors for invasive organisms, such as bay barnacle or zebra mussels, which are transported in hull fouling or ballast water and threaten native species (*11*, *12*). The Brazilian government has not made public any information about how it will inspect ships or protect the marine ecosystems from these perturbations as the new plan takes effect.

Considering the risks, the new initiative should be put on hold until the government can evaluate the potential for damages and propose a plan to prevent them. To move forward with the ship traffic program responsibly, the government will have to allocate more funding to research, create action plans for endangered species, expand biomonitoring programs (*13*, *14*), and encourage cargo transportation that uses cleaner energy sources. If these measures are not addressed, the Brazilian government will jeopardize ecosystems with immeasurable value.

Lucas Rodriguez Forti[1]*, Marcos R. Rossi-Santos[2,3], José Anchieta C. C. Nunes[1]
[1]Universidade Federal da Bahia, 40170-115 Salvador, Bahia, Brazil. [2]Universidade Federal do Recôncavo da Bahia, Cruz das Almas, BA 44380-000, Brazil. [3]Centre for Marine Science and Technology, Curtin University, Bentley, WA 6102, Australia.
*Corresponding author. Email: lucas.forti@ufba.br

REFERENCES AND NOTES

1. Governo Federal, Ministério da Infraestrutura, "Br do Mar" (2020); www.gov.br/infraestrutura/pt-br/brdomar [in Portuguese].
2. T. R. Walker *et al*., *World Seas* **3**, 505 (2019).
3. M. Girin, E. Mamaca, *Pollutions Chimiques Accidentelles du Transport Maritime* (Editions Quæ, Versailles, 2010).
4. B.S. Halpern *et al*., *Sci. Rep*. **9**, 11609 (2019).
5. H. Escobar *Science*, **366**, 672 (2019).
6. S.F. Câmara *et al*., *Ocean Coast. Manag*. **202**, 105506 (2021).
7. R. A. Dunlop, *Soc. Open Sci*. **6**, 6190967 (2019).
8. C. Duarte *et al*., *Science* **371**, eaba4658 (2021).
9. D. T. L. Martins *et al*., *Mar. Biol. Assoc. U.K*. **98**, 215 (2018).
10. C. Erbe *et al*., *Front. Mar. Sci*. **6**, 606 (2019).
11. E. Lakshmi *et al*., *Ocean Coast. Manag*. **199**, 105296 (2021).
12. International Maritime Organization, "Common Hull Fouling Invasive Species" (2019); www.imo.org/en/OurWork/Environment/Pages/Common-Hull-Fouling-Invasive-Species.aspx.
13. Programa Ambiental, "Paisagem Acústica" (2021); www.comunicabaciadesantos.com.br/programa-ambiental/projeto-de-monitoramento-da-paisagem-acustica-submarina-pmpas.html [in Portuguese].
14. Programa Ambiental, "Cetáceos" (2021); www.comunicabaciadesantos.com.br/programa-ambiental/projeto-de-monitoramento-de-cetaceos-pmc.html [in Portuguese].

COMPETING INTERESTS

L.R.F. received a fellowship from the Coordination for the Improvement of Higher Education Personnel (CAPES Finance Code 001).

10.1126/science.abh3608

Northeast Brazil's imperiled Cerrado

Brazil's Cerrado region, a tropical savanna ecosystem globally recognized for its rich and endemic biodiversity (*1*) and its importance in water regulation (*2*), faces escalating threats to its environmental services due to deforestation (*3*). The state of Maranhão, with an area of 33 million hectares, contains both Cerrado (65%) and Amazon (35%) biomes (*4*). In the state's Amazonian region, predatory deforestation has led to poverty and violence against traditional and Indigenous peoples (*4*). Maranhão, which is currently deliberating zoning policies, must ensure that the mistakes made in the Amazon are not repeated in the Cerrado.

Millions of hectares of native vegetation are legally available for agricultural conversion in the Cerrado region of Maranhão (*5*), including lands susceptible to desertification (*6*). The large-scale replacement of native vegetation by a single crop results in expropriation and violence against traditional communities (*7*). Large-scale agriculture also changes the water cycle (*2*), erodes (*8*) and extinguishes (*9*) biodiversity, and contaminates soil and water with agrochemicals (*10*).

The Maranhão state government is carrying out technical studies to define zones for management and territorial planning (locally known as ZEE-Cerrado). The zoning decisions will determine which lands will be designated for conservation and which will be used for agriculture expansion. The process is expected to conclude in November with the proposal of a bill (*11*). In March 2020 (*12*), the Maranhão state parliament passed a similar zoning law for its Amazon region (*4*) through a process that excluded most external discussion and therefore failed to prioritize forest protection and restoration. Maranhão should make sure that both the scientific community and civil society (i.e., nongovernmental organizations, community and social action groups, and other not-for-profit associations) are integrally involved throughout the development of the Cerrado zoning law to avoid environmental setbacks and enable sustainable development in the region.

Celso H. L. Silva Junior[1,2,3]*, Swanni T. Alvarado[3], Danielle Celentano[3,4], Guillaume X. Rousseau[3], Luis M. Hernández[3], Tiago M. Ferraz[3], Fabrício B. Silva[5], Maycon H. F. de Melo[5], Taissa C. S. Rodrigues[6], Josué C. Viegas[7,3], Ulisses D. V. Souza[8,9], Andre L. S. Santos[10], Denilson Bezerra[11]
[1]Tropical Ecosystems and Environmental Sciences Laboratory, São José dos Campos, SP, Brazil. [2]Instituto Nacional de Pesquisas Espaciais, São José dos Campos, SP, Brazil. [3]Universidade Estadual do Maranhão, São Luís, MA, Brazil. [4]Conservação Internacional, Brasília, DF, Brazil. [5]Universidade Ceuma, São Luís, MA, Brazil. [6]Universidade Estadual da Região Tocantina do Maranhão, Imperatriz, MA, Brazil. [7]Universidade de Coimbra, Coimbra, Portugal. [8]Colégio Universitário da Universidade Federal do Maranhão, São Luís, MA, Brazil. [9]Universidade de São Paulo, São Paulo, SP, Brazil. [10]Instituto Federal do Maranhão, São Luís, MA, Brazil. [11]Universidade Federal do Maranhão, São Luís, MA, Brazil.
*Corresponding author.
Email: celsohlsj@gmail.com

REFERENCES AND NOTES

1. N. Myers, R. A. Mittermeier, C. G. Mittermeier, G. A. B. da Fonseca, J. Kent, *Nature* **403**, 853 (2000).
2. S. A. Spera, G. L. Galford, M. T. Coe, M. N. Macedo, J. F. Mustard, *Glob. Chang. Biol.* **22**, 3405 (2016).
3. Instituto Nacional de Pesquisas Espaciais, Portal TerraBrasilis (2020); http://terrabrasilis.dpi.inpe.br.
4. C. H. L. Silva Junior *et al*., *Land Use Pol*. **97**, 104806 (2020).
5. Ministério do Meio Ambiente, *Plano Nacional de Recuperação da Vegetação Nativa* (2017); www.gov.br/mma/pt-br/assuntos/servico-sambientais/ecossistemas-1/conservacao-1/politica-nacional-de-recuperacao-da-vegetacao-nativa/planaveg_plano_nacional_recuperacao_vegetacao_nativa.pdf [in Portuguese].
6. R. M. S. P. Vieira *et al*., *Solid Earth* **6**, 347 (2015).
7. F. T. Pitta, G. C. Vega, *Impacts of Agribusiness Expansion in the Matopiba Region: Communities and the Environment* (ActionAid, Rio de Janeiro, 2017); https://actionaid.org.br/wp-content/

files_mf/1520602943ACTIONAID_MATOPIBA_ENG_WEB.pdf.
8. C. A. Klink, R. B. Machado, *Conserv. Biol.* **19**, 707 (2005).
9. T. Newbold *et al.*, *Science* **353**, 288 (2016).
10. L. M. Bombardi, *Geografia do Uso de Agrotóxicos no Brasil e Conexões com a União Europeia* (FFLCH-USP, São Paulo, 2017); http://conexaoagua.mpf.mp.br/arquivos/agrotoxicos/05-larissa-bombardi-atlas-agrotoxico-2017.pdf [in Portuguese].
11. Governo do Maranhão, "ZEE dos Biomas Cerrado e Costeiro maranhense será finalizado em novembro de 2021" (2020); www.ma.gov.br/agenciadenoticias/?p=291618 [in Portuguese].
12. J. Barros, "Aprovado projeto que institui o Zoneamento Ecológico-Econômico do Maranhão" (2020); www.al.ma.leg.br/noticias/39800 [in Portuguese].

10.1126/science.abg0556

TECHNICAL COMMENT ABSTRACTS

Comment on "Tumor-initiating cells establish an IL-33–TGF-β niche signaling loop to promote cancer progression"

Jasper B. J. Kamphuis, William P. M. Worrall, Julien Stackowicz, Aurélie Mougel, Emilie Mauré, Eva Conde, Pierre Bruhns, Laurent Guilleminault, Nicolas Gaudenzio, Jinmiao Chen, Rebecca Gentek, Laurent L. Reber

Taniguchi *et al*. (Research Articles, 17 July 2020, p. 269) claim that the cytokine interleukin-33 induces accumulation of tumor-associated macrophages expressing the immunoglobulin E receptor FcεRI. Although these findings hold great therapeutic promise, we provide evidence that the anti-FcεRI antibody used in this study is not specific for FcεRI on macrophages, which raises concerns about the validity of some of the conclusions.

Full text: dx.doi.org/10.1126/science.abf2022

Response to Comment on "Tumor-initiating cells establish an IL-33–TGF-β niche signaling loop to promote cancer progression"

Sachiko Taniguchi, Ajit Elhance, Avery Van Duzer, Sushil Kumar, Justin Leitenberger, Naoki Oshimori

Kamphuis *et al*. argue that macrophages accumulated in the proximity of tumor-initiating cells do not express the high-affinity immunoglobulin E receptor FcεRIα. Although we cannot exclude the possibility of nonspecific binding of anti-FcεRIα antibody (clone MAR-1), we provide evidence that macrophages in squamous cell carcinomas express FcεRIα and that IL-33 induces FcεRIα expression in bone marrow cell–derived macrophages.

Full text: dx.doi.org/10.1126/science.abf3316

ERRATA

Erratum for the Report "PML Regulates Apoptosis at Endoplasmic Reticulum by Modulating Calcium Release" by C. Giorgi *et al*., *Science* **371**, eabi4740 (2021). Published online 26 March 2021; 10.1126/science.abi4740

Where Science Gets Social.

AAAS.ORG/COMMUNITY

AAAS' Member Community is a one-stop destination for scientists and STEM enthusiasts alike. It's "Where Science Gets Social": a community where facts matter, ideas are big and there's always a reason to come hang out, share, discuss and explore.

Member COMMUNITY AAAS

AMERICAN ASSOCIATION FOR THE ADVANCEMENT OF SCIENCE

RESEARCH

IN *SCIENCE* JOURNALS

Edited by **Michael Funk**

PLANT SCIENCE

Competing signal peptides hold the key

When a pollen grain lands on a receptive flower's pistil, a complex dance leading to sexual reproduction begins. Liu *et al.* show some of the early steps that help to distinguish a compatible pollen grain from a random piece of dust. Normally, a stigmatic gatekeeper, the ANJEA–FERONIA receptor kinase complex, perceives signaling peptides produced by the stigma that drive the production of reactive oxygen species at the stigma papillae. Upon pollination, POLLEN COAT PROTEIN B-class peptides compete with those stigmatic peptides for binding to the stigmatic receptor kinase complex. The subsequent decline of stigmatic reactive oxygen species production allows hydration and opens the gates to pollen germination. —PJH

Science, this issue p. 171

Germination of pollen grains, such as these from a lily, depends on a complex exchange of signals between the pollen and receiving stigma.

PHOTO: SUSUMU NISHINAGA/SCIENCE SOURCE

REGENERATION

Repairing the fish heart

Although humans show minimal regenerative capability, zebrafish can regenerate their hearts through a mechanism whereby heart muscle cells (cardiomyocytes) revert to a less mature state and then proliferate to replace the damaged tissue. Ogawa *et al*. show that Krüppel-like factor 1 (Klf1/Eklf), a transcription factor well known for its role in red blood cell development, is an essential factor for heart regeneration in zebrafish. Klf1 is specifically expressed in cardiomyocytes after injury, and its activation is sufficient to stimulate new cardiomyocyte production without injury. This potent effect is achieved through reprogramming of gene networks regulating cardiomyocyte differentiation and mitochondrial metabolism. —BAP

Science, this issue p. 201

ORGANIC CHEMISTRY

Slipping boron into alkyl ethers

The carbon–oxygen bonds that hold alkyl ethers together are relatively inert. Lyu *et al*. report that zinc and nickel can team up to insert boron between the carbon and oxygen using an unusual mechanism. First, a dibromoborane pries open the bond with help from a zinc ion. Next, the nickel stitches together the carbon and boron, and the oxidation of metallic zinc starts the cycle over again. Versatile reactivity at the inserted boron center can then add carbons to the original ether or swap out oxygen for nitrogen. —JSY

Science, this issue p. 175

NEUROEVOLUTION

Dating the ipsilateral visual pathway

In primates, visual connections are bilateral: Each eye sends neural connections to both sides of the brain. Vigouroux *et al*. looked at the evolutionary underpinnings of the bilateral visual system. A close look at the connections between the retina and the brain in a variety of fish species representing a span of evolutionary divergence revealed that contralateral connections seem to be universal. The ipsilateral connections, which add to the contralateral connections to form a bilateral visual system, arrived later in evolution but before the transition to land-dwelling animals. —PJH

Science, this issue p. 150

TIME-DOMAIN ASTRONOMY

X-rays from giant radio pulses

Pulsars are spinning, magnetized neutron stars that are observed as a regular sequence of radio pulses. Most pulses are

of consistent intensity, but occasionally one is brighter by orders of magnitude. The cause of these unpredictable giant radio pulses (GRPs) is unknown. Enoto *et al*. observed the Crab Pulsar simultaneously with x-ray and radio telescopes. They found that x-ray emission during GRPs was slightly brighter than that during normal pulses. Comparing the radio and x-ray enhancements provides constraints on the GRP emission mechanism and the possible connections with other transient radio phenomena. —KTS

Science, this issue p. 187

NANOMATERIALS

Seeding 2D crystals

Small, single crystals are often used to direct the growth of larger, bulk single crystals. Xu *et al*. modified these methods to grow single-crystal films of a two-dimensional (2D) semiconductor, 2H molybdenum ditelluride (2H $MoTe_2$), on an amorphous glass surface. After coating the wafer with a 1T′ $MoTe_2$ film, a small 2H $MoTe_2$ crystallite was placed on the wafer. The wafer was capped with an alumina film, except for a small hole above the seed region that allowed entry of additional tellurium during the heating process that drove the phase transition and epitaxial growth of 2H $MoTe_2$. —PDS

Science, this issue p. 195

BIOSYNTHESIS

Cabbage blue boosted

Naturally occurring, edible blue food colorants are limited and rarely absorb light greater than 630 nanometers. Denish *et al*. amplified to gram scale the biosynthetic production of a naturally occurring, minor red cabbage anthocyanin. A trimeric complex with an aluminum ion produced the desired cyan blue colorant, which can be further developed for use in food chemistry in place of the synthetic FD&C Blue No. 1 (Brilliant Blue). —SRC

Sci. Adv. 10.1126/sciadv.abe7871 (2021).

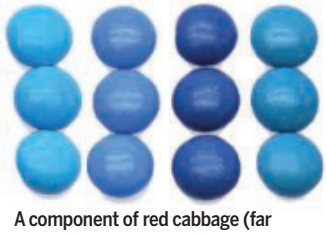

A component of red cabbage (far right column) is a better substitute for synthetic blue (far left column) than other natural dyes (middle two columns).

CANCER

MPO in myeloid cells mitigates melanoma

Myeloid cells such as neutrophils and macrophages generate hypochlorous acid (HOCl) through the enzymatic activity of myeloperoxidase (MPO) to kill microbes. Using cocultured cells and real-time intravital tumor imaging in mice, Liu *et al*. found that HOCl generated by MPO in myeloid cells inhibited the early development of subcutaneous melanoma tumors by suppressing nuclear factor-κB activity in nearby tumor cells. HOCl promoted a transcriptional profile in T cells associated with T cell activation and in B16F10 cells, which is suggestive of an antioxidant response. —WW

Sci. Signal. **14**, eaax5971 (2021).

GLASS

Shaping silica like a polymer

Glass is tremendously useful, but it is energy intensive to make because of the high melting temperature and processing methods that require melts. Mader *et al*. circumvented the need for melting glass using a plastic silica nanocomposite for injection molding (see the Perspective by Dylla-Spears). The low-temperature injection molding can produce parts in as little as 5 seconds with high spatial resolution. The strategy provides a different and potentially less energy-intensive method for mass producing parts made of glass. —BG

Science, this issue p. 182; see also p. 126

STRUCTURAL BIOLOGY

Conformational ensembles

G–protein coupled receptors (GPCRs) mediate signals across the cell membrane that regulate diverse biological processes and thus are important drug targets. Signaling involves ligand binding, GPCR binding to heterotrimeric G protein, nucleotide exchange, and dissociation of the G protein. High-resolution snapshots of GPCRs, alone and in complexes, provide insight into the activation mechanism but do not reveal the full landscape of conformations. Huang *et al*. used fluorine nuclear magnetic resonance spectroscopy to monitor the key states of a prototypical GPCR, the adenosine A_{2A} receptor, in a lipid bilayer as a function of ligand, G protein, and nucleotide. The authors identified a conformational ensemble composed of at least five key functional states involving two inactive states and three active states. Ligands and nucleotide shift the distribution of conformations. Understanding the conformational ensemble may inform drug design. —VV

Cell 10.1016/j.cell.2021.02.041 (2021).

STEM CELLS

Chromatin coordinates stemness

Blood cells are produced from stem cells in the bone marrow and thymus and transition between quiescence and activation depending on the body's needs. Although generally quiescent, long-term hematopoietic stem cells (LT-HSCs) self-renew and can transform into short-term HSCs (ST-HSCs) to produce multilineage blood cells. Takayama *et al*. used single-cell analysis and a sequencing approach called ATAC-seq on various human hematopoietic cell populations. The method identified chromatin accessibility signatures that distinguish LT-HSCs and activated hematopoietic stem and progenitor cells (HSPCs). The activated HSPC signature displays binding

PHOTOS: (LEFT TO RIGHT) DENISH ET AL., *SCI. ADV.* 10.1126/SCIADV.ABE7871 (2021); BERNARDO M. FLORES

TROPICAL ECOLOGY

Fire in the flooded forest

Seasonal flooding affects large tracts of the forests of the Amazon Basin as the rivers are swelled by the seasonal rains. However, like forest elsewhere in the Basin, these forests are prone to dry-season fire. Using 40 years of satellite imagery coupled with fieldwork on vegetation and soils in burned areas, Flores and Holmgren show how increased and repeated fire is converting some areas of seasonally flooded forest to white-sand savannas. The authors show that this process is driven by topsoil erosion where the tree canopy has been repeatedly opened by fire. As erosion proceeds, the clay-rich soils convert to white-sand soils that favor the growth of native savanna species. —AMS

Ecosystems 10.1007/s10021-021-00607-x (2021).

White-sand savanna (campina) in the Rio Negro basin may form because of leaching, river deposition, or forest fire.

to sites on the transcription factor CTCF, which is a mediator of three-dimensional (3D) genome organization. As HSCs differentiate, CTCF interacts with chromatin to silence loops that enclose genes. Thus, CTCF acts as a gatekeeper for coordinating the 3D chromatin interactions that regulate hematopoietic cell dynamics. —BAP

Cell Stem Cell **28**, P488 (2021).

METASURFACES

A metasurface performance enhancer

The detection and emission of light plays a key role in applications such as free-space communications, biosensing, and optical imaging. Fluorescent dye molecules or nanoparticles in a cavity are typically used for photodetection but can be limited in sensitivity and efficiency. Traverso *et al.* fabricated a low-loss plasmonic metasurface made from silver nanocubes scattered across the surface of the cavity. Modification of the local optical density of states results in a device that can collect fast-modulated light (>14 gigahertz) with a high acceptance angle (120°) and convert it to a directional source with enhanced overall efficiency (>30%). The approach could be incorporated into the design of other ultrafast optoelectronic components to enhance performance. —ISO

Optica **8**, 202 (2021).

CELL BIOLOGY

It's a wrap(pER)

Organelles such as the endoplasmic reticulum (ER) and mitochondria regulate intracellular functions. However, a role for such interactions at a systemic level is less clear. Anastasia *et al.* report the morphological, functional, and biochemical characterization of a species of interorganelle contact that regulates systemic lipid homeostasis. In mouse liver, the authors observed contacts occurring between mitochondria and a type of rough ER, dubbed wrappER because of the way in which it envelopes the mitochondria. Mitochondria-wrappER contacts regulated the rate of secretion of hepatic very-low density lipoprotein (VLDL; also known as "bad cholesterol"). As mice went from a fasting to a fed state, the organelle contacts changed in response to loss of VLDL synthesis. It appears that liver-wrappER mitochondrial contacts do indeed function in the direct control of tissue and systemic homeostasis. —SMH

Cell Rep. **34**, 108873 (2021).

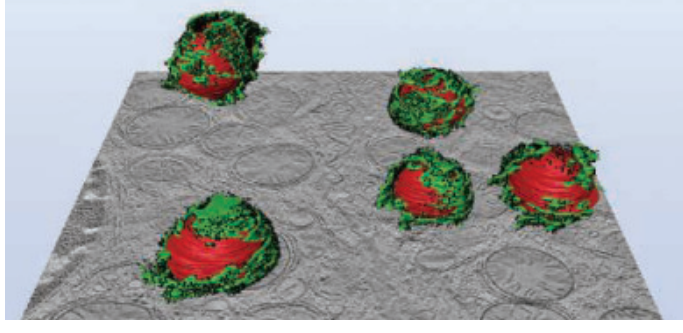

WrappER-associated mitochondria in mouse liver hepatocytes

IMAGE: ANASTASIA *ET AL.*, *CELL REP.* **34**, 108873 (2021)

CLIMATE CHANGE

Wet winters awaiting

Wet weather occurring simultaneously in many places within a given region can cause widespread flooding. To assess whether climate change will affect the incidence of that type of flooding, Bevacqua *et al.* performed climate model simulations of wintertime precipitation. These simulations showed that the areal extent of extratropical extreme wintertime precipitation in the Northern Hemisphere would nearly double if global warming were to increase the mean surface air temperature by 2.0°C above the preindustrial average. Only small increases of precipitation intensity are needed to cause relative growth of the spatial coverage of extreme precipitation events of an order of magnitude or more. —HJS

Geophys. Res. Lett. 10.1029/2020GL091990 (2021).

F-BLOCK CHEMISTRY

Hard, soft, hot, cold

Efficient sequestration of radioactive americium (Am) ions remains a challenge in nuclear waste remediation. Part of the difficulty is that the ions have a similar size and charge to stable lanthanide ions. Goodwin *et al.* systematically explored whether differences in covalency might manifest when Am and neodymium (Nd) are coordinated by more or less polarizable ligands (often termed soft or hard). They compared the crystal structures and spectral and computational electronic properties of Am(III) and Nd(III) with soft selenium (Se) or hard oxygen ligands. The upshot was that Am showed signs of covalency with Se, whereas Nd did not. —JSY

Angew. Chem. Int. Ed. 10.1002/anie.202017186 (2021).

REVIEW SUMMARY

MEDICINE

Epigenetics, fragmentomics, and topology of cell-free DNA in liquid biopsies

Y. M. Dennis Lo*, Diana S. C. Han, Peiyong Jiang, Rossa W. K. Chiu

BACKGROUND: Liquid biopsies that are based on analysis of cell-free DNA from plasma offer diagnostic information that is otherwise accessible conventionally through invasive biopsies. Noninvasive prenatal testing has been used globally for the screening of fetal chromosomal aneuploidies and has led to a considerable reduction in invasive prenatal testing, such as use of amniocentesis. Cancer liquid biopsies have been used for the selection of targeted therapies and monitoring of disease progression. Liquid biopsies for organ transplant patients have been used to monitor graft dysfunction. The first applications of liquid biopsies are based on the detection of genetic markers in cell-free DNA, such as sex differences, genetic polymorphisms, or mutations. By studying nongenetic features of cell-free DNA molecules—including DNA methylation, fragmentation, and topology—understanding of cell-free DNA biology has expanded the spectrum and utilities of liquid biopsies.

ADVANCES: Cell-free DNA in plasma consists of a mixture of fragmented DNA molecules released from various tissues within the body. Each cell-free DNA fragment bears molecular signatures of its cell of origin, such as DNA methylation status. The methylation profile of circulating fetal DNA in the mother's plasma correlates with that of the placenta and has been exploited as a means to develop noninvasive fetus-specific biomarkers that are not dependent on fetal sex or genotype. Circulating tumor-derived DNA bear methylation states that resemble the tumor tissue and have enabled the development of tests for the screening and localization of cancer. The fragmentation of plasma DNA is related to the nucleosomal organization, chromatin structure, gene expression, and nuclease content of the tissue of origin, resulting in characteristic signatures in the form of fragment size, nucleotide motifs at the fragment ends, single-stranded jagged ends, and the genomic locations of the fragmentation endpoints. For mitochondrial DNA that is originally in a circular form, fragmentation will also change its topology into a linear form. By noting these features of cell-free DNA fragments, the anatomical site of pathology could potentially be deduced, providing additional information than just quantifying mitochondrial DNA without regard to its form. The study of such characteristics has also enhanced our understanding of the biology and generation of cell-free DNA. The roles of nucleases in plasma DNA biology, such as deoxyribonuclease 1–like-3, have been explored by using gene-deletion mouse models and confirmed in humans bearing nuclease gene mutations, with potential implications for the pathogenesis of autoimmune diseases.

OUTLOOK: The use of DNA methylation, fragmentomic, and topologic analyses of circulating DNA, either in a targeted fashion or in a genomewide manner, will be expected to impact clinical practice. Clinical specimens covering more disease entities will need to be investigated to identify tissue-specific and disease-relevant signatures. During the discovery phase, to better delineate these signatures, mining is performed on high volumes of DNA data pooled within and across samples by using customized bioinformatics algorithms. Once these putative sets of signatures have been identified, signature- and target-specific assays could be developed, and large-scale clinical trials will be needed to validate these approaches. One application is in the development of plasma DNA–based cancer screening. One advantage of these approaches is the potentially large number of markers that can be developed to differentiate cancer and noncancer cells and in the ability to locate the tissue of origin of the detected cancer, possibly including cancers of unknown primary. In the area of noninvasive prenatal testing, the correlation of DNA methylation, fragmentomic, and topologic aberrations in circulating DNA to clinical outcomes would expand the spectrum of diagnostic applications beyond current ones. Fragmentomic approaches have the potential for enriching the cell-free DNA species of interest, such as through the use of automated platforms that allow the size separation of circulating DNA. In the area of organ transplant monitoring, the development of DNA methylation, fragmentomic, and topologic markers would provide an alternative to genetic markers for detecting rejection. These nongenetic markers may enable further differentiation of the donor's contribution to the circulating DNA pool into its constituent tissue components. The understanding between circulating DNA and nucleases is in its infancy. Circulating DNA signatures attributable to changes in nuclease expression in health and disease need to be elucidated and may have emerging diagnostic applications. ■

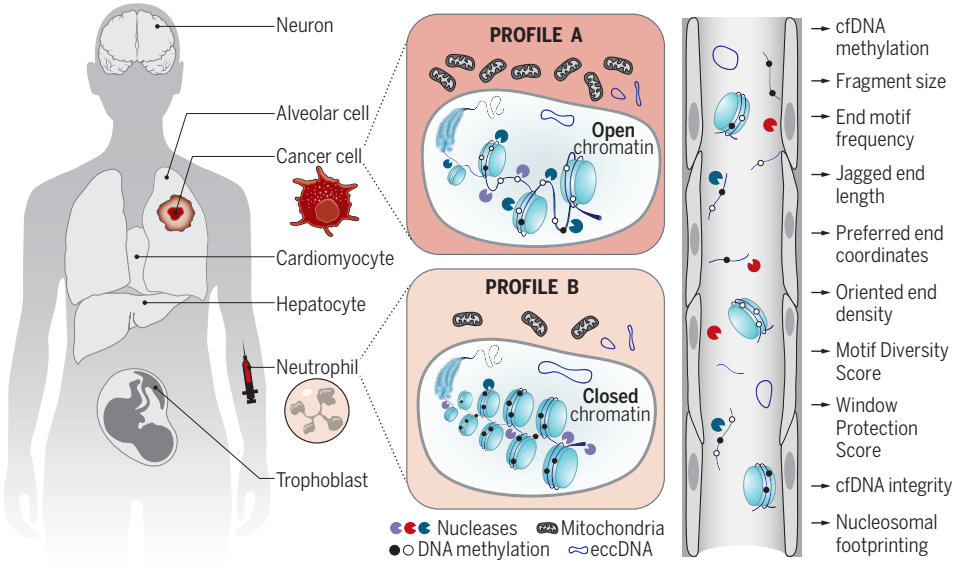

Cell-free DNA contains molecular features characteristic of their tissues of origin. Different tissues, including cancer cells and trophoblasts in pregnancy, contribute cell-free DNA to the circulation. The cell-free DNA molecules may bear methylation states reflective of the cell of origin. The DNA molecule size, fragment end locations, and end motifs are influenced by the nucleosome organization, chromatin structure, nuclease content, and gene expression of the tissue of origin. Parameters that can be measured to quantify these characteristics are shown on the right.

The list of author affiliations is available in the full article online.
*Corresponding author. Email: loym@cuhk.edu.hk
Cite this article as Y. M. D. Lo *et al.*, *Science* 372, eaaw3616 (2021). DOI: 10.1126/science.aaw3616

READ THE FULL ARTICLE AT
https://doi.org/10.1126/science.aaw3616

RESEARCH ARTICLE SUMMARY

IMAGING DEVELOPMENT

Imaging cell lineage with a synthetic digital recording system

Ke-Huan K. Chow†, Mark W. Budde†, Alejandro A. Granados, Maria Cabrera, Shinae Yoon, Soomin Cho, Ting-hao Huang, Noushin Koulena, Kirsten L. Frieda, Long Cai, Carlos Lois*, Michael B. Elowitz*

INTRODUCTION: Cell lineage plays pivotal roles in cell fate determination in development, homeostasis, and disease. The ability to visualize cell lineage relationships directly within their native tissue context could provide insight into the roles of intrinsic and extrinsic factors in cell fate specification. Inspired by the recovery of lineage information from naturally occurring somatic mutations, engineered lineage recording systems actively generate stochastic, heritable mutations at defined genomic target sites, identify those edits in individual cells, and use them to reconstruct cell lineages. However, most existing recording systems have relied on sequencing to read out edits, necessarily disrupting tissue organization. Therefore, a recording system that permits accurate imaging-based in situ readout of both single-cell edit history and transcriptional state is needed.

RATIONALE: To address this challenge, we developed a digital, image-readable lineage recording system based on site-specific serine integrases, such as Bxb1. This system, called integrase-editable memory by engineered mutagenesis with optical in situ readout (intMEMOIR), introduces a design based on an array of 10 three-state memory elements. Each memory element can be digitally and irreversibly edited to generate a theoretical maximum of 3^{10}, or 59,049, distinct edit outcomes. These digital states can be read out alongside endogenous transcripts using fluorescence in situ hybridization (FISH) methods. Further, the arrays can be integrated at defined genomic sites for germline heritability. Editing can operate in different organisms and contexts, including mouse embryonic stem (mES) cells and *Drosophila melanogaster* embryos.

RESULTS: To assess the accuracy of lineage reconstruction using intMEMOIR, we first engineered a mES cell line containing the intMEMOIR system and then acquired time-lapse movies of these cells undergoing editing and growing into colonies. We then compared ground truth lineage relationships from the movies with reconstructions based on endpoint analysis of intMEMOIR edits. intMEMOIR allowed accurate assignment of cells to clones on the basis of shared edit patterns (clonal classification). Further, stochastic and progressive editing throughout the experiment allowed reconstruction of more detailed trees (lineage tree reconstruction), with accuracy approaching the expected theoretical limit.

We then engineered an intMEMOIR recording fly termed *Drosophila memoiphila*. We induced editing in neuroblasts during early embryonic development and then analyzed their descendants in four adult fly brains, reading out both the intMEMOIR array and eight endogenous genes that mark diverse neuronal cell types. Within a clone, but not between different clones, spatially proximal cell pairs were more similar in cell state than more distant pairs, highlighting the importance of neuroblast ancestry in cell fate determination during fly brain development.

CONCLUSION: intMEMOIR enables simultaneous analysis of single-cell lineage, gene expression, and spatial organization in the same tissue. This ability allows it to directly capture otherwise hidden relationships, as demonstrated here in the case of fly brain development. intMEMOIR should be readily adaptable to other model organisms and developmental contexts. Further, by adding more memory arrays and orthogonal integrases, the system can be extended to enable deeper lineage tree reconstruction and multiple recording "channels." intMEMOIR should thus facilitate the creation of cell atlases that integrate lineage and spatial information alongside molecular profiles. ■

The list of author affiliations is available in the full article online.
†These authors contributed equally to this work.
*Corresponding author. Email: melowitz@caltech.edu (M.B.E.); clois@caltech.edu (C.L.)
Cite this article as K.-H. K. Chow *et al.*, *Science* **372**, eabb3099 (2021). DOI: 10.1126/science.abb3099

READ THE FULL ARTICLE AT
https://doi.org/10.1126/science.abb3099

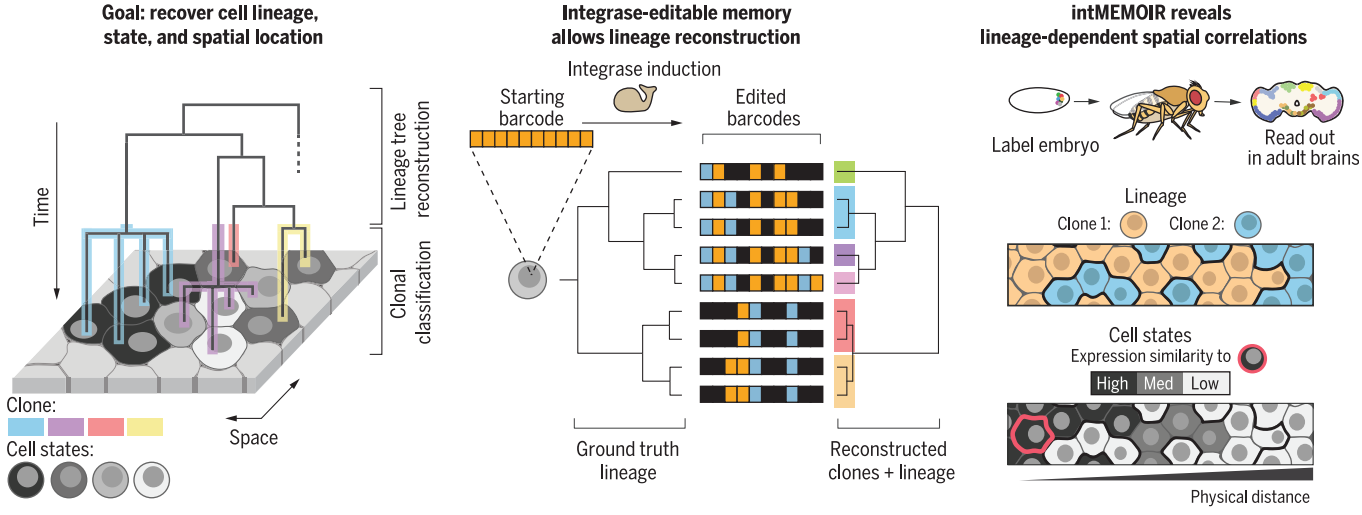

intMEMOIR enables simultaneous analysis of cell lineage, state, and spatial organization. By stochastically generating image-readable edits on an array of memory elements, intMEMOIR allows clonal labeling and lineage reconstruction, together with measurement of cell state, in situ (left). This ability enabled accurate lineage reconstruction in mouse embryonic stem cells (middle) and revealed a spatially graded, lineage-dependent correlation in cell state within *Drosophila* brains (right).

RESEARCH ARTICLE SUMMARY

EPIGENETICS

QSER1 protects DNA methylation valleys from de novo methylation

Gary Dixon†, Heng Pan†, Dapeng Yang, Bess P. Rosen, Therande Jashari, Nipun Verma, Julian Pulecio, Inbal Caspi, Kihyun Lee, Stephanie Stransky, Abigail Glezer, Chang Liu, Marco Rivas, Ritu Kumar, Yahui Lan, Ingrid Torregroza, Chuan He, Simone Sidoli, Todd Evans, Olivier Elemento*, Danwei Huangfu*

INTRODUCTION: DNA methylation is essential to mammalian development, and dysregulation can cause serious pathological conditions, including immunodeficiency-centromeric instability-facial anomalies syndrome (ICF) and microcephalic dwarfism. The DNMT and TET enzymes are responsible for the addition and removal of DNA methylation, but how they coordinate to regulate the methylation landscape remains a central question. Using a knockin DNA methylation reporter, we performed a genome-wide CRISPR-Cas9 screen in human embryonic stem cells (hESCs) to discover DNA methylation regulators.

RATIONALE: We focused on bivalent promoters, defined by the presence of both active (H3K4me3) and repressive (H3K27me3) histone marks and typically occupied by Polycomb-repressive complexes 1 and 2 (PRC1 and PRC2). In stem or progenitor cells, bivalent promoters are believed to maintain developmental regulators in a "poised state" ready for activation upon differentiation, and they are sensitive to DNA hypermethylation in dysfunctional cellular contexts such as cancer or aging. Creation of a knockin DNA methylation reporter line provided a singular opportunity to visualize epigenetic alterations otherwise "invisible" in terms of gene expression changes in the stem cell state. Using the bivalent *PAX6* P0 promoter as a representative locus, we aimed to discover mechanisms that regulate DNA methylation at regions with similar chromatin features, which would inform not only gene regulation during development but also epigenetic dysregulation in disease.

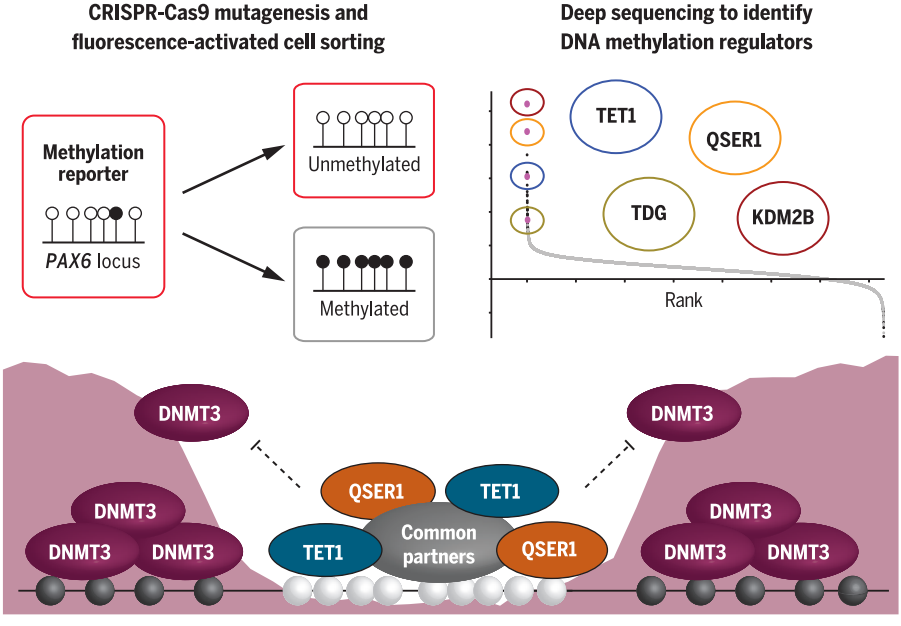

QSER1 safeguards DNA methylation valleys from de novo methylation. A fluorescence reporter hESC line (indicated by the red outline for fluorescence) was generated to track DNA methylation levels of the *PAX6* promoter region in a genome-scale CRISPR-Cas9 screen for regulators of DNA methylation. A top screen hit, QSER1, cooperates with TET1 to antagonize DNMT3-mediated de novo methylation (depicted by the purple shading) at DMVs.

RESULTS: Our screen successfully identified not only known methylation regulators such as *TET1*, *TDG*, and *KDM2B* but also functionally uncharacterized genes, including *QSER1*. Like the TET proteins, QSER1 safeguards bivalent promoters and poised enhancers (marked by H3K4me1 but not H3K27ac) against hypermethylation. However, distinct from the more general protective effect of the TET proteins on regulatory regions, QSER1 preferentially protects broad PRC2-bound and H3K27me3-marked regions and DNA methylation valleys (DMVs). Also known as DNA methylation canyons, DMVs identify large (≥5 kb) hypomethylated regions present in cells of many lineages and conserved across vertebrates. They are enriched with bivalent promoters, developmental genes, and transcription factors, including *PAX6* and the *HOX* genes. QSER1 and TET1 showed high correlation in genomic occupancy measured by chromatin immunoprecipitation sequencing (ChIP-seq) and both were high at DMVs, whereas the binding of de novo methyltransferases DNMT3A and DNMT3B was excluded in DMVs and relatively enriched in the flanking regions. Further proteomic and genomic analyses revealed that QSER1 and TET1 share many common interacting proteins, depend on each other for efficient recruitment to DNA, and cooperate to limit the encroachment of DNMT3A and DNMT3B in DMVs. In addition, deleting *DNMT3B* reversed the hypermethylation in *QSER1* knockout (KO) hESCs. Furthermore, combined KO of *QSER1* and *TET1* had a stronger impact on DNA methylation and gene expression than either single KO and resulted in a failure of hESC differentiation to $PDX1^{+}NKX6.1^{+}$ pancreatic progenitors.

CONCLUSION: We show that QSER1 cooperates with TET1 to safeguard transcriptional and developmental programs from DNMT3-mediated de novo methylation at important genomic loci, especially in DMVs and bivalent promoters where hypermethylation has been linked to developmental disorders and cancers. Our work provides mechanistic insight into the region-specific regulation of the TET pathway and highlights the utility of unbiased genome-wide screens and locus-specific epigenetic measurements, including, but not limited to, DNA methylation for probing the epigenetic regulatory mechanisms relevant to human health. ■

The list of author affiliations is available in the full article online.
†These authors contributed equally to this work.
*Corresponding author. Email: huangfud@mskcc.org (D.H.); ole2001@med.cornell.edu (O.E.)
Cite this article as G. Dixon *et al.*, *Science* **372**, eabd0875 (2021). DOI: 10.1126/science.abd0875

READ THE FULL ARTICLE AT
https://doi.org/10.1126/science.abd0875

RESEARCH ARTICLE SUMMARY

STRUCTURAL BIOLOGY

Structure and dynamics of the CGRP receptor in apo and peptide-bound forms

Tracy M. Josephs†, Matthew J. Belousoff†, Yi-Lynn Liang†, Sarah J. Piper, Jianjun Cao, Daniel J. Garama, Katie Leach, Karen J. Gregory, Arthur Christopoulos, Debbie L. Hay, Radostin Danev*, Denise Wootten*, Patrick M. Sexton*

INTRODUCTION: G protein–coupled receptors (GPCRs) are key regulators of information transmission between cells and organs. Among these, class B1 GPCRs are activated by major peptide hormones and neuropeptides that play important roles in the physiological regulation of metabolic, cardiovascular, and immunological responses. Understanding both how natural and synthetic ligands bind to GPCRs and how agonists activate receptors to recruit transducer proteins is critical to understanding how the body regulates the flow of complex information that is presented to different cells and tissues to enable coordinated biological responses.

RATIONALE: Despite advances in structural biology, our understanding of the dynamic molecular processes that enable ligand binding and subsequent receptor activation and G protein recruitment is incomplete because of the difficulty in elucidating structural information for unmodified receptors in key intermediate states (e.g., apo and agonist-bound). To address the gap, we have applied single-particle cryo–electron microscopy (cryo-EM) to determine structures of these intermediate states for the calcitonin gene–related peptide (CGRP) receptor, a class B1 GPCR. The CGRP receptor, a key mediator in the pathology of migraines, is the primary target for the actions of the neuropeptide CGRP that has diverse physiological functions including the regulation of vascular tone and the modulation of inflammatory and metabolic responses.

RESULTS: After expression and purification of unmodified apo and peptide-bound CGRP receptors, we determined structures of these complexes using cryo-EM at global resolutions [Fourier shell correlation (FSC) = 0.143] of 3.2 and 3.5 Å, respectively. In the consensus structures, the intracellular face of both the apo and peptide-bound receptors are very similar, and both structures lacked the key hallmark features of activated class B1 GPCRs, including the large outward movement of the base of transmembrane helix 5 (TM5), TM6, and the interconnecting intracellular loop 3 (ICL3) that is required to accommodate G protein binding. Instead, the apo and CGRP-bound receptors exhibited a relatively straight TM6, and the base of TM5 and TM6 was packed closely with TMs 2, 4, and 7 and ICL2. Moreover, the CGRP N terminus that is required for receptor activation was not resolved, and only small differences in the static structures were observed between the apo and peptide-bound CGRP receptors. Consequently, we interrogated the conformational dynamics of both states of the receptor. Three-dimensional (3D) variance analysis of the cryo-EM data revealed that the CGRP N terminus formed only transient interactions with the receptor core that was more dynamic when the peptide was bound, and CGRP N-terminal engagement was correlated with the destabilization of ground-state interactions at the intracellular face of the receptor. Hydrogen-deuterium exchange mass spectrometry (HDX-MS) provided complementary data that supported the observations from the cryo-EM variance analysis. In combination with our previously published structure of the fully active CGRP-bound receptor in complex with the Gs protein, these results support a model of receptor activation whereby the apo receptor is in an inactive state that is stabilized by ground-state interactions at the base of the receptor. CGRP binds initially to the extracellular domain of the receptor, thereby increasing the dynamics of the extracellular face of the receptor that enables transient interaction of the CGRP N-terminal activation domain with the receptor core. Interactions of the peptide N terminus with the receptor core allosterically destabilize ground-state networks at the intracellular face of the receptor, which facilitates G protein binding with subsequent cooperative interactions between both the G protein and CGRP that drive the larger conformational changes required for full engagement of the G protein and stabilization of the binding of the peptide N terminus observed in the fully active structure.

CONCLUSION: Collectively, our work provides understanding of the structure and dynamics of the apo state of class B1 GPCRs and the mechanisms of receptor activation. The use of essentially unmodified receptor allowed us to interrogate the changes to conformational dynamics that occur upon agonist binding by complementary implementation of cryo-EM and HDX-MS, which provided insight into peptide agonist binding and the activation of the CGRP receptor. ■

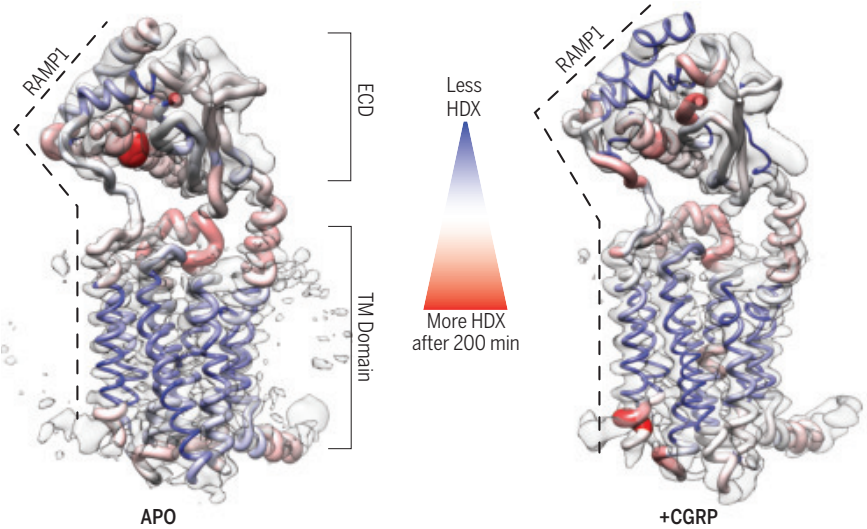

CGRP binding alters the dynamics of the CGRP receptor. HDX-MS and 3D variance analysis of the cryo-EM data provide strongly correlated data on the conformational dynamics of apo and CGRP-bound CGRPRs. The cryo-EM density map (starting frame) is shown in transparent gray surface representation. HDX-MS data are illustrated in licorice ribbon format, where the thickness and color correspond to the extent of deuterium uptake. RAMP1, receptor activity–modifying protein 1; ECD, extracellular domain; TM, transmembrane.

The list of author affiliations is available in the full article online.
†These authors contributed equally to this work.
*Corresponding author. Email: rado@m.u-tokyo.ac.jp (R.D.); denise.wootten@monash.edu (D.W.); patrick.sexton@monash.edu (P.M.S.)
Cite this article as T. M. Josephs *et al.*, *Science* **372**, eabf7258 (2021). DOI: 10.1126/science.abf7258

READ THE FULL ARTICLE AT
https://doi.org/10.1126/science.abf7258

RESEARCH ARTICLE SUMMARY

PHOTOENZYMES

Mechanism and dynamics of fatty acid photodecarboxylase

D. Sorigué, K. Hadjidemetriou, S. Blangy, G. Gotthard, A. Bonvalet, N. Coquelle, P. Samire, A. Aleksandrov, L. Antonucci, A. Benachir, S. Boutet, M. Byrdin, M. Cammarata, S. Carbajo, S. Cuiné, R. B. Doak, L. Foucar, A. Gorel, M. Grünbein, E. Hartmann, R. Hienerwadel, M. Hilpert, M. Kloos, T. J. Lane, B. Légeret, P. Legrand, Y. Li-Beisson, S. L. Y. Moulin, D. Nurizzo, G. Peltier, G. Schirò, R. L. Shoeman, M. Sliwa, X. Solinas, B. Zhuang, T. R. M. Barends, J.-P. Colletier, M. Joffre, A. Royant, C. Berthomieu*, M. Weik*, T. Domratcheva*, K. Brettel, M. H. Vos*, I. Schlichting*, P. Arnoux*, P. Müller*, F. Beisson*

INTRODUCTION: Photoenzymes are rare biocatalysts driven by absorption of a photon at each catalytic cycle; they inspire development of artificial photoenzymes with valuable activities. Fatty acid photodecarboxylase (FAP) is a natural photoenzyme that has potential applications in the bio-based production of hydrocarbons, yet its mechanism is far from fully understood.

RATIONALE: To elucidate the mechanism of FAP, we studied the wild-type (WT) enzyme from *Chlorella variabilis* (*Cv*FAP) and variants with altered active-site residues using a wealth of techniques, including static and time-resolved crystallography and spectroscopy, as well as biochemical and computational approaches.

RESULTS: A 1.8-Å-resolution *Cv*FAP x-ray crystal structure revealed a dense hydrogen-bonding network positioning the fatty acid carboxyl group in the vicinity of the flavin adenine dinucleotide (FAD) cofactor. Structures solved from free electron laser and low-dose synchrotron x-ray crystal data further highlighted an unusual bent shape of the oxidized flavin chromophore, and showed that the bending angle (14°) did not change upon photon absorption (step 1) or throughout the photocycle. Calculations showed that bending substantially affected the energy levels of the flavin. Structural and spectroscopic analysis of WT and mutant proteins targeting two conserved active-site residues, R451 and C432, demonstrated that both residues were crucial for proper positioning of the substrate and water molecules and for oxidation of the fatty acid carboxylate by ^{1}FAD* (~300 ps in WT FAP) to form FAD$^{\bullet-}$ (step 2). Time-resolved infrared spectroscopy demonstrated that decarboxylation occured quasi-instantaneously upon this forward electron transfer, consistent with barrierless bond cleavage predicted by quantum chemistry calculations and with snapshots obtained by time-resolved crystallography. Transient absorption spectroscopy in H_2O and D_2O buffers indicated that back electron transfer from FAD$^{\bullet-}$ was coupled to and limited by transfer of an exchangeable proton or hydrogen atom (step 3). Unexpectedly, concomitant with FAD$^{\bullet-}$ reoxidation (to a red-shifted form FAD_{RS}) in 100 ns, most of the CO_2 product was converted, most likely into bicarbonate (as inferred from FTIR spectra of the cryotrapped FAD_{RS} intermediate). Calculations indicated that this catalytic transformation involved an active-site water molecule. Cryo-Fourier transform infrared spectroscopy studies suggested that bicarbonate formation (step 4) was preceded by deprotonation of an arginine residue (step 3). At room temperature, the remaining CO_2 left the protein in 1.5 µs (step 4′). The observation of residual electron density close to C432 in electron density maps derived from time-resolved and cryocrystallography data suggests that this residue may play a role in stabilizing CO_2 and/or bicarbonate. Three routes for alkane formation were identified by quantum chemistry calculations; the one shown in the figure is favored by the ensemble of experimental data.

CONCLUSION: We provide a detailed and comprehensive characterization of light-driven hydrocarbon formation by FAP, which uses a remarkably complex mechanism including unique catalytic steps. We anticipate that our results will help to expand the green chemistry toolkit. ■

The list of author affiliations is available in the full article online.
*Corresponding author. Email: frederic.beisson@cea.fr (F.B.), pavel.muller@i2bc.paris-saclay.fr (P.M.), pascal.arnoux@cea.fr (P.A.), Ilme.schlichting@mpimf-heidelberg.mpg.de (I.S.), marten.vos@polytechnique.edu (M.H.V.), tatjana.domratcheva@mpimf-heidelberg.mpg.de (T.D.), martin.weik@ibs.fr (M.W.), catherine.berthomieu@cea.fr (C.B.)
Cite this article as D. Sorigué *et al.*, *Science* **372**, eabd5687 (2021). DOI: 10.1126/science.abd5687

READ THE FULL ARTICLE AT
https://doi.org/10.1126/science.abd5687

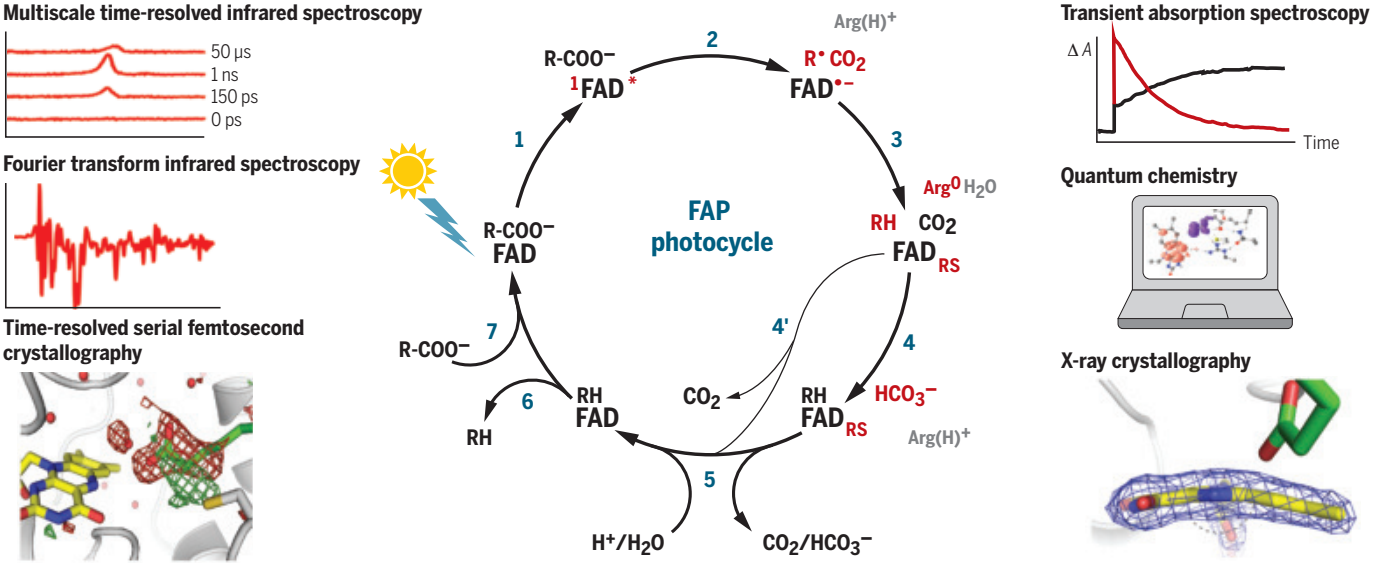

Elucidation of the FAP photocycle by combining spectroscopic, biochemical, crystallographic, and computational studies.

RESEARCH ARTICLE SUMMARY

CORONAVIRUS

Estimated transmissibility and impact of SARS-CoV-2 lineage B.1.1.7 in England

Nicholas G. Davies*, Sam Abbott†, Rosanna C. Barnard†, Christopher I. Jarvis†, Adam J. Kucharski†, James D. Munday†, Carl A. B. Pearson†, Timothy W. Russell†, Damien C. Tully†, Alex D. Washburne†, Tom Wenseleers†, Amy Gimma, William Waites, Kerry L. M. Wong, Kevin van Zandvoort, Justin D. Silverman, CMMID COVID-19 Working Group‡, COVID-19 Genomics UK (COG-UK) Consortium‡, Karla Diaz-Ordaz, Ruth Keogh, Rosalind M. Eggo, Sebastian Funk, Mark Jit, Katherine E. Atkins, W. John Edmunds

INTRODUCTION: Several novel variants of severe acute respiratory syndrome coronavirus 2 (SARS-CoV-2), the virus that causes COVID-19, emerged in late 2020. One of these, Variant of Concern (VOC) 202012/01 (lineage B.1.1.7), was first detected in southeast England in September 2020 and spread to become the dominant lineage in the United Kingdom in just a few months. B.1.1.7 has since spread to at least 114 countries worldwide.

RATIONALE: The rapid spread of VOC 202012/01 suggests that it transmits more efficiently from person to person than preexisting variants of SARS-CoV-2. This could lead to global surges in COVID-19 hospitalizations and deaths, so there is an urgent need to estimate how much more quickly VOC 202012/01 spreads, whether it is associated with greater or lesser severity of disease, and what control measures might be effective in mitigating its impact. We used social contact and mobility data, as well as demographic indicators linked to SARS-CoV-2 community testing data in England, to assess whether the spread of the new variant may be an artifact of higher baseline transmission rates in certain geographical areas or among specific demographic subpopulations. We then used a series of complementary statistical analyses and mathematical models to estimate the transmissibility of VOC 202012/01 across multiple datasets from the UK, Denmark, Switzerland, and the United States. Finally, we extended a mathematical model that has been extensively used to forecast COVID-19 dynamics in the UK to consider two competing SARS-CoV-2 lineages: VOC 202012/01 and preexisting variants. By fitting this model to a variety of data sources on infections, hospitalizations, and deaths across seven regions of England, we assessed different hypotheses for why the new variant appears to be spreading more quickly, estimated the severity of disease associated with the new variant, and evaluated control measures including vaccination and nonpharmaceutical interventions. Combining multiple lines of evidence allowed us to draw robust inferences.

RESULTS: The rapid spread of VOC 202012/01 is not an artifact of geographical differences in contact behavior and does not substantially differ by age, sex, or socioeconomic stratum. We estimate that the new variant has a 43 to 90% higher reproduction number (range of 95% credible intervals, 38 to 130%) than preexisting variants. Similar increases are observed in Denmark, Switzerland, and the United States. The most parsimonious explanation for this increase in the reproduction number is that people infected with VOC 202012/01 are more infectious than people infected with a preexisting variant, although there is also reasonable support for a longer infectious period and multiple mechanisms may be operating. Our estimates of severity are uncertain and are consistent with anything from a moderate decrease to a moderate increase in severity (e.g., 32% lower to 20% higher odds of death given infection). Nonetheless, our mathematical model, fitted to data up to 24 December 2020, predicted a large surge in COVID-19 cases and deaths in 2021, which has been borne out so far by the observed burden in England up to the end of March 2021. In the absence of stringent nonpharmaceutical interventions and an accelerated vaccine rollout, COVID-19 deaths in the first 6 months of 2021 were projected to exceed those in 2020 in England.

CONCLUSION: More than 98% of positive SARS-CoV-2 infections in England are now due to VOC 202012/01, and the spread of this new variant has led to a surge in COVID-19 cases and deaths. Other countries should prepare for potentially similar outcomes. ■

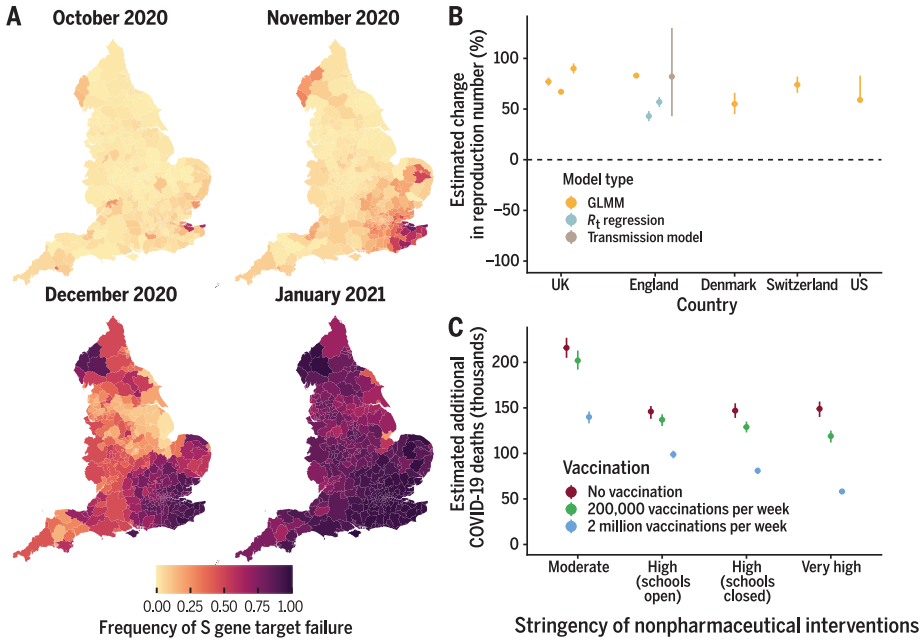

Impact of SARS-CoV-2 Variant of Concern 202012/01. (**A**) Spread of VOC 202012/01 (lineage B.1.1.7) in England. (**B**) The estimated relative transmissibility of VOC 202012/01 (mean and 95% confidence interval) is similar across the United Kingdom as a whole, England, Denmark, Switzerland, and the United States. (**C**) Projected COVID-19 deaths (median and 95% confidence interval) in England, 15 December 2020 to 30 June 2021. Vaccine rollout and control measures help to mitigate the burden of VOC 202012/01.

The list of author affiliations is available in the full article online.
*Corresponding author. Email: nicholas.davies@lshtm.ac.uk
†These authors contributed equally to this work.
‡See supplementary materials for list of consortium members and affiliations.
Cite this article as N. G. Davies *et al.*, *Science* **372**, eabg3055 (2021). DOI: 10.1126/science.abg3055
This is an open-access article distributed under the terms of the Creative Commons Attribution license (https://creativecommons.org/licenses/by/4.0/), which permits unrestricted use, distribution, and reproduction in any medium, provided the original work is properly cited.

READ THE FULL ARTICLE AT
https://doi.org/10.1126/science.abg3055

RESEARCH ARTICLES

NEUROEVOLUTION

Bilateral visual projections exist in non-teleost bony fish and predate the emergence of tetrapods

Robin J. Vigouroux[1], Karine Duroure[1], Juliette Vougny[2], Shahad Albadri[1], Peter Kozulin[3], Eloisa Herrera[4], Kim Nguyen-Ba-Charvet[1], Ingo Braasch[5], Rodrigo Suárez[3]†, Filippo Del Bene[1]*, Alain Chédotal[1]*

In most vertebrates, camera-style eyes contain retinal ganglion cell neurons that project to visual centers on both sides of the brain. However, in fish, ganglion cells were thought to innervate only the contralateral side, suggesting that bilateral visual projections appeared in tetrapods. Here we show that bilateral visual projections exist in non-teleost fishes and that the appearance of ipsilateral projections does not correlate with terrestrial transition or predatory behavior. We also report that the developmental program that specifies visual system laterality differs between fishes and mammals, as the Zic2 transcription factor, which specifies ipsilateral retinal ganglion cells in tetrapods, appears to be absent from fish ganglion cells. However, overexpression of human ZIC2 induces ipsilateral visual projections in zebrafish. Therefore, the existence of bilateral visual projections likely preceded the emergence of binocular vision in tetrapods.

Eye position on the head is highly variable between species, but frontal eyes have long been considered critical for depth perception (stereopsis) because this position increases the overlap between the visual field of each eye (*1*). In vertebrates, ganglion cell axons from each eye cross through each other at the optic chiasm and enter the brain on the contralateral side. In mammals, visual axons from each eye meet and interweave at the chiasm. However, optic nerve crossing modalities are more diverse in fish, and in most species the two optic nerves remain fully separated and overlap only at the chiasm (*2*, *3*).

Classic neuroanatomical studies have shown that, in mammals, eye projections are bilateral, with a variable fraction of retinal ganglion cell (hereafter "ganglion cell") axons continuing in the ipsilateral optic tract after crossing the chiasm. The proportion of ipsilateral projections is low (2 to 3%) in rodents but reaches ~40% in primates (*4*, *5*). The comparative analysis of many vertebrate species conducted over several decades suggests that ipsilateral visual axons exist in all mammals, anuran amphibians, and some reptiles and that they are essentially absent or were secondarily lost in birds (*5*–*8*). Accordingly, developmental transcriptional programs that specify ipsilateral ganglion cells described in mammals are conserved in *Xenopus* but not in chicks or zebrafish (*5*, *9*). This textbook view implies that visual axon bilaterality emerged in early tetrapods and might have provided a visual advantage, in particular for nocturnal and predatory terrestrial species (*10*). However, a review of the extensive literature on fish visual systems provides a more complex image, with reports (sometimes contradictory) of ipsilateral ganglion cell projections in some fish species (*6*, *11*). Most of these pioneering studies relied on imprecise histological staining methods such as the Nauta-Gygax staining method or autoradiography (*12*). In this study, we assessed the laterality of visual projections in bony fishes (Fig. 1A) by using the B fragment of the cholera toxin (*12*) coupled to fluorescent dyes. Dye-coupled cholera toxins have not been previously used in fish, although they proved to be highly reliable tracers for visual projections in rodents, owing to their efficient endocytosis by neurons, slow elimination, high photostability, and brightness (*13*). They are also compatible with whole-brain clearing and thereby enable mapping of visual pathways in intact brains by using three-dimensional (3D) light-sheet fluorescence microscopy (*14*, *15*).

With more than 30,000 species, fishes account for at least half of the extant vertebrate species (*16*). We initially focused on ray-finned fishes (actinopterygians; Fig. 1A and fig. S1), which separated from lobe-finned fishes (sarcopterygians, including tetrapods) around 450 million years ago (Ma) (*17*). Within the ray-finned fishes, we initially selected six species among the clupeocephalan lineage (fig. S1), the largest of the three lineages of teleost fishes, which account for most (~96%) extant teleosts (*18*). Of the clupeocephalans, three represent ostariophysians [Mexican tetra (*Astyanax mexicanus*), redeye piranha (*Serrasalmus rhombeus*), and zebrafish (*Danio rerio*)] and three are percomorphs [green-spotted pufferfish (*Tetraodon nigroviridis*), Atlantic mudskipper (*Periophthalmus barbarus*), and four-eyed fish (*Anableps anableps*)]. With 9000 and 16,000 species, respectively, ostariophysians and percomorphs are the two largest clades of teleosts. Fishes in these clades have diverse eye positions, feeding behaviors, and habitats, and some were previously reported to have ipsilateral visual projections (*11*).

Totally crossed visual projections in teleosts

The visual system of the zebrafish has been extensively studied with lipophilic dye tracing or genetic methods and shown to be exclusively contralateral (*19*). Accordingly, we found that fluorescent (cholera toxin–labeled) axons were present only on the contralateral side of adult zebrafish brains [Fig. 1B and movie S1; $n = 6$ biological replicates (unless otherwise indicated, n denotes the number of biological replicates)]. Previously identified retino-recipient visual nuclei (*20*) could be detected with cholera toxin, thereby validating the use of this tracing method in fish (Fig. 1C). Light-sheet microscopy imaging of fish injected with cholera toxin showed that visual projections were only contralateral in Mexican tetra surface fish (Fig. 1, D and E, and movie S1; $n = 7$), in contrast to previous findings (*21*). Likewise, eyes in the redeye piranha only projected contralaterally (Fig. 1, F and G, and movie S1; $n = 3$), in disagreement with earlier work in other piranha species (*22*, *23*). This suggests that ostariophysians only have crossed visual projections.

In the freshwater green-spotted pufferfish (*24*), a percomorph, the two optic nerves stay separated at the chiasm, and visual projections were exclusively contralateral (Fig. 1, H and I, fig. S2, and movie S1; $n = 4$), as previously described in another pufferfish (*25*). We next studied the four-eyed fish, a percomorph surface-dweller fish whose large protruding eyes with duplicated corneas and pupils allow seeing under and above the water (*26*). Again, one optic nerve passed over the other at the chiasm (fig. S2), and cholera toxin tracing showed that visual projections were also completely crossed (Fig. 1, J and K; $n = 3$). Similar results were obtained in the mudskipper, a percomorph with an amphibious lifestyle (Fig. 1, L and M, fig. S2, and movie S1; $n = 3$). Together, these results show that in percomorph eyes, ganglion cells also likely project only to visual nuclei on the opposite side of the brain (fig. S1).

Osteoglossomorphs (bonytongues), a teleost sister group of clupeocephalans (Fig. 1A and fig. S1), are considered a group of basal (i.e.,

[1]Sorbonne Université, INSERM, CNRS, Institut de la Vision, 17 Rue Moreau, 75012 Paris, France. [2]Institut Curie, PSL Research University, INSERM U934, CNRS UMR3215, Paris, France. [3]Queensland Brain Institute, The University of Queensland, Building 79, St Lucia Campus, Brisbane, QLD 4072, Australia. [4]Instituto de Neurociencias, Av. Ramón y Cajal s/n, San Juan de Alicante, 03550 Spain. [5]Department of Integrative Biology and Program in Ecology, Evolution, and Behavior, Michigan State University, 288 Farm Lane, East Lansing, MI 48824, USA.
†Present address: School of Biomedical Sciences, The University of Queensland, St Lucia Campus, Brisbane, QLD 4072, Australia.
*Corresponding author. Email: filippo.delbene@inserm.fr (F.D.B.); alain.chedotal@inserm.fr (A.C.)

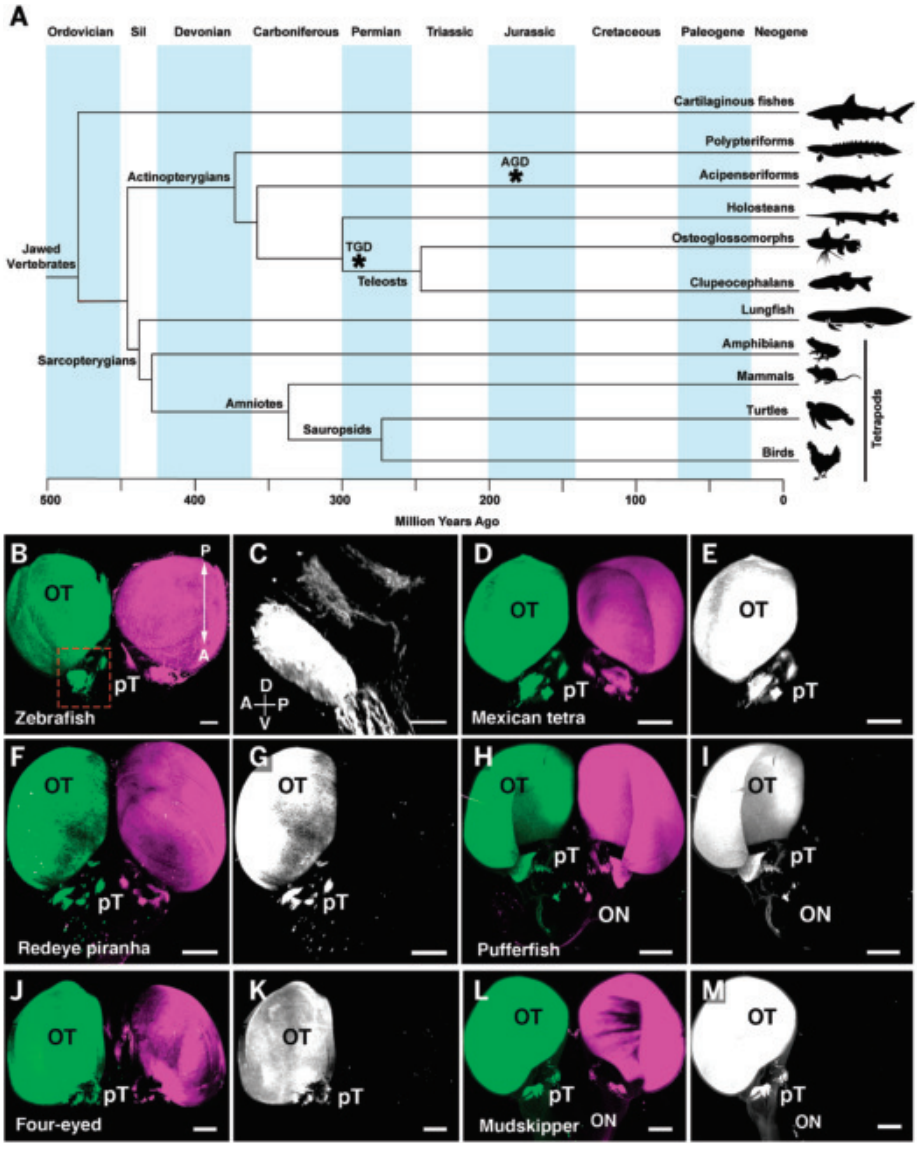

Fig. 1. Visual projections are only contralateral in clupeocephalan teleosts. (**A**) Simplified phylogenetic tree of the major groups of vertebrates. Divergence of each major group is displayed in millions of years ago. Asterisks indicate whole-genome duplication events in the teleost (TGD) and sturgeon (AGD) ancestors. (**B**) Whole-brain visualization of a juvenile zebrafish injected with an AlexaFluor-555–conjugated CTb (left eye, green) and AlexaFluor-647–conjugated CTb (right eye, magenta), highlighting complete contralateral projections. (**C**) High-magnification view of the area surrounded by the red box in (B), showing pretectal nuclei. (**D** to **M**) 3D rendering of visual projections labeled by injecting AlexaFluor-555–conjugated CTb (left eye) and AlexaFluor-647–conjugated CTb (right eye), followed by iDISCO+ (immunolabeling-enabled 3D imaging of solvent-cleared organs) whole-brain clearing and 3D imaging with light-sheet fluorescence microscopy. (D and E) Mexican tetra. (F and G) Redeye piranha. (H and I) Green-spotted pufferfish. (J and K) Four-eyed fish. (L and M) Atlantic mudskipper. In all species, visual axons project to the brain on the contralateral side only. A, anterior; Ctb, cholera toxin B; D, dorsal; ON, optic nerve; OT, optic tectum; P, posterior; pT, pretectal nuclei; V, ventral; Sil, Silurian. Scale bars are 500 μm in (B) and (D) to (M) and 200 μm in (C).

the group that gave rise to later forms) teleosts encompassing ~200 living species (*16*). We chose to trace visual projections in the African butterflyfish (*Pantodon buchholzi*), a predator that lives close to the surface of freshwater systems, and found that a small contingent of retinal axons (Fig. 2, A and B, and movie S1; 2.33 ± 0.23% ipsilateral projections in the optic tectum, $n = 3$) project to the ipsilateral side, corroborating the findings of an earlier report (*27*). The main portion of ipsilateral axons targeted the tectum, and some others targeted pretectal nuclei. Ipsilateral visual axons have also been described in a mormyrid electric fish (*Gnathonemus petersii*) (*28*), another osteoglossomorph that exhibits a more nocturnal predatory behavior and can orient by active electrolocation (*29*). These results show that bilateral visual projections exist in osteoglossomorph teleosts, regardless of their predatory strategy and lifestyle history. Therefore, within teleosts, ipsilateral projections could have been secondarily lost in clupeocephalans or independently acquired in osteoglossomorphs. In mammals, binocular inputs to visual targets or areas are either segregated (thalamus, colliculus) or intermingled (suprachiasmatic nucleus). Because both eyes were injected with two distinct Alexa-conjugated cholera toxins, we also studied the relative distribution of ipsilateral and contralateral ganglion cell axons in butterflyfish brain areas innervated by both eyes. In African butterflyfish (Fig. 2C), we found that retinal inputs from both sides segregated, as in the thalamus and superior colliculus of mammals.

Bilateral visual projections exist in basal ray-finned fishes

These results on teleosts led us to study retinal projections in non-teleost ray-finned fish lineages (holosteans, acipenseriforms, and polypteriforms; Fig. 1A), which split from teleosts before the teleost whole-genome duplication event (TGD; Fig. 1A) that occurred around 320 Ma in the ancestor of extant teleosts [reviewed in (*30*)]. Holosteans and acipenseriforms are considered to have evolved slowly since they branched from other vertebrates 350 Ma (*31*). Bilateral visual projections (movie S2; $n = 5$ of 5) were observed in the spotted gar (*Lepisosteus oculatus*), one of the seven extant species of garfish and a representative of the holosteans. The spotted gar is a unique vertebrate model system, as its genome is thought to provide a "bridge" between tetrapods and teleosts (*32*). Bilateral cholera toxin injections revealed an ipsilateral projection in the rostral optic tectum of the spotted gar, with visual axons targeting several pretectal nuclei. There was no overlap of the contralateral and ipsilateral axons (Fig. 2, D to F, and movie S2; $n = 5$ of 5) that represented 4.78 ± 0.46% of visual inputs in the tectum, a ratio comparable to that in rodents. Next, we traced visual projections in the acipenseriform sterlet sturgeon (*Acipenser ruthenus*; $n = 2$ of 2). Cholera toxin tracing demonstrated the existence of a binocular domain in the tectum of the sterlet sturgeon as well as in several pretectal nuclei (Fig. 2, G to J, and movie S2; 9.77 ± 1.28% ipsilateral projections in the tectum, $n = 2$). No recrossing of visual inputs after entering the brain was detected, contrary to previous observations in the Russian sturgeon (*Acipenser güldenstädtii*) (*33*). We then studied the armored bichir (*Polypterus delhezi*; $n = 2$ of 2), a carnivorous nocturnal fish that represents the most basally diverging lineage of extant ray-finned fishes, the polypteriforms. In the bichir, the two optic nerves meet at the

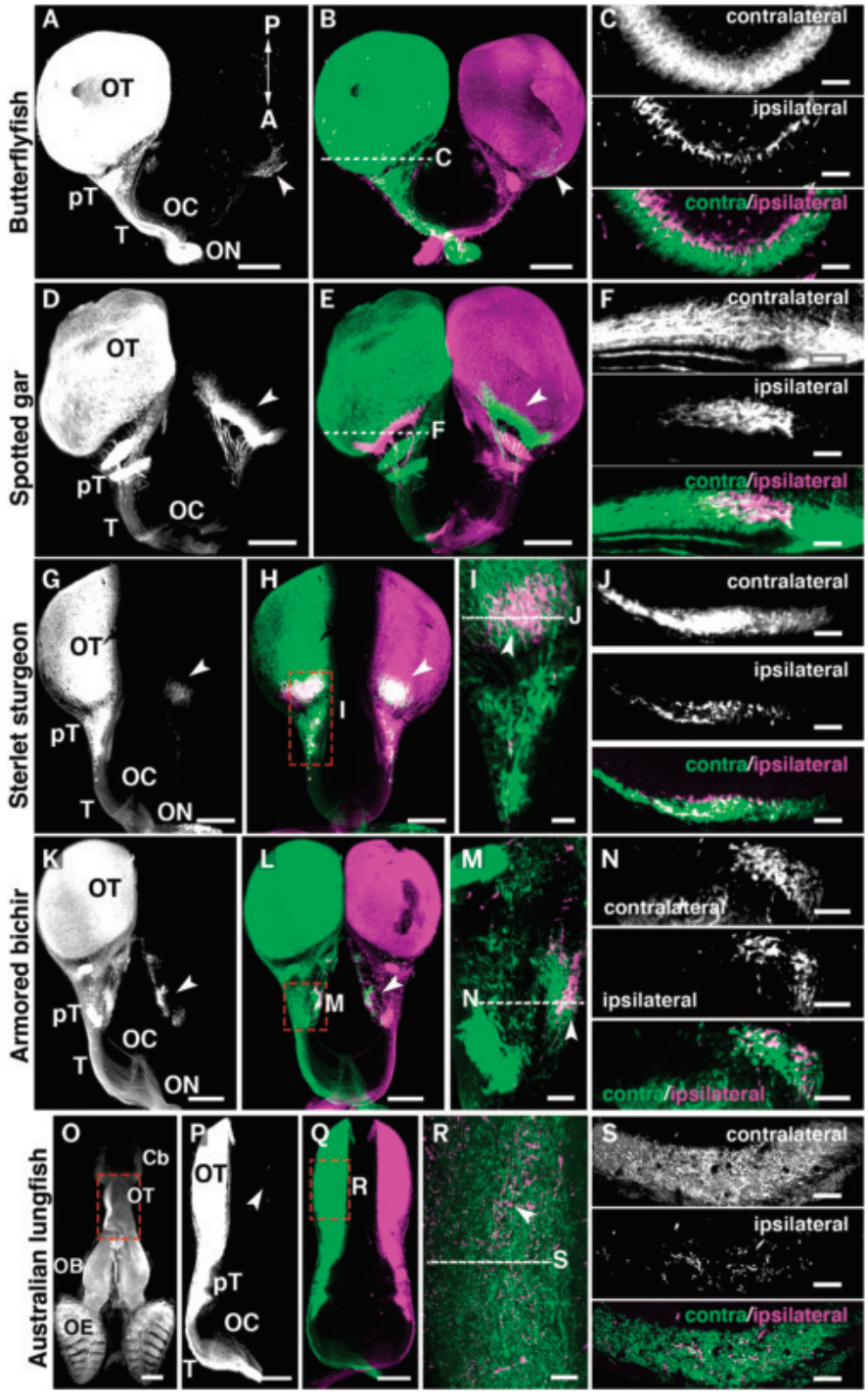

Fig. 2. Bilateral visual projections in basal ray-finned fishes and lobe-finned fishes. (**A** to **S**) 3D light-sheet fluorescence microscopy images of iDISCO+-cleared brains from fish injected in the eyes with two cholera toxins. The left panels [(A), (D), (G), and (K)] show only one channel. (C, F, J, N, and S) Optical sections through the brain region receiving bilateral visual inputs. Sections were taken from the areas indicated by dashed lines in (B), (E), (I), (M), and (R). (I, M, and R) High-magnification views of the area surrounded by the red boxes in (H), (L), and (Q), taken from whole-mount brains. (A to C) Butterflyfish. (D to F) Spotted gar. (G to J) Sterlet sturgeon. (K to N) Armored bichir. (O to S) Australian lungfish. (C, F, J and N) In all fishes except the lungfish, contralateral and ipsilateral projections segregate in two different OT layers. (S) In the lungfish, contralateral and ipsilateral projections are intermingled in the OT. Arrowheads indicate ipsilateral projections. Cb, cerebellum; OB, olfactory bulb; OE, olfactory epithelium; OC, optic chiasm; T, optic tract. Scale bars are 500 μm in (A), (B), (D), (E), (G), (H), (K), (L), (P), and (Q); 80 μm in (C), (F), (J), (N), and (S); 100 μm in (M) and (O); and 150 μm in (I) and (R).

chiasm, and ganglion cells axons interweave during decussation (fig. S2). Ipsilateral axons projected to numerous pretectal nuclei, such as the nucleus opticus dorsolateralis anterior thalami, the area optica ventrolateralis thalami, and the nucleus commissurae posterior par magnocellularis (Fig. 2, K to N, and movie S2). This corroborates previous studies in gray bichir (*Polypterus senegalus*) (*34*). These results, together with similar observations in two holosteans, the longnose gar (*Lepisosteus osseus*) and the bowfin (*Amia calva*) (*35*, *36*), indicate that bilateral visual projections likely are ancestral among actinopterygians and arose before their diversification, and that the ipsilateral component likely was subsequently lost in clupeocephalans. To further test this hypothesis, we analyzed visual projections in the Australian lungfish (*Neoceratodus forsteri*), a basal member of the lobe-finned fishes (sarcopterygians), the monophyletic group that includes tetrapods. Lobe-finned fishes diverged from ray-finned fishes ~450 Ma, and lungfish are now considered the closest living fish relative of tetrapods (*17*). In all injected animals ($n = 6$ of 6), a small ipsilateral projection was found to innervate the optic tectum (Fig. 2, O to S, and movie S3; $n = 6$). In contrast to the other fish species analyzed in our study, ipsilateral projections intermingled with contralateral ones (Fig. 2, R and S; $n = 6$). This was consistent with an earlier analysis of a single specimen of Australian lungfish (*37*) and supports the existence of bilateral visual projections in the bony vertebrate ancestor of actinopterygians and sarcopterygians (fig. S1). This intermingling of ipsilateral and contralateral axons could have some functional implications, as it suggests that some tectal neurons might receive and integrate inputs from both eyes. Alternatively, it could represent an immature stage of visual system development that could be resolved in adult animals in an activity-dependent manner, as is the case in mammals. Together, these results indicate that the bilateral organization of the visual system likely did not appear in amniotes but is an ancestral vertebrate feature that emerged much earlier in evolution, before the water-to-land transition and aerial vision adaptation in tetrapods.

ZIC2 expression in the ipsilateral human embryonic retina

Our results raised questions about the evolution and conservation of the genetic mechanisms that underlie visual system binocularity. Are they conserved in ray-finned fish with bilateral visual projections? The zinc-finger transcription factor Zic2 specifies the ipsilateral identity of ganglion cells in developing mice, ferrets, and *Xenopus* (*5*). In *Xenopus*, Zic2 is absent from the neural retina of premetamorphic tadpoles that have crossed visual projections only, but Zic2 is expressed in ipsilaterally projecting ganglion cells after metamorphosis

(*5*). To further evaluate and support the implication of Zic2 in the control of mammalian ganglion cell laterality, we analyzed the expression of ZIC2 in the human eye and compared this to expression in mice by performing immunohistochemistry in whole-mount retinas. In human embryos, ganglion cell axons reach the brain by the seventh post-conception week (pcw7), and the optic nerve is well formed at pcw10 (*38*). Using the EyeDISCO clearing protocol (*15*) in mice, we observed that at embryonic day 16 (E16), the peak of Zic2 expression in mice (*5*), the retinal domain positive for Zic2 represented ~5.34 ± 0.36% of the total retinal surface (Fig. 3, A to C, and fig. S3A; n = 6 eyes). Post-mitotic ganglion cells, the first neurons generated in the retina (*39*), migrate to the basal side to accumulate at the inner surface of the retina and express the transcription factors Islet1 (*40*) and RNA binding protein with multiple splicing (RBPMS) (*41*) (Fig. 3). At pcw9, RBPMS+ and ISLET1+ ganglion cells were present all over the retina (Fig. 3, D to I). Flat-mounted and sections of human retinas from pcw9 embryos, an age equivalent to E16 in mice (*40*), showed that ZIC2+ cells were restricted to the temporal quadrant of the retina (representing ~18.95 ± 0.98% of the retina surface), which contains ipsilaterally projecting ganglion cells in primates (Fig. 3, D to J, and movie S4; n = 3 eyes). ZIC2+ ganglion cells coexpressed ISLET1 and RBPMS (Fig. 3, F to H). In the temporal retina, the density of ZIC2+ and ISLET1+ ganglion cells was higher near the ciliary marginal zone, at the edge of the retina (Fig. 3G), than in more medial regions where it was absent from the most superficial ISLET1+ (Fig. 3H and fig. S3B) and RBPMS+ ganglion cells (Fig. 3F and fig. S3). ZIC2 was not detectable in the nasal retina (Fig. 3, D, E, and I). Unlike in the mouse (*42*), ZIC2 was not present in the neuroblastic layer, which contains SOX2 (sex determining region Y–box 2)+ progenitors (Fig. 3, J to L, and fig. S3C). At pcw14, at the end of ganglion cell neurogenesis (*39*), ZIC2 was still only present in the temporal retina (Fig. 3, K and L). Although we could not access later stages of development, the absence of ZIC2 from the most superficial ganglion cells in the inner retina suggests that human ZIC2 is expressed in recently differentiated ipsilateral ganglion cells in the temporal retina and might be down-regulated as they mature, as is the case in mice.

Zic2 is not expressed in differentiating ganglion cells in fish with bilateral visual projections

The pivotal role for Zic2 in the specification of an ipsilateral axonal growth program in mammals was also well correlated with the absence of transcripts of the two *zic2* co-orthologs (*zic2a* and *zic2b*, generated in the TGD) in

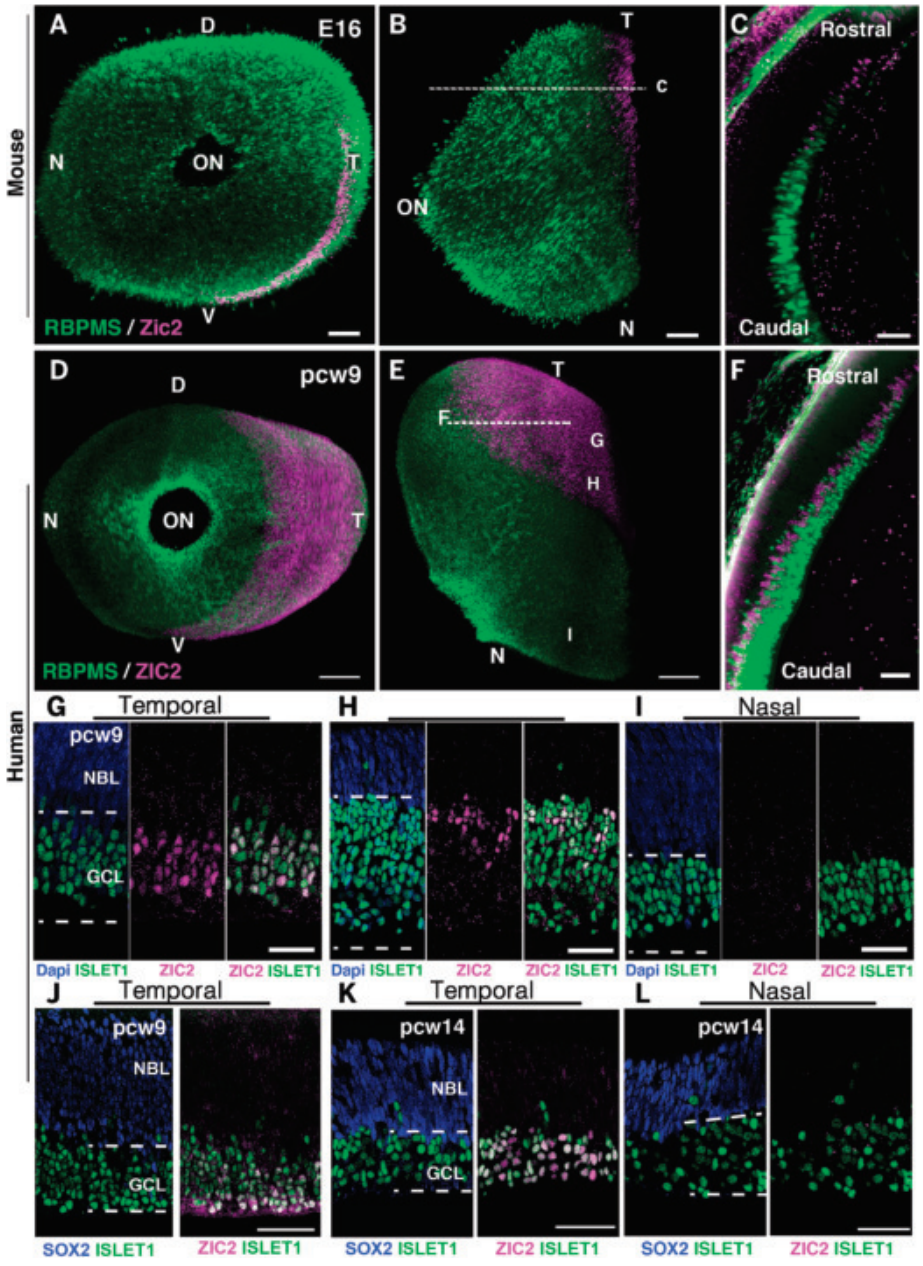

Fig. 3. Zic2 is expressed in the temporal retina of human embryos. (**A** to **C**) Whole-mount immunohistochemistry of an E16 mouse eye labeled with the pan–ganglion cell marker RBPMS and the ipsilateral ganglion cell marker Zic2. (A) Frontal view. (B) Top view. (C) Optical section at the level indicated by the dashed line in (B). (**D** to **F**) 3D light-sheet fluorescence microscopy of pcw9 human embryonic eye tissue cleared using EyeDISCO and labeled for RBPMS and ZIC2. (D) Frontal view. (E) Top view. (F) Optical section at the level indicated by the dashed line in (E). In panel (E), the letters G, H, and I indicate the approximate positions of images in panels (G) to (I). (**G** to **I**) Retinal cryosections of a pcw9 human embryo eye labeled with ZIC2 and ISLET1 at three different levels: temporal and close to retinal outer limit (G), temporo-medial (H), and nasal (I). ZIC2 cells are in the ganglion cell layer (GCL) and coexpress ISLET1, but they are absent from the neuroblastic layer (NBL). (**J**) Retinal cryosection of a pcw9 human embryo eye labeled with ZIC2 and SOX2. ZIC2 is absent from the NBL, which contains SOX2+ progenitors. (**K** and **L**) Retinal cryosections of a pcw14 human embryo eye labeled with ZIC2, SOX2, and ISLET1. ZIC2 is only present in ISLET1+ ganglion cells in the temporal retina and is absent from SOX2+ progenitors (K). Dapi, 4′,6-diamidino-2-phenylindole; N, nasal; T, temporal. Scale bars are 70 μm in (A) and (B), 20 μm in (C), 300 μm in (D) and (E), and 50 μm in (F) to (L).

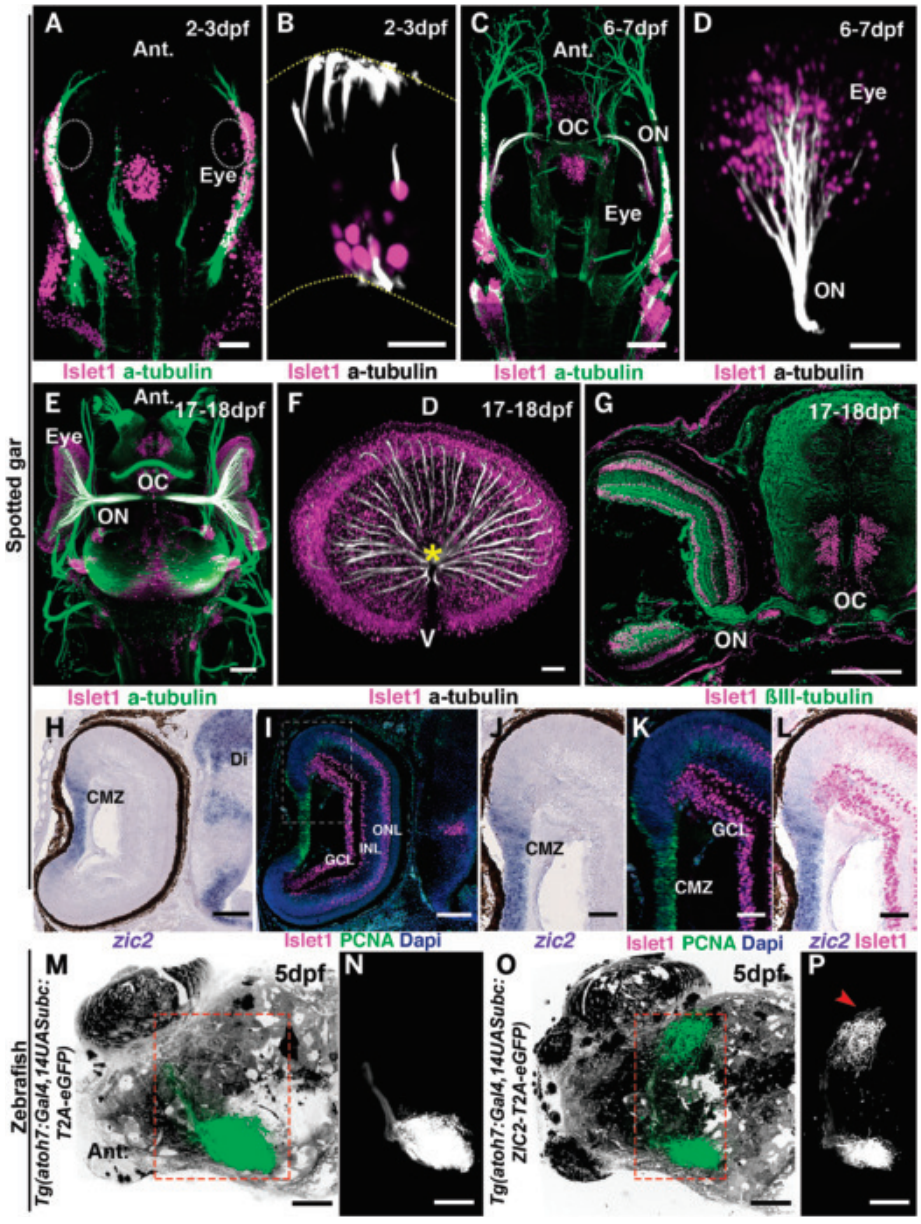

Fig. 4. Zic2 is not expressed by ganglion cells in spotted gar and zebrafish. (**A** to **F**) Development of the visual system in the spotted gar. All images are 3D light-sheet fluorescence microscopy images of EyeDISCO-cleared spotted gar embryos labeled with Islet1 and acetylated tubulin. (A and C and E) Top (dorsal) views of spotted gars at 2 to 3 dpf (A), 6 to 7 dpf (C), and 17 to 18 dpf (E). (B and D and F) Frontal views of whole spotted gar eyes at 2 to 3 dpf (B), 6 to 7 dpf (D), and 17 to 18 dpf (F). The optic nerve (ON and asterisk) starts to form by 6 to 7 dpf and is well developed by 17 to 18 dpf. The optic chiasm (OC) is formed by 6 to 7dpf. (**G**) Coronal cryosection of spotted gar embryos at 17 to 18 dpf, labeled for βIII-tubulin and Islet1. (**H** to **L**) Cryosection from spotted gar eyes at 17 to 18 dpf, hybridized with *zic2* riboprobe [(H) and (J)] and labeled for proliferating cell nuclear antigen (PCNA) and Islet1 [(I), (K), and (L)]. (J to L) Higher-magnification views of the ciliary margin zone [area framed in (I)]. (**M** to **P**) 3D renderings of whole brains, viewed from the top of zebrafish injected with Tg(*atoh7:Gal4,14UASubc:T2A-eGFP-pA*) [(M) and (N)] or *Tg*(*atoh7:Gal4,14UASubc:ZIC2-T2A-eGFP-pA*) [(O) and (P)]. (N) and (P) are views of the GFP signal in the areas framed in (M) and (O), respectively, showing segmented ganglion cell projections. (P) A large ipsilateral projection (arrowhead) is seen in the *Tg*(*atoh7:Gal4,14UASubc:ZIC2-T2A-eGFP-pA*)–injected fish. Ant.; anterior; CMZ, ciliary marginal zone; Di, diencephalon; INL, inner nuclear layer; ONL, outer nuclear layer. Scale bars are 50 μm in (A), (D), (F), and (J) to (P); 15 μm in (B); 80 μm in (C), (H), and (I); 150 μm in (E); and 200 μm in (G).

zebrafish ganglion cells (*43*) (fig. S4, A to C and E to G). Double fluorescent in situ hybridization for *zic2b* and *atoh7* (a committed precursor marker) from 24 to 48 hours post-fertilization confirmed that *zic2b* did not colocalize with differentiating *atoh7*+ ganglion cells. By contrast, and as reported for Zic2 in the mouse (*44*), *zic2b* was detected in the ciliary marginal zone, (fig. S4M; $n = 3$), which contains dividing progenitors and stem cells that produce all retinal cell types, even in adult teleosts (*45*, *46*) (fig. S4, H to L; $n = 5$).

The presence of an ipsilateral visual projection in the spotted gar, as extensive as that in mice, together with its well-characterized genome and the accessibility of gar embryos (*32*, *47*), led us to evaluate the expression of *zic2* in the developing gar retina. We first analyzed the development of the gar visual system using whole-mount immunolabeling, EyeDISCO clearing, and light-sheet microscopy (table S1) (*15*). In the spotted gar, a few Islet1- immunoreactive ganglion cells were detected at 2 to 3 days post-fertilization (dpf) (Fig. 4, A and B, fig. S5C, and movie S5; $n = 5$). At 6 to 7 dpf, optic nerves could be observed and had reached the optic chiasm (Fig. 4, C and D, and movie S5; $n = 5$). Development is slower in gar than in zebrafish, and it is temperature dependent (*48*). The next 10 days of development are characterized only by changes in fin opercular and gill formation, not changes in eye morphogenesis (*48*). By 17 to 18 dpf, the retina contained many ganglion cells, and the optic tract was well developed (Fig. 4, E to G, and movie S5; $n = 5$). The highly proliferative ciliary marginal zone could be identified by the presence of cells expressing the S-phase marker, proliferating cell nuclear antigen marker, and overlapping with *zic2* expression, which was absent from neighboring post-mitotic Islet1+ ganglion cells (Fig. 4, H to L). At 2 to 3 dpf and 6 to 7 dpf, *zic2* mRNA was detected in proliferating cells of the developing neuroretina and progressively became restricted to the ciliary marginal zone (fig. S5, A to D). Its paralogs, *zic1* and *zic5*, also enriched in ipsilateral ganglion cell in mice (*49*), were absent from the embryonic gar retina (fig. S5, E to L). These results show that Zic2, Zic1, and Zic5 do not specify ipsilateral ganglion cells in the spotted gar, suggesting that *zic* genes might be dispensable for gar ipsilateral projections. By contrast, the presence of Zic2 in the ciliary marginal zone of fish and mammals suggests that Zic2 might have a function in retinal precursors that is evolutionarily conserved.

In mammals, Zic2 acts in part by activating the expression of the receptor tyrosine kinase EphB1 in ipsilateral axons (*8*, *50*), whose ligand ephrinB2, localized at the chiasm, prevents crossing (*7*). According to the lack of Zic2 in the gar ganglion cells, we did not detect *ephB1* mRNA in the developing retina, and

ephrinB2 was absent from the chiasm (fig. S5, M to W).

ZIC2 overexpression induces ipsilateral projections in zebrafish

In mice, *Zic2* overexpression in the retina, outside the ipsilateral domain, increases the proportion of ipsilaterally projecting ganglion cell axons (*50*). Therefore, we tested the hypothesis that despite its absence in fish ganglion cells, the forced expression of Zic2 in zebrafish ganglion cells could affect their axonal targeting. We used a human *ZIC2-T2A-GFP* overexpression construct to express ZIC2 and GFP (green fluorescent protein) in the zebrafish eye under the control of the *atoh7* promoter. Vertebrate Zic2 proteins are highly conserved (*51*), with 81.1% identity between human ZIC2 and zebrafish Zic2a and more than 93% similarity in the zinc finger domain (fig. S6). To visualize the projections coming from ZIC2-overexpressing ganglion cells derived from a single eye, we removed one eye at 2 dpf. As previously reported, under normal conditions retinal fibers from the remaining eye projected exclusively to the contralateral tectum (Fig. 4, M and N; n = 10) (*52*, *53*). By contrast, ZIC2-expressing ganglion cells generated ipsilateral retinotectal afferent fibers representing a mean of 19.6 ± 8.5% of the GFP+ axons (Fig. 4, O and P; n = 10 of 13). Expression of *ZIC2* did not seem to bias the targeting of ganglion cell axons to their topographic position, as previously reported in mice (*54*). These results show that *zic2*, although not normally expressed in zebrafish ganglion cells, can still specify an ipsilateral program. In mice, the receptor tyrosine kinase EphB1 is expressed by ipsilateral ganglion cell axons, and the ectopic expression of Zic2 in the contralateral retina induces EphB1 and reduces midline crossing at the chiasm (*8*, *50*). However, we could not detect EphB1 protein or mRNA (fig. S7) in zebrafish ganglion cells in either controls injected with GFP (n = 13) or in ZIC2-overexpressing fish (n = 11), suggesting that these may be guided by alternative cues.

Discussion

It has been proposed that the evolution of terrestrial vertebrates followed an increase of eye size in aquatic vertebrates able to see through air, in a process that has occurred also in modern crocodiles or fish species similar to the four-eyed fish and mudskippers (*55*). The existence of ipsilateral projections in the most basally branching groups of both actinopterygians and sarcopterygians indicates that ipsilateral connections were likely already present in the common ancestor of bony vertebrates, a bony fish, thus preceding aerial vision adaptation of tetrapods. This example highlights how the comparative study of a variety of species outside the list of the classical model species allows drawing evolutionary conclusions that may otherwise remain obscured (*56*). Moreover, all the teleost species analyzed in our study can be described as diurnal predators that heavily rely on visual cues to detect and consume their prey. These prey may vary in size from large vertebrates (redeye piranha) to small invertebrates (Mexican tetra, zebrafish, green-spotted puffer, Atlantic mudskipper, and the four-eyed fish). In all cases, our data show that ipsilateral projections in teleosts are not required for a visually mediated predatory behavior, as is usually assumed in mammals. Recent studies have confirmed this also in larval zebrafish, where possible alternative neuronal circuits have been described (*53*).

On the other hand, lungfish and some basally branching actinopterygians, in which ipsilateral projections are present, show reduced visual system development, as they are bottom-dwellers that exhibit nocturnal predatory behavior (lungfish and bichir) or feed on benthic organisms (sturgeon). Overall, our data show that the presence of ipsilateral projections in the visual system of fishes appears to correlate with phylogeny and not with lifestyle or predatory behavior. Along these lines, it is therefore unlikely that ipsilateral retinal projections serve a function similar to what is commonly considered in mammals. On the contrary, visual system bilaterality might have been used as the neural substrate to compute stereopsis after diurnal mammals acquired visual-based predatory abilities after the Cretaceous–Paleogene extinction event. In support of this view, the number of ipsilateral projections in reptiles (chelonians and squamates) does not correlate with eye position or degree of binocular field (*11*, *57*). It has been hypothesized that ipsilateral ganglion cells facilitate motor coordination by providing a direct visual feedback to the limb-steering brain centers (*6*). However, the function of ipsilateral ganglion cells in fish remains elusive, and behavioral studies in noncanonical model species such as the gar will be required to address this question.

The conservation of the main families of axon guidance cues and receptors in bilateria suggested that the mechanisms underlying the development of neuronal connectivity are evolutionarily conserved (*58*, *59*). However, the loss of the gene encoding the DCC (Deleted in Colorectal Carcinoma) receptor in some bird species (*60*) and the uniqueness of the Roundabout3 receptor in mammals (*61*) have challenged this view. Here we show that the guidance program specifying visual axon ipsilaterality does not appear to be entirely conserved, as we failed to detect expression of *zic2* and other *zic* genes or *ephB1* in spotted gar ganglion cells. Hence, the textbook model of Zic2 and EphB1 in orchestrating retinal ganglion cell laterality does not simply translate to fish. In rodents, the contralateral identity of ganglion cells is specified by *Islet2* (*62*) and *SoxC* (*63*) transcription factors, but whether they influence the development of visual axons in fish is unknown. Therefore, further experiments are needed to address the molecular mechanisms underlying visual bilaterality in bony fish species. Are there other pathways, apart from Zic2, that could direct ipsilateral projections or block the contralateral fate that occurs normally? A recent study (*64*) shows that in mice, contralateral ganglion cells activate a noncanonical Wnt signaling pathway to cross the midline. In ipsilateral ganglion cells, Zic2 prevents midline crossing by inducing a genetic module that changes the expression of a set of genes to jointly inhibit this noncanonical Wnt pathway.

In fact, the ectopic expression of human ZIC2 in the developing zebrafish retina still induces the formation of ipsilateral visual axons without causing other targeting defects. This finding suggests a possible conservation in fishes of downstream components of the genetic program specifying ipsilateral axons in mammals, although the factor initiating its expression and its relationship to Zic2 remain unclear in the gar and other non-teleost fish. By the parsimony principle, given our data, we propose that the presence of ipsilaterality in the bony vertebrate ancestor is the most likely explanation. In particular, the Australian lungfish data show that ipsilateral projections were likely present in the sarcopterygian fish ancestor of tetrapods. Lungfish also functions as an outgroup to the actinopterygians, thereby making an independent origin of ipsilateral visual axons within actinopterygians a less plausible hypothesis. An alternative yet less parsimonious explanation could be that ipsilaterality has evolved independently multiple times among bony vertebrates, by means of different genetic mechanisms.

REFERENCES AND NOTES

1. S. Ramón y Cajal, *Histologie du Système Nerveux de l'Homme and des Vertébrés* (Maloine, 1909).
2. G. L. Walls, *The Vertebrate Eye and Its Adaptative Radiation* (Hafner, 1942).
3. K. Mogi *et al.*, *Laterality* **14**, 495–514 (2009).
4. G. Jeffery, L. Erskine, *Prog. Retin. Eye Res.* **24**, 721–753 (2005).
5. E. Herrera *et al.*, *Cell* **114**, 545–557 (2003).
6. M. L. Larsson, *Front. Ecol. Evol.* **3**, 89 (2015).
7. S. Nakagawa *et al.*, *Neuron* **25**, 599–610 (2000).
8. S. E. Williams *et al.*, *Neuron* **39**, 919–935 (2003).
9. A. Seth *et al.*, *Development* **133**, 725–735 (2006).
10. C. P. Heesy, *Evol. Anthropol.* **18**, 21–35 (2009).
11. R. Ward, J. Repérant, S. Hergueta, D. Miceli, M. Lemire, *Brain Res. Rev.* **20**, 155–170 (1995).
12. C. Saleeba, B. Dempsey, S. Le, A. Goodchild, S. McMullan, *Front. Neurosci.* **13**, 897 (2019).
13. W. L. Conte, H. Kamishina, R. L. Reep, *Brain Struct. Funct.* **213**, 367–373 (2009).
14. X. Luo *et al.*, *Exp. Neurol.* **247**, 653–662 (2013).
15. R. J. Vigouroux, Q. Cesar, A. Chédotal, K. T. Nguyen-Ba-Charvet, *eLife* **9**, e51275 (2020).
16. L. C. Hughes *et al.*, *Proc. Natl. Acad. Sci. U.S.A.* **115**, 6249–6254 (2018).

17. C. T. Amemiya *et al.*, *Nature* **496**, 311–316 (2013).
18. R. Betancur-R *et al.*, *BMC Evol. Biol.* **17**, 162 (2017).
19. R. O. Karlstrom *et al.*, *Development* **123**, 427–438 (1996).
20. E. Robles, E. Laurell, H. Baier, *Curr. Biol.* **24**, 2085–2096 (2014).
21. T. J. Voneida, C. M. Sligar, *J. Comp. Neurol.* **165**, 89–105 (1976).
22. E. Fiebig, S. O. E. Ebbesson, D. L. Meyer, *Cell Tissue Res.* **231**, 55–72 (1983).
23. S. O. Ebbesson, H. Ito, *Cell Tissue Res.* **213**, 483–495 (1980).
24. O. Jaillon *et al.*, *Nature* **431**, 946–957 (2004).
25. D. L. Meyer, E. Fiebig, S. O. E. Ebbesson, *Neurosci. Lett.* **23**, 111–115 (1981).
26. L. N. Perez *et al.*, *Proc. Biol. Sci.* **284**, 20170157 (2017).
27. A. B. Butler, W. M. Saidel, *Brain Behav. Evol.* **38**, 127–153 (1991).
28. G. Lázár, S. Libouban, T. Szabo, *J. Comp. Neurol.* **230**, 1–12 (1984).
29. G. von der Emde *et al.*, *J. Physiol. Paris* **102**, 279–290 (2008).
30. I. Braasch, J. H. Postlethwait, in *Polyploidy and Genome Evolution*, P. Soltis, D. Soltis, Eds. (Springer, 2012), pp. 341–383.
31. K. Du *et al.*, *Nat. Ecol. Evol.* **4**, 841–852 (2020).
32. I. Braasch *et al.*, *Nat. Genet.* **48**, 427–437 (2016).
33. J. Repérant *et al.*, *Brain Res.* **251**, 1–23 (1982).
34. J. Repérant, J. P. Rio, D. Miceli, M. Amouzou, J. Peyrichoux, *Brain Res.* **217**, 225–243 (1981).
35. R. G. Northcutt, A. B. Butler, *J. Comp. Neurol.* **166**, 1–15 (1976).
36. A. B. Butler, R. G. Northcutt, *Brain Behav. Evol.* **39**, 169–194 (1992).
37. R. G. Northcutt, *Brain Res.* **185**, 85–90 (1980).
38. J. M. Provis, D. van Driel, F. A. Billson, P. Russell, *J. Comp. Neurol.* **238**, 92–100 (1985).
39. Y. Lu *et al.*, *Dev. Cell* **53**, 473–491.e9 (2020).
40. A. Hoshino *et al.*, *Dev. Cell* **43**, 763–779.e4 (2017).
41. J. M. K. Kwong, J. Caprioli, N. Piri, *Investig. Opthalmol. Vis. Sci.* **51**, 1052–1058 (2010).
42. Q. Wang, F. Marcucci, I. Cerullo, C. Mason, *eNeuro* **3**, ENEURO.0169-16.2016 (2016).
43. R. Toyama, D. M. Gomez, M. D. Mana, I. B. Dawid, *Gene Expr. Patterns* **4**, 345–350 (2004).
44. F. Marcucci *et al.*, *Cell Rep.* **17**, 3153–3164 (2016).
45. D. C. Otteson, A. R. D'Costa, P. F. Hitchcock, *Dev. Biol.* **232**, 62–76 (2001).
46. M. Fernández-Nogales, V. Murcia-Belmonte, H. Y. Chen, E. Herrera, *Prog. Retin. Eye Res.* **68**, 110–123 (2019).
47. I. Braasch *et al.*, *J. Exp. Zool. B* **324**, 316–341 (2015).
48. W. L. Long, W. W. Ballard, *BMC Dev. Biol.* **1**, 6 (2001).
49. Q. Lo Giudice, M. Leleu, G. La Manno, P. J. Fabre, *Development* **146**, dev178103 (2019).
50. C. García-Frigola, M. I. Carreres, C. Vegar, C. Mason, E. Herrera, *Development* **135**, 1833–1841 (2008).
51. J. Aruga, M. Hatayama, *Adv. Exp. Med. Biol.* **1046**, 3–26 (2018).
52. A. L. Dell, E. Fried-Cassorla, H. Xu, J. A. Raper, *J. Neurosci.* **33**, 11076–11088 (2013).
53. C. Gebhardt *et al.*, *Nat. Commun.* **10**, 5471 (2019).
54. C. García-Frigola, E. Herrera, *EMBO J.* **29**, 3170–3183 (2010).
55. M. A. MacIver, L. Schmitz, U. Mugan, T. D. Murphey, C. D. Mobley, *Proc. Natl. Acad. Sci. U.S.A.* **114**, E2375–E2384 (2017).
56. G. Laurent, *Nat. Rev. Neurosci.* **21**, 395–396 (2020).
57. S. Hergueta *et al.*, *Brain Res. Bull.* **29**, 427–433 (1992).
58. C. S. Goodman, *Cell* **78**, 353–356 (1994).
59. P. Heger, W. Zheng, A. Rottmann, K. A. Panfilio, T. Wiehe, *eLife* **9**, e45530 (2020).
60. F. Friocourt *et al.*, *Sci. Rep.* **7**, 37569 (2017).
61. P. Zelina *et al.*, *Neuron* **84**, 1258–1272 (2014).
62. W. Pak, R. Hindges, Y.-S. S. Lim, S. L. Pfaff, D. D. M. M. O'Leary, *Cell* **119**, 567–578 (2004).
63. T. Kuwajima, C. A. Soares, A. A. Sitko, V. Lefebvre, C. Mason, *Neuron* **93**, 1110–1125.e5 (2017).
64. C. Morenilla-Palao *et al.*, *Sci. Adv.* **6**, eaaz8797 (2020).

ACKNOWLEDGMENTS

We thank A. Favre and A. Abjaghou for assistance with light-sheet microscopy, F. Cortesi for help with lungfish experiments, S. Dufour and all members of the Chédotal and Del Bene teams for helpful discussions and input during the project, S. Rétaux (Paris Saclay University) for help with Mexican tetra work and helpful comments on the manuscript, and A. Ferrara and S. David (Nicholls State University) and members of the Braasch Lab for help with gar work. **Funding:** This work was supported by Programme Investissements d'Avenir IHU FOReSIGHT (ANR-18-IAHU-01) (A.C. and F.D.B.), INSERM cross-cutting program HuDeCA 2018 (A.C.), NIH R01OD011116 (I.B.), and UQ Amplify Fellowship (R.S.). **Author contributions:** A.C., F.D.B., and R.J.V. designed the experiments. F.D.B., K.D., K.N.-B.-C., J.V., S.A., R.J.V., P.K., and R.S. conducted the experiments. A.C., K.N.-B.-C., and F.D.B. obtained funding for the project. I.B. provided *Lepisosteus* samples and E.H. provided the human *ZIC2* cDNA. A.C., F.D.B., and R.J.V. designed the figures and wrote the manuscript. All authors discussed the results and commented on the manuscript. **Competing interests:** The authors declare no competing interests. **Data and materials availability:** All data are available in the manuscript or the supplementary materials. Materials and methods and references cited therein can be found in the main article online.

SUPPLEMENTARY MATERIALS

science.sciencemag.org/content/372/6538/150/suppl/DC1
Figs. S1 to S7
Table S1
MDAR Reproducibility Checklist
Movies S1 to S5

15 September 2020; accepted 23 February 2021
10.1126/science.abe7790

CANCER

Targeting the nucleotide salvage factor DNPH1 sensitizes *BRCA*-deficient cells to PARP inhibitors

Kasper Fugger[1]*, Ilirjana Bajrami[1], Mariana Silva Dos Santos[1], Sarah Jane Young[1], Simone Kunzelmann[1], Geoff Kelly[2], Graeme Hewitt[1], Harshil Patel[1], Robert Goldstone[1], Thomas Carell[3], Simon J. Boulton[1], James MacRae[1], Ian A. Taylor[1], Stephen C. West[1]*

Mutations in the *BRCA1* or *BRCA2* tumor suppressor genes predispose individuals to breast and ovarian cancer. In the clinic, these cancers are treated with inhibitors that target poly(ADP-ribose) polymerase (PARP). We show that inhibition of DNPH1, a protein that eliminates cytotoxic nucleotide 5-hydroxymethyl-deoxyuridine (hmdU) monophosphate, potentiates the sensitivity of *BRCA*-deficient cells to PARP inhibitors (PARPi). Synthetic lethality was mediated by the action of SMUG1 glycosylase on genomic hmdU, leading to PARP trapping, replication fork collapse, DNA break formation, and apoptosis. *BRCA1*-deficient cells that acquired resistance to PARPi were resensitized by treatment with hmdU and DNPH1 inhibition. Because genomic hmdU is a key determinant of PARPi sensitivity, targeting DNPH1 provides a promising strategy for the hypersensitization of *BRCA*-deficient cancers to PARPi therapy.

The *BRCA1* and *BRCA2* gene products are required for the repair of DNA double-strand breaks (DSBs) by homologous recombination (HR) (*1*, *2*), and *BRCA*-defective cells exhibit gross chromosomal rearrangements owing to their defects in DNA repair (*3*). Treatment of *BRCA*-defective cells with poly(ADP-ribose) polymerase inhibitors (PARPi) leads to synthetic lethality (*4*–*6*), which is now exploited in the clinic for the treatment of breast, ovarian, prostate, and pancreatic cancers. PARPi-induced cytotoxicity is thought to be caused, at least in part, by the trapping of PARP1 on DNA lesions such as base excision repair (BER) intermediates and genomic ribonucleotides (*7*, *8*). However, despite good initial response, many tumors develop PARPi resistance leading to aggressive tumor growth (*9*). We therefore sought to identify ways to potentiate PARPi therapy and overcome acquired resistance of HR-deficient cancer cells. To do this, we carried out a genome-wide CRISPR-Cas9 screen using HR-deficient eHAP *MUS81*$^{-/-}$ cells, which are defective in the resolution of recombination intermediates (*10*). *MUS81*$^{-/-}$ cells were generated by CRISPR genome editing (*11*) (fig. S1A) and found to be hypersensitive to the PARPi olaparib (fig. S1B), as reported previously (*8*). Sensitivity was rescued by complementation with wild-type (WT) *MUS81* but not a nuclease dead allele (fig. S1, A and B).

[1]The Francis Crick Institute, 1 Midland Road, London NW1 1AT, UK. [2]MRC Biomedical NMR Centre, The Francis Crick Institute, 1 Midland Road, London NW1 1AT, UK. [3]Faculty of Chemistry and Pharmacy, Ludwig-Maximilians-Universität München, Butenandtstrasse 5-13, Building F, 81377 Munich, Germany.
***Corresponding author. Email: stephen.west@crick.ac.uk (S.C.W.); kasper.fugger@crick.ac.uk (K.F.)**

CRISPR screen for modulators of PARPi sensitivity

MUS81$^{-/-}$ cells were transduced with the lentiviral-based Brunello genome-wide CRISPR single guide RNA (sgRNA) library (*12*), followed by treatment with olaparib for 10 days (fig. S1C). The LD_{80} (lethal dose corresponding to 80% cell death) used allowed us to identify both dropout (sensitizing) and enriched (resistance-causing) guide RNAs (gRNAs). Bioinformatic analyses of the gRNA reads using the MAGeCK (Model-based Analysis of Genome-wide CRISPR-Cas9 Knockout) algorithm identified several determinants of PARPi sensitivity (Fig. 1A and table S1). PARPi resistance was observed

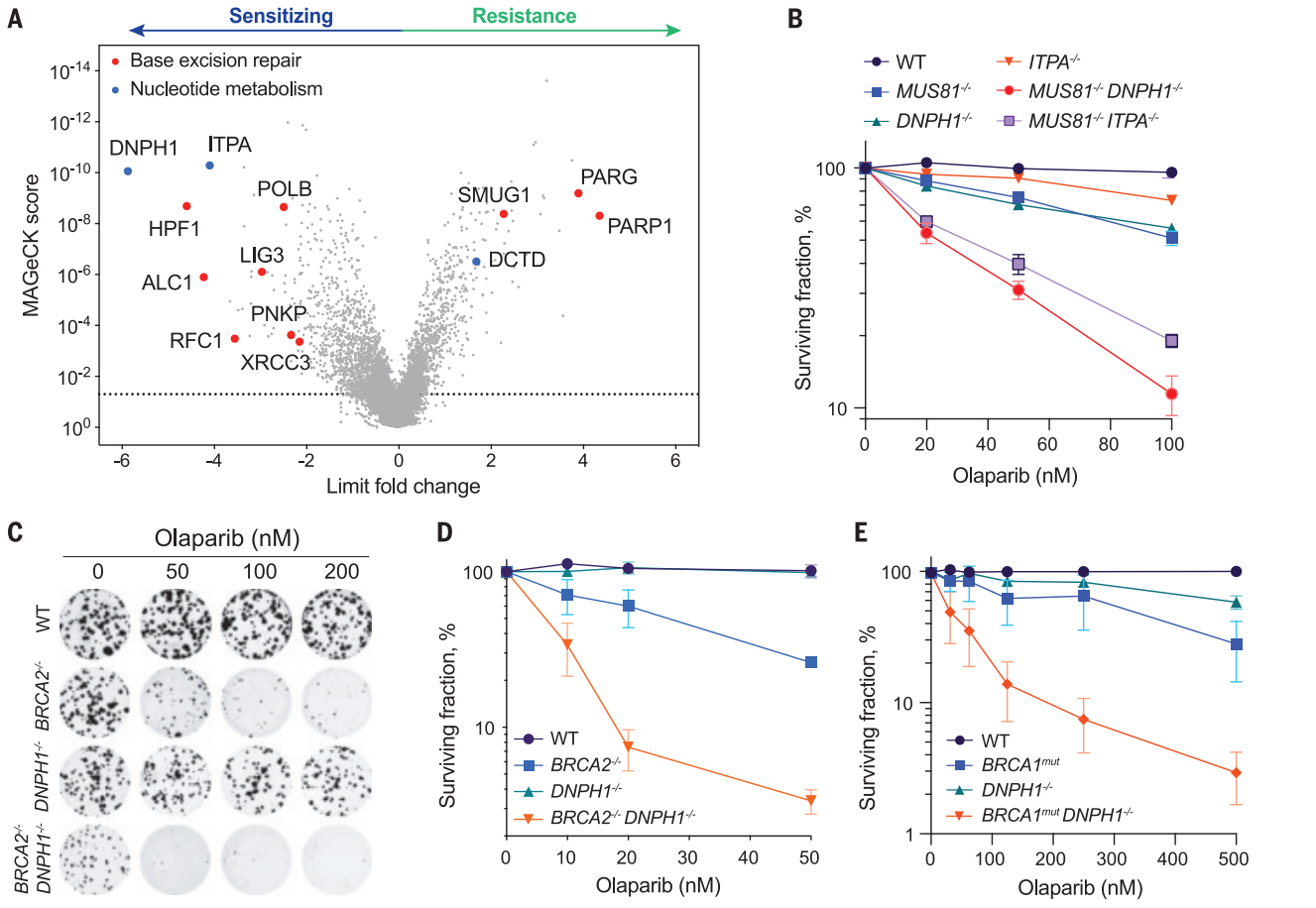

Fig. 1. Loss of DNPH1 sensitizes HR-deficient cells to PARP inhibitors. (**A**) Volcano plot showing sgRNA scores from MAGeCK analysis of a genome-wide CRISPR-Cas9 dropout/enrichment screen in eHAP *MUS81*$^{-/-}$ cells (olaparib versus mock). Each point represents limit fold change (sensitizing sgRNAs to the left, and resistance to the right) with corresponding MAGeCK score. BER and nucleotide metabolism factors are highlighted. (**B**) eHAP WT or KO cell lines were treated for 6 days with the indicated doses of olaparib, and viability was determined using CellTiter-Glo (mean with SEM; $n = 3$). Data were analyzed using analysis of variance for multiple comparisons. *MUS81*$^{-/-}$ versus *MUS81*$^{-/-}$ *DNPH1*$^{-/-}$, $P = 0.0013$; *MUS81*$^{-/-}$ versus *MUS81*$^{-/-}$ *ITPA*$^{-/-}$, $P = 0.0144$. (**C**) DLD1 WT or KO cell lines were seeded for colony formation and treated continuously for 10 days with olaparib. Colonies were fixed and stained with crystal violet. Well diameter, 22 mm. (**D**) DLD1 WT or KO cell lines were treated continuously for 10 days with olaparib. Cell viability was determined and data were analyzed as in (B). *BRCA2*$^{-/-}$ versus *BRCA2*$^{-/-}$ *DNPH1*$^{-/-}$, $P < 0.0001$. (**E**) SUM149 WT (revertant) *BRCA1*^{mut} and KO cell lines were treated for 10 days with olaparib. Cell viability was determined and data were analyzed as in (B). *BRCA1*^{mut} versus *BRCA1*^{mut} *DNPH1*$^{-/-}$, $P = 0.0021$.

with gRNAs that targeted PARP1 and the de-PARylation factor poly(ADP-ribose) glycohydrolase (PARG), which counteracts the cytotoxic effects of PARP trapping (*7*, *13*) or restores PARP activity (*14*). Sensitizing gRNAs included several BER factors (Fig. 1A), indicating that defective BER is synthetic lethal with PARPi, likely through increased PARP trapping on repair intermediates. Furthermore, Gene Ontology and STRING protein interaction analyses revealed an enrichment of DNA repair enzymes involved in BER and Fanconi anemia (fig. S1, D and E), as previously observed (*15*). Inactivation of factors involved in nicotinamide adenine dinucleotide metabolism and mitochondrial homeostasis also sensitized cells to PARPi, potentially through the formation of increased reactive oxygen species as a result of mitochondrial dysfunction (*16*), induced DNA damage, and PARP trapping (*17*).

The highest-ranking hit from the screen was DNPH1 (2′-deoxynucleoside 5′-monophosphate N-glycosidase, also known as RCL) (Fig. 1A), a c-Myc target that is overexpressed in various tumors (*18*, *19*). It has been suggested that DNPH1 is involved in nucleotide salvage pathways and acts as a sanitizer that removes modified or anomalous nucleotides from the nucleotide pool to prevent their incorporation into DNA (*20*). Disruption of a second nucleotide sanitizer, ITPA (inosine triphosphatase), which dephosphorylates deoxyinosine triphosphate to limit its incorporation into DNA (*21*), also sensitized *MUS81*$^{-/-}$ cells to olaparib. *DNPH1* and *ITPA*, which were also identified in previous PARPi screens (*8*, *22*), were validated as bona fide hits using individual CRISPR-generated knockout (KO) cell lines (fig. S2, A and B). Disruption of either gene in eHAP cells did not affect cell growth or viability but sensitized HR-deficient *MUS81*$^{-/-}$ cells to treatment with olaparib (Fig. 1B and fig. S2, C and D). These results indicate that the target nucleotides of DNPH1 and ITPA are a source of endogenous DNA lesions underlying PARPi cytotoxicity.

The marked olaparib sensitivity of the *MUS81*$^{-/-}$ *DNPH1*$^{-/-}$ cells, combined with the uncharacterized biological function of DNPH1, led us to focus on the role of this gene in potentiating the effect of PARPi on HR-deficient cells. DNPH1 was found to be expressed in various cell lines, including nontumorigenic epithelial cells (RPE-1 and MCF10A) and the breast tumor–derived *BRCA1*-deficient cancer cell line SUM149 (*BRCA1*^{mut}) (*23*) (fig. S2E). Genetic disruption of *DNPH1* in SUM149 *BRCA1*- or DLD1 *BRCA2*-defective cells (fig. S2, F and G), resulted in their sensitization to olaparib (Fig. 1, C to E, and fig. S2H). This effect was exclusive to PARPi, as little or no sensitization was observed

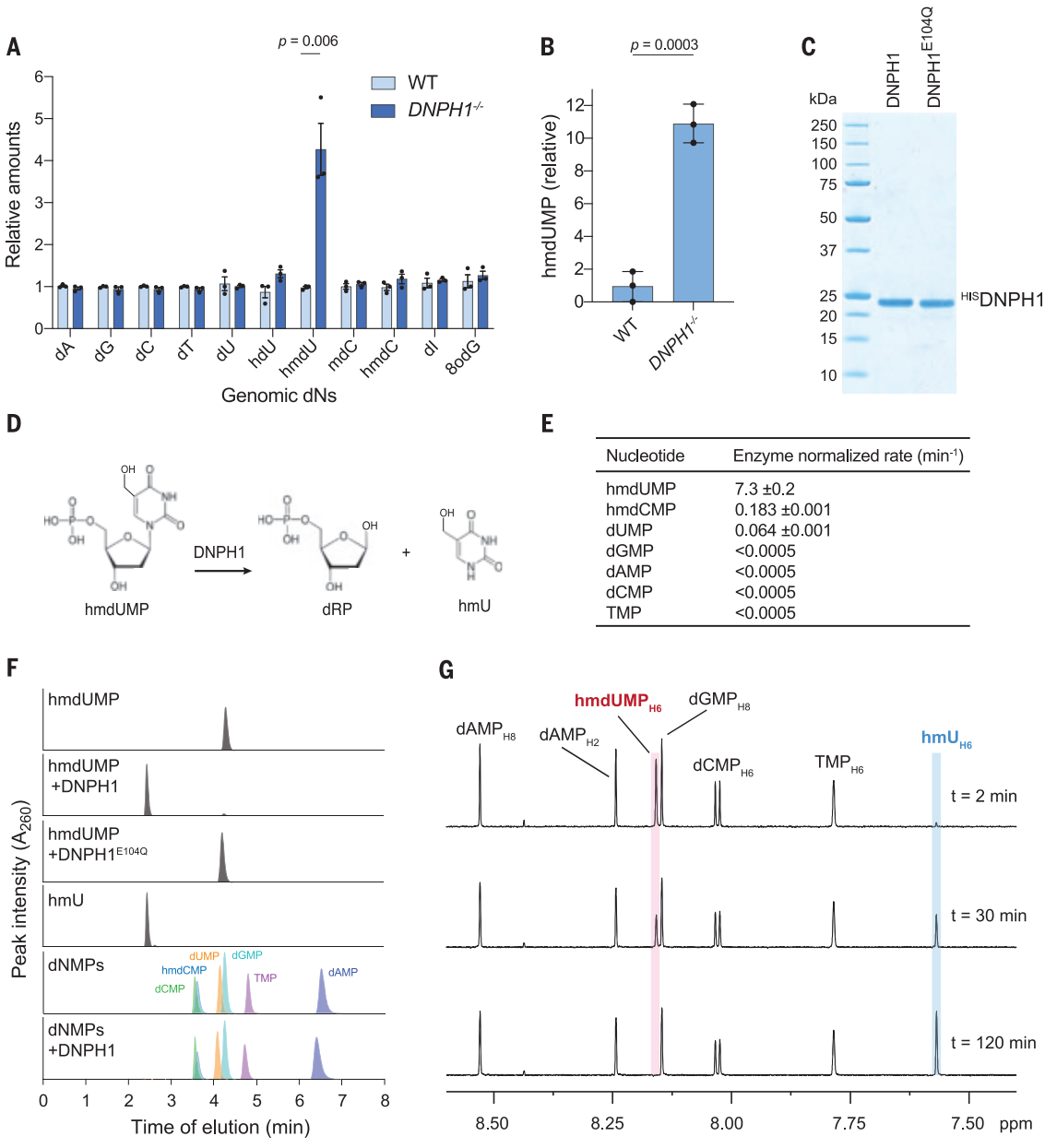

Fig. 2. DNPH1 is a nucleotide sanitizer that hydrolyzes hmdUMP to prevent genomic DNA incorporation. (**A**) Genomic DNA was extracted from eHAP WT or *DNPH1*$^{-/-}$ cells, digested, and analyzed for its nucleoside composition by liquid chromatography–mass spectrometry (LC-MS). The graph depicts the ratio of the indicated nucleosides in *DNPH1*$^{-/-}$ versus WT genomic DNA (mean with SEM; $n = 3$). (**B**) Nucleotide pools were extracted from eHAP WT or *DNPH1*$^{-/-}$ cells treated with 0.5 μM hmdU for 4 hours and analyzed for hmdUMP by LC-MS. (**C**) SDS-PAGE of purified HIS-tagged DNPH1 and catalytic site mutant DNPH1^{E104Q} visualized by InstantBlue stain. (**D**) Schematic indicating the hydrolysis of hmdUMP by DNPH1 to form dRP and hmU. (**E**) Rates of dNMP hydrolysis by DNPH1 were determined by linear regression of data from fig. S3E. Each dNMP was analyzed independently. (**F**) Analysis of DNPH1 activity with dNMPs. DNPH1 or DNPH1^{E104Q} (4 μM) was incubated individually with the indicated substrates (1 mM) for 45 min. Products were analyzed by reversed-phase high-performance liquid chromatography (RP-HPLC) and visualized as chromatograms. Untreated dNMPs and the nucleobase hmU are indicated. A_{260}, absorption at 260 nm. (**G**) ^{1}H NMR time-resolved spectroscopy of an equimolar mixture of dAMP, dCMP, dGMP, TMP, and hmdUMP (0.5 mM each) after incubation with 1 μM DNPH1 for the indicated times. Time-dependent disappearance of hmdUMP (red bar) and appearance of hmU are highlighted (blue bar). The resonances of nonlabile base protons from each nucleotide are shown. ppm, parts per million.

in *DNPH1*-deficient cells exposed to a variety of DNA damaging agents, including cisplatin, methyl methanesulfonate (MMS), camptothecin, ultraviolet, or ionizing irradiation (fig. S2, I to M). The *BRCA2*$^{-/-}$ *DNPH1*$^{-/-}$ cells exhibited a smaller colony size indicative of decreased growth rate (Fig. 1C). *BRCA2* WT and SUM149 isogenic revertant cells, in which the reading frame of *BRCA1* had reverted to WT (*23*), were insensitive to *DNPH1* loss and olaparib treatment. Together, these results show that *DNPH1* inactivation specifically sensitizes clinically relevant *BRCA*-deficient cells to PARPi treatment.

DNPH1 targets hmdUMP to limit genomic incorporation

DNPH1 hydrolyzes deoxyribonucleoside monophosphates (dNMPs) in vitro (*20*), but its biological nucleotide target(s) and function(s) remain unknown. To determine the precise target of DNPH1, we carried out metabolomic analyses of the nucleoside composition of genomic DNA in WT, *DNPH1*$^{-/-}$, and *ITPA*$^{-/-}$ cells. As expected, increased amounts of genomic deoxyinosine (dI) were found in the *ITPA*$^{-/-}$ cells (fig. S3A), validating our metabolomic approach. In the *DNPH1*$^{-/-}$ cells, however, we observed a specific increase of 5-hydroxymethyl-deoxyuridine (hmdU) in genomic DNA (Fig. 2A). hmdU is a cytotoxic nucleoside arising from either oxidative damage to thymidine (*24*) or deamination of 5-hydroxymethyl-deoxycytidine (hmdC) during epigenetic regulation (*25*). No significant change in other genomic nucleosides was observed (Fig. 2A). Quantification of genomic hmdU showed ~5 per million deoxyribonucleosides (dNs) in WT and ~15 per million in *DNPH1*$^{-/-}$ cells (fig. S3B). Because DNPH1 hydrolyzes dNMPs, these results suggest that DNPH1 acts on hmdU monophosphate (hmdUMP) in

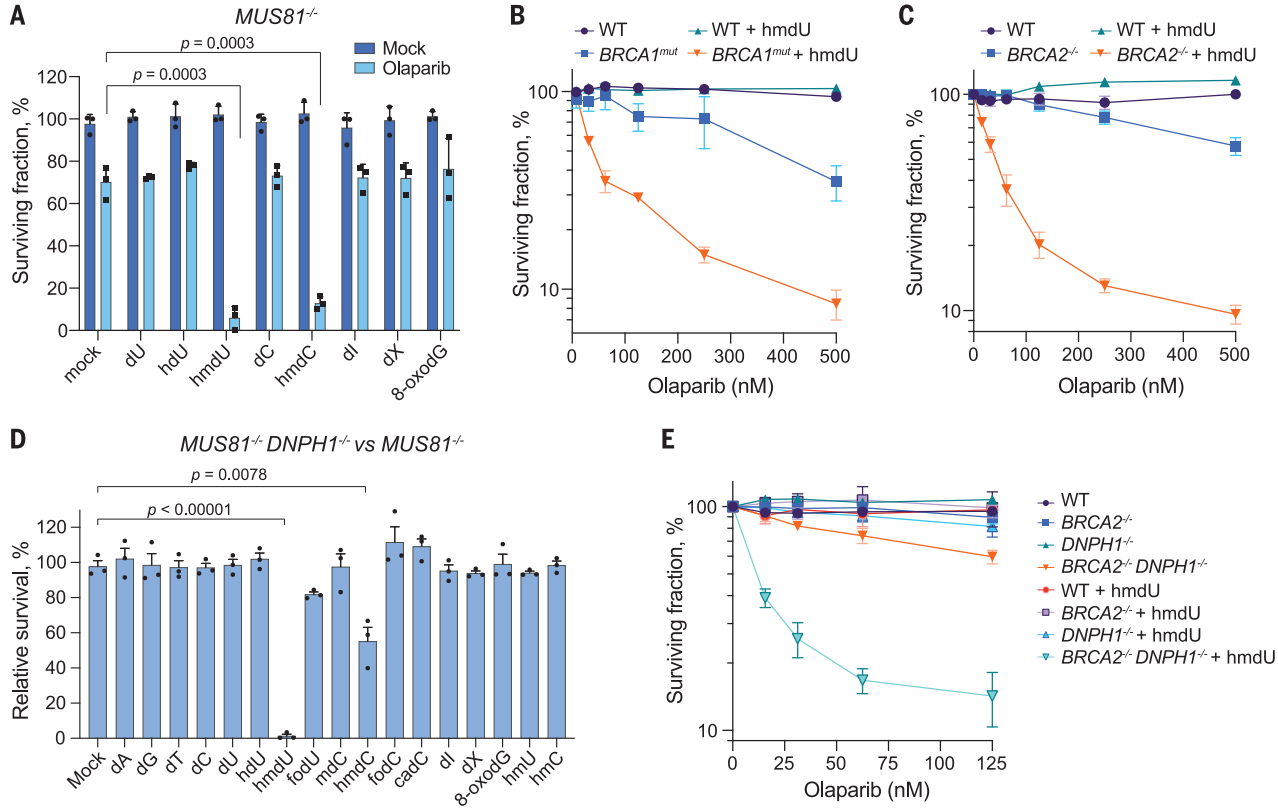

Fig. 3. Sensitization of HR-deficient cells to PARPi by hmdU. (**A**) eHAP *MUS81*$^{-/-}$ cells were either untreated or treated with the indicated nucleosides (200 nM) in the presence or absence of olaparib (25 nM) for 6 days. Cell viability was determined using CellTiter-Glo (mean with SEM; n = 3). (**B**) Patient-derived SUM149 *BRCA1*^{mut} (parental) and revertant (WT) cells were treated for 8 days with olaparib in the presence or absence of hmdU (1 μM). Cell viability was determined using CellTiter-Glo. *BRCA1*^{mut} versus *BRCA1*^{mut} + hmdU, P = 0.0004. (**C**) DLD1 WT and *BRCA2*$^{-/-}$ cells were treated for 10 days with olaparib in the presence or absence of hmdU (1 μM). Cell viability was determined as in (B). *BRCA2*$^{-/-}$ versus *BRCA2*$^{-/-}$ + hmdU, $P < 0.0001$. (**D**) eHAP *MUS81*$^{-/-}$ and *MUS81*$^{-/-}$ *DNPH1*$^{-/-}$ cells were either left untreated or treated with the indicated nucleosides (200 nM) for 6 days. Cell viability was determined as in (A). Bar chart shows the ratio of cell viability between *MUS81*$^{-/-}$ *DNPH1*$^{-/-}$ and *MUS81*$^{-/-}$ (mean with SEM; n = 3). (**E**) DLD1 WT or KO cell lines were treated for 10 days with olaparib in the absence or presence of hmdU (50 nM). Cell viability was determined as in (B). *BRCA2*$^{-/-}$ *DNPH1*$^{-/-}$ versus *BRCA2*$^{-/-}$ *DNPH1*$^{-/-}$ + hmdU, $P < 0.0001$. DLD1 WT and *BRCA2*$^{-/-}$ cells treated with olaparib only are from (C).

the nucleotide pool to limit genomic DNA incorporation. Upon analysis of the nucleotide pool, we observed an ~10-fold increase in hmdUMP in *DNPH1*$^{-/-}$ cells treated with hmdU as compared with WT cells (Fig. 2B). However, we only observed an approximately threefold increase in genomic hmdU compared with WT (fig. S3C). These results show that DNPH1 acts on hmdUMP to limit its incorporation into DNA.

To determine whether DNPH1 directly hydrolyzes hmdUMP, we purified recombinant human DNPH1 as well as the active-site mutant DNPH1^{E104Q} (E104Q, Glu^{104}→Gln) (Fig. 2C). DNPH1, but not DNPH1^{E104Q}, efficiently hydrolyzed hmdUMP to yield hydroxymethyl uracil (hmU) nucleobase (shown schematically in Fig. 2D) with a reaction rate of 7.3 ± 0.2 min^{-1} (Fig. 2E and fig. S3, D and E). No detectable activity was observed toward any of the canonical dNMPs (Fig. 2F). The related nucleotides hydroxymethyl deoxycytidine monophosphate (hmdCMP) and deoxyuridine monophosphate (dUMP) were hydrolyzed ~40 and ~110 times slower, respectively (Fig. 2E). To strengthen these findings and directly assess the dNMP preference of DNPH1, we used time-resolved proton nuclear magnetic resonance (^{1}H NMR) spectroscopy for the simultaneous detection of dNMP hydrolysis, in a mixture that combined hmdUMP with canonical dNMPs in a single reaction. We found that under these conditions, while hmdUMP was fully hydrolyzed after 120 min, there was no detectable hydrolysis of any of the canonical dNMPs (Fig. 2G and fig. S3, F and G). These results confirm that hmdUMP is the direct biological target of DNPH1.

hmdU hypersensitizes HR-deficient cells to PARPi

To determine whether the observed increase in genomic hmdU in *DNPH1*-deficient cells was responsible for the sensitization of HR-deficient cells to PARPi, *MUS81*$^{-/-}$ cells were treated with a panel of deoxynucleosides carrying nucleobases modified by methylation, hydroxylation, deamination, and oxidation, in the presence or absence of olaparib. Cotreatment with hmdU and olaparib induced strong synthetic lethality (Fig. 3A), showing that hmdU potentiates PARPi treatment. hmdU/PARPi cotreatment also induced synthetic lethality in the SUM149 *BRCA1* mutant cell line (Fig. 3B and fig. S4, A and B) as well as in DLD1 *BRCA2*-defective cells (Fig. 3C and fig. S4C). In contrast, *BRCA*-proficient isogenic cell lines were insensitive to the treatment (Fig. 3, B and C, and fig. S4, A to C).

We also observed that hmdC induced synthetic lethality with PARPi (Fig. 3A). To determine whether PARPi potentiation by hmdC was caused by increased hmdU incorporation, we analyzed the genomic nucleotide composition of hmdC-treated cells and found increased amounts of genomic hmdU (fig. S4D). hmdU was further increased in *DNPH1*$^{-/-}$ cells, indicating that hmdC is converted to hmdU in the nucleotide pool, where it is targeted by DNPH1. We did not observe any increase in genomic hmdC, in agreement with previous reports (*26*). Comparison of genomic hmdU incorporation after exposure of WT cells to hmdU (fig. S3C) or hmdC nucleosides (fig. S4D) revealed that hmdC treatment resulted in ~1/15 the

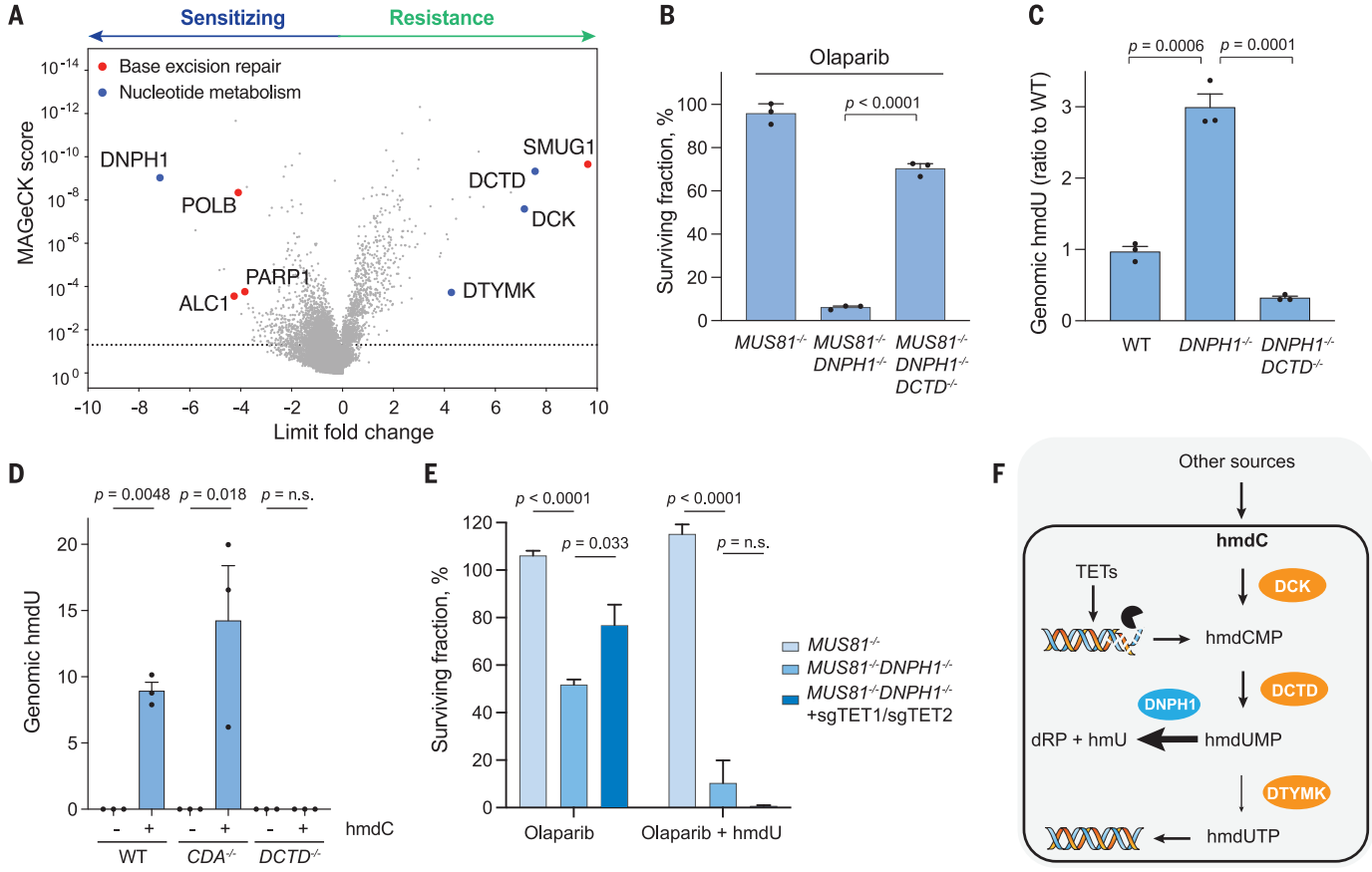

Fig. 4. hmdU is produced by metabolism of epigenetically modified nucleotides. (**A**) Volcano plot showing sgRNA scores from MAGeCK analysis of CRISPR-Cas9 hmdC dropout/enrichment screen. Data are represented as in Fig. 1A (n = 3). (**B**) eHAP KO cell lines were continuously treated with olaparib (50 nM) for 6 days, and cell viabilities were determined using CellTiter-Glo. (**C**) Genomic DNA was extracted from the indicated eHAP cell lines, digested, and analyzed for hmdU by LC-MS. The ratio of hmdU levels to WT is indicated (mean with SEM; n = 3). (**D**) eHAP cell lines were treated with hmdC (0.2 μM) for 24 hours. Genomic DNA was extracted, digested, and analyzed for hmdU by LC-MS. The relative genomic hmdU levels are indicated (mean with SEM; n = 3). (**E**) eHAP *MUS81*$^{-/-}$, *MUS81*$^{-/-}$ *DNPH1*$^{-/-}$, or *MUS81*$^{-/-}$ *DNPH1*$^{-/-}$ cells transduced with lentiCRISPR-sgTET1 and sgTET2 were treated with olaparib (25 nM) in the absence or presence of hmdU (50 nM) for 6 days. Cell viability was determined as in (B). (**F**) Schematic showing the metabolism of hmdC originating from TET-mediated hydroxymethylated cytosine and other extracellular sources. Breakdown of DNA (for example, during DNA repair) releases epigenetically marked nucleotides, such as hmdCMP. To prevent their reincorporation, they are degraded in a two-step process: (i) hmdCMP is deaminated to cytotoxic hmdUMP by DCTD, and (ii) DNPH1 hydrolyzes hmdUMP into hmU and dRP. DNPH1 deficiency leads to excess hmdUMP that becomes phosphorylated to hmdUTP by DTYMK and incorporated into DNA.

amount of hmdU incorporation, in accord with its lower cytotoxicity (Fig. 3, A and D).

To explore the biological function of DNPH1 in response to aberrant nucleotides, *DNPH1*$^{-/-}$ cells were exposed to a panel of ribonucleosides and deoxyribonucleosides, and cell viability was measured. Notably, HR-deficient *MUS81*$^{-/-}$ *DNPH1*$^{-/-}$ double KOs were hypersensitive to treatment with hmdU and, to a lesser extent, hmdC (Fig. 3D), even in the absence of PARPi. Treatment with their ribonucleoside counterparts hmU (hydroxymethyl uridine) or hmC (hydroxymethyl cytosine) did not affect cell viability (Fig. 3D), demonstrating that the cytotoxic effect requires DNA incorporation. Complementation with WT DNPH1, but not the active site mutant DNPH1^{E104A} (*20*), rescued DNPH1-deficient cells from hmdU-induced cytotoxicity (fig. S4, E and F).

Because HR-deficient *DNPH1*$^{-/-}$ cells are sensitive to hmdU treatment, we speculated that hmdU treatment could hypersensitize these cells to PARPi and found that *BRCA2*$^{-/-}$ *DNPH1*$^{-/-}$ cells were particularly sensitive to PARPi when cotreated with a low dose of hmdU (50 nM). Indeed, approximately one-tenth the amount of PARPi was required to achieve the same level of killing (Fig. 3E). Our results show that synthetic lethality can be induced in a variety of HR-deficient backgrounds and that DNPH1 and its target hmdU may have therapeutic potential.

The cellular origins of hmdU

Nucleotide salvage pathways provide an energy-efficient way to recycle deoxyribonucleosides that arise from the breakdown of DNA or extracellular uptake. Cytidine nucleotides carrying epigenetic marks such as hmdC are thought to be deaminated to produce the uridine counterpart hmdU (*26*). To determine whether hmdU arises from hmdC deamination and to identify factors involved in this pathway, we carried out a CRISPR screen in *MUS81*$^{-/-}$ cells exposed to hmdC. Bioinformatic analysis revealed that the loss of factors involved in nucleoside phosphorylation such as deoxycytidine kinase (DCK) and thymidylate kinase (DTYMK) rendered cells resistant to hmdC treatment (Fig. 4A). The screen also showed that loss of *DNPH1* sensitized cells to hmdC, confirming the critical role that DNPH1 plays in the survival of HR-deficient cells by eliminating hmdUMP.

The loss of the gene encoding dCMP deaminase, DCTD, rendered eHAP cells resistant to hmdC (Fig. 4A), indicating that DCTD

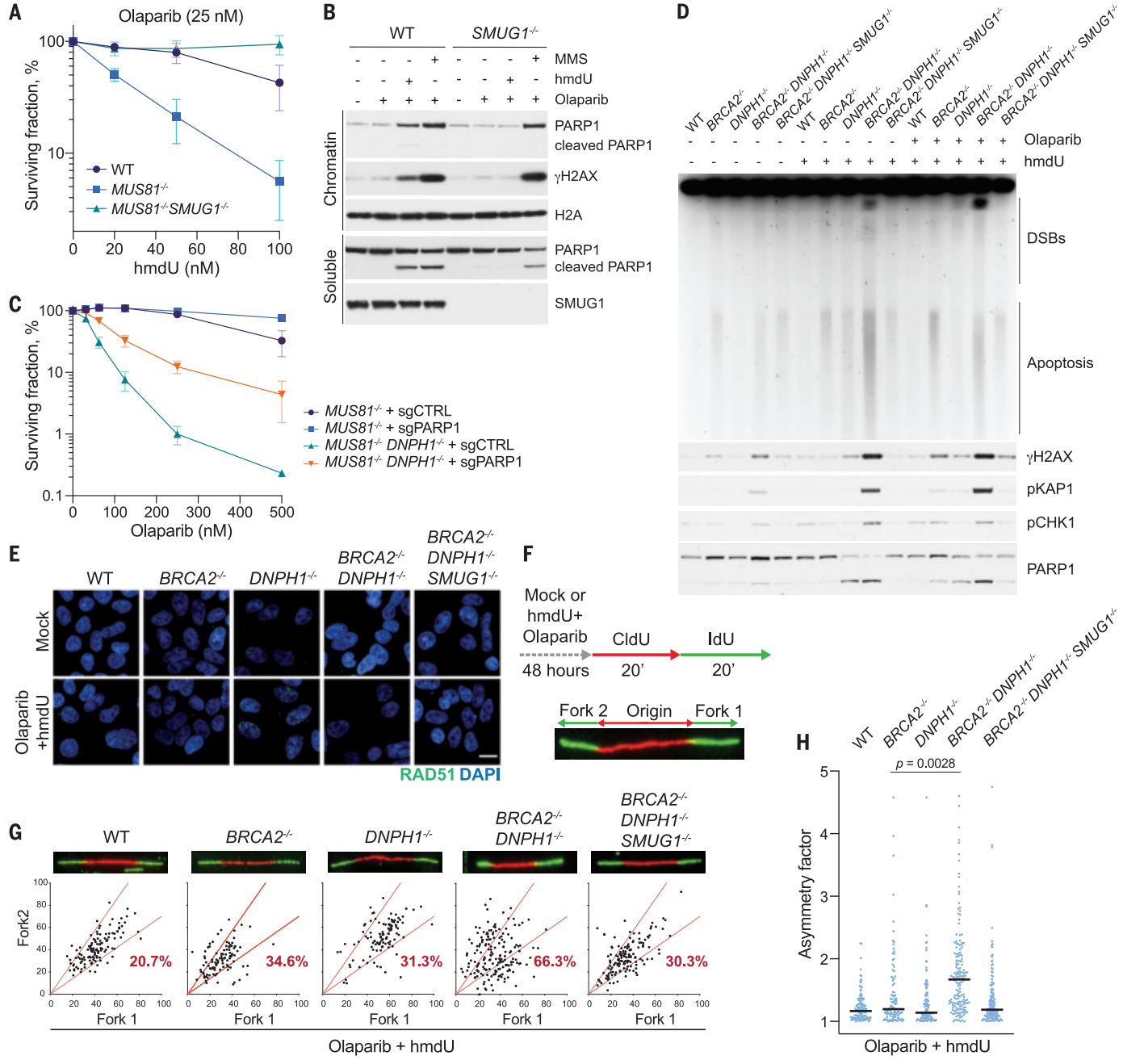

Fig. 5. hmdU promotes PARP trapping, DSB formation, and cell death through the actions of SMUG1. (**A**) eHAP WT and KO cell lines were treated with olaparib (25 nM) and the indicated doses of hmdU for 6 days. Cell viability was determined using CellTiter-Glo (n = 3). *MUS81*$^{-/-}$ versus *MUS81*$^{-/-}$ *SMUG1*$^{-/-}$, P = 0.0014. (**B**) eHAP WT and *SMUG1*$^{-/-}$ cells were either untreated or pretreated for 24 hours with hmdU (0.35 μM) or 2 hours with MMS (0.01%) followed by olaparib (10 μM) for 4 hours. After subcellular fractionation, the nuclear soluble or chromatin fractions were analyzed by immunoblotting with the indicated antibodies. (**C**) eHAP *MUS81*$^{-/-}$ or *MUS81*$^{-/-}$ *DNPH1*$^{-/-}$ cells were transduced with lentiCRISPR-sgPARP1 or control (sgCTRL) and treated with olaparib for 6 days. Cell viability was determined as in (A). *MUS81*$^{-/-}$ *DNPH1*$^{-/-}$/sgCTRL versus *MUS81*$^{-/-}$ *DNPH1*$^{-/-}$/sgPARP1, P < 0.0001. (**D**) (Top) PFGE analysis of DNA break formation in DLD1 WT or KO cell lines either untreated or treated with hmdU (2 μM) or cotreated with olaparib (0.1 μM) and hmdU (100 nM) for 72 hours. DNA breaks were visualized by ethidium bromide staining. (Bottom) The same samples were analyzed by immunoblotting. (**E**) DLD1 WT and KO cell lines were either untreated or treated with olaparib (10 nM) and hmdU (0.1 μM) for 48 hours and subjected to immunofluorescence staining with a RAD51 antibody (green). DNA was stained by 4′,6-diamidino-2-phenylindole (DAPI; blue). Scale bar, 10 μm. (**F**) Schematic overview of DNA fiber analysis. DLD1 WT or KO cells were untreated or cotreated with olaparib and hmdU for 48 hours. Cells were labeled with 5-chloro-2′-deoxyuridine (CldU) (20 min; 20 μM) followed by iododeoxyuridine (IdU) (20 min; 150 μM). DNA fibers were spread on glass slides and subjected to immunofluorescence staining with CldU (red) and IdU (green) antibodies. Fork symmetry was assessed by measuring the lengths of the two bidirectional forks. (**G**) Plots showing the lengths of the bidirectional forks in DLD1 cell lines treated with olaparib (0.1 μM) and hmdU (1 μM) for 48 hours. Bidirectional forks with >30% difference in lengths (outside red lines) were scored as asymmetrical and shown as a percentage. (**H**) Plots showing the asymmetry factor from forks in (G). Horizontal line represents the median. *BRCA2*$^{-/-}$ versus *BRCA2*$^{-/-}$ *DNPH1*$^{-/-}$, P = 0.0028.

deaminates hmdCMP to produce hmdUMP in the nucleotide pool. Loss of *DCTD* also conferred resistance to olaparib (Fig. 1A), presumably as a consequence of decreased genomic hmdU incorporation. To test this possibility, we generated *DCTD*$^{-/-}$ cell lines in the *MUS81*-deficient cells (fig. S4G) and found that they were resistant to cotreatment with olaparib and hmdC but not cotreatment with olaparib and hmdU (fig. S4H). The increased sensitization of *MUS81*$^{-/-}$ cells to olaparib upon *DNPH1* ablation was reversed by codisruption of *DCTD* (Fig. 4B), showing that the synthetic lethality results from DCTD-mediated formation of hmdUMP. Consistent with these results, the increase in genomic hmdU observed in *DNPH1*$^{-/-}$ cells was also reversed by disruption of *DCTD* (Fig. 4C).

Because cytidine deaminase (CDA) targets dNs and DCTD targets dNMPs, we next determined whether the deamination of hmdC to hmdU occurs at the nucleoside or nucleoside monophosphate level. To do this, we generated *CDA*$^{-/-}$ and *DCTD*$^{-/-}$ cell lines (fig. S4I). We found that loss of *DCTD*, but not *CDA*, completely abolished hmdC-mediated deamination and hmdU incorporation (Fig. 4D), showing that hmdCMP deamination in eHAP cells occurs at the dNMP level, similar to hmdUMP hydrolysis by DNPH1.

During epigenetic regulation, genomic hmdC is produced by dioxygenase-mediated hydroxylation of methylated cytosine by the ten-eleven translocation (TET) enzymes (*27*). To determine whether breakdown and subsequent deamination of hmdC-containing genomic DNA were responsible for the increased sensitivity of *DNPH1*-deficient cells to PARPi, cells were depleted of *TET1* and *TET2* using CRISPR-Cas9 (fig. S4J). Loss of TET1 and TET2 partially reversed PARPi sensitivity in *MUS81*$^{-/-}$ *DNPH1*$^{-/-}$ cells (Fig. 4E). Furthermore, the *TET1* and *TET2* depleted cells were sensitive to hmdU/olaparib cotreatment (Fig. 4E), indicating that the observed rescue was not due to a general resistance of TET-deficient cells to the cytotoxic effects of hmdU. Moreover, these data support the hypothesis that hmdUMP, produced by DCTD-dependent deamination of hmdCMP, is the biological target of DNPH1, thereby constituting a metabolic pathway that disposes of epigenetically modified nucleotides (shown schematically in Fig. 4F).

SMUG1 mediates synthetic lethality through PARP trapping

Our screens further revealed that loss of single-strand selective monofunctional uracil DNA glycosylase 1 (SMUG1) caused resistance to olaparib or hmdC treatment in HR-defective cells (Figs. 1A and 4A). Because SMUG1 is the primary glycosylase responsible for removing hmdU from genomic DNA (*28*), we speculated that the action of SMUG1 on hmdU drives synthetic lethality. To test this, we generated *SMUG1*$^{-/-}$ cells (fig. S5A) and found that while *MUS81*$^{-/-}$ cells were hypersensitive to hmdU/olaparib cotreatment, *MUS81*$^{-/-}$ *SMUG1*$^{-/-}$ cells were completely resistant (Fig. 5A). Similar observations were made in DLD1 *BRCA2*-deficient cells after *SMUG1* disruption (fig. S5B). Furthermore, the increased PARPi sensitivity observed in *DNPH1*$^{-/-}$ *BRCA2*$^{-/-}$ cells was reversed by loss of *SMUG1* (fig. S5C). Complementation of the *MUS81*$^{-/-}$ *SMUG1*$^{-/-}$ cells with WT SMUG1, but not catalytically inactive SMUG1^{G87Y}, restored cell death upon hmdU/olaparib cotreatment (fig. S5, D and E). Together, these results show that SMUG1-dependent excision of genomic hmdU is the underlying basis for the synthetic lethality.

PARPi-induced synthetic lethality is caused, at least in part, by PARP trapping, whereby PARP proteins are trapped on various DNA structures, including single-strand breaks (SSBs) and BER intermediates (*7*). Consequently, and also as confirmed by our screen (Fig. 1A), loss of PARP1 causes PARPi resistance by alleviating the dominant-negative effect of PARP trapping (*7*, *13*). We therefore analyzed PARP trapping in cells exposed to hmdU and olaparib and found increased chromatin association of PARP1 in comparison with olaparib treatment alone (Fig. 5B). Additionally, we observed the induction of DNA damage checkpoint signaling (γH2AX phosphorylation) and apoptosis (PARP1 cleavage). Ablation of *SMUG1* fully reversed these hmdU/olaparib-induced phenotypes (Fig. 5B), showing that PARP trapping occurs on BER intermediates that arise from SMUG1-mediated hmdU excision. In contrast, we did not observe any difference in PARP trapping or DNA damage signaling between WT and *SMUG1*-deficient cells treated with the alkylating agent MMS (Fig. 5B), confirming that the lack of PARP trapping in *SMUG1*-deficient cells was not due to a general BER defect. Consistent with the hypothesis that PARP trapping was responsible for increased cell killing in *DNPH1*-defective cells after PARPi, we found that olaparib sensitivity in *DNPH1*$^{-/-}$ cells was PARP1-dependent (Fig. 5C and fig. S5F). Similar results were observed with other PARPi such as veliparib (fig. S5G) and talazoparib (fig. S5H). These results show that PARP trapping occurs in a hmdU- and SMUG1-dependent manner after PARPi treatment.

To understand the hmdU/SMUG1-induced mechanism of cell death, DNA DSB formation and DNA damage checkpoint signaling were analyzed in DLD1 isogenic cell line models. Untreated *BRCA2*$^{-/-}$ *DNPH1*$^{-/-}$ cells showed an increase in checkpoint signaling and replication stress, as evidenced by immunoblotting of phosphorylated H2A histone family member X (γH2AX), phosphorylated KRAB-associated protein-1 (pKAP1), or checkpoint kinase 1 (pCHK1), and PARP1 cleavage (apoptosis) (Fig. 5D and fig. S5I). In addition, low amounts of small molecular weight DNA were observed as smears by pulsed-field gel electrophoresis (PFGE), indicative of apoptosis (Fig. 5D). Taken together with the slight growth defect observed in *BRCA2*$^{-/-}$ *DNPH1*$^{-/-}$, as compared with *BRCA2*$^{-/-}$ cells (Fig. 1C), these results indicate that DNPH1 loss causes endogenous DNA damage because of replication stress.

After exposure to hmdU or hmdU and olaparib, but not olaparib alone, we observed a large increase in DSB formation; increased amounts of γH2AX, pKAP1, and pCHK1; and PARP1 cleavage in the *BRCA2*$^{-/-}$ *DNPH1*$^{-/-}$ cells (Fig. 5D and figs. S5J and S6, A and B). Upon cotreatment with a caspase inhibitor (Z-VAD-FMK), we observed increased DSB formation and a reduction in the low molecular weight smears (fig. S6C), consistent with apoptosis occurring from elevated DSB formation in *BRCA2*$^{-/-}$ *DNPH1*$^{-/-}$ cells. All phenotypes were reversed by disruption of *SMUG1*, demonstrating that SMUG1-induced DSB formation is the underlying cause of PARPi-induced synthetic lethality brought about by PARP trapping at sites of hmdU excision.

Excision of aberrant bases by DNA glycosylases leads to the formation of abasic sites that interfere with replication fork progression (*29*). We therefore explored the possibility that synthetic lethality results from replication fork collapse at hmdU-induced abasic sites. We found that hmdU/olaparib treatment of the *DNPH1*$^{-/-}$ cells led to increased RAD51 foci, which were suppressed by loss of *BRCA2* (Fig. 5E and fig. S6D), indicative of HR-mediated DSB repair. We next analyzed replication fork progression by measuring the symmetry of bidirectional forks (Fig. 5F). Whereas forks from untreated cell lines were largely indistinguishable from each other (fig. S6, E and F), an increase in asymmetric forks was observed in *BRCA2*$^{-/-}$ *DNPH1*$^{-/-}$ cells upon hmdU/olaparib treatment, as compared with *BRCA2*$^{-/-}$ cells (Fig. 5, G and H). These results indicate that the observed DSBs are a consequence of replication fork collapse. Consistent with this, fork asymmetry induced by hmdU/olaparib was suppressed by loss of SMUG1.

Killing of PARPi-resistant *BRCA1*-deficient cells

PARPi resistance arises by (i) reversion of the *BRCA* genes to WT (*9*), (ii) loss or mutation of *PARP1* (*7*, *13*) or *PARG* (*14*), or (iii) in the case of *BRCA1*-deficient cells, restoration of HR-proficiency through inactivation of the p53-binding protein 1 (53BP1)–SHIELDIN pathway (*9*, *30*). We have shown that *BRCA*-deficient cells can be efficiently killed by either potentiating PARPi by hmdU or in a PARPi-independent manner by hmdU treatment upon *DNPH1* ablation. To determine whether these treatment strategies resensitize PARPi-resistant *BRCA1*-deficient cells, we compared their effects in *BRCA1* mutant, WT SUM149,

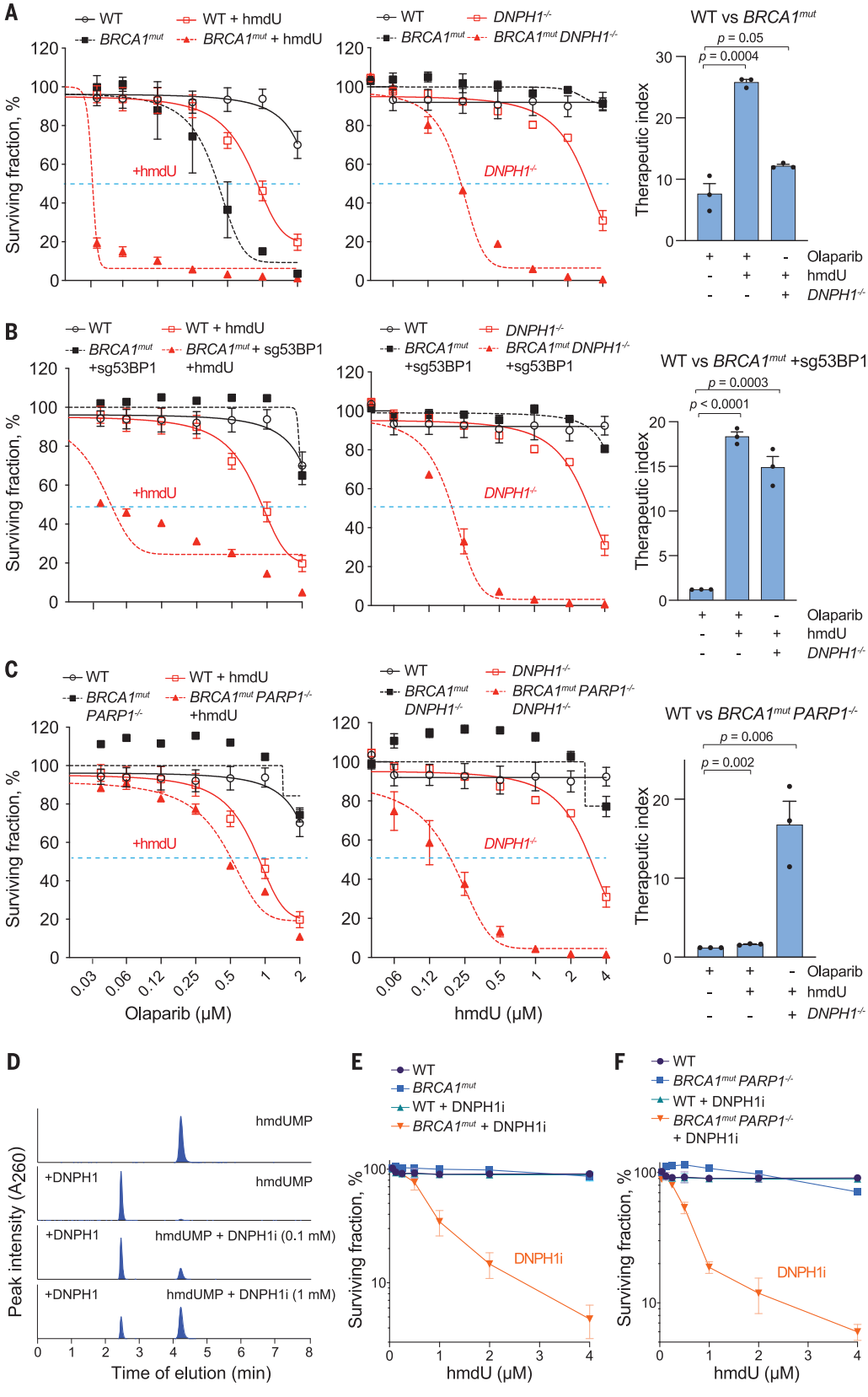

Fig. 6. Killing of PARPi-resistant *BRCA1* cells by targeting DNPH1. (**A**) Left panel: SUM149 *BRCA1*^{mut} (parental) and WT (revertant) cell lines were either untreated or treated with olaparib in the absence (black lines) or presence of hmdU (2 μM; red lines) for 8 days. Cell viability was determined using CellTiter-Glo (mean with SEM; $n = 3$). Blue dotted line represents median effective concentration (EC_{50}). Center panel: As in left panel, but SUM149 *BRCA1*^{mut} (parental) and WT cell lines were either untreated or treated with the indicated doses of hmdU in the absence (black lines) or presence of *DNPH1* KO (red lines) for 8 days. Right panel: Therapeutic index of the indicated treatments calculated from the ratio of EC_{50} values from left and center in SUM149 WT versus *BRCA1*^{mut} cells. (**B**) Left: SUM149 *BRCA1*^{mut}/sg53BP1 or WT (revertant) cell lines were treated as in left panel of (A). For direct comparison, curves of WT and WT + hmdU from left panel of (A) are shown (solid black and red lines, respectively). Center: SUM149 *BRCA1*^{mut}/sg53BP1 or WT cell lines were treated as in center panel of (A). For direct comparison, curves of WT and *DNPH1*$^{-/-}$ from center panel of (A) are shown (solid black and red lines, respectively). Right: Therapeutic index of the indicated treatments calculated from the ratio of EC_{50} values from left and center in SUM149 *BRCA1*^{mut}/sg53BP1 cells. (**C**) Left: SUM149 *BRCA1*^{mut} *PARP1*$^{-/-}$ or WT cell lines were treated as in left panel of (A). For direct comparison, curves of WT and WT + hmdU from left panel of (A) are shown (solid black and red lines, respectively). Center: SUM149 *BRCA1*^{mut} *PARP1*$^{-/-}$ or WT cell lines were treated as in center panel of (A). For direct comparison, curves of WT and *DNPH1*$^{-/-}$ from center panel of (A) are shown (solid black and red lines, respectively). Right: Therapeutic index of the indicated treatments calculated from the ratio of EC_{50} values from left and center in *BRCA1*^{mut} *PARP1*$^{-/-}$ cells. (**D**) Inhibition of DNPH1 activity toward hmdUMP by DNPH1i. DNPH1 (4 μM) was incubated with hmdUMP (1 mM) in the absence or presence of DNPH1i for 45 min. Products were analyzed by RP-HPLC and visualized as chromatograms. (**E**) SUM149 *BRCA1*^{mut} (parental) and WT (revertant) cell lines were either untreated or treated with hmdU in the absence or presence of DNPH1i (0.3 μM) for 8 days. Viability was determined using CellTiter-Glo (mean with SEM; $n = 3$). *BRCA1*^{mut} versus *BRCA1*^{mut} + DNPH1i, $P < 0.0001$. (**F**) SUM149 *BRCA1*^{mut} *PARP1*$^{-/-}$ or WT (revertant) cell lines were treated as in (E) (mean with SEM; $n = 3$). *BRCA1*^{mut} *PARP1*$^{-/-}$ versus *BRCA1*^{mut} *PARP1*$^{-/-}$ + DNPH1i, $P < 0.0001$.

or PARPi-resistant cell lines depleted of 53BP1, SHLD1, or PARP1 using lentiCRISPR (fig. S7, A and B). Compared with olaparib alone, we found that cotreatment with hmdU and olaparib led to about a threefold expansion of the therapeutic window (Fig. 6A, left and right panels). hmdU treatment efficiently resensitized PARPi-resistant *BRCA1*^{mut} cells depleted of *53BP1*, *SHLD1* (Fig. 6B and fig. S7C, left and right panels), and to a lesser extent *PARP1* (Fig. 6C, left and right panels), to olaparib treatment.

While ablation of *DNPH1* in *BRCA1*-deficient cells or treatment with hmdU alone had only mild effects on cell viability, hmdU selectively killed the *BRCA1*^{mut} *DNPH1*$^{-/-}$ cells (Fig. 6A, center and right panels). PARPi-resistant *BRCA1*^{mut} *DNPH1*$^{-/-}$ cell lines depleted of *53BP1* (Fig. 6B, center panel), *SHLD1* (fig. S7C, center panel), or *PARP1 (*Fig. 6C, center panel) were efficiently killed by hmdU treatment. The therapeutic windows increased ~10- to 20-fold compared with olaparib alone (Fig. 6, B and C, right panels, and fig. S7C, right panel). There was no significant effect on the sensitivity of HR-proficient *DNPH1*$^{-/-}$ cells depleted of *53BP1* or *PARP1* to olaparib or hmdU treatment compared with *DNPH1*$^{-/-}$ cells (fig. S7, D and E), indicating that 53BP1 or PARP1 alone were not required for the repair of DSBs resulting from hmdU lesions.

To determine whether chemical inhibition of DNPH1 could also sensitize cells to hmdU, we used the DNPH1 competitive inhibitor N^6-benzyladenosine (DNPH1i) (*31*), which limits the activity of DNPH1 in vitro (Fig. 6D). Whereas treatment of *MUS81*-deficient cells with DNPH1i or hmdU alone had a mild effect on cell viability, cotreatment with hmdU/DNPH1i selectively killed the HR-deficient cells (fig. S7F). This concentration of DNPH1i did not further sensitize *MUS81*$^{-/-}$ *DNPH1*$^{-/-}$ cells to hmdU, confirming its specificity (fig. S7G). Similarly, hmdU/DNPH1i treatment killed *BRCA1*-defective cells (Fig. 6E), as well as PARPi-resistant *BRCA1*-mutant cell lines depleted of *PARP1* (Fig. 6F) or *53BP1* (fig. S7H). These results provide proof of concept that DNPH1 inhibition can be used to sensitize *BRCA*-deficient cells to PARPi or hmdU treatment. DNPH1i treatment did not decrease the viability of *BRCA1*^{mut} *DNPH1*$^{-/-}$ cells treated with hmdU, demonstrating on-target effects of the drug (fig. S7I).

Discussion

Rapidly proliferating cancer cells are dependent on a steady supply of nucleotides, which is achieved by de novo synthesis and salvage pathways that are up-regulated in many cancers. However, the reincorporation of recycled nucleotides carrying epigenetic marks is undesirable owing to their potential to alter gene expression, and they are therefore excluded from DNA incorporation by the selectivity of nucleotide kinases (*26*). How cells deal with these modified nucleotides is largely unknown. Here we define a metabolic pathway whereby cells eliminate epigenetically modified hmdCMP in a two-step process entailing deamination to cytotoxic hmdUMP by DCTD, followed by DNPH1-mediated hydrolysis into hmU and deoxyribose phosphate (dRP) (Fig. 4F). Our results indicate that hmdCMP originates in part from the breakdown of TET hydroxymethylated DNA. Indeed, exonucleolytic processing that occurs during DNA repair yields nucleoside monophosphates such as hmdCMP, which is the level at which both DCTD and DNPH1 operate, thereby constituting a linear pathway for disposal of hmdCMP. In addition to DNA metabolism, other sources of salvaged nucleotides include extracellular uptake, which is also targeted by the DCTD/DNPH1 pathway to dispose of exogenous hmdU and hmdC nucleosides.

Although we found that genomic hmdU in our cell models predominantly arises through deamination of hmdCMP by DCTD rather than CDA, it is likely that the increased formation of hmdU observed in breast and pancreatic cancer cells with high levels of CDA (*26*) might result from a gain-of-function activity. Furthermore, high DCTD expression has been shown to correlate with poor prognosis in patients with malignant glioma (*32*). We therefore speculate that cancers with high levels of hmdC and/or expression of CDA or DCTD may depend on DNPH1 for survival, because of increased levels of cytotoxic hmdUMP. As *DNPH1* is a c-Myc targeted gene, its expression is directly linked to activation of the nucleotide salvage pathway (*33*) and as such could help cancer cells cope with increased nucleotide metabolism and hmdUMP levels.

Our work demonstrates that the underlying mechanism of PARPi-induced synthetic lethality of HR-deficient cells after exposure to hmdU is widespread replication fork collapse, DSB formation, and apoptotic cell death (fig. S8). These events are dependent on SMUG1-mediated PARP trapping. In addition to DNPH1 ablation, we found that loss of ITPA also sensitized cells to PARPi, presumably through increased genomic dI, suggesting that other types of aberrant nucleotides might also lead to PARP trapping and contribute to synthetic lethality. In addition to PARP trapping at BER intermediates (*7*, *8*), several hypotheses have been proposed as causes of synthetic lethality, such as excessive fork speed (*34*), persistent single-strand breaks at unligated Okazaki fragments (*35*), and/or the formation of replication-associated single-stranded DNA gaps (*36*). Our present work does not exclude these possibilities as intermediary steps during replication fork collapse.

We have shown that hmdU is an endogenous DNA lesion that potentiates the response to PARPi therapy. Furthermore, we discovered that PARPi-resistant *BRCA1*-defective cells with loss of either PARP1 or the 53BP1-SHIELDIN pathway were effectively killed by hmdU (by genetic or chemical ablation of DNPH1) to a similar extent as the nonresistant *BRCA1*-defective cells. As loss of the 53BP1-SHIELDIN pathway restores HR proficiency through reactivation of DNA end resection (*30*, *37*), our data indicate that BRCA1's role in mediating replication fork protection, rather than HR, is a key event in safeguarding against hmdU/DNPH1i-induced cell death (*38*, *39*). The distinctive effect of DNPH1 inhibition on the sensitization of *BRCA*-deficient cancer cells to PARPi and hmdU treatment indicates that DNPH1 should be investigated as a potential druggable target.

REFERENCES AND NOTES

1. M. E. Moynahan, J. W. Chiu, B. H. Koller, M. Jasin, *Mol. Cell* **4**, 511–518 (1999).
2. M. E. Moynahan, A. J. Pierce, M. Jasin, *Mol. Cell* **7**, 263–272 (2001).
3. I. P. Ewald *et al*., *Genet. Mol. Biol.* **32**, 437–446 (2009).
4. H. E. Bryant *et al*., *Nature* **434**, 913–917 (2005).
5. H. Farmer *et al*., *Nature* **434**, 917–921 (2005).
6. Y. Pommier, M. J. O'Connor, J. de Bono, *Sci. Transl. Med.* **8**, 362ps17 (2016).
7. J. Murai *et al*., *Cancer Res.* **72**, 5588–5599 (2012).
8. M. Zimmermann *et al*., *Nature* **559**, 285–289 (2018).
9. S. M. Noordermeer, H. van Attikum, *Trends Cell Biol.* **29**, 820–834 (2019).
10. H. D. M. Wyatt, S. Sarbajna, J. Matos, S. C. West, *Mol. Cell* **52**, 234–247 (2013).
11. F. A. Ran *et al*., *Nat. Protoc.* **8**, 2281–2308 (2013).
12. J. G. Doench *et al*., *Nat. Biotechnol.* **34**, 184–191 (2016).
13. S. J. Pettitt *et al*., *Nat. Commun.* **9**, 1849 (2018).
14. E. Gogola *et al*., *Cancer Cell* **33**, 1078–1093.e12 (2018).
15. K. E. Mengwasser *et al*., *Mol. Cell* **73**, 885–899.e6 (2019).
16. D. B. Zorov, M. Juhaszova, S. J. Sollott, *Physiol. Rev.* **94**, 909–950 (2014).
17. X. Luo, W. L. Kraus, *Genes Dev.* **26**, 417–432 (2012).
18. S. Shin, D. G. Bosc, J. N. Ingle, T. C. Spelsberg, R. Janknecht, *J. Cell. Biochem.* **105**, 866–874 (2008).
19. B. C. Lewis *et al*., *Cancer Res.* **60**, 6178–6183 (2000).
20. Y. K. Ghiorghi, K. I. Zeller, C. V. Dang, P. A. Kaminski, *J. Biol. Chem.* **282**, 8150–8156 (2007).
21. S. Lin *et al*., *J. Biol. Chem.* **276**, 18695–18701 (2001).
22. P. C. DeWeirdt *et al*., *Nat. Commun.* **11**, 752 (2020).
23. A. Dréan *et al*., *Mol. Cancer Ther.* **16**, 2022–2034 (2017).
24. Y. Yu, Y. Cui, L. J. Niedernhofer, Y. Wang, *Chem. Res. Toxicol.* **29**, 2008–2039 (2016).
25. J. U. Guo, Y. Su, C. Zhong, G. L. Ming, H. Song, *Cell* **145**, 423–434 (2011).
26. M. Zauri *et al*., *Nature* **524**, 114–118 (2015).
27. X. Yin, Y. Xu, *Adv. Exp. Med. Biol.* **945**, 275–302 (2016).
28. A. Masaoka *et al*., *Biochemistry* **42**, 5003–5012 (2003).
29. C. Kunz *et al*., *PLOS Biol.* **7**, e1000091 (2009).
30. J. E. Jaspers *et al*., *Cancer Discov.* **3**, 68–81 (2013).
31. C. Amiable, S. Pochet, A. Padilla, G. Labesse, P. A. Kaminski, *PLOS ONE* **8**, e80755 (2013).
32. H. Hu *et al*., *Sci. Rep.* **7**, 11568 (2017).
33. J. T. Cunningham, M. V. Moreno, A. Lodi, S. M. Ronen, D. Ruggero, *Cell* **157**, 1088–1103 (2014).
34. A. Maya-Mendoza *et al*., *Nature* **559**, 279–284 (2018).
35. H. Hanzlikova *et al*., *Mol. Cell* **71**, 319–331.e3 (2018).
36. K. Cong *et al*., bioRxiv 781989 [Preprint]. 25 September 2019. https://doi.org/10.1101/781989.
37. S. F. Bunting *et al*., *Cell* **141**, 243–254 (2010).
38. M. Daza-Martin *et al*., *Nature* **571**, 521–527 (2019).
39. K. P. Bhat, D. Cortez, *Nat. Struct. Mol. Biol.* **25**, 446–453 (2018).

ACKNOWLEDGMENTS

We thank members of the West lab for their help and encouragement; the Francis Crick Institute's Advanced Sequencing, Peptide Chemistry, Equipment Park, and High Throughput Screening science technology platforms; M. O'Connor

and J. Forment (AstraZeneca) for help and insightful comments; C. Lord (ICR, London) for providing cell lines; P.-A. Kaminski (Institute Pasteur, Paris) for the DNPH1 bacterial expression plasmids; and J. Christensen (BRIC, Copenhagen) for TET1 antibody. **Funding:** This work was supported by the Francis Crick Institute grant FC0010212 (S.C.W.; the Francis Crick Institute receives core funding from Cancer Research UK, the Medical Research Council, and the Wellcome Trust); the European Research Council grant ERC-ADG-666400 (S.C.W.); the Louis-Jeantet Foundation (S.C.W.); the Benzon Foundation (K.F.); and the Lundbeck Foundation (K.F.). **Author contributions:** Conceptualization: K.F. Methodology: K.F., I.B., M.S.D.S., and I.A.T. Investigation: K.F., I.B., M.S.D.S., R.G., H.P., S.J.Y., S.K., I.A.T., G.K., and G.H. Data curation: K.F. and I.B. Resources: T.C. Visualization: K.F., I.B., and S.C.W. Project administration: K.F. and S.C.W. Funding acquisition: S.C.W. Supervision: S.C.W., S.J.B., I.A.T., and J.M. Writing – original draft: K.F., I.B., and S.C.W. Writing – review and editing: K.F. and S.C.W. **Competing interests:** K.F. and S.C.W. are inventors on patent WO2021/048235 that pertains to the use of DNPH1 inhibitors and hmdU as a mechanism to sensitize HR-deficient cells to PARPi. S.J.B. is scientific cofounder and vice president of science strategy at Artios Pharma Ltd. The other authors declare no competing interests. **Data and materials availability:** All cell lines and reagents will be provided on request. Data are available in the manuscript and supplementary materials.

SUPPLEMENTARY MATERIALS

science.sciencemag.org/content/372/6538/156/suppl/DC1
Materials and Methods
Figs. S1 to S8
Tables S1 to S4
References (*40*–*49*)
MDAR Reproducibility Checklist

25 February 2020; resubmitted 31 December 2020
Accepted 24 February 2021
10.1126/science.abb4542

HUMAN EVOLUTION

The primitive brain of early *Homo*

Marcia S. Ponce de León[1]*, Thibault Bienvenu[1], Assaf Marom[2], Silvano Engel[1], Paul Tafforeau[3], José Luis Alatorre Warren[1,4,5], David Lordkipanidze[6], Iwan Kurniawan[7], Delta Bayu Murti[8], Rusyad Adi Suriyanto[9], Toetik Koesbardiati[7], Christoph P. E. Zollikofer[1]*

The brains of modern humans differ from those of great apes in size, shape, and cortical organization, notably in frontal lobe areas involved in complex cognitive tasks, such as social cognition, tool use, and language. When these differences arose during human evolution is a question of ongoing debate. Here, we show that the brains of early *Homo* from Africa and Western Asia (Dmanisi) retained a primitive, great ape–like organization of the frontal lobe. By contrast, African *Homo* younger than 1.5 million years ago, as well as all Southeast Asian *Homo erectus*, exhibited a more derived, humanlike brain organization. Frontal lobe reorganization, once considered a hallmark of earliest *Homo* in Africa, thus evolved comparatively late, and long after *Homo* first dispersed from Africa.

Human brains are substantially larger than those of our closest living relatives, the great apes, and also bear evidence of important structural reorganization, notably in cortical association areas related to higher cognitive functions, such as toolmaking and language capabilities (*1*, *2*). Clarifying when these structural innovations appeared during human evolution remains a major challenge (*3*, *4*). Brains do not fossilize, and so the only direct physical evidence for the actual course of brain evolution comes from natural or virtual fillings of fossil hominin brain cases, so-called endocasts, which show a complex but spatially reliable pattern of imprints representing cerebral gyri and sulci, as well as vascular structures surrounding the brain (*5*).

The endocranial region that holds key information about frontal lobe reorganization and possible language capabilities is Broca's cap (BC), a bulge on the lateral fronto-orbital surface of endocasts (Fig. 1). BC is present on both human and great ape endocasts and often assumes similar morphologies (*6*, *7*). However, the underlying brain areas are not the same across groups (*7*, *8*) (Fig. 1). In great apes, BC largely comprises Brodmann area 44, and its inferior border is formed by the fronto-orbital sulcus (fo) (Fig. 1A). In humans, BC largely comprises Brodmann areas 45 and 47, and its inferior delimitation tends to coincide with the lateral orbital sulcus (*9*) (Fig. 1B). Inferring brain reorganization from the morphology of the BC region of fossil endocasts thus remains ambiguous. The BC of *Australopithecus* endocasts is typically interpreted as being delimited inferiorly by fo, indicating a great ape–like organization of the underlying brain areas (*7*). However, endocranial evidence from *Australopithecus africanus* and *Australopithecus sediba* has been interpreted as showing incipient reorganization of the frontal lobe (*10*, *11*). This proposition has been challenged on various grounds (*12*, *13*), such that basic questions about the timing and mode of the

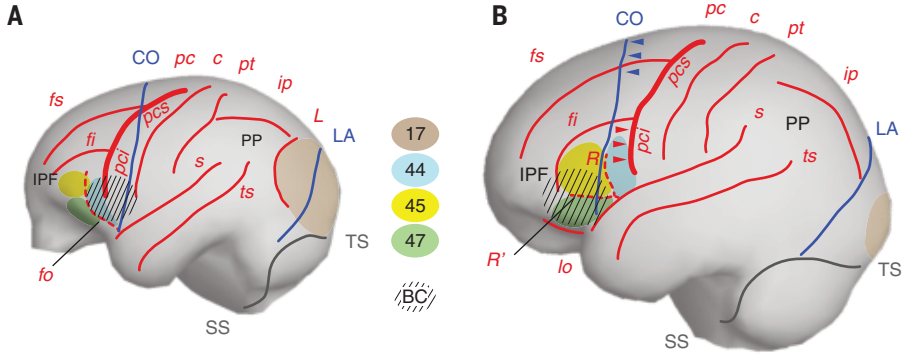

Fig. 1. Topographical relationships between neurocranial and brain structures on endocasts of great apes and humans. Cranial sutures are indicated in blue, cerebral sulci in red, and brain regions in other colors. (**A**) In great apes, the precentral sulcus (pc) crosses the coronal suture (CO), such that its inferior portion (pci) is located anterior to CO. The lunate sulcus (L) marks the anterior border of the primary visual cortex (Brodmann area 17). (**B**) In humans, evolutionary expansion of the inferior prefrontal cortex (IPF) resulted in a shift of the pci toward the posterior side of CO (red arrowheads). Concomitant expansion of the parietal bone resulted in anterior shift (blue arrowheads) of the apical portion of CO. Expansion of the posterior parietal cortex (PP) resulted in fragmentation and eventual disappearance of L. Numbers indicate Brodmann areas. Neurocranial structures: BC, Broca's cap; CO, coronal suture; LA, lambdoid suture. Cerebral sulci: c, central; fi, inferior frontal; fs, superior frontal; fo, fronto-orbital; ip, intraparietal; lo, lateral orbital; pc (pcs/pci), precentral (superior/inferior); pt, postcentral; ts, superior temporal; s, Sylvian (lateral); L, lunate; R/R', ascending/horizontal rami of anterior lateral sulcus. Vascular structures: SS, sigmoid sinus; TS, transverse sinus. Figure was redrawn from (*34*, *35*).

[1]Department of Anthropology and Anthropological Museum, University of Zurich, CH-8052 Zurich, Switzerland. [2]Rappaport Faculty of Medicine, Technion – Israel Institute of Technology, Haifa 31096, Israel. [3]European Synchrotron Radiation Facility, 38043 Grenoble, France. [4]Fetal Neonatal Neuroimaging and Developmental Science Center, Boston Children's Hospital, Harvard Medical School, Boston, MA 02115, USA. [5]Division of Newborn Medicine, Boston Children's Hospital, Harvard Medical School, Boston, MA 02115, USA. [6]Georgian National Museum, 3 Purtseladze Str., 0105 Tbilisi, Georgia. [7]Museum of Geology, Jln. Diponegoro 57, Bandung 40122, Indonesia. [8]Department of Anthropology, Airlangga University, Surabaya, 60115 Jawa Timur, Indonesia. [9]Laboratory of Bioanthropology and Paleoanthropology, Gadjah Mada University, Yogyakarta 55281, Indonesia.
***Corresponding author. Email: marcia@aim.uzh.ch (M.S.P.d.L.); zolli@aim.uzh.ch (C.P.E.Z.)**

evolutionary transition from great ape–like to humanlike frontal lobe organization remain largely unanswered.

Uncertainties also exist regarding the evolutionary reorganization of the parieto-occipital cortex. All great ape brains exhibit a lunate sulcus (L), which marks the anterior boundary of the primary visual cortex (Brodmann area 17) (Fig. 1A), whereas human brains are characterized by complete loss of L (*14*), reflecting an expanded parieto-occipital cortex (*13*, *15*) (Fig. 1B). L rarely leaves endocranial imprints (*7*, *16*, *17*), such that, in fossil hominin endocasts, absence of evidence of L is not evidence of absence, and it remains unclear when during human evolution this cortical area started expanding (*3*, *4*, *7*, *9*, *18*–*20*).

Traditionally, it has been assumed that a derived, humanlike organization of the frontal and parieto-occipital lobes (see legend of Fig. 1) characterizes the genus *Homo* from its beginnings (*21*–*23*). However, testing this hypothesis explicitly on fossil endocasts has proven difficult. The African fossil record extends back to the origins of *Homo* at around 2.8 million years ago (Ma) (*24*), but critical endocranial evidence is only preserved from ~1.8 Ma onward and represented by single finds dispersed in space and geological time (Table 1). This makes it difficult to identify diachronic trends in brain evolution against a background of interindividual variation in endocranial morphology. *Homo erectus* from Southeast Asia, on the other hand, is represented by numerous well-preserved neurocrania from a geographically restricted area, but with younger geological dates (*25*, *26*) (Table 1).

The fossil hominins from the early Pleistocene site of Dmanisi, dated to 1.85 to 1.77 Ma (*27*, *28*), play a key role in assessing brain reorganization in early *Homo* and its potential importance for hominin dispersals from Africa.

Table 1. Endocranial features of early *Homo* fossils. Fields marked as "—" indicate data absent or missing; "?" indicates indeterminate.

Region	Specimen	Label*	Geological age (Ma)	ECV (cm^3)	Petalia†	pci/CO topography‡	Frontal lobe state§	Criteria¶	CBA1 (°)#	Reference(s)
Africa	KNM-ER 1470	1470	2.03	752	L o	L ?	?	?	—	(*57*, *58*)
	KNM-ER 1805	1805	1.75	582	—	L,R ant	p	1a	—	(*59*)
	KNM-ER 1813	1813	1.78	509	R o	L,R ant	p	1a	—	(*59*)
	KNM-ER 3733	3733	1.65	848	—	R ant	p	3a	139	(*59*)
	KNM-ER 3883	3883	1.65–1.50	804	L o, R f	R coi	d	2a, 3b	145	(*59*)
	WT 15000	WT15K	1.60–1.50	750	R o, R f	L ant	p	1a	—	(*60*)
	DAN5/P1	DAN5	1.60–1.50	598	—	—	—	—	—	(*51*)
	OH 9	OH9	1.50	983	(R o)	R ant?	?	1a?	—	(*61*)
	KNM-ER 42700		1.55	732	L o, L f	L post	d	2a	138	(*62*)
	BOU-VP-2/66	BOU	1.00	998	(L o)	L,R post	d	2a	123	(*63*)
	UA-31 (Buia)		1.00	995	—	L post	d	2a		(*64*)
	Bodo	Bodo	0.6	1250	—	L,R post	d	1b	150	(*65*)
	Kabwe	Kabwe	0.30	1325	L o, R f	L post	d	1b	143	(*66*)
	Au. sediba MH1	MH1	1.98	420	—	L ant	p	1a	—	(*10*)
	H. naledi DH1,3	DH	0.34–0.24	460	—	L ant	i or p?	1a	—	(*9*)
West Asia	D2280	D1	1.77	730	R o, L f	L,R ant	p	1a	—	(*28*, *67*)
	D2282	D2	1.77	650	—	L ant	p	1a	—	(*28*, *67*)
	D2700	D3	1.77	601	L f	L,R ant	p	1a	135	(*28*)
	D3444	D4	1.77	641	(R f)	L,R ant	p	1a	—	(*28*)
	D4500	D5	1.77	546	R o	L,R ant	p	1a	156	(*28*)
Europe	Steinheim	St	0.40–0.30	1200	L o, R f	L,R post	d	1b	135	
	Petralona	Pe	0.40–0.30	1170	L o	L,R post	d	1b	—	
Northeast Asia	Zhoukoudian XII	Z12	0.77	1030	R o	R post	d	2a	—	(*68*)
	Hexian	Hex	0.40–0.30	1025	—	L,R post	d	2a	N/A	(*69*)
Southeast Asia	Trinil 2 (P I)		<1.0	940	—	R post	d	2a	—	(*17*, *68*, *70*, *71*)
	Sangiran 2 (P II)	Sa2	~1.3	813	—	R post	d	2a	—	(*26*, *68*, *72*)
	Sangiran 9	Sa9	~1.3	870	—	L post	d	2a	—	(*26*, *73*, *74*)
	Sangiran 17	Sa17	~1.3	1004	R o, L f	L coi	d	2b	—	(*26*, *75*)
	Bukuran	Buk	<1.49	850	(R f)	L coi	d	2a	—	(*76*, *77*)
	Mojokerto	Mojo	<1.49	630	(R o)	L post	d	2a	N/A	(*78*, *79*)
	Sambungmacan 3	Sm3	0.30–0.20	917	(L f)	R coi or post	d	2a, 3b	—	(*80*)
	Sambungmacan 4	Sm4	0.30–0.20	1006	L o, R f	L coi or post	d	2a, 3b	141	(*81*)
	Ngawi	Ngawi	0.50–0.00	1000	—	L coi	d	2a	146	(*82*)
	Solo 4 (Ng 5)	So4	0.117–0.108	1000	R f	R coi	d	2b	—	(*25*, *83*)
	Solo 5 (Ng 6)	So5	0.117–0.108	1251	R o, R f	L,R post	d	2a, 3b	—	(*25*, *83*)
	Solo 6 (Ng 7)	So6	0.117–0.108	1013	L o, R f	L post	d	2a, 3b	147	(*25*, *83*)
	Solo 10 (Ng 13)	So10	0.117–0.108	1231	L o, L f	L,R post	d	2a	—	(*25*, *83*)
	Solo 11 (Ng 14)	So11	0.117–0.108	1090	L o, R f	L,R post	d	2a	151	(*25*, *83*)
	LB1 (Liang Bua)	LB1	0.07	426	R o	?	?	?	130	(*84*–*86*)

*Specimen labels used in Figs. 3 and 4. †L, left; R, right; f, frontal; o, occipital; parentheses indicate weak petalial expression. ‡L, left; R, right; ant, location of inferior precentral sulcus (pci) anterior to coronal suture (CO); coi, location of pci coincident with CO; post, location of pci posterior to CO. §p, primitive; i, intermediate; d, derived. ¶Frontal lobe state criteria (*33*). #Cranial base angle [see (*36*)].

Dmanisi has yielded five exceptionally well-preserved crania representing individuals from adolescence to old age, which likely represent natural variation in a paleodeme of early *Homo* (*27*, *29*–*32*). Also, the site preserves a rich record of faunal remains and Mode I (Oldowan) lithic artifacts co-occurring in taphonomic context, which permits inferences on tool use and site-specific behaviors of the Dmanisi hominins and, more broadly, on subsistence strategies, social organization, and cognitive capabilities of early *Homo* (*28*, *30*, *31*).

Here, we track key changes in brain organization of early *Homo* from ~1.8 Ma onward by analyzing the endocranial morphology of the

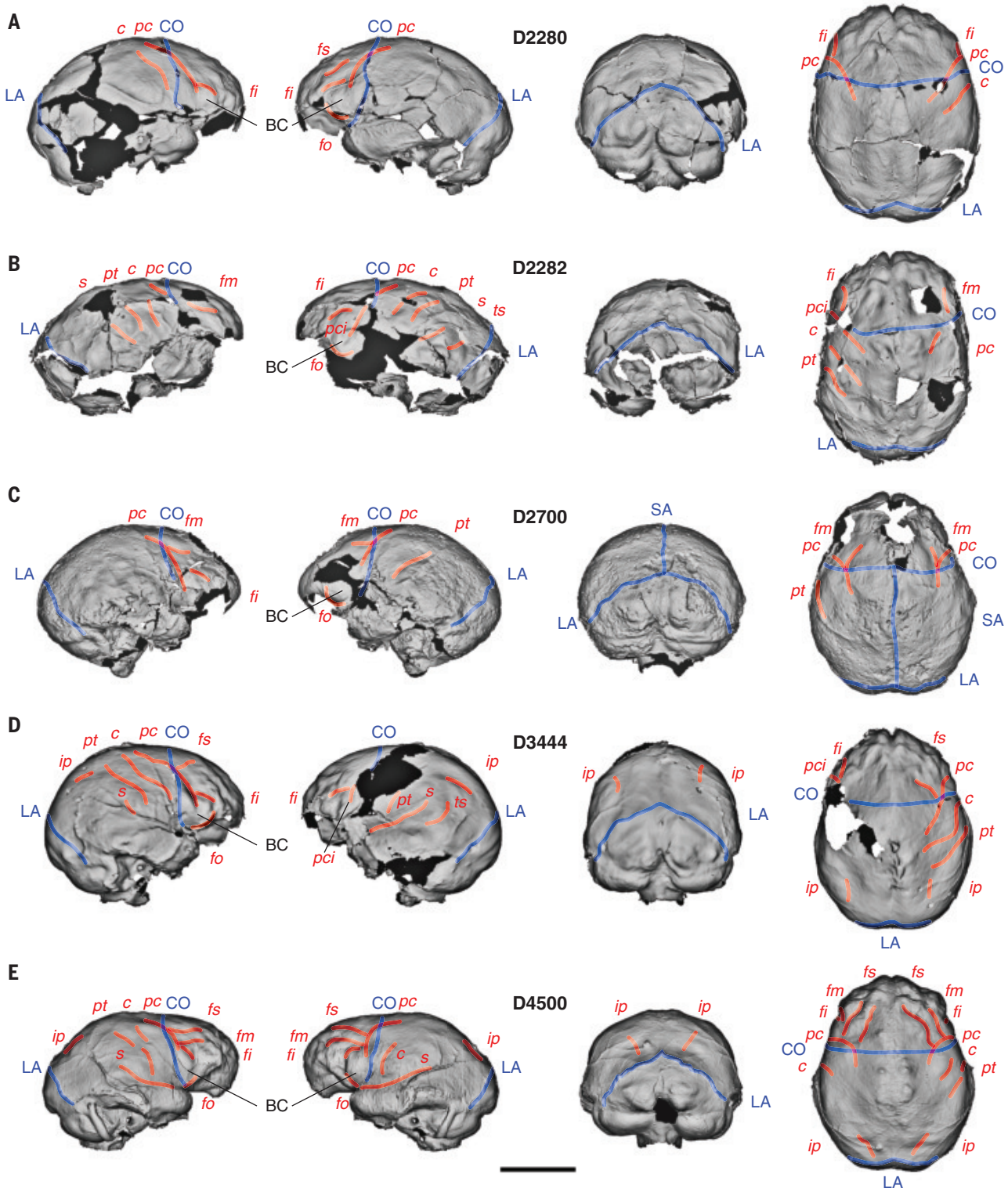

Fig. 2. Endocranial organization of the Dmanisi crania. (**A** to **E**) Left and right lateral, posterior, and superior views of (A) D2280, (B) D2282, (C) D2700, (D) D3444, and (E) D4500. Red, sulcal imprints; blue, sutures. Abbreviations are as in Fig. 1. SA, sagittal suture. Scale bar, 5 cm. (See also fig. S2.) In all specimens, the precentral sulcus (pc) crosses the coronal suture (CO), such that its inferior portion (pci) lies anterior to CO, indicating a primitive organization of the frontal lobe (see Fig. 1A).

five Dmanisi specimens and reevaluating an extended comparative sample of African and Southeast Asian fossil endocasts (*33*) (Table 1). To identify primitive versus derived aspects of frontal lobe organization in fossil endocasts, we use the highly distinct cranio-cerebral topographies of humans and great apes as a frame of reference (Fig. 1) (*34*, *35*). A characteristic signal of inferior frontal lobe expansion is the posterior shift of the inferior precentral sulcus (pci) relative to the coronal suture (CO) (*35*) (Fig. 1). Both structures are typically well represented on fossil endocasts, such that their topographical relationships reliably indicate frontal lobe reorganization (supplementary method M3). In addition, we use geometric morphometric methods to identify which endocranial and brain regions underwent differential expansion during frontal lobe reorganization (supplementary methods M4 and M5).

Results

The Dmanisi endocasts

The endocast of the adult individual D2280 (Fig. 2A, fig. S1A, and supplementary text S1) is generally well preserved but lacks parts of the basicranial region. It has a rounded overall shape, with a comparatively wide anterior cranial fossa, and right occipital and left frontal petalia. The cerebellar fossa is large and bulges inferiorly. Imprints of the frontal sulci course toward the precentral sulcus (pc). This latter structure originates near the apex of the endocast, crosses the coronal suture at mid-height, and courses toward BC, such that its inferior portion (pci) lies anterior to the coronal suture.

The cranium of the adult individual D2282 (Fig. 2B, fig. S1B, and supplementary text S1) is fragmentary and exhibits substantial taphonomic distortion, which required digital retrodeformation and reconstruction. Petalial asymmetry cannot be ascertained. Several key endocranial structures are nevertheless visible. Similar to D2280, the endocranium is rounded and exhibits wide frontal lobes. The cerebellar fossa is only moderately bulging. On the left side, the precentral sulcus crosses the coronal suture at mid-height and courses toward the center of BC.

The endocranial cavity of the adolescent individual D2700 (Fig. 2C, fig. S1C, and supplementary text S1) is generally well preserved. Structural detail in the parietal and occipital region is blurred by a thin but dense calcite layer, which tightly adheres to the bone surface. In lateral and posterior views, the endocast appears rounded; in superior view, it presents a marked precoronal constriction, a feature that is often seen in Asian fossils attributed to *H. erectus*. The endocast exhibits left frontal petalia. The occipital poles are moderately projecting, and the cerebellar fossa is only moderately bulging. On both sides, the imprint of the medial frontal sulcus courses toward the coronal suture, where it reaches the precentral sulcus. The inferior portion of the precentral sulcus (pci) lies in front of the coronal suture and courses toward BC. Preservation of the endocranial base region permits estimation of cranial base angulation. The angle between landmarks basion, sella, and foramen caecum is 135° [cranial base angle CBA1 (*36*)]. The angle between the clivus plane and the midplane of the anterior cranial fossa (planum sphenoideum) is 124° [cranial base angle CBA4 (*36*)]. These values are at the upper end or above the range of variation of modern humans of similar dental age [CBA1, 132° to 137°; CBA4, 106° to 118° (*37*)].

The endocranial cavity of the edentulous cranium D3444 (Fig. 2D, fig. S1D, and supplementary text S1) suffered some taphonomic damage, such as dislocation of the left temporal pyramid, and loss of parts of the anterior cranial base and of the internal table on the left fronto-parietal region. The endocast has a globular shape that is similar to that of some modern human endocasts (Fig. 3) but exhibits precoronal constriction similar to D2700. The endocast exhibits slight right frontal petalia. The frontal sulci are represented by marked endocranial imprints, which course toward the imprint of the precentral sulcus. On both sides, the pci lies anterior to the coronal suture and courses toward the center of BC.

Cranium D4500, together with mandible D2600, represents the most complete skull of early *Homo* found to date (*32*). The endocast is fully preserved, except for a small area of the internal table in the occipital region (Fig. 2E, fig. S1E, and supplementary text S1). Sediment adhering to the middle and anterior cranial fossae was removed using synchrotron imaging and semiautomated image segmentation procedures (supplementary method M2). The D4500 endocast exhibits right occipital petalia. Precoronal constriction is marked, but the

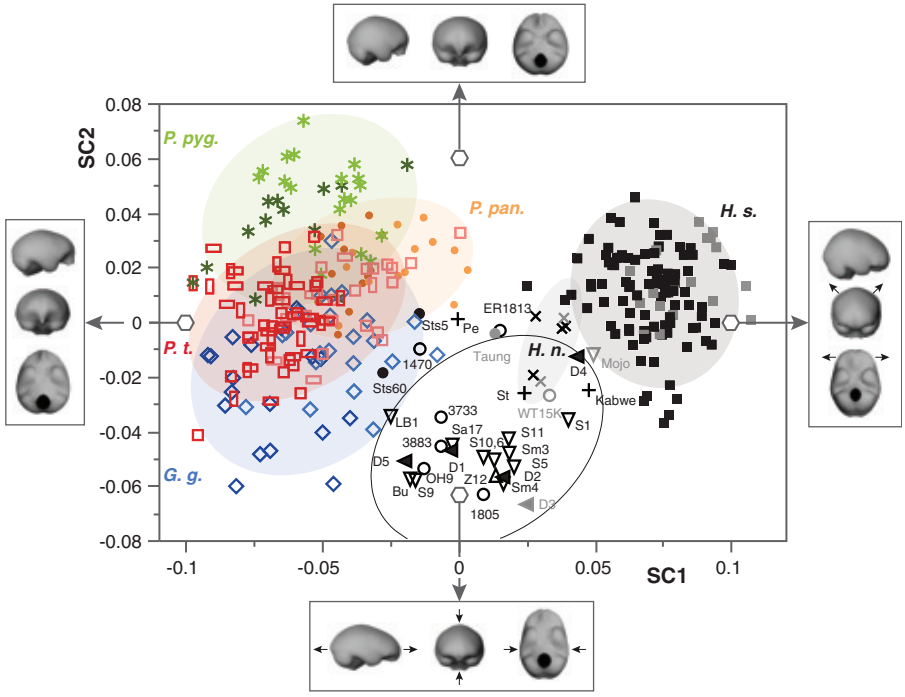

Fig. 3. Endocranial shape variation in fossil hominins, great apes, and humans. The central graph shows patterns of intragroup and intergroup variation in shape space. The surrounding panels visualize endocranial shapes at the extremes of the distribution. Shape component SC1 accounts for 57% of the total variation in the sample and captures major differences in endocranial shape between great apes and hominins, notably in relative width of frontal lobes (arrows) and in foramen magnum position. Shape component SC2 (10%) captures variation in endocranial length, height, and width relationships (arrows) within and among groups. Green stars, *Pongo pygmaeus*; red, *Pan troglodytes* (open squares, *P. t. troglodytes*; horizontal rectangles, *P. t. verus*; vertical rectangles, *P. t. schweinfurthii*); orange dots, *P. paniscus*; blue diamonds, *Gorilla gorilla*; filled circles, *Australopithecus*; open circles, African early *Homo*; triangles, Asian early *Homo* (left, upward, and downward triangles indicate Dmanisi, Northeast Asia, and Southeast Asia, respectively); + signs, mid- to late-Pleistocene African and European *Homo*; × signs, *Homo neanderthalensis*; black squares, modern *Homo sapiens*. Light and dark hues indicate immature and adult individuals, respectively. The 90% density ellipses are drawn for great ape species, modern *H. sapiens*, early *Homo* between 2 and 1 Ma (black outline), and *H. neanderthalensis*. For fossil specimen labels, see Table 1. Hexagons indicate the location in shape space of the visualized endocasts.

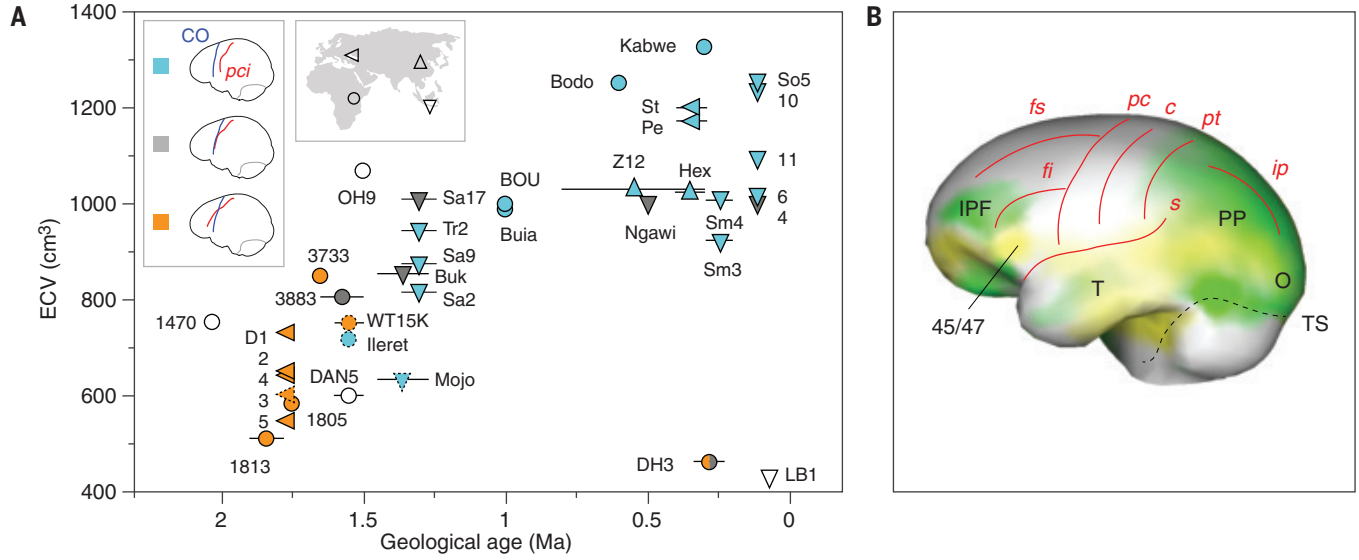

Fig. 4. Evolution of endocranial morphology of early *Homo*. (**A**) Changes in ECV and craniocerebral topography over the past 2 Ma. Orange, gray, and turquoise symbols indicate the position of the inferior precentral sulcus (pci) anterior to, coincident with, and posterior to the coronal suture (CO), respectively (see inset graph). White symbols indicate missing or indeterminate data. Circles indicate Africa, left-facing triangles indicate Western Asia and Europe, and upward and downward triangles indicate Northeast and Southeast Asia, respectively (see inset world map). Dashed symbols indicate immature specimens, and horizontal lines indicate geological age ranges. (**B**) Endocranial shape change associated with frontal lobe reorganization (left lateral view). Colors denote above-average expansion (green) and bulging (yellow) of the endocranial surface, indicating differential enlargement of labeled brain regions (IPF, inferior prefrontal cortex; 45/47, Brodmann areas 45/47; PP, posterior parietal cortex; T, temporal lobe, O, occipital lobe). Also note endocranial surface expansion along the transverse sinus (TS). Brain sulci (red): fs/fi, superior/inferior frontal; pc/c/pt, precentral/central/postcentral; s, Sylvian; ip, intraparietal.

frontal lobes remain relatively wide. The frontal sulci are represented by marked imprints; they course toward the precentral sulcus, which is clearly represented on both sides of the endocast. The precentral sulcus crosses the coronal suture at mid-height, such that pci is located anterior to the coronal suture and courses toward BC. The occipital poles are protruding. The internal cranial base of D4500 is substantially less flexed than that of D2700, with a CBA1 of 156° and CBA4 of 144°. Both values are outside the range of variation of adult modern humans.

Altogether, the Dmanisi endocasts indicate a consistent topographic pattern of external cortical morphology, where the precentral sulcus crosses the coronal suture such that its inferior portion is anterior to the suture and courses toward BC (Fig. 2, Table 1, and fig. S1). Using great ape and human craniocerebral topographies as a reference (Fig. 1), the Dmanisi individuals largely reflect a great ape pattern of frontal lobe organization, in which BC is delimited inferiorly by the frontoorbital sulcus and likely housed Brodmann cortical area 44 and parts of area 45 (Fig. 1A).

Endocasts of African and East Asian Homo *fossils*

A comparative analysis of the endocasts of early to mid-Pleistocene *Homo* fossils from Africa reveals greater endocranial topographic diversity (Table 1, supplementary text S2, and fig. S2). Specimens KNM-ER1805 and KNM-ER1813, with disputed taxonomic affiliation but dated to before ~1.7 Ma, show endocranial imprints that are compatible with a great ape–like organization of the frontal lobe (fig. S2, A and B). Specimen KNM-ER 1470 (fig. S2C), which has been put forward as key evidence for a derived frontal lobe organization (*21*), is too fragmented to reveal diagnostic endocranial imprints. The endocasts of fossils dated to ~1.7 to 1.5 Ma, and variably attributed to *Homo ergaster* or *H. erectus*, show variation in frontal endocranial topography that suggests a range of primitive to derived frontal lobe morphologies (fig. S2, D to F). By contrast, African fossils younger than ~1.5 Ma exhibit endocranial topographies that are compatible with a derived, modern human–like frontal lobe organization (Table 1 and supplementary text S2).

The endocasts of *H. erectus* from Java typically exhibit marked imprints of the frontal sulci, whereas imprints of the precentral and central sulci are faint to absent. In all specimens reexamined here, imprints of the inferior and/or middle frontal sulci course anteroposteriorly to reach the coronal suture (Table 1, supplementary text S3, and fig. S3, A to E). This topography constrains the inferior precentral sulcus to a location that either roughly coincides with the coronal suture or is posterior to it, thus representing a derived organization of the frontal lobe. The endocasts of Chinese *H. erectus*, represented here by Zhoukoudian XII (fig. S3F) and Hexian, exhibit a clearly derived topography of the frontal lobe region (supplementary text S3).

Endocranial shape, size, and topography

Figure 3 shows endocranial shape variation in fossil *Homo* and in a comparative sample of great apes and modern humans (see supplementary method M4). Great ape endocrania are low but wide in the parietal region and exhibit a tapering frontal region and a posteriorly situated foramen magnum. Modern human endocrania are comparatively high and have wide frontal lobes and an inferiorly situated foramen magnum. The great ape–human contrast in endocranial shape is largely an effect of variation in relative encephalization [measured here as brain size relative to the size of the cranial base and face (*38*)] (fig. S4). Fossil hominin endocrania occupy the region in morphospace between great apes and humans. Endocranial shape in the genus *Homo* between 2 and 1 Ma shows wide intragroup and intergroup variation (Fig. 3). Variation in the Dmanisi sample is congruent in range and pattern with intragroup variation in other taxa (fig. S5).

Correlating our data about endocranial topography (Table 1) with geological dates permits inferences on the timing of frontal lobe reorganization and its possible correlation with brain expansion and changes in brain shape (Fig. 4). The transition from primitive to

derived frontal lobe morphologies likely took place during the time between 1.7 and 1.5 Ma, with derived morphologies largely established in the fossil record after 1.5 Ma. During that time interval, frontal lobe reorganization occurred in tandem with brain expansion (Fig. 4A and Table 1) [mean endocranial volume (ECV) increased from 650 to 830 cm^3]. It is likely that the two processes had similar evolutionary causes. However, the possible presence of derived frontal lobe morphologies in small-brained (ECV ~460 cm^3) but geologically younger fossils, such as *H. floresiensis* and *H. naledi* (*9*) (supplementary text S4), suggests that frontal lobe organization is not mechanistically linked to large brain volumes.

Our data further indicate that the transition from primitive to derived frontal lobe organization was accompanied by specific changes in endocranial shape (Fig. 4B and supplementary method M5). The posterior shift of pci (Fig. 4A) is associated with differential expansion of the inferior prefrontal (IPF) region (Figs. 1 and 4B). Furthermore, expansion of IPF is correlated with marked expansion of the posterior parietal (PP) and occipital (O) cortical regions.

Discussion

Pattern and timing of brain reorganization in early Homo

Cranio-cerebral topography reveals that the earliest members of the genus *Homo* had a primitive frontal lobe organization, featuring an ape-like anterior location of the inferior precentral sulcus relative to the coronal suture (Fig. 4A and Table 1). Our data indicate that the derived frontal lobe organization emerged relatively late during the evolution of *Homo*, between 1.7 and 1.5 Ma—not at the transition from *Australopithecus* to *Homo* (*10*, *39*), but clearly later than the first dispersals of *Homo* from Africa. Endocranial shape change associated with frontal lobe reorganization reveals differential expansion of the inferior prefrontal cortex and also of the posterior parietal and occipital cortex (Fig. 4B) (*39*). This pattern indicates that the anterior and posterior cortical association areas evolved in tandem (*13*, *40*, *41*) rather than in sequence (*3*). We infer from this that endocasts of early *Homo* predating frontal lobe reorganization potentially exhibit imprints of remnant ape-like lunate sulci in the parieto-occipital region (supplementary text S1 and fig. S1).

The temporal and geographic patterning of primitive and derived brain organization in early *Homo* (Table 1) cannot be explained by a single-dispersal scenario but must have involved greater spatiotemporal complexity, as suggested earlier (*42*–*45*). Given the current evidence (Fig. 4 and Table 1), the most parsimonious scenario is that the first *Homo* populations to disperse from Africa, probably as early as 2.1 Ma (*46*), retained the primitive frontal lobe organization, as represented in Dmanisi. The Southeast Asian *H. erectus* fossils, now dated to <1.5 Ma (*26*), represent a second dispersal, after the derived frontal lobe morphology emerged in Africa between 1.7 and 1.5 Ma. Additional fossil and archaeological evidence will be required to assess whether the earliest populations of *Homo* outside Africa merged with, and/or were replaced by, populations exhibiting the derived morphology.

Neurofunctional implications

In modern human brains, the inferior frontal lobe is an important neurofunctional substrate for advanced social cognition, toolmaking and tool use, and articulated language (*2*, *47*, *48*). We may thus ask whether its evolutionary reorganization around 1.7 to 1.5 Ma was accompanied by major changes in technocultural performance. The earliest evidence for Mode II (Acheulean) technocultures in Africa [1.76 Ma (*49*, *50*)] largely coincides with incipient frontal lobe reorganization, and Mode I and Mode II lithic technologies were used concurrently during the critical time period (*51*). We hypothesize that this pattern reflects interdependent processes of brain-culture coevolution (*52*), where cultural innovation triggered changes in cortical interconnectivity (*4*, *53*) and ultimately in external frontal lobe topography. On the other hand, the cerebral innovations that characterize *Homo* at ~1.5 Ma might have constituted the foundations of the "language-ready" brain of later *Homo* species (*54*).

Taxonomic implications

Our findings also have implications for the taxonomy of early *Homo*. The notable morphological diversity of early Pleistocene fossils attributed to *Homo* has been interpreted alternatively as population diversity within a single hominin species lineage versus species diversity in Africa. The former view is supported by patterns of continuous variation in metric and nonmetric cranial traits (*32*) and by evidence for substantial sexual dimorphism (*51*, *55*). The latter view is supported by the observation that metric variation in gnathic morphology is greater than expected for a single taxon, suggesting dietary specialization rather than brain expansion as a major driver of speciation in early *Homo* (*56*). The data on brain structural variation presented here provide additional evidence for diversity in early *Homo* in Africa. However, the pattern of cerebral structural diversity (Fig. 4A) does not match the pattern of gnathic diversity (*56*), such that the question of taxonomic diversity in early *Homo* remains unresolved. Deciphering evolutionary process in early *Homo* remains a challenge that will be met only through the recovery of expanded fossil samples from well-controlled chronological contexts.

REFERENCES AND NOTES

1. C. C. Sherwood, F. Subiaul, T. W. Zawidzki, *J. Anat.* **212**, 426–454 (2008).
2. D. Stout, T. Chaminade, *Phil. Trans. R. Soc. London Ser. B* **367**, 75–87 (2012).
3. R. L. Holloway, C. C. Sherwood, P. R. Hof, J. K. Rilling, in *Encyclopedia of Neuroscience* (Springer, 2009), pp. 1326–1334.
4. D. Falk, in *Evolution of the Primate Brain: From Neuron to Behavior*, vol. 195 of *Progress in Brain Research*, M. Hofman, D. Falk, Eds. (Elsevier, 2012), pp. 255–272.
5. J. Dumoncel *et al.*, *J. Anat.* **238**, 480–488 (2021).
6. A. Balzeau, E. Gilissen, R. L. Holloway, S. Prima, D. Grimaud-Hervé, *J. Hum. Evol.* **76**, 116–128 (2014).
7. D. Falk, *Front. Hum. Neurosci.* **8**, 134 (2014).
8. D. Falk, *IBRO Hist. Neurosci.* **2007**, 2513–2518 (2007).
9. R. L. Holloway *et al.*, *Proc. Natl. Acad. Sci. U.S.A.* **115**, 5738–5743 (2018).
10. K. J. Carlson *et al.*, *Science* **333**, 1402–1407 (2011).
11. D. Falk, C. P. E. Zollikofer, N. Morimoto, M. S. Ponce de León, *Proc. Natl. Acad. Sci. U.S.A.* **109**, 8467–8470 (2012).
12. R. L. Holloway, D. C. Broadfield, K. J. Carlson, *Proc. Natl. Acad. Sci. U.S.A.* **111**, 13022–13027 (2014).
13. D. Falk *et al.*, *Brain Behav. Evol.* **91**, 45–58 (2018).
14. J. S. Allen, J. Bruss, H. Damasio, *Anat. Rec. A Discov. Mol. Cell. Evol. Biol.* **288**, 867–876 (2006).
15. A. A. de Sousa *et al.*, *J. Hum. Evol.* **58**, 281–292 (2010).
16. W. E. LeGros Clark, D. M. Cooper, S. Zuckerman, *J. R. Anthropol. Inst. G* **66**, 249–268 (1936).
17. C. J. Connolly, *External Morphology of the Primate Brain* (C. C. Thomas, 1950).
18. R. A. Dart, *Nature* **115**, 195–199 (1925).
19. A. Beaudet *et al.*, *J. Hum. Evol.* **126**, 112–123 (2019).
20. P. Gunz *et al.*, *Sci. Adv.* **6**, eaaz4729 (2020).
21. D. Falk, *Science* **221**, 1072–1074 (1983).
22. P. V. Tobias, *J. Hum. Evol.* **16**, 741–761 (1987).
23. A. N. Parks, J. B. Smaers, in *Digital Endocasts*, E. Bruner, N. Ogihara, H. Tanabe, Eds. (Springer, 2018), pp. 205–218.
24. B. Villmoare *et al.*, *Science* **347**, 1352–1355 (2015).
25. Y. Rizal *et al.*, *Nature* **577**, 381–385 (2020).
26. S. Matsu'ura *et al.*, *Science* **367**, 210–214 (2020).
27. L. Gabunia *et al.*, *Science* **288**, 1019–1025 (2000).
28. R. Ferring *et al.*, *Proc. Natl. Acad. Sci. U.S.A.* **108**, 10432–10436 (2011).
29. A. Vekua *et al.*, *Science* **297**, 85–89 (2002).
30. D. Lordkipanidze *et al.*, *Nature* **434**, 717–718 (2005).
31. D. Lordkipanidze *et al.*, *Anat. Rec. A Discov. Mol. Cell. Evol. Biol.* **288**, 1146–1157 (2006).
32. D. Lordkipanidze *et al.*, *Science* **342**, 326–331 (2013).
33. See supplementary materials.
34. C. P. E. Zollikofer, M. S. Ponce de León, *Evol. Anthropol.* **22**, 20–33 (2013).
35. J. L. Alatorre Warren, M. S. Ponce de León, W. D. Hopkins, C. P. E. Zollikofer, *Proc. Natl. Acad. Sci. U.S.A.* **116**, 22115–22121 (2019).
36. D. E. Lieberman, C. F. Ross, M. J. Ravosa, *Yearb. Phys. Anthropol.* **43** (suppl. 31), 117–169 (2000).
37. D. E. Lieberman, R. C. McCarthy, *J. Hum. Evol.* **36**, 487–517 (1999).
38. C. P. E. Zollikofer, T. Bienvenu, M. S. Ponce de León, *J. Anat.* **230**, 85–105 (2017).
39. R. L. Holloway, in *Handbook of Paleoanthropology*, W. Henke, I. Tattersall, Eds. (Springer, 2015), vol. 3, pp. 1961–1987.
40. J. K. Rilling *et al.*, *Nat. Neurosci.* **11**, 426–428 (2008).
41. J. B. Smaers, D. R. Vanier, *Cortex* **118**, 292–305 (2019).
42. O. Bar-Yosef, A. Belfer-Cohen, *Quat. Int.* **75**, 19–28 (2001).
43. S. C. Antón, C. C. Swisher III, *Annu. Rev. Anthropol.* **33**, 271–296 (2004).
44. R. Dennell, W. Roebroeks, *Nature* **438**, 1099–1104 (2005).
45. Y. Kaifu, *Curr. Anthropol.* **58** (S17), S418–S433 (2017).
46. Z. Zhu *et al.*, *Nature* **559**, 608–612 (2018).
47. S. S. Putt, S. Wijeakumar, R. G. Franciscus, J. P. Spencer, *Nat. Hum. Behav.* **1**, 0102 (2017).
48. S. S. J. Putt, S. Wijeakumar, J. P. Spencer, *Neuroimage* **199**, 57–69 (2019).
49. C. J. Lepre *et al.*, *Nature* **477**, 82–85 (2011).
50. Y. Beyene *et al.*, *Proc. Natl. Acad. Sci. U.S.A.* **110**, 1584–1591 (2013).
51. S. Semaw *et al.*, *Sci. Adv.* **6**, eaaw4694 (2020).
52. M. González-Forero, A. Gardner, *Nature* **557**, 554–557 (2018).

53. K. Teffer, K. Semendeferi, *Prog. Brain Res.* **195**, 191–218 (2012).
54. B. Dubreuil, C. S. Henshilwood, *Lang. Cogn.* **5**, 251–260 (2014).
55. F. Spoor *et al*., *Nature* **448**, 688–691 (2007).
56. F. Spoor *et al*., *Nature* **519**, 83–86 (2015).
57. M. G. Leakey *et al*., *Nature* **488**, 201–204 (2012).
58. I. McDougall *et al*., *J. Geol. Soc. London* **169**, 213–226 (2012).
59. P. N. Gathogo, F. H. Brown, *J. Hum. Evol.* **51**, 471–479 (2006).
60. A. Walker, R. Leakey, *The Nariokotome Homo erectus Skeleton* (Springer, 1993).
61. L. J. McHenry, I. G. Stanistreet, *J. Hum. Evol.* **120**, 7–18 (2018).
62. S. Neubauer *et al*., *J. Hum. Evol.* **121**, 25–39 (2018).
63. W. H. Gilbert, B. Asfaw, *Homo erectus: Pleistocene Evidence from the Middle Awash, Ethiopia* (Univ. California Press, 2009), vol. 1.
64. E. Bruner *et al*., *Am. J. Phys. Anthropol.* **160**, 458–468 (2016).
65. G. C. Conroy *et al*., *Am. J. Phys. Anthropol.* **113**, 111–118 (2000).
66. R. Grün *et al*., *Nature* **580**, 372–375 (2020).
67. D. Grimaud-Hervé, D. Lordkipanidze, in *Paleoneurological Studies in Honor of Ralph L. Holloway*, D. Broadfield, M. Yuan, K. Schick, N. Toth, Eds. (Stone Age Institute Press, 2010), pp. 59–82.
68. F. Weidenreich, *Am. J. Phys. Anthropol.* **5**, 387–428 (1947).
69. X. Wu, L. A. Schepartz, D. Falk, W. Liu, *Am. J. Phys. Anthropol.* **130**, 445–454 (2006).
70. F. Tilney, H. A. Riley, *The Brain from Ape to Man* (P. B. Hoeber, 1928).
71. J. C. A. Joordens *et al*., *Nature* **518**, 228–231 (2015).
72. X. J. Wu, L. A. Schepartz, C. J. Norton, *Quat. Int.* **211**, 4–13 (2010).
73. J. Ash, G. G. Gallup Jr., *Hum. Nat.* **18**, 109–124 (2007).
74. Y. Kaifu *et al*., *J. Hum. Evol.* **61**, 270–294 (2011).
75. H. Baba, F. Aziz, S. Narasaki, *Bull Natl. Sci. Mus. Tokyo* **24**, 1–8 (1998).
76. E. Indriati, S. C. Antón, *Homo* **61**, 225–243 (2010).
77. D. Grimaud-Hervé, H. Widianto, F. Détroit, F. Sémah, *J. Hum. Evol.* **63**, 637–652 (2012).
78. A. Balzeau, D. Grimaud-Hervé, T. Jacob, *J. Hum. Evol.* **48**, 535–553 (2005).
79. M. J. Morwood, P. O'Sullivan, E. Susanto, F. Aziz, *Aust. Archaeol.* **57**, 1–4 (2003).
80. D. C. Broadfield *et al*., *Anat. Rec.* **262**, 369–379 (2001).
81. H. Baba *et al*., *Science* **299**, 1384–1388 (2003).
82. Y. Kaifu *et al*., *Anthropol. Sci.* **123**, 161–176 (2015).
83. R. L. Holloway, *Am. J. Phys. Anthropol.* **53**, 285–295 (1980).
84. P. Brown *et al*., *Nature* **431**, 1055–1061 (2004).
85. D. Kubo, R. T. Kono, Y. Kaifu, *Proc. Biol. Sci.* **280**, 20130338 (2013).
86. T. Sutikna *et al*., *Nature* **532**, 366–369 (2016).

ACKNOWLEDGMENTS

We thank T. White, S. Moran, C. Finlayson, J. M. Jiménez-Arenas, and anonymous reviewers for comments on earlier versions of this manuscript. **Funding:** Supported by Swiss National Science Foundation grants IZ73Z0_127940 and 31003A_135470 and ESRF grant EC-767. M.S.P.d.L. was supported by the A.H. Schultz Foundation. D.L. was supported by the Rustaveli Science Foundation. **Author contributions:** C.P.E.Z., M.S.P.d.L., A.M., and T.B. conceived the study. P.T. performed synchrotron analyses. P.T., D.L., I.K., D.B.M., R.A.S., and T.K. contributed fossil data; J.L.A.W. contributed analyses and data. T.B., A.M., S.E., M.S.P.d.L., C.P.E.Z., and P.T. analyzed data; and C.P.E.Z., M.S.P.d.L., A.M., and T.B. wrote the paper. **Competing interests:** The authors declare no competing interests. **Data and materials availability:** Endocranial 3D landmark data are available from https://osf.io/9k4zm/.

SUPPLEMENTARY MATERIALS

science.sciencemag.org/content/372/6538/165/suppl/DC1
Materials and Methods
Supplementary Text
Figs. S1 to S5
References (*87*–*107*)

8 August 2019; resubmitted 8 October 2020
Accepted 8 March 2021
10.1126/science.aaz0032

PLANT SCIENCE

Pollen PCP-B peptides unlock a stigma peptide–receptor kinase gating mechanism for pollination

Chen Liu[1], Lianping Shen[1], Yu Xiao[2], David Vyshedsky[3], Chao Peng[4], Xiang Sun[1], Zhiwen Liu[1], Lijun Cheng[1], Hua Zhang[1], Zhifu Han[2], Jijie Chai[2], Hen-Ming Wu[3], Alice Y. Cheung[3], Chao Li[1]*

Sexual reproduction in angiosperms relies on precise communications between the pollen and pistil. The molecular mechanisms underlying these communications remain elusive. We established that in *Arabidopsis*, a stigmatic gatekeeper, the ANJEA–FERONIA (ANJ–FER) receptor kinase complex, perceives the RAPID ALKALINIZATION FACTOR peptides RALF23 and RALF33 to induce reactive oxygen species (ROS) production in the stigma papillae, whereas pollination reduces stigmatic ROS, allowing pollen hydration. Upon pollination, the POLLEN COAT PROTEIN B-class peptides (PCP-Bs) compete with RALF23/33 for binding to the ANJ–FER complex, leading to a decline of stigmatic ROS that facilitates pollen hydration. Our results elucidate a molecular gating mechanism in which distinct peptide classes from pollen compete with stigma peptides for interaction with a stigmatic receptor kinase complex, allowing the pollen to hydrate and germinate.

In angiosperms, multiple layers of male-female interactions occur throughout pollination (*1*, *2*). During this process, pollen grains land on the stigma and germinate, each producing a pollen tube that elongates into the stylar transmitting tissue and grows toward the ovule for fertilization (*3*). Immediately after adhering to the stigma, compatible pollen must be distinguished from incompatible pollen and other unwanted invasive agents, such as pathogenic spores (*4*, *5*). In response to compatible pollen, stigmas initiate a basal response pathway that transfers water to the desiccated pollen grain for pollen hydration and germination (*6*). The signaling components and the underlying mechanism that regulate this first crucial event in pollination are largely unknown (*6*).

Numerous cysteine-rich peptides (CRPs) have been identified in plant reproduction (*7*). In *Arabidopsis thaliana*, a highly polymorphic family of pollen-borne CRPs, the POLLEN COAT PROTEIN B-class peptides (PCP-Bs), play a role in pollen hydration. The loss of PCP-Bs notably slows pollen hydration and germination (*8*). In a wide spectrum of angiosperms, considerable amounts of reactive oxygen species (ROS) have been detected in the mature, unpollinated stigmas (*9*). In this work, we established that pollination in wild-type (WT) *Arabidopsis* triggered a significant reduction of ROS levels in stigmatic papilla cells in the first 20 min after pollination (MAP) (Fig. 1A and fig. S1A) (*9*). Decreased ROS levels were detected at the pollen adhesion site as early as 1 MAP (Fig. 1B), and by 10 MAP, obvious ROS decline extended to the adjacent area along the papillar cell edge (fig. S1B). Upon pollination by pollen from loss-of-function *PCP-B* mutants (*pcp-b*γ and *pcp-b*β/γ), WT stigmas showed significantly slower pollen hydration and a significantly reduced capacity to suppress stigmatic ROS levels compared to WT stigmas pollinated by WT pollen (Fig. 1C).

We then expressed and purified the PCP-Bβ/γ peptides from insect cells and obtained chemically synthesized PCP-Bγ (cPCP-Bγ). Mass spectrometry analysis showed that both forms of the peptides had molecular masses that were 8 Da lower than expected, suggestive of four disulfide bonds: one between Cys1 and 2; one between Cys7 and 8; one connecting Cys3, 4, or 5; and one connecting Cys6 and either one of Cys3, 4, or 5 (fig. S1, C to E). The latter two we were not able to pinpoint because Cys3, 4, and 5 are too close. WT stigmas treated with PCP-Bγ showed a significant and dose-dependent reduction in ROS (Fig. 1D and fig. S2, A and B). The PCP-B$\gamma_{C30A/C32S/C33A}$ (mPCP-Bγ) did not induce a significant reduction in stigmatic ROS and did not restore pollen hydration (Fig. 1, D and E). We also performed a pistil feeding assay (*10*) with an ROS production inhibitor and ROS scavengers (fig. S2, C and D). It has been reported that the first 10 min of pollen hydration determines the rate of pollen germination (*11*). The ROS-repressed pistils displayed significantly faster pollen hydration in the initial 10 min (Fig. 1F), as well as longer pollen tubes by 4 hours after pollination, probably because of a head start in germination (fig. S2E). These results suggest that pollen PCP-Bs induce a decrease in stigmatic ROS levels that facilitates pollen hydration.

We next explored the signaling components on the stigma that recognize PCP-Bs. Many receptor-like kinases (RLKs) have been identified

[1]School of Life Sciences, East China Normal University, Shanghai, China. [2]School of Life Sciences, Innovation Center for Structural Biology, Tsinghua-Peking Joint Center for Life Sciences, Tsinghua University, Beijing, China. [3]Department of Biochemistry and Molecular Biology, Molecular and Cell Biology Program, Plant Biology Graduate Program, University of Massachusetts, Amherst, MA, USA. [4]National Facility for Protein Science in Shanghai, Zhangjiang Lab, Shanghai Advanced Research Institute, CAS, Shanghai, China.
***Corresponding author. Email: cli@bio.ecnu.edu.cn**

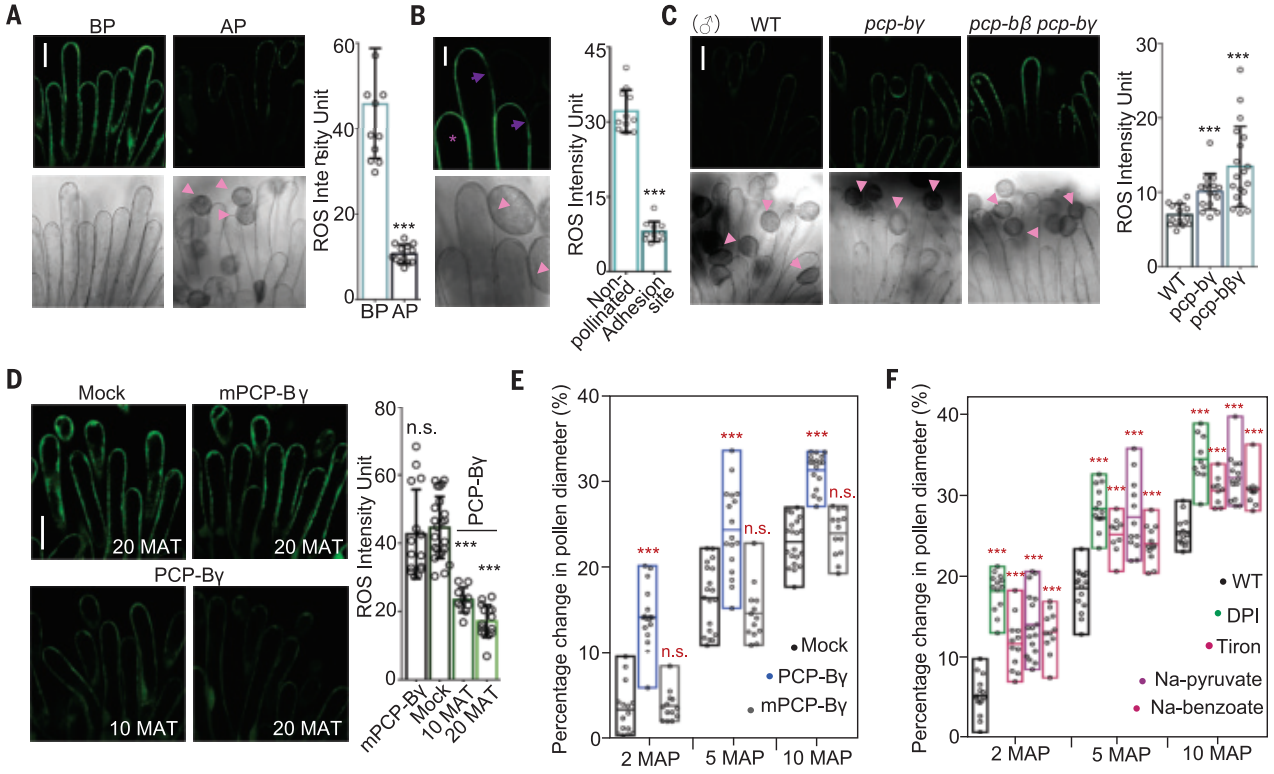

Fig. 1. PCP-Bs in pollen trigger reductions in stigmatic ROS levels. (**A**) ROS dye H_2DCF-DA staining (left) and quantification (right) of ROS level of stigmatic papilla cells from WT *Arabidopsis* before pollination (BP) and 20 min after pollination (AP) with compatible pollen. Bottom, bright-field images. (**B**) ROS dye DHE staining of stigmatic papillae after 1 min of pollination by a single pollen grain. Arrowheads point to the pollen grain adhesion site. Asterisk indicates nonpollinated papilla. (**C**) H_2DCF-DA staining and quantification of ROS levels of papilla cells 20 MAP with *pcp-b*γ and *pcp-b*βγ pollen. Arrowheads indicate pollen grains (A to C). (**D**) H_2DCF-DA staining showing stigmatic ROS levels upon treatment with 0.5 μM PCP-Bγ or mPCP-Bγ. MAT, minutes after treatment. (**E** and **F**) Altered pollen hydration profiles in WT stigmas treated with PCP-Bs (E) or with the NADPH oxidase inhibitor DPI or the ROS scavengers (F). (A) to (F): means ± SD. ***$P < 0.001$ (two-tailed Student's t test); n.s., not significant. n = 13 (A), 11 (B), 14 (C), 10 (D), 15 (E), or 10 (F) stigmas. Scale bars, 20 μm (A, C, and D) or 10 μm (B).

in male-female interactions functioning to perceive peptide signals (*12*, *13*). Therefore, stigmatic RLKs could very likely be involved in mediating pollen PCP-B signals to initiate the stigmatic response. A whole-genome transcriptional analysis has revealed that the ANJEA (ANJ) receptor kinase is highly expressed in the stigma (*14*). *ANJ* belongs to the 17-member *Catharanthus roseus* receptor-like kinase 1–like (CrRLK1L) gene family (*15*). FERONIA (FER), the most extensively studied member of this family, functions as a receptor for several RAPID ALKALINIZATION FACTOR (RALF) CRPs, which control cell growth and immune responses (*16*–*18*). By mining the Genevestigator and TraVA databases, we established that *ANJ* and *FER* are highly expressed in the stigma (fig. S3A), as confirmed by an analysis of *pANJ::GUS* and *pFER::GUS* transgenic plants (fig. S3B).

We identified two *anj* mutant alleles, both knockouts of *ANJ* as revealed by reverse transcription polymerase chain reaction (RT-PCR) analysis (fig. S3C). Compared to the WT, compatible pollen hydrated more rapidly in the *anj* and *fer* single mutant and most rapidly in the *anj-1 fer-4* double-mutant stigmas. The phenotypes were rescued in mutant lines complemented with either the *pANJ::ANJ*–green fluorescent protein (*GFP*) or *pFER::FER-GFP* transgenic constructs (Fig. 2, A and B; fig. S3D; and movie S1). Longer pollen tubes were observed in the *anj-1 fer-4* pistils than in WT pistils 4 hours after pollination (fig. S3E). Lower ROS levels were detected in the *anj* and *fer* mutant stigmas than in WT stigmas, and these were restored by treatment with H_2O_2 (Fig. 2C and fig. S3, F to G). Moreover, regardless of whether pollen from WT or *pcp-b*γ was used for pollination, the *anjfer* stigmas showed faster pollen hydration and longer pollen tubes relative to the WT stigmas (Fig. 2D and fig. S4A).

The similar expression patterns of *ANJ* and *FER* and the similar phenotypes of the *anj* and *fer* mutants suggested that ANJ and FER might function in a protein complex. To test this hypothesis, we performed co-immunoprecipitation (Co-IP) and bimolecular fluorescence complementation assays and established that kinase domain–deleted FERΔK and ANJΔK interacted with each other (fig. S4, B and C). Luciferase complementation assays showed that cytoplasmic domain–deleted ANJΔC and FERΔC also interacted (fig. S4D). Furthermore, a pull-down assay established that the extracellular domains (ECDs) of ANJ and FER interact with each other (fig. S4E). These results demonstrate that ANJ and FER function in a complex and are consistent with yeast two-hybrid assay results in a previous study that focused on late pollination events (*19*). We observed that ANJ and FER were expressed in the stigmatic papillae from flower stage 11 to 14, during which the stigma matures and becomes receptive to pollen (fig. S4F). Given that the ANJ–FER complex and PCP-Bs are both involved in pollination-induced reductions in ROS levels, we hypothesized that ANJ–FER senses the pollen-derived PCP-Bs for compatible pollen recognition. We established that PCP-Bs, but not the mPCP-Bγ, efficiently pulled down maltose-binding protein (MBP)–FER_{ecd}/ANJ_{ecd} (Fig. 2E and fig. S4, G and H). We also detected an interaction between nLuc-FERΔC/ANJΔC and PCP-Bγ-cLuc in a luciferase complementation assay (Fig. 2F). These results indicate that the ANJ–FER complex interacts with PCP-Bs and so could

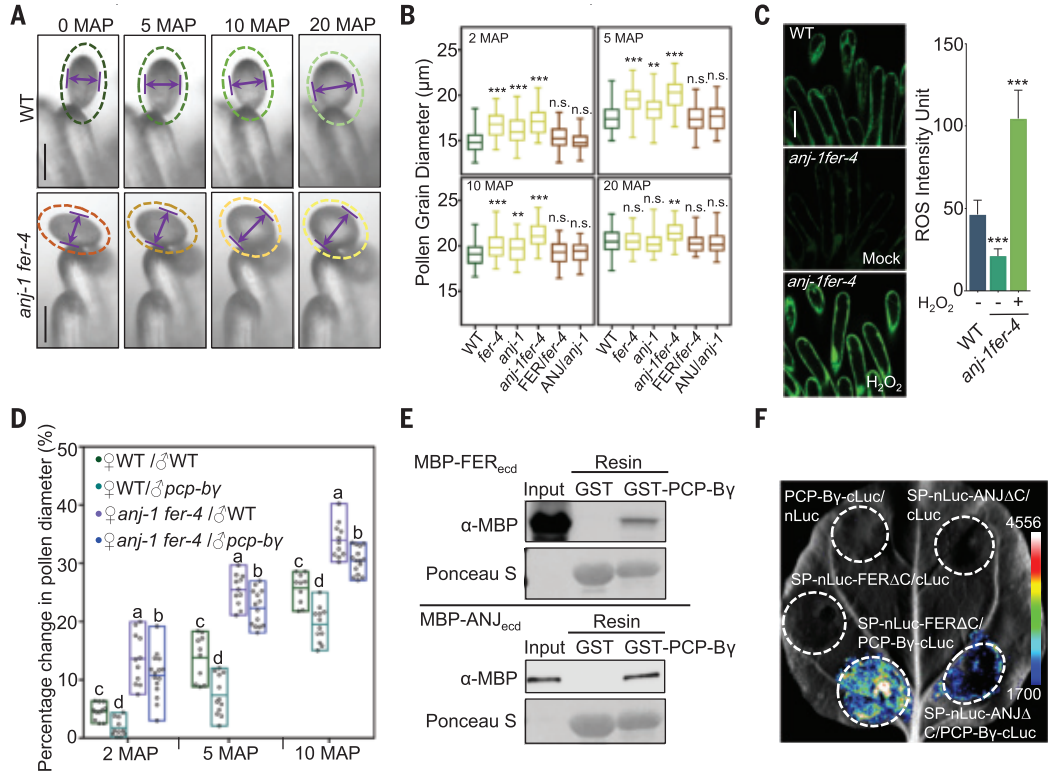

Fig. 2. ANJ and FER are crucial for pollen hydration and PCP-Bγ–induced decreases in ROS levels in stigmatic papilla cells. (**A**) Pollination-induced pollen hydration on stigmas. Equatorial diameters of pollen grains were measured as indicated. (**B**) Pollen hydration rates on stigmas from *fer-4* and *anj-1* single and double mutants with and without genetic complementation. (**C**) H_2DCF-DA staining of *anj-1 fer-4* stigma papillae with and without 10 mM H_2O_2 treatment. (B) and (C): data are means ± SD. $^{**}P < 0.01$; $^{***}P < 0.001$ (two-tailed Student's *t* test). (**D**) Both WT and *pcp-bγ* pollen had faster hydration rates on *anj-1 fer-4* stigmas. One-way analysis of variance ($P < 0.01$). (**E**) Pull-down assay showing interaction of GST-PCP-Bγ with MBP-FER_{ecd} and ANJ_{ecd}. (**F**) Luciferase complementation assay showing interaction between PCP-Bγ-cLuc and nLuc-FERΔC–ANJΔC. SP, signal peptide. In (A) to (C), WT pollen was used for pollination. Scale bars, 20 μm (A and C). *n* = 7 (B), 5 (C), or 16 (D) stigmas.

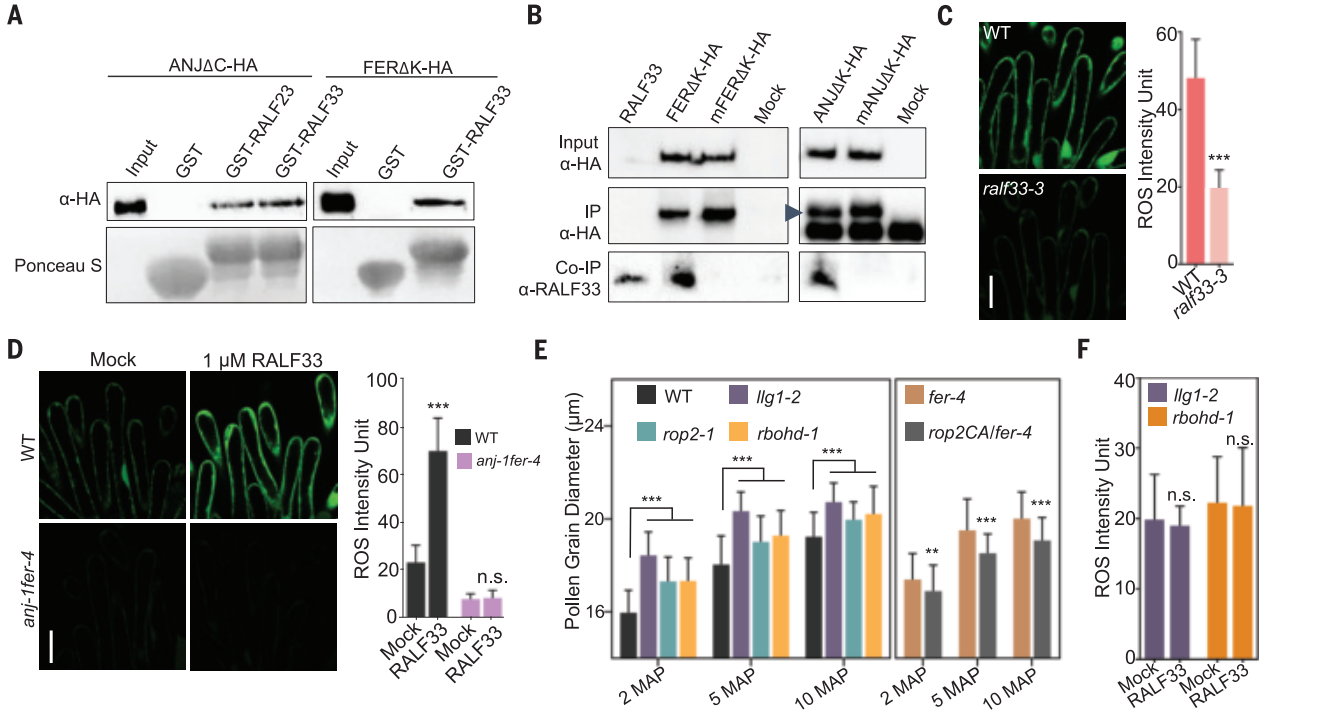

Fig. 3. RALF33 stimulates the ANJ–FER receptor complex to induce ROS production through the RAC/ROP–NADPH oxidase pathway. (**A**) Pull-down assay showing interaction of RALF23/33 with ANJΔC-hemagglutinin (HA). (**B**) Co-IP showing interaction of RALF33 with FERΔk/mFERΔk/ANJΔk/mANJΔk-HA. Arrowhead indicates immunoglobulin heavy chain. (**C**) H_2DCF-DA staining of the stigmatic papillae of *ralf33-3*. (**D**) ROS levels in WT and *anj-1 fer-4* stigmas treated with 1 μM RALF33 for 20 min. (**E**) Pollen hydration profiles of WT, *llg1-2*, *rop2-1*, *rbohd-1*, and *pROP2::rop2CA fer-4* stigmas. (**F**) ROS levels in *llg1-2* and *rbohd-1* papilla cells with or without (Mock) treatment with 1 μM RALF33 for 20 min. (C) to (F): means ± SD. $^{**}P < 0.01$, $^{***}P < 0.001$ (two-tailed Student's *t* test). Scale bars, 20 μm (C and D). *n* = 16 (C), 10 (D), 10 (E), or 11 (F) stigmas.

function as the receptor complex that senses the PCP-Bs.

RALF peptides have been characterized as the ligand of FER in different tissues (*16*, *17*, *20*). Based on Genevestigator data and the quantitative RT-PCR analysis, *RALF23* and *RALF33* are the most highly expressed RALF genes in the stigma (fig. S5, A and B). FER and RALF23 are known to interact (*17*, *18*), and our pull-down and Co-IP assays showed that FERΔK and ANJΔC interacted with RALF33 (Fig. 3, A and B, and fig. S5C). On the basis of structural information (*18*), we mutated the amino acids in FER and analogous positions in ANJ that are critical for FER–RALF–LLG complex formation and observed that the resulting proteins showed a much weaker interaction with RALF33 (Fig. 3B). The interactions of nLuc-FERΔC/ANJΔC with RALF33-cLuc in a luciferase complementation assay further confirmed their interactions (fig. S5D). To investigate the function of RALF33 in stigmatic papillae, we obtained the published *ralf33-2* mutant (*17*) and characterized *ralf33-3*, an independent knockout mutant of RALF33 (fig. S5E). Similar to the phenotypes of *anj*- and *fer*-related mutants, *ralf33* mutants produced pistils that supported more rapid pollen hydration, which led to longer pollen tubes (fig. S5, F and G). ROS staining showed that loss of RALF33 resulted in reduced ROS accumulation in the stigmatic papilla cells (Fig. 3C and fig. S5H), whereas treatment with 1 μM RALF33 significantly induced ROS production in stigmatic papillae (Fig. 3D).

FER and its co-receptor LLG1 activate the guanine nucleotide exchange factors (GEFs) of Rho-like GTPases from plants (RAC/ROP) and the reduced form of nicotinamide adenine dinucleotide phosphate (NADPH) oxidase, thereby inducing ROS production in roots and root hairs (*21*, *22*). Because ANJ–FER binds to RALF33 and RALF33 induces ROS production, we propose a pathway in which RALF33 stimulates the ANJ–FER receptor complex to activate ROS production through the RAC/ROP–NADPH oxidase pathway. RALF33 treatment did not induce a marked increase in ROS levels in *anj-1 fer-4* mutant stigmas (Fig. 3D). Based on a transcriptional analysis of the *LORELEI* family genes, we established that LLG1 is the most abundant member of that family in the stigma (fig. S6A). Similar to the *fer-4* mutant, the *llg1-2* mutant showed reduced ROS accumulation in stigmatic papillae (fig. S6B). RAC/ROP-regulated NADPH oxidases play a major role in cytoplasmic ROS production (*23*). Based on Genevestigator data and the RT-PCR analysis, we identified RBOHD as the most abundantly expressed gene of the RBOH family in the stigma (fig. S6C). We obtained the published *rbohd* mutant (*24*) and a knockout mutant of RBOHD, *rbohd-1*, both of which showed lower stigmatic ROS than the WT plants in the unpollinated pistils (fig. S6, D and E). Next, we found that a mutant of the most abundant stigmatic RAC/ROP, ROP2, had reduced stigmatic ROS levels before pollination (fig. S6, F and G). Similar to *fer-4* mutant stigmas, the *llg1-2*, *rop2-1*, and *rbohd-1* mutant stigmas all supported significantly more rapid pollen hydration than WT stigmas (Fig. 3E). By contrast, a transgenic complementation mutant of ROP2 (*ROP2p::rop2CA*) showed partial reversion of the faster pollen hydration and reduced stigmatic ROS of the *fer-4* mutant, consistent with rop2CA being a constitutive activator of RBOH (22) (Fig. 3E and fig. S6G). Moreover, the *llg1-2* and *rbohd-1* mutants were both less responsive to RALF33-induced ROS elevation than the WT, as shown earlier (Fig. 3F). These results suggest that the ANJ–FER complex senses the autocrine RALF33 peptides and then activates ROS production in stigmatic papillae through the ROP2–RBOHD pathway, which suppresses pollen hydration.

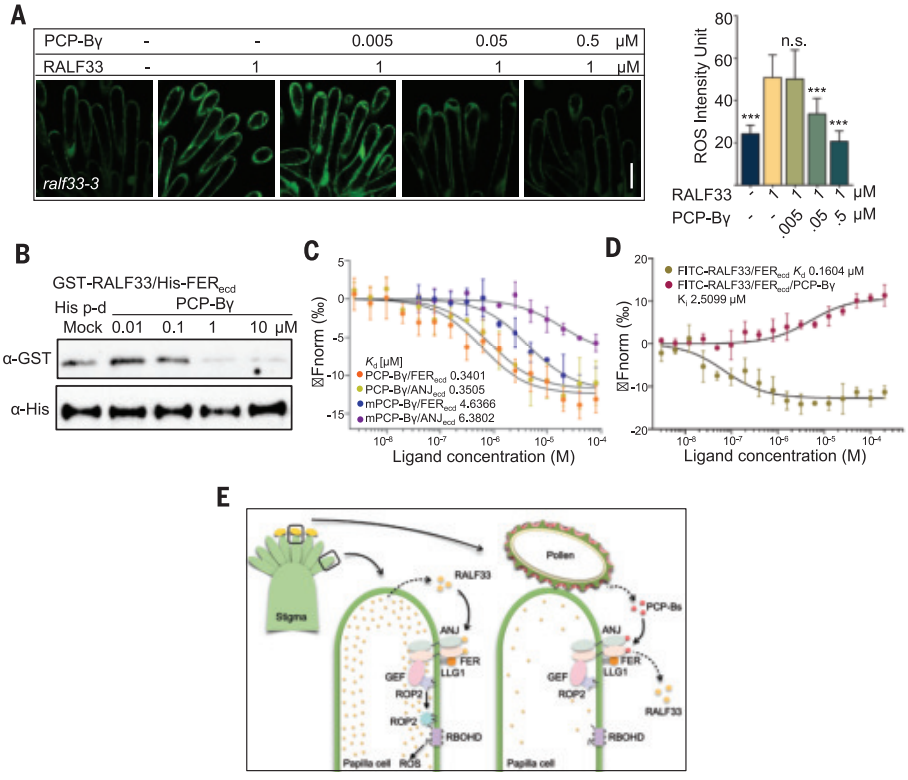

Fig. 4. PCP-Bs compete with RALF23/33 for interaction with the ANJ–FER receptor complex. (**A**) H_2DCF-DA staining and quantification of ROS levels of *ralf33-3* mutant stigma co-treated with PCP-Bγ and RALF33 (means ± SD; n = 10 stigmas). ***P < 0.001 (two-tailed Student's t test). Scale bar, 20 μm. (**B**) Pull-down assay showing competition by PCP-Bγ with GST-RALF33 in interaction with His-FER_{ecd}. His-FER_{ecd} was used to pull down GST-RALF33. (**C**) Quantification of binding affinity between fluorescently labeled FER_{ecd}/ANJ_{ecd} and PCP-Bγ/mPCP-Bγ by microscale thermophoresis (MST). (**D**) MST analysis of the inhibition of PCP-Bγ in the interaction of FITC-RALF33 with FER_{ecd}. (**E**) Model of pollen peptide repression of stigma-peptide–induced ROS production by means of receptor kinases. Before pollination, RALF23/33 induces ROS production in the stigmatic papilla cells through an ANJ–FER–ROP2–RBOHD pathway. Upon pollination, PCP-Bs from the pollen coat compete with RALF23/33 for interaction with the ANJ–FER complex, repressing ROS production and initiating stigmatic responses.

Next, we examined how the ANJ–FER complex coordinates PCP-Bs and RALF33 to regulate ROS levels in the stigma. We mixed PCP-Bγ and RALF33 to co-treat stigmas in ROS and pollen hydration assays. The application of PCP-Bγ suppressed the effect of RALF33 in inducing stigmatic ROS in a dose-dependent manner (Fig. 4A). Consistent with this, RALF33 treatment reversed the faster pollen hydration of *ralf33-3* stigmas, and the addition of PCP-Bγ, but not mPCP-Bγ, countered this effect (fig. S7A). In a luciferase complementation assay that used the nLuc-FERΔC/RALF33-cLuc combination, the addition of cPCP-Bγ significantly and dose-dependently reduced the luciferase signal (fig. S7B). Pull-down assays showed that PCP-Bγ, but not mPCP-Bγ, competed dose-dependently with glutathione *S*-transferase (GST)–RALF33 for interaction with His-FER_{ecd} (Fig. 4B and fig. S7, C and D). Microscale thermophoresis confirmed that RALF23 and RALF33 each interacted with FER_{ecd} and ANJ_{ecd} (fig. S7E). FER_{ecd}

and ANJ_{ecd} interacted with PCP-Bγ with dissociation constants (K_d) of 0.34 and 0.35 μM, respectively, but showed K_d of only 4.63 and 6.38 μM when interacting with mPCP-Bγ (Fig. 4C). Furthermore, fluorescein isothiocyanate (FITC)–RALF33 interacted with FER_{ecd} with a K_d of 0.1604 μM, and the PCP-Bγ added to the mixture competed with the RALF33–FER_{ecd} interaction with an inhibition constant (K_i) of 2.5099 μM (Fig. 4D). Together, these results suggest that PCP-Bγ competes with RALF33 for binding to FER_{ecd}/ANJ_{ecd}, which results in the suppression of RALF33-induced ROS production in the stigma.

Once pollen lands on a stigma, signal communications between pollen and the stigma papilla are initiated; this is thus likely to be the earliest checkpoint in pollen-stigma interactions. In this work, we identified a RALF33–ANJ/FER receptor kinase–RAC/ROP–RBOHD signaling pathway that controls the generation of stigmatic ROS. Our findings further uncovered an intricate regulatory mechanism by which pollen-derived PCP-Bs compete with stigma-produced RALF33, thereby repressing stigmatic ROS levels to facilitate pollen hydration (Fig. 4E). This work demonstrates the versatility of a receptor kinase in being able to perceive and switch interactions with different types of peptide ligands. Together with the earlier findings on peptide competitions in stomatal patterning (*25*), pollen tube burst (*20*), and pollen germination (*26*), our work reinforces the concept that antagonistic peptide–receptor kinase pairs fine-tune plant developmental processes (*27*). As CrRLK1L, RALFs, PCP-Bs, RAC/ROPs, and NADPH oxidases are all conserved in the plant kingdom, the antagonistic control of ROS levels by PCP-Bs and RALFs through CrRLK1L might represent a fundamental mechanism by which compatible pollen disengages stigma gating in flowering plants.

REFERENCES AND NOTES

1. L. A. Chapman, D. R. Goring, *J. Exp. Bot.* **61**, 1987–1999 (2010).
2. M. A. Johnson, J. F. Harper, R. Palanivelu, *Annu. Rev. Plant Biol.* **70**, 809–837 (2019).
3. R. Swanson, A. F. Edlund, D. Preuss, *Annu. Rev. Genet.* **38**, 793–818 (2004).
4. S. J. Hiscock, A. M. Allen, *New Phytol.* **179**, 286–317 (2008).
5. P. A. Bedinger, A. K. Broz, A. Tovar-Mendez, B. McClure, *Plant Physiol.* **173**, 79–90 (2017).
6. J. Doucet, H. K. Lee, D. R. Goring, *Trends Plant Sci.* **21**, 1058–1067 (2016).
7. L. J. Qu, L. Li, Z. Lan, T. Dresselhaus, *J. Exp. Bot.* **66**, 5139–5150 (2015).
8. L. Wang *et al.*, *New Phytol.* **213**, 764–777 (2017).
9. S. M. McInnis, R. Desikan, J. T. Hancock, S. J. Hiscock, *New Phytol.* **172**, 221–228 (2006).
10. Q. Duan *et al.*, *Nat. Commun.* **5**, 3129 (2014).
11. F. Rozier *et al.*, *J. Exp. Bot.* **71**, 2513–2526 (2020).
12. H. Li, W. C. Yang, *Sci. China Life Sci.* **59**, 867–877 (2016).
13. S. Zhong, L. J. Qu, *Curr. Opin. Plant Biol.* **51**, 7–14 (2019).
14. C. W. Tung, K. G. Dwyer, M. E. Nasrallah, J. B. Nasrallah, *Plant Physiol.* **138**, 977–989 (2005).
15. C. Li, H. M. Wu, A. Y. Cheung, *Plant Physiol.* **171**, 2379–2392 (2016).
16. M. Haruta, G. Sabat, K. Stecker, B. B. Minkoff, M. R. Sussman, *Science* **343**, 408–411 (2014).
17. M. Stegmann *et al.*, *Science* **355**, 287–289 (2017).
18. Y. Xiao *et al.*, *Nature* **572**, 270–274 (2019).
19. S. Galindo-Trigo *et al.*, *EMBO Rep.* **21**, e48466 (2020).
20. Z. Ge *et al.*, *Science* **358**, 1596–1600 (2017).
21. Q. Duan, D. Kita, C. Li, A. Y. Cheung, H. M. Wu, *Proc. Natl. Acad. Sci. U.S.A.* **107**, 17821–17826 (2010).
22. C. Li *et al.*, *eLife* **4**, e06587 (2015).
23. C. H. Hu *et al.*, *Cells* **9**, 437 (2020).
24. J. Zhang *et al.*, *Cell Host Microbe* **1**, 175–185 (2007).
25. J. S. Lee *et al.*, *Nature* **522**, 439–443 (2015).
26. W. Tang, D. Kelley, I. Ezcurra, R. Cotter, S. McCormick, *Plant J.* **39**, 343–353 (2004).
27. J. S. Lee, I. De Smet, *Trends Plant Sci.* **21**, 991–993 (2016).

ACKNOWLEDGMENTS

We thank the staff members of the Large-scale Protein Preparation System at the National Facility for Protein Science in Shanghai, Zhangjiang Laboratory, China, for providing technical support and assistance in data collection and analysis; W.-G. Zheng (U. Mass) for generating the *anj-1 fer-4* mutant; J. Yu. for generating the transgenic line of *pROP2:rop2CA/fer-4*; J.-M. Zhou and C. Zipfel for the gifts of the *rbohd* and *ralf33-2* mutants, respectively; and M. Sun and members of the Cheung-Wu laboratory for comments on the manuscript. **Funding:** Work from the Li laboratory was supported by grants from the National Science Foundation of China (31972863 and 31770307) and by East China Normal University. Work from the Cheung-Wu laboratory was supported by US-NSF (IOS-1147165, 1146941, and 1645854 and MCB-1715764) and U. Mass NIFA/USDA (MAS00525). Z.H. was supported by the National Natural Science Foundation of China (31971119). **Author contributions:** C.Li designed and led the project and prepared the manuscript. C.Liu conducted all the experiments and helped prepare the manuscript. L.S. contributed to all the experiments. Y.X. purified all the protein and peptides from insect cells and contributed to the protein interaction experiments. D.V. genetically characterized the *anj-1 fer-4* mutant and performed founding analyses of mutant phenotypes, transgenic lines for *pANJ:GUS*, and ANJ-GFP localization. C.P. performed the mass spectrometry and data analysis. X.S. performed the bioinformatics, data analysis, and figure designing. L.C. contributed to ROS assays. Z.L. contributed to protein interaction assays. H.Z. contributed to the MST assays. A.Y.C. and H.-M.W. supervised D.V. and edited the manuscript. All authors discussed and approved the manuscript. **Competing interests:** The authors declare no competing interests. **Data and materials availability:** All data are available in the manuscript or the supplementary materials.

SUPPLEMENTARY MATERIALS

science.sciencemag.org/content/372/6538/171/suppl/DC1
Materials and Methods
Figs. S1 to S7
Tables S1 and S2
References (*28*–*35*)
Movie S1
MDAR Reproducibility Checklist

5 May 2020; resubmitted 3 January 2021
Accepted 1 March 2021
10.1126/science.abc6107

REPORTS

ORGANIC CHEMISTRY

Boron insertion into alkyl ether bonds via zinc/nickel tandem catalysis

Hairong Lyu[1], Ilia Kevlishvili[2], Xuan Yu[1], Peng Liu[2]*, Guangbin Dong[1]*

Mild methods to cleave the carbon-oxygen (C–O) bond in alkyl ethers could simplify chemical syntheses through the elaboration of these robust, readily available precursors. Here we report that dibromoboranes react with alkyl ethers in the presence of a nickel catalyst and zinc reductant to insert boron into the C–O bond. Subsequent reactivity can effect oxygen-to-nitrogen substitution or one-carbon homologation of cyclic ethers and more broadly streamline preparation of bioactive compounds. Mechanistic studies reveal a cleavage-then-rebound pathway via zinc/nickel tandem catalysis.

Ether moieties are commonly found in feedstock and fine chemicals (*1*). In particular, cyclic ethers are prevalent in a wide array of biologically important molecules, including drugs, agrochemicals, and natural products (Fig. 1A). In addition, ethers often act as effective structural linkers and protecting groups in organic synthesis owing to their high chemical stability toward acids, bases, reductants, and oxidants (*2*). Thus, mild methods that directly edit an ether moiety, i.e., replacing the oxygen or inserting an intervening atom into the C–O bond, could be strategically important for convenient introduction of new functional groups into existing molecular scaffolds (*3*–*6*). From a synthesis-planning viewpoint, it would also be attractive to use robust ethers as surrogates for more-sensitive chemical groups that could be installed at a later stage.

Conventionally, alkyl ether bonds can be cleaved under harsh and strongly acidic conditions, e.g., treatment with concentrated HBr/HI and heat, or through the use of strong Lewis acids, such as BBr_3 and trimethylsilyl iodide [for a review of C–O cleavage of alkyl ethers, see (*7*)]. Although insertion of a low-valent transition metal into C–O bonds via oxidative addition has emerged as a mild and effective approach for constructively forming C–C bonds (Fig. 1B), the scope is mainly restricted to sp^2

[1]Department of Chemistry, University of Chicago, Chicago, IL 60637, USA. [2]Department of Chemistry, University of Pittsburgh, Pittsburgh, PA 15260, USA.
***Corresponding author. Email: gbdong@uchicago.edu (G.D.); pengliu@pitt.edu (P.L.)**

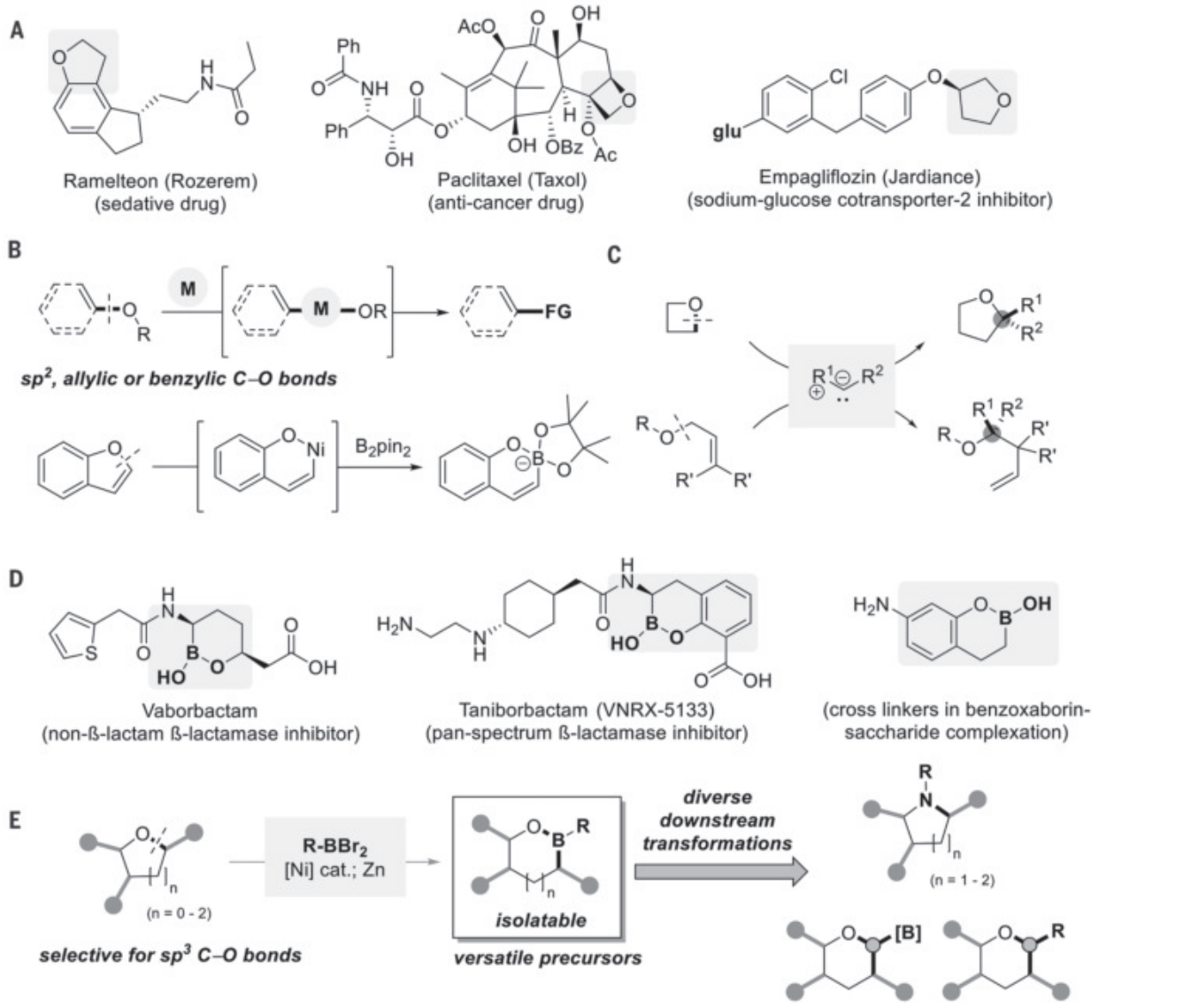

Fig. 1. Functionalization of ether bonds. (**A**) Small-molecule drugs containing cyclic ether moieties. Ph, phenyl; Ac, acetyl; Bz, benzoyl; glu, glucose. (**B**) Transition metal–catalyzed C–O cleavage via oxidative addition. R, alkyl; M, transition metal; FG, functional group; B_2pin_2, bis(pinacolato)diboron. (**C**) Carbene insertion into activated ethers. (**D**) Cyclic boronate derivatives as drug candidates or cross-linkers for biomedical materials. (**E**) This work: a Ni-catalyzed direct boron insertion via a cleavage-then-rebound pathway.

or benzylic and allylic C–O bonds (*3*–*6*, *8*–*17*). Notably, a formal boron insertion into benzofuran C(sp^2)–O bonds through catalytic coupling with bis(pinacolato)diboron was recently reported by Yorimitsu and colleagues (*17*); this condition is not suitable for cleaving alkyl ethers. Alternatively, carbene insertion into C(sp^3)–O bonds represents a more straightforward tactic to form C(sp^3)–C(sp^3) bonds but typically requires strained cyclic ethers such as oxetanes, or allyl ethers (Fig. 1C) [(*18*); for a selected example of carbene insertion into the C–O bond of strained cyclic ethers, see (*19*)].

In 1984, Pachaly and West reported that a silyl-borylene generated under photochemical conditions inserted into the C–O bond of tetrahydrofuran (THF) in solid state at –196°C (*20*), which represents the sole example of such a transformation. We wondered whether a general ether-editing method could be realized through a direct boron insertion into unactivated C(sp^3)–O bonds. Given the versatility of the resulting C–B bond, this strategy could facilitate conversion of common inert ethers to diverse other functional groups. Moreover, the direct boron-insertion products from cyclic ethers, namely cyclic boronates, have established utility in drug development and biomedical material synthesis (Fig. 1D) (*21*–*23*). Here, we describe the development of a mild and direct boron-insertion method for ether editing (Fig. 1E).

Inspired by the recent advances in borylene chemistry (*24*, *25*), our initial strategy was to functionalize ether bonds through insertion of an active borylene species, which we originally expected to form in situ by a transition metal–catalyzed reduction of dihaloboranes. To establish a practical method with broad functional group tolerance, we sought to avoid strong reductants, expensive catalysts, and forcing reaction conditions. Hence, our study started with 2,3-dihydrobenzofuran as the model ether substrate and $MesBBr_2$ (**2a**; Mes, mesityl) as the boron reagent, and various first-row transition metal catalysts and mild reductants were examined (table S1). The bulky Mes group was intended to prevent dimerization of reduced boron species (*26*) and to enhance the stability of the boron-insertion product for isolation. The combination of a Ni catalyst and zinc powder

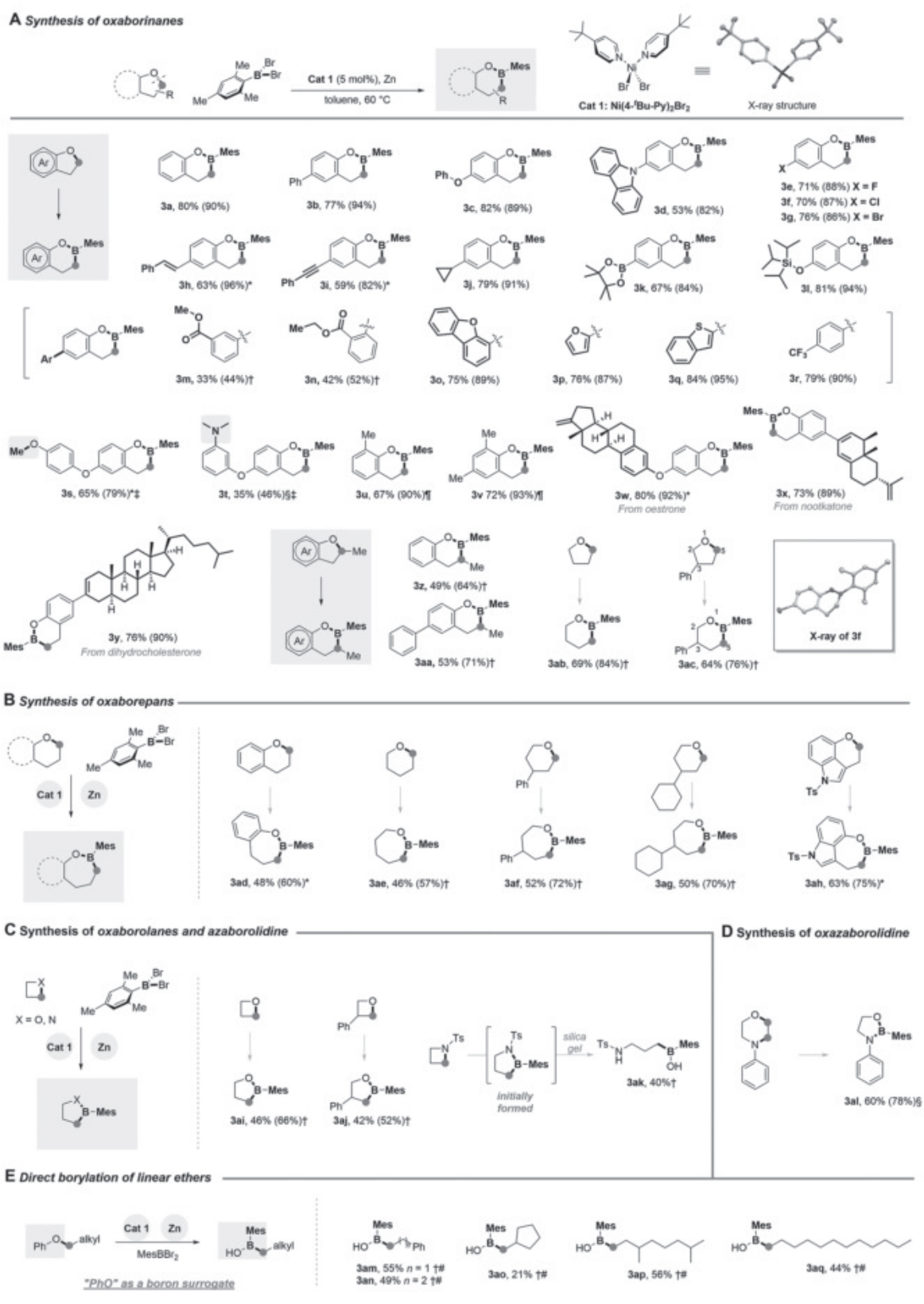

Fig. 2. Nickel-catalyzed borylation of cyclic ethers. (**A**) Synthesis of oxaborinanes via direct borylation of five-membered cyclic ethers. Me, methyl; Ar, aryl. (**B**) Synthesis of oxaborepans via direct borylation of six-membered cyclic ethers. Ts, tosyl. (**C**) Synthesis of oxaborolanes and azaborolidine via direct borylation of cyclooxabutanes and azetidine. (**D**) Synthesis of the oxazaborolidine via direct borylation of 4-phenyl-morpholine. (**E**) Synthesis of borinic acids via direct borylation of linear ethers. Reactions were conducted with 0.2 mmol ether, 0.24 mmol $MesBBr_2$, 0.01 mmol **Cat 1**, and 1 mmol zinc powder in 0.5 ml of toluene at 60°C under nitrogen for 24 hours. Isolated yields after silica gel chromatography are given; the numbers in parentheses are nuclear magnetic resonance yields before purification. *Reaction was run at 80°C. †Reaction was run at 100°C. ‡0.2 mmol $MesBBr_2$ was used. §Reaction was run at 130°C. ¶Ni$(PMe_3)_2Cl_2$ (0.01 mmol) was used as the catalyst, and the reaction was run at 130°C for 18 hours. #Reaction time was 36 hours.

(unactivated) was found to be most effective. Ultimately, the desired boron insertion product, 2*H*-benzoxaborin (**3a**), was obtained in 90% yield in toluene at 60°C (table S1, entry 1).

Boron selectively inserted into the C(sp^3)–O bond rather than the C(sp^2)–O bond, which is opposite to the selectivity of the known Ni-catalyzed C–O cleavages via oxidative addition (*3*–*6*), thus implying a starkly different reaction pathway (see below). An air-stable tetrahedral Ni(II) complex, Ni(4-^{t}Bu-Py)$_2$Br$_2$ (**Cat 1**, 5 mol %), the structure of which was

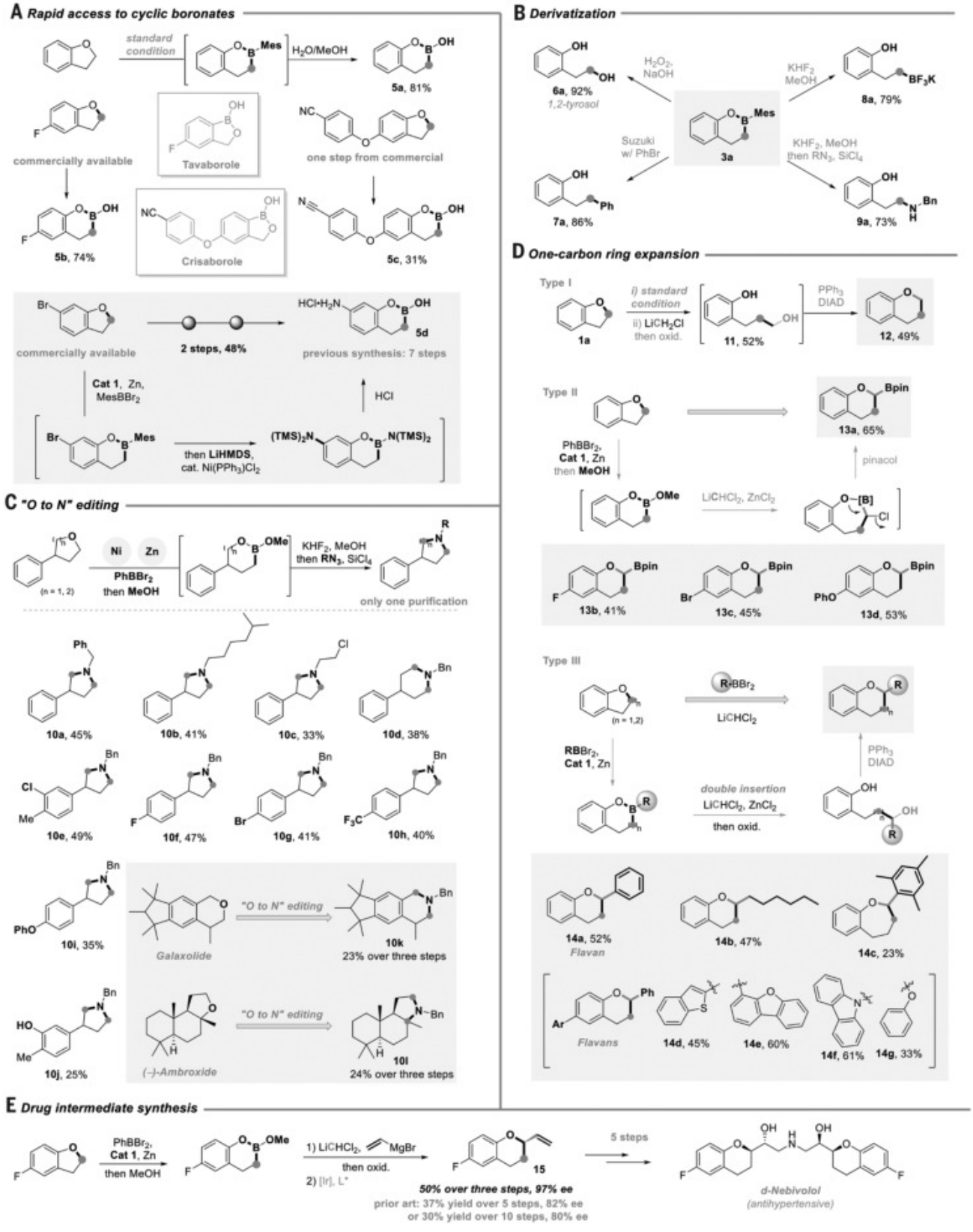

Fig. 3. Synthetic elaboration. (**A**) Rapid access to cyclic boronates via one-pot hydrolysis. The boronate products (**5a** to **5c**) are substantially more stable toward air and moisture. (**B**) Further functionalization of the borylation product through derivatization of the C–B bond. Bn, benzyl. (**C**) O-to-N editing to access pyrrolidines and piperidines from tetrahydrofurans and tetrahydropyrans, respectively. (**D**) Three approaches for one-carbon ring expansion of cyclic ethers. DIAD, diisopropyl azodicarboxylate. (**E**) Streamlined synthesis of the antihypertensive drug nebivolol. For detailed reaction protocols, see the supplementary materials.

confirmed by x-ray crystallography, was superior to other Ni precatalysts or other metals (for more details, see table S2).

In the absence of **Cat 1**, less than 1% of 2*H*-benzoxaborin (**3a**) was observed, and the ring-opening alkyl bromide intermediate (**4a**) was formed in high yield (table S1, entry 2). $Ni(PMe_3)_2Cl_2$ also gave the desired product, albeit in a much lower yield (table S1, entry 3). Similar efficiency was observed using an in situ generated catalyst from $NiBr_2$ and 4-^{t}Bu-Py (**L1**) (table S1, entry 4); in contrast, $NiBr_2$ alone was not effective (table S1, entry 5). Given the critical role of the **L1** ligand, other nitrogen-based ligands were examined (table S1, entry 6). In general, monodentate ligands worked better than bidentate ligands (**L1** to **L7** versus **L8** to **L12**). 3-Methylpyridine (**L5**) exhibited slightly lower reactivity, while most other monopyridines (**L2**, **L3**, **L4**, and **L6**) and oxazoline (**L7**) were much less effective (for a discussion of

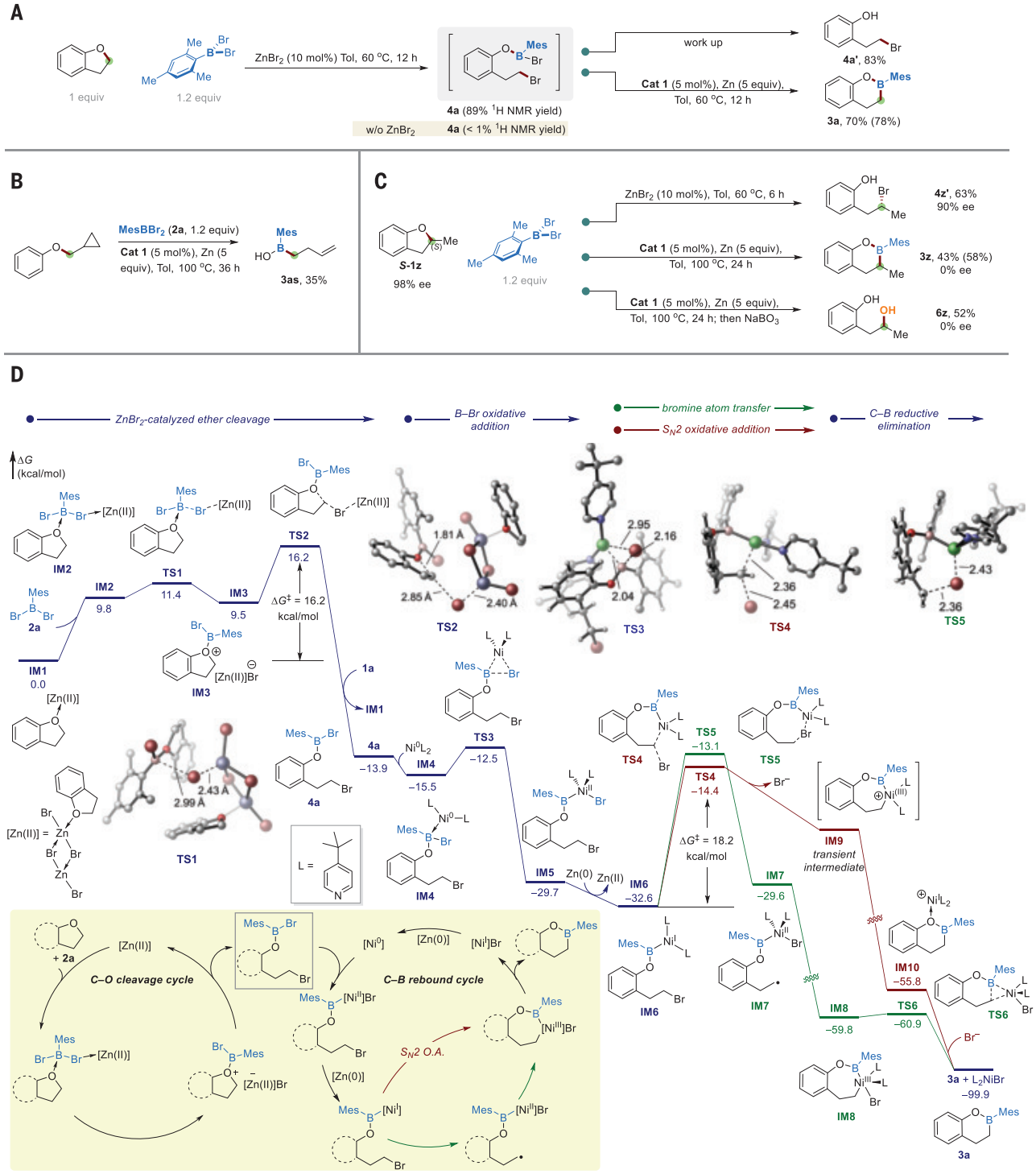

Fig. 4. Mechanistic studies. (**A**) Identification of the reaction intermediate. (**B**) Radical-clock experiment. (**C**) Control experiments with a 98% ee substrate. (**D**) Computed energy profile of the catalytic borylation of ether **1a**. Calculations were performed at the M06/SDD-6-311+G(d,p)/SMD(toluene)//B3LYP-D3/SDD-6-31G(d) level of theory. Inset shows proposed Zn/Ni tandem catalysis.

ligand effect, see table S3 and related descriptions). Zinc powder also proved to be essential, as almost no conversion of ether **1a** was observed without Zn (table S1, entry 7). Use of Mn powder or an even stronger Mg reductant gave almost no desired product (table S1, entries 8 and 9), implying additional roles of Zn besides reductant (see below). Although toluene was the optimal solvent, good yield was still obtained using benzene (table S1, entry 10); in contrast, no 2*H*-benzoxaborin product **3a** was formed in 1,2-dichloroethane (table S1, entry 11). Finally, the boron-insertion reaction could still proceed at room temperature, albeit at a low reaction rate (table S1, entry 12).

The ether scope was subsequently examined for this boron-insertion reaction (Fig. 2). First, a range of substituted 2,3-dihydrobenzofurans reacted with $MesBBr_2$ smoothly to afford the desired boron-insertion products in good-to-excellent yields. Substrates bearing halogens, such as F, Cl, and Br, which are known to undergo Ni-catalyzed cross-couplings (*4*), were compatible to give the corresponding 2*H*-benzoxaborins **3e**, **3f**, and **3g** in >70% isolated yield. Various C(sp^2)–O bonds remained inert under the standard reaction conditions, while the boron insertion occurred chemoselectively at the C(sp^3)–O bond (**3c**, **3l**, and **3o**). Substrates containing unsaturated alkenyl, alkynyl, and cyclopropyl groups produced **3h**, **3i**, and **3j** in 63, 59, and 79% isolated yields, respectively, without reduction of these unsaturated moieties. Both pinacol boronate and silyl ether moieties were well tolerated in this reaction (**3k** and **3l**). In addition, the ester substituent on dihydrobenzofuran was compatible, albeit with moderate yields (**3m** and **3n**), probably owing to the coordination effect of the carbonyl moiety to boron. Moreover, heterocycles, such as carbazole (**3d**), dibenzofuran (**3o**), furan (**3p**), and benzothiophene (**3q**), were also tolerated. Substrates containing trifluoromethyl (**3r**), amino (**3t**), or *ortho*-methyl (**3u** and **3v**) substituents all reacted in high yields. A substrate containing a methyl ether moiety still afforded the desired oxaborinane (**3s**) in good yield, suggesting that the boron insertion occurs preferentially at the five-membered ether (fig. S10). Further control experiments showed that primary alkyl chloride was fully compatible and primary alkyl bromide was partially compatible under the current reaction conditions, while the corresponding primary alkyl fluoride was not tolerated, likely because of strong boron–fluorine interactions (fig. S9).

Complex substrates derived from terpene natural products, including oestrone, nootkatone, and dihydrocholestrone, smoothly underwent the boron-insertion reaction to deliver the desired products **3w**, **3x**, and **3y** in high yields. Bulkier 2-methyl-2,3-dihydrobenzofurans still afforded the corresponding oxaborinanes **3z** and **3aa**, and the diminished reactivity was likely due to sterics. In addition to dihydrobenzofurans, tetrahydrofuran gave the expected mono boron-insertion product (**3ab**) in 69% isolated yield. When unsymmetrical 3-phenyl-tetrahydrofuran was used as the coupling partner, the boron insertion occurred regioselectively at the less bulky C5 position (**3ac**), further indicating the influence of sterics. Less strained six-membered cyclic ethers were also examined. Although all the substrates exhibited good reactivity, the resultant seven-membered oxaborepans (**3ad**, **3ae**, **3af**, **3ag**, and **3ah**) were isolated in moderate yields. Among them, an indole-fused chromane substrate gave an interesting 5-6-7 tricyclic boron-containing scaffold (**3ah**).

The boron insertion into more-strained oxetanes proceeded as well, which provided an entry to five-membered oxaborolanes **3ai** and **3aj** (Fig. 2C). Compromised selectivity resulted in linear side products. Similarly, the C(sp^3)–N bond in Ts-protected azetidines could also be cleaved under the standard conditions; the desired azaborolidine was formed initially but then hydrolyzed to the corresponding borinic acid **3ak** during chromatography. Unexpectedly, the reaction of a morpholine moiety with $MesBBr_2$ directly afforded oxazaborolidine **3al** in good yield, in which both the C(sp^3)–N and C(sp^3)–O bonds were cleaved and formation of ethylene as a by-product was detected (Fig. 2D and fig. S1). The C(sp^3)–O bond in linear ethers could also be borylated under the standard conditions (Fig. 2E). The corresponding borinic acids (**3am**, **3an**, **3ao**, **3ap**, and **3aq**) were instead isolated owing to the rapid hydrolysis of the linear boron-insertion products during chromatography. This transformation directly replaces the OPh group in the substrate with a boryl moiety that could serve as a handle for further functionalization.

From the viewpoint of synthetic utility, the B–Mes bond in products can easily undergo one-pot hydrolysis by adding water in methanol to give the corresponding hydroxyl boronate products (e.g., **5a**), which are much more stable in air (Fig. 3A). From readily available 2,3-dihydrobenzofurans, functionalized cyclic boronates (**5b** and **5c**) were synthesized in one step, which could be considered as ring-expanded C/O swapped analogs of tavaborole (an approved antifungal drug) and crisaborole (an approved drug for treatment of dermatitis). In addition, the amine-substituted hydroxyl benzoxaborin (**5d**), a known cross-linker for constructing saccharide-based hydrogels, was recently prepared in seven steps (*23*); for comparison, subjection of commercially available 6-bromo-2,3-dihydrobenzofuran to this boron-insertion condition, followed by one-pot aminolysis of the B–Mes bond and a Ni-catalyzed C–N bond formation using lithium bis(trimethylsilyl)amide (LiHMDS) as the amine source (*27*), provided the cyclic boronate product **5d** in 48% yield in two steps.

As expected, the boron moiety in the insertion products could be conveniently converted to various other functional groups (Fig. 3B). For example, treatment of the crude product **3a** with hydrogen peroxide and base afforded 1,2-tyrosol (**6a**) in excellent yield. The Suzuki–Miyaura coupling of **3a** with bromobenzene efficiently provided *o*-phenethylphenol (**7a**). The 2*H*-benzoxaborin product could be easily transformed to the potassium trifluoroborate (Molander salt) **8a**, which could serve as a precursor of a carbon radical or nucleophile (*28*). Treatment of **8a** with BnN_3 converted the C–B bond to a C–N bond (**9a**). In addition, an O-to-N editing strategy was conveniently achieved when using less-bulky $PhBBr_2$ as the reagent for the boron insertion (Fig. 3C) (*29*). The resulting methanolysis intermediates could be first transformed to the Molander salts, followed by amination of the C–B bonds and in situ dehydration, to afford the corresponding pyrrolidines and piperidines (**10a** to **10k**) from tetrahydrofurans and tetrahydropyrans, respectively. The drug molecule (–)-ambroxide that contains a trisubstituted tetrahydrofuran moiety was also a suitable substrate (**10l**).

This method also enables efficient one-carbon ring expansion reactions (Fig. 3D). Type I ring expansion involves direct homologation of the boron-insertion product with $LiCH_2Cl$ (*30*, *31*) followed by an intramolecular Mitsunobu reaction, which converts 2,3-dihydrobenzofuran to chromane **12**. Type II expansion capitalizes on the boronate intermediate after the methanolysis, which can initiate a boron-based homologation with $LiCHCl_2$ followed by a $ZnCl_2$-mediated (*32*) intramolecular chloride displacement (*33*) to provide a boron-retentive ring expansion. Although not explicitly shown here, the resulting B(pin)-substituted chromane (**13a** to **13d**) could potentially undergo various boron-mediated downstream transformations. Type III expansion takes advantage of the carbon substituent on the borylation reagent ($RBBr_2$). Double 1,2-migration (*34*) with the resulting cyclic borinate took place when the $LiCHCl_2$/$ZnCl_2$ combination was used. Upon oxidation of the C–B bond, the subsequent Mitsunobu reaction delivered the ring-expansion products (**14a** to **14 g**) containing the carbon substituent from the boron reagent in good overall yield. Finally, the utility of the ether editing method, together with the one-carbon ring expansion strategy, was demonstrated in a streamlined formal enantioselective synthesis of the antihypertensive drug nebivolol (Fig. 3E). The key chiral chromane intermediate (**15**) was previously prepared, either in 37% yield with 82% enantiomeric excess (ee) in five steps using a chiral auxiliary approach (*35*) or 30% yield with 80% ee in 10 steps using chiral catalysis (*36*). Here, from the commercially available

5-fluoro-2,3-dihydrobenzofuran, the same compound (**15**) was accessed in just three steps, with a 50% overall yield and 97% ee, through a sequence of boron-insertion, one-carbon ring expansion, and an Ir-catalyzed asymmetric allylic alkylation (*37*).

To gain some insights into the reaction mechanism, control experiments were first carried out (Fig. 4). In the absence of the Ni catalyst and Zn, no reaction occurred between $MesBBr_2$ and substrate **1a** under the standard conditions; however, upon addition of a catalytic amount of $ZnBr_2$, the ring-opening product **4a** was formed in 89% yield (Fig. 4A). The alkylbromide **4a** could be efficiently transformed to the 2*H*-benzoxaborin product (**3a**) under the standard conditions, which suggests the intermediacy of **4a**. This result also suggests that zinc not only serves as the reductant but also plays a critical role in the C–O bond cleavage, which is also consistent with the fact that other reductants (Mn or Mg) were not effective (see below and table S1). The intermediacy of the alkyl bromide was further supported by a competition experiment with a linear ether, where an added alkyl bromide could also be borylated (see supplementary materials). In addition, 2,2-dimethylcoumaran competently underwent the C–O borylation reaction using less-bulky $PhBBr_2$ as the reagent (see supplementary materials), implying that the mechanism for the C–O bond cleavage may not be limited to a S_N2 pathway and could be substrate-dependent.

The nature of the alkyl group in the coupling reaction and the role of the Ni catalyst were key to understanding the subsequent C–B bond formation step. First, the use of a cyclopropyl-substituted ether as substrate led only to the ring-opening product (**3as**), suggesting the possibility of radical intermediates (Fig. 4B). In addition, a substrate (***S*-1z**) containing an α-stereocenter initially enriched to 98% ee was observed to racemize completely in both the oxaborinane and the alcohol products (Fig. 4C). In contrast, the ring-opening intermediate (the secondary alkyl bromide) retained high enantiopurity (90% ee), which further supports the generation of sp^3 carbon radicals in the C–B bond formation, probably via single electron transfer between active Ni species and the $C(sp^3)$-Br moiety (*38*, *39*). Finally, kinetic studies were performed, showing an induction period to form product **3a** (fig. S11) and rapid buildup of intermediate **4a** during this period. This observation is consistent with the hypothesis of an initial transformation of **1a** to **4a** and also implies that the subsequent Ni-catalyzed C–Br/B–Br coupling step is rate-determining (for more details, see supplementary materials, section 6).

To gain deeper understanding of the reaction mechanism, density functional theory (DFT) calculations were carried out with cyclic ether **1a** as the model substrate. The most favorable pathway from the calculations supported the cleavage-then-rebound mechanism via Zn/Ni tandem catalysis (Fig. 4D). First, $MesBBr_2$ binds to the ether oxygen assisted by the in situ generated **1a**·$ZnBr_2$ dimer (**IM1**) to form complex **IM2**, which then undergoes facile Zn-promoted bromide anion abstraction (**TS1**) with an activation free energy ($\Delta G^{\ddagger}$) of 11.4 kcal/mol to form an ion pair **IM3**, followed by an S_N2-type C–O cleavage (**TS2**, $\Delta G^{\ddagger}$ = 16.2 kcal/mol) (*40*). The low barriers in this ring-opening process are consistent with the facile formation of alkyl bromide **4a** observed experimentally. Several mechanistic pathways are possible in the subsequent Ni-catalyzed C–Br/B–Br coupling with intermediate **4a** (*41*). Among these, a radical chain reaction and a double oxidative addition would both be consistent with the radical clock experiment. Our DFT calculations suggest that the most favorable pathway involves the facile B–Br bond oxidative addition of **4a** with $Ni^{(0)}(\mathbf{L1})_2$ [**TS3**, $\Delta G^{\ddagger}$ = 3.0 kcal/mol with respect to the **4a**·Ni(0) complex **IM4**] (*42*) to generate a Ni(II) boryl species **IM5** (*43*). Single electron reduction of **IM5** by zinc powder forms a Ni(I) boryl complex **IM6**. From **IM6**, the C–Br bond cleavage may occur via either the S_N2-type C–Br oxidative addition (**TS4**, $\Delta G^{\ddagger}$ = 18.2 kcal/mol) (*44*) or the bromine atom transfer (**TS5**, $\Delta G^{\ddagger}$ = 19.5 kcal/mol) to form an alkyl radical **IM7** (*27*, *28*), which then recombines intramolecularly with the Ni(II) center. The comparable barriers of these transition states suggest that either pathway may operate depending on the steric environment of the alkyl bromide intermediate (e.g., primary versus secondary). For example, the reaction with the α-substituted ether (***S*-1z**) favors the bromine-atom-transfer pathway by 4.2 kcal/mol (fig. S37), consistent with the complete product racemization observed in experiment. Both C–Br bond cleavage pathways lead to transient Ni(III) species (**IM8** and **IM9**), which then undergo fast reductive elimination to form the cyclic boron-insertion product **3a**. The resulting Ni(I)Br intermediate could be reduced by Zn(0) to form $ZnBr_2$ and regenerate the Ni(0) catalyst.

As ethers are readily available and robust substrates, this boron-insertion method could be used to streamline synthesis of complex target molecules by minimizing functional group manipulations or protecting group usages. Moreover, the distinct reaction mode revealed by the mechanistic studies could have implications on Lewis acid/transition metal tandem catalysis beyond this work.

REFERENCES AND NOTES

1. G. W. Huber, S. Iborra, A. Corma, *Chem. Rev.* **106**, 4044–4098 (2006).
2. C. Thebtaranonth, Y. Thebtaranonth, *Cyclization Reaction* (CRC Press, ed. 1, 1993).
3. J. Cornella, C. Zarate, R. Martin, *Chem. Soc. Rev.* **43**, 8081–8097 (2014).
4. B. Su, Z. C. Cao, Z. J. Shi, *Acc. Chem. Res.* **48**, 886–896 (2015).
5. B. M. Rosen *et al*., *Chem. Rev.* **111**, 1346–1416 (2011).
6. E. J. Tollefson, L. E. Hanna, E. R. Jarvo, *Acc. Chem. Res.* **48**, 2344–2353 (2015).
7. B. C. Ranu, S. Bhar, *Org. Prep. Proced. Int.* **28**, 371–409 (1996).
8. E. Wenkert, E. L. Michelotti, C. S. Swindell, *J. Am. Chem. Soc.* **101**, 2246–2247 (1979).
9. B. T. Guan *et al*., *J. Am. Chem. Soc.* **130**, 3268–3269 (2008).
10. R. Matsubara, T. F. Jamison, *J. Am. Chem. Soc.* **132**, 6880–6881 (2010).
11. A. G. Sergeev, J. F. Hartwig, *Science* **332**, 439–443 (2011).
12. C. Zarate, R. Manzano, R. Martin, *J. Am. Chem. Soc.* **137**, 6754–6757 (2015).
13. L. Hie *et al*., *Angew. Chem. Int. Ed.* **55**, 2810–2814 (2016).
14. M. Tobisu, T. Takahira, T. Morioka, N. Chatani, *J. Am. Chem. Soc.* **138**, 6711–6714 (2016).
15. Q. Zhou, H. D. Srinivas, S. Zhang, M. P. Watson, *J. Am. Chem. Soc.* **138**, 11989–11995 (2016).
16. L. W. Erickson, E. L. Lucas, E. J. Tollefson, E. R. Jarvo, *J. Am. Chem. Soc.* **138**, 14006–14011 (2016).
17. H. Saito, S. Otsuka, K. Nogi, H. Yorimitsu, *J. Am. Chem. Soc.* **138**, 15315–15318 (2016).
18. A. Padwa, S. F. Hornbuckle, *Chem. Rev.* **91**, 263–309 (1991).
19. S. Jana, Z. Yang, C. Pei, X. Xu, R. M. Koenigs, *Chem. Sci.* **10**, 10129–10134 (2019).
20. B. Pachaly, R. West, *Angew. Chem. Int. Ed.* **23**, 454–455 (1984).
21. S. J. Baker *et al*., *Future Med. Chem.* **1**, 1275–1288 (2009).
22. B. Liu *et al*., *J. Med. Chem.* **63**, 2789–2801 (2020).
23. T. Figueiredo *et al*., *Biomacromolecules* **21**, 230–239 (2020).
24. M. Soleilhavoup, G. Bertrand, *Angew. Chem. Int. Ed.* **56**, 10282–10292 (2017).
25. M. A. Légaré, C. Pranckevicius, H. Braunschweig, *Chem. Rev.* **119**, 8231–8261 (2019).
26. Y. Wang *et al*., *J. Am. Chem. Soc.* **129**, 12412–12413 (2007).
27. G. E. Martinez, J. W. Nugent, A. R. Fout, *Organometallics* **37**, 2941–2944 (2018).
28. J. C. Tellis, D. N. Primer, G. A. Molander, *Science* **345**, 433–436 (2014).
29. V. H. Tran, M. T. La, S. Kang, H. K. Kim, *Org. Biomol. Chem.* **18**, 5008–5016 (2020).
30. S. Namirembe, J. P. Morken, *Chem. Soc. Rev.* **48**, 3464–3474 (2019).
31. J. Wu *et al*., *Nature* **547**, 436–440 (2017).
32. D. S. Matteson, K. M. Sadhu, *J. Am. Chem. Soc.* **105**, 2077–2078 (1983).
33. D. S. Matteson, *Chem. Rev.* **89**, 1535–1551 (1989).
34. H. C. Brown, T. Imai, P. T. Perumal, B. Singaram, *J. Org. Chem.* **50**, 4032–4036 (1985).
35. M. C. Carreño, G. Hernández-Torres, A. Urbano, F. Colobert, *Eur. J. Org. Chem.* **2008**, 2035–2038 (2008).
36. B. M. Trost, H. C. Shen, L. Dong, J. P. Surivet, C. Sylvain, *J. Am. Chem. Soc.* **126**, 11966–11983 (2004).
37. M. A. Schafroth, S. M. Rummelt, D. Sarlah, E. M. Carreira, *Org. Lett.* **19**, 3235–3238 (2017).
38. S. Biswas, D. J. Weix, *J. Am. Chem. Soc.* **135**, 16192–16197 (2013).
39. Z. Wang, H. Yin, G. C. Fu, *Nature* **563**, 379–383 (2018).
40. T. M. Kosak, H. A. Conrad, A. L. Korich, R. L. Lord, *Eur. J. Org. Chem.* **2015**, 7460–7467 (2015).
41. K. M. Korch, D. A. Watson, *Chem. Rev.* **119**, 8192–8228 (2019).
42. A. Yamamoto, M. Suginome, *J. Am. Chem. Soc.* **127**, 15706–15707 (2005).
43. W. K. Chow *et al*., *RSC Advances* **3**, 12518–12539 (2013).
44. I. Funes-Ardoiz, D. J. Nelson, F. Maseras, *Chemistry* **23**, 16728–16733 (2017).

ACKNOWLEDGMENTS

S. Ochi and X. Liu are acknowledged for x-ray crystallography. Y. Wu is thanked for preparing starting materials. We thank V. Rawal and J. Wang for helpful discussions and S. Hou for checking the experimental procedure. **Funding:** This project was supported by the University of Chicago. P.L. received funding from the NSF (CHE-1654122). Calculations were performed at the Center for Research Computing at the University of Pittsburgh,

TACC Frontera, and NSF XSEDE supercomputers. H.L. acknowledges the Suzuki Postdoctoral Fellowship from the University of Chicago. **Author contributions:** H.L. and G.D. conceived of and designed the experiments. H.L. performed the experiments. X.Y. prepared several substrates. I.K. and P.L. designed and conducted the density functional theory calculations. H.L., I.K., P.L., and G.D. wrote the manuscript. P.L. and G.D. directed the research. **Competing interests:** The authors declare no competing interests. **Data and materials availability:** All data are available in the manuscript or the supplementary materials. Metrical parameters for the structure of **3f** and **Cat 1** are available free of charge from the Cambridge Crystallographic Data Centre (www.ccdc.cam.ac.uk/) under reference numbers CCDC 2009520 and CCDC 2009521.

SUPPLEMENTARY MATERIALS

science.sciencemag.org/content/372/6538/175/suppl/DC1
Materials and Methods
Supplementary Text
Figs. S1 to S43
Tables S1 to S3
Spectral Data
Calculation Data
References (*45*–*101*)

14 January 2021; accepted 5 March 2021
10.1126/science.abg5526

GLASS

High-throughput injection molding of transparent fused silica glass

Markus Mader[1,2], Oliver Schlatter[3], Barbara Heck[4], Andreas Warmbold[2], Alex Dorn[5], Hans Zappe[5], Patrick Risch[1,6], Dorothea Helmer[1,2,6,7], Frederik Kotz[1,2,6,7]*, Bastian E. Rapp[1,2,6,7]

Glass is one of the most relevant high-performance materials that has the benefit of a favorable environmental footprint compared with that of other commodity materials. Despite the advantageous properties of glasses, polymers are often favored because they can be processed using scalable industrial replication techniques like injection molding (IM). Glasses are generally processed through melting, which is both energy intensive and technologically challenging. We present a process for glassworks using high-throughput IM of an amorphous silicon dioxide nanocomposite that combines established process technologies and low-energy sintering. We produce highly transparent glass using classical IM and sintering, allowing for a potentially substantial reduction in energy consumption. Our strategy merges polymer and glass processing, with substantial implications for glass utilization.

Glasses are among the most important high-performance materials of the 21st century, with applications ranging from packaging, architecture, renewable energy technologies, and electronic devices to applications in medicine, high-throughput data transmission devices, optics, and photonics (*1*–*5*). Today, >120 million metric tons of glass are produced annually, mainly for container glass, flat glass, and fibers (*6*, *7*). Sustainable process technologies with high energy efficiency are key to ensuring resource-efficient material production and use (*8*), but although glasses are among the oldest materials used by humankind, the technology used to shape glass has remained virtually unchanged over the centuries. In particular, glass processing has not kept up with process technology breakthroughs such as injection molding (IM), which eventually ensured the marked success of polymers. Many components are made in polymers rather than glasses because IM allows polymer components to be mass-market manufactured quickly, cost-efficiently, and at high precision (*9*, *10*). One consequence of the lack of scalable manufacturing processes for glass is that key components for mass-market optical systems, such as microlenses, are made from polymers, in spite of glass having superior optical properties to those of the polymer-based components (*11*–*13*).

The optical, thermal, mechanical, and chemical properties of silicate glasses make them the material of choice for many applications in optics, miniaturized chemical synthesis, and packaging (*12*–*15*). In contrast to thermoplastic polymers, which are accessible through IM at relatively moderate temperatures of ~200° to 250°C, glasses are still mostly processed by melting at temperatures of ~2000°C for fused silica and of 1500°C for other silicate glasses (*16*, *17*). These temperatures not only make these processes very difficult to scale industrially, they also require remarkable amounts of energy—in the range of 5 to 6 MJ per ton of glass (*6*, *16*). This energy requirement is a key inhibitor in the development of a sustainable glass economy and prevents one of the most important non–carbon-based, high-performance materials from being more widely used. The only viable option for the replication of fused silica glass is precision glass molding, a process that requires expensive, low-durability molding tools made from glassy carbon and only allows cycle times of several minutes at temperatures of 1400°C that only achieves low-to-medium throughput (*18*, *19*). On the micrometer level, grinding and polishing or chemical etching, often with hazardous hydrofluoric acid, can be used for shaping. However, these processes are likewise severely limited in terms of shapes and throughput (*20*, *21*).

The main problem is thus two-fold: (i) The processing of glass is energy-consuming because of the high temperatures involved, and (ii) glass is not accessible to mass-market manufacturing methods such as IM. These problems are codependent, and solving one inherently helps solve the other. On the basis of our previous work on glass nanocomposites (*22*–*25*), we used a similar approach to structure glasses through IM using a thermoplastic nanocomposite in a process similar to powder injection molding (PIM). Once shaped using IM, we converted the nanocomposites to high-quality silicate glass through a debinding and sintering protocol. Although PIM is already used regularly for ceramics and a number of metals (*26*, *27*), it has only yielded nontransparent, porous borosilicates and soda lime frits (*28*–*31*). Our approach would open up the scalable process technology that is inherent to IM to glasses, and it would allow for the fabrication of complex glass components, potentially requiring <60% of the energy required in conventional glass melting (*32*, *33*).

Our process uses thermoplastic silica nanocomposites and combines a low-temperature, low-energy shaping process with a water-based debinding and low-temperature sintering process. Additionally, the water debinding allows for the partial recycling of the thermoplastic binder. The process uses standard IM machinery and is capable of fabricating complex parts with single-micrometer resolution and optically smooth surfaces [arithmetic average roughness (R_a) < 4 nm; root mean square roughness (R_q) < 5 nm], requiring no further postprocessing, polishing, or surface etching. We generated a range of technical glasses, including binary-colored fused silica glasses, by doping the injection-molded fused silica glasses with metal salts.

We prepared the feedstock by premixing silica nanopowder, with a mean diameter of 50 to 100 nm and a surface area of 30 to 50 m^2 g^{-1}, with a solution of polyvinyl butyral (PVB), with a molar mass in the range of 30,000 to 110,000 g mol^{-1}, and polyethylene glycol (PEG),

[1]Laboratory of Process Engineering, NeptunLab, Department of Microsystems Engineering (IMTEK), Albert Ludwig University of Freiburg, 79110 Freiburg, Germany. [2]Freiburg Materials Research Center (FMF), Albert Ludwig University of Freiburg, 79104 Freiburg, Germany. [3]Injex AG, 8952 Schlieren, Switzerland. [4]Institute of Physics, Albert Ludwig University of Freiburg, 79104 Freiburg, Germany. [5]Gisela and Erwin Sick Chair of Micro-optics, Department of Microsystems Engineering (IMTEK), Albert Ludwig University of Freiburg, 79110 Freiburg, Germany. [6]Glassomer GmbH, 79110 Freiburg, Germany. [7]FIT Freiburg Center of Interactive Materials and Bioinspired Technologies, Albert Ludwig University of Freiburg, 79110 Freiburg, Germany.
*Corresponding author. Email: frederik.kotz@imtek.uni-freiburg.de

with a molar mass in the range of 400 to 4000 g mol^{-1} in a solvent (Fig. 1, A and B). After homogenizing the mixture, we evaporated the solvent, which resulted in a solid thermoplastic silica nanocomposite. We then plasticized and extruded the thermoplastic silica nanocomposite using a twin screw extruder, yielding the final feedstock as granules (Fig. 1, C and D). We optimized the feedstock to allow for a markedly high solid loading of up to 60 vol %. For successful IM, the viscosity of the molten feedstock should not exceed 1000 Pa·s at typical shear rates of ~10^3 s^{-1} (*34*, *35*). We engineered our feedstock to achieve shear thinning behavior with viscosities well below 1000 Pa·s at temperatures >130°C, as we determined using a capillary rheometer (fig. S1A). The feedstock is injection molded at a moderate temperature of ~130°C and specific injection pressures of 700 to 1000 bar, which results in the so-called green part. After the shaping process, we immersed the green part in water at 40°C for a first solvent-debinding step. The majority (>95 wt %) of PEG was removed from the green part after 3 hours for parts where one dimension is <2 mm (fig. S1B). For larger parts, the aqueous debinding duration was increased—e.g., to 6 hours for 5 mm and 12 hours for 10 mm (fig. S1C). For 10-mm-thick components, ~80 wt % PEG is removed in 12 hours. We removed the residual binder in a second debinding step at elevated temperatures. We optimized the parameters for thermal debinding using thermal gravimetric analysis (TGA) measurements (fig. S1D), setting holding steps at the critical temperatures of polymer decomposition. Because of the previous debinding in water, the removal of the residual binder in the thermal debinding step was possible at high heating rates up to 1°C min^{-1} and short holding times (1 hour each at 270°, 460°, and 600°C) without crack formation.

We sintered the resulting brown part to full density in vacuum at 1300°C, which resulted in high-quality transparent fused silica glass. Because of the optimized two-step debinding procedure, the conversion of the injection-molded green parts—with at least one dimension <2 mm—into transparent fused silica could be done in 24 hours total (fig. S1E). Larger parts, with lateral dimension of up to 10 mm, were also successfully converted to fused silica glass (fig. S1F) with an increased process duration resulting from the prolonged liquid debinding.

Our glass fabrication process has several advantages over conventional glass melting. Our process may be more energy efficient and also allows the use of established high-throughput polymer processing machinery for mass-market manufacturing (Fig. 2). Our feedstock is based on widely used, nontoxic polymers and silica powders. The processing and shaping can be done using moderate temperatures of 130°C, decreasing energy consumption. The water-based debinding step is nonhazardous and allows for the recycling of most of the PEG binder. This reduces the amount of polymer that needs to be thermally decomposed in the second debinding step down to 12 wt % of the total feedstock. The conversion to transparent fused silica glass can also be performed using a low-energy sintering process at 1300°C instead of the usual melting temperature of >2000°C (*36*).

The sintered fused silica parts have a full density of 2.204 ± 0.002 g cm^{-3} (table S1). The shrinkage during the final sintering step is isotropic, and we can calculate it depending on the solid loading (*33*) (eq. S2). We measured exemplary linear shrinkage for a 50 vol % feedstock (20.78 ± 0.11%; table S2), which was in agreement with our calculated shrinkage of 20.6%. The minor deviations are likely from manual weighing and manual introduction of the powder. We used x-ray diffraction (XRD) (fig. S2A) to confirm that the silica glass we obtained is crystal free and amorphous.

We demonstrated high-throughput fabrication on a commercial IM machine from Babyplast Christmann. Without additional optimization, we found that fully automated IM of our silica nanocomposite was possible with cycle times as low as 20 s. Complex-shaped fused silica parts can be produced at industrial levels of throughput (Fig. 3, A and B). Over a time span of 18 min, we produced >200 parts (Fig. 3, A and B) at a per-piece cycle time of ~5 s. Furthermore, the silica feedstock can be processed using continuous tube extrusion. Using an annular gap nozzle with an outer diameter of 16 mm, tubes up to 1 m in length can be generated at a speed of 30 m h^{-1}. These tubes were subsequently sintered to transparent fused silica glass (fig. S3, A to C).

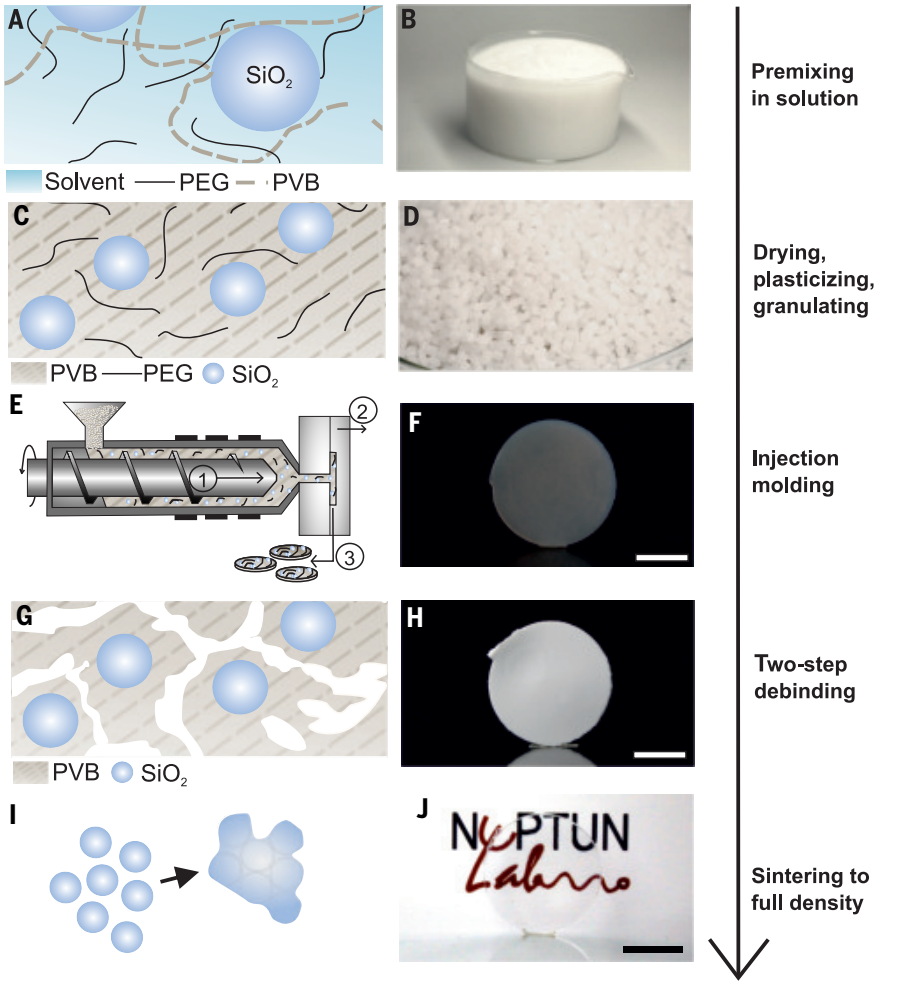

Fig. 1. IM of fused silica using thermoplastic nanocomposites. (**A** and **B**) Silica powder and binder matrix are premixed in solution, resulting in a white paste (B). (**C** and **D**) Evaporating the solvent results in a thermoplastic silica nanocomposite, which is plasticized, extruded, and granulated (D). (**E** and **F**) Shaping the granules by IM results in the green part (F). (**G**) A first debinding step dissolves the PEG component in water, creating a porosity, which allows for a fast thermal debinding of the residual binder. (**H**) The injection-molded part after the first debinding step. (**I** and **J**) After thermal debinding, the brown part is sintered to full density at 1300°C to a transparent fused silica glass (J). Scale bars, 10 mm.

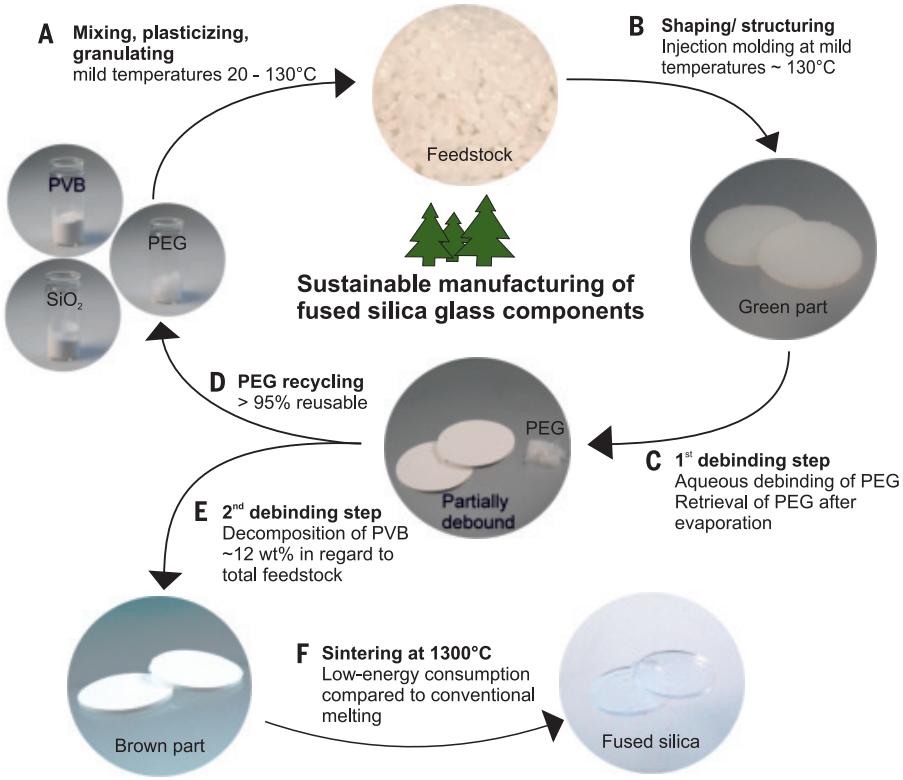

Fig. 2. Sustainability of the IM process for fabrication of fused silica glass components. (**A**) The nanocomposite, composed of nontoxic components (PVB, PEG, and silica), is mixed, plasticized, and granulated to a feedstock using standard machinery at low temperatures (20° to 130°C). (**B**) The nanocomposite can be shaped using established polymer processing techniques such as IM at temperatures of 130°C. (**C**) In a first aqueous debinding step, PEG is removed. (**D**) After evaporating the water, up to 95% of the initial amount of PEG can be recuperated and reused for the next feedstock preparation. (**E**) The residual binder is removed by thermal decomposition. The amount of polymer decomposed in this second debinding step is only 12 wt % of the total feedstock. (**F**) Using a low-energy sintering process—where the energy consumption is substantially smaller than that of a conventional melting process—yields transparent fused silica glass components.

The variety of exemplary structures we produced (Fig. 3, C to E) show that complex-shaped fused silica objects can be easily made available using common rapid-tooling techniques, which enables quick and flexible fused silica manufacturing not only for high-quantity products but also for smaller product series or prototypes (fig. S3, D and E). Molding tools made of steel, nickel, and brass as well as commercial rapid-tooling resins—e.g., ASIGA Fusion Gray—can be used to yield high-quality, defect-free fused silica glass components. Tools made of aluminum, on the other hand, show a high tendency for crystallization during sintering (see XRD in fig. S2B), which indicates abrasion during IM.

Besides macroscopic structures, our IM approach also facilitates the fabrication of fused silica glass components with micrometer resolution. Comparable structures are required for the next generation of micro-optics, photonics, high-energy lasers, and lab-on-a-chip devices (*3*, *37*–*39*). Microstructures, such as refractive and diffractive optics (Fig. 4), can be easily replicated by IM and sintered to highly transparent fused silica glass at optical-surface quality. An additional example created with this method is an injection-molded fused silica microstructured Fresnel lens (fig. S4). Additionally, our method opens a different route for facile, high-throughput fabrication of fused silica microfluidic devices. Micrometer-sized channel structures in fused silica, such as an exemplary serpentine channel with 240-μm width and 580-μm height, are easily produced using IM and sintering (Fig. 4H). Simple thermal or solvent-bonding procedures of the green part allow for the fabrication of closed and leak-proof microfluidics (Fig. 4I).

Without further postprocessing, the sintered fused silica components show an exceptionally low surface roughness R_a of 3.74 nm and R_q of 4.9 nm, as determined from atomic force microscopy (AFM) (measured on a surface of 100 μm^2; Fig. 5A). We measured the surface roughness of the injection-molded micro-optical lenses shown in Fig. 4A using white light microscopy and compared it with the surface roughness of the metal mold (fig. S5, A and B). Both lens structures have a similar surface roughness R_a of 140 nm, which shows that the surface quality of the mold is directly transferred to the injection-molded and sintered fused silica glass. This suggests that even small surface defects are reliably reproduced in the molding process, which indicates a high dependence of the final structure quality on the mold.

The high optical transparency of injection-molded fused silica glass was confirmed by light microscopy (fig. S5C), ultraviolet-visible (UV-Vis), and infrared (IR) measurements (Fig. 5B). Transmitted light microscopy images of sintered fused silica glass reveal a low bulk defect density, mainly from dust contamination. In future works, these defects may be eliminated by performing the whole process in a clean-room environment. The sintered fused silica shows an exceptionally high transmission of >90% in the range of 1000 to 400 nm and a transmission >70% at 200 nm. Fourier transform infrared (FTIR) measurements show a high transmission of >90% up to 3400 nm, comparable to that of commercial fused silica. The characteristic IR peak at 2750 nm can be assigned to the vibration of free hydroxyl groups (*40*) and can be used to calculate the OH concentration (*41*, *42*). Fused silica is known to show higher OH concentration than fused quartz (*43*). The fused silica prepared by our process shows an only slightly higher absorption at 2750 nm than that of fused quartz and a much lower signal than that of regular, fused silica. The calculation gives an OH concentration of 12 parts per million (ppm) for the injection-molded glass and 5 and 102 ppm for fused quartz and commercial fused silica, respectively (*33*). The presented IR data are thus in agreement with the OH concentration generally accepted for type I and type III silicas (*43*) and also with the data provided by the manufacturers. Therefore, we conclude that that the fused silica glass prepared by our process has a low amount of hydroxyl groups. We determined the refractive index n_{D20} and Abbe number ν_D of the sintered fused silica glass to be 1.4589 ± 0.0002 and 67.1 ± 1.1 (table S3), respectively, which are in agreement with those for commercial fused silica glass (n_{D20} = 1.4585; ν_D = 67.82) (*44*).

In addition to pure fused silica, our approach also allows for the fabrication of technical glasses, as we demonstrated using binary glasses doped with metal salts. To do so, the partially debound green parts can be soaked in aqueous solutions of various metals salts. The doped green parts are afterward thermally debinded and sintered to a transparent, binary-colored glass (Fig. 5, D and E). Doping with $HAuCl_4$ and $CoSO_4$ results in red- or blue-colored silica glass, respectively (*45*), whereas doping with rare-earth element

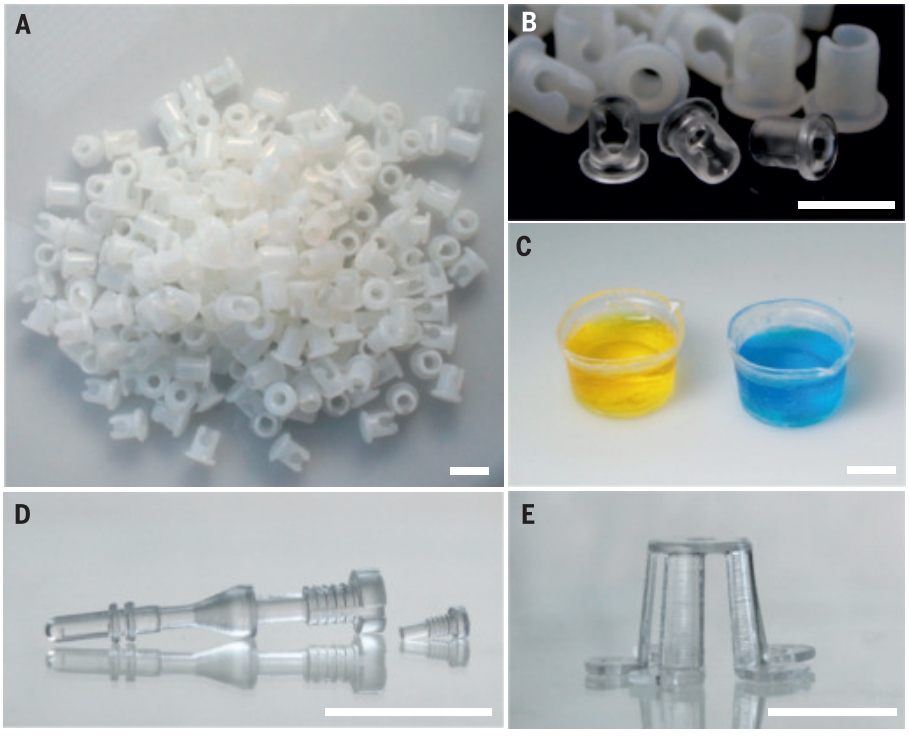

Fig. 3. IM of bulk fused silica glass components. (**A** and **B**) More than 200 parts produced by fully automated IM over a duration of 18 min at cycle times of ~5 s per piece, demonstrating the capability for high-throughput mass-market production of complex-shaped components, which are subsequently sintered to full density and transparency (B). (**C** to **E**) Exemplary components fabricated by IM using three-dimensional printed molds, showing that complex macroscopic structures can be produced using our process. Scale bars, 10 mm.

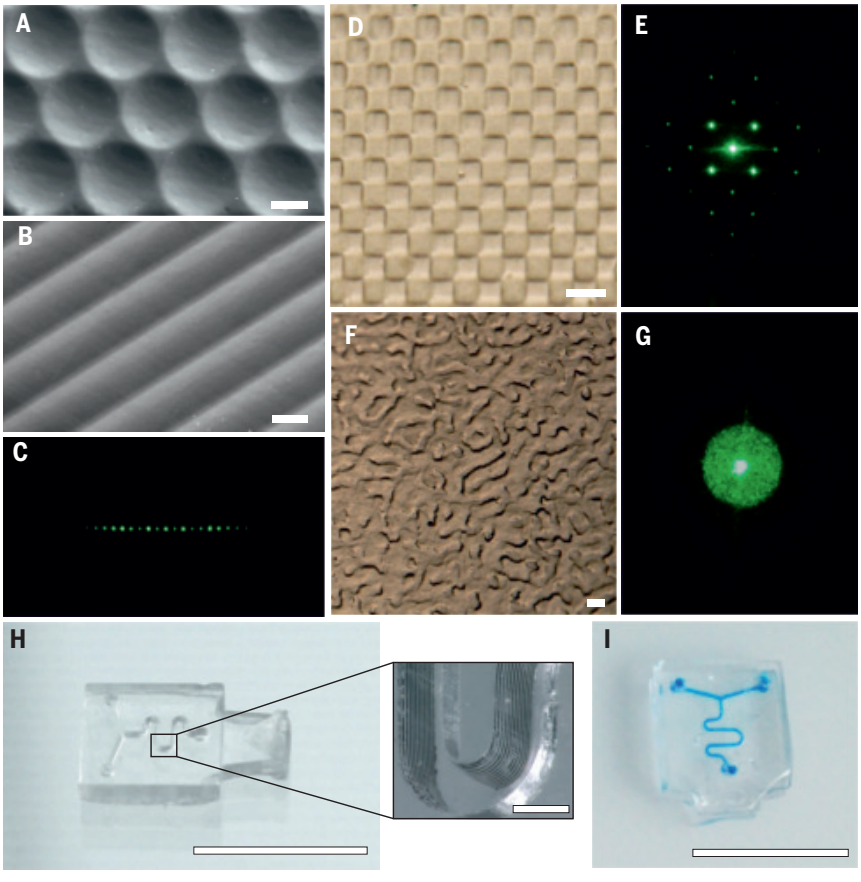

Fig. 4. IM of microstructured fused silica glass components. (**A** and **B**) Scanning electron micrographs of injection-molded and sintered fused silica components containing spherical (A) and cylindrical (B) microlens arrays. Scale bars, 20 μm. (**C**) The refraction pattern observed when illuminating the microlens array of (B) with a green laser (532 nm). (**D** and **E**) Microscopic image of injection-molded and sintered fused silica components with a checkerboard microstructure (D) and its corresponding diffraction pattern (E) when illuminated with a green laser (532 nm). Scale bar, 20 μm. (**F** and **G**) Microscopic image of injection-molded and sintered fused silica component with a diffractive optical element (F) and its diffraction pattern when illuminated with a green laser (532 nm) displaying a circular-shaped far-field pattern (G). Scale bar, 20 μm. (**H**) Injection-molded and sintered fused silica component with a microfluidic channel structure. Scale bar, 10 mm. The inset shows a magnification of the channel. Scale bar, 300 μm. (**I**) Bonded fused silica microfluidic device filled with dyed water. Scale bar, 10 mm.

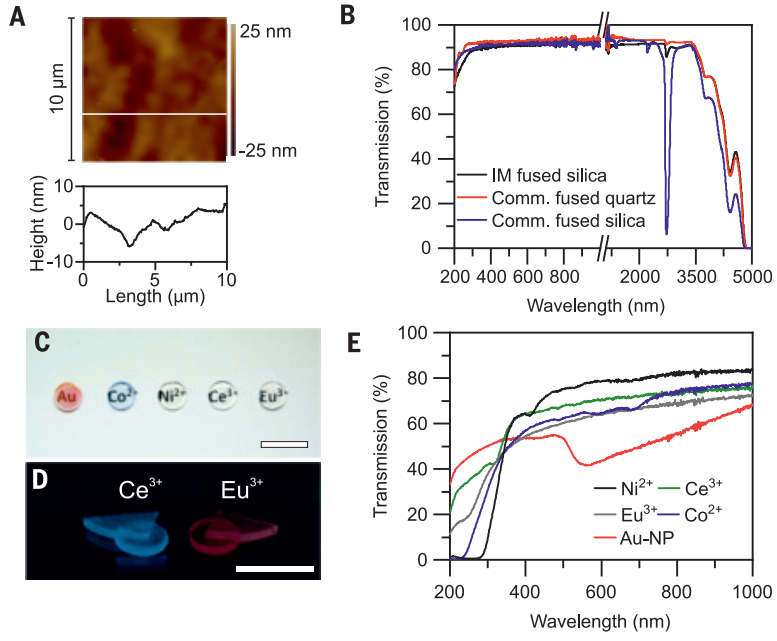

Fig. 5. Optical characterization of injection-molded fused silica glass. (**A**) AFM of injection-molded and sintered fused silica glass showing a surface roughness of R_a = 3.7 nm and R_q = 4.9 nm (optical-surface quality) without any postprocessing. (**B**) The optical transparency was confirmed by UV-Vis and IR transmission spectroscopy. The injection-molded fused silica glass (1-mm thickness) was compared with commercial (comm.) fused silica (2-mm thickness) and commercial fused quartz (1-mm thickness). (**C**) Photographs of the sintered binary silica glasses. Scale bar, 10 mm. (**D**) Doping with Ce^{3+} (left) or Eu^{3+} (right) results in transparent binary silica glasses showing luminescence when irradiated with UV light at 254 nm. Scale bar, 10 mm. (**E**) UV-Vis spectra of sintered binary silica glasses obtained by doping the injection-molded nanocomposite with metal salts.

salts like $Eu(NO_3)_3$ or $Ce(NO_3)_3$ gives transparent, colorless silica glasses that show luminescent behavior when irradiated with UV light at 254 nm (Fig. 4F) (*46*–*48*). A transparent, colorless glass with high UV absorbance for filter applications can be prepared by doping with $NiCl_2$ (*45*).

Our process enables the use of industrially scalable processing techniques such as IM for glass manufacturing and likely decreases the energy consumption compared with that of classical glass processing. The process builds on widely available machinery for shaping high-quality fused silica glass using high-throughput IM of thermoplastic silica nanocomposites, which are subsequently converted to pure, high-quality glasses with optical-surface quality (R_a < 4 nm; R_q < 5 nm) by sintering at 1300°C. The sintered fused silica glass shows high transparency and low surface roughness and can be used for optical applications without the need for further postprocessing. Our process offers the possibility of producing complex-shaped, high-quality glass components using the same high-throughput fabrication methods that allowed polymers to become one of the most important material classes of the 21st century. This strategy may upgrade glass processing to be more economically competitive with polymer processing by harnessing the inherent advantages of glasses over polymers while relying on established and commercially available machinery.

REFERENCES AND NOTES

1. J. C. Mauro, *Front. Mater.* **1**, 20 (2014).
2. F. Quintero *et al.*, *Sci. Adv.* **6**, eaax7210 (2020).
3. E. A. Peralta *et al.*, *Nature* **503**, 91–94 (2013).
4. J. He *et al.*, *Sci. Rep.* **8**, 14907 (2018).
5. L. L. Hench, D. E. Day, W. Höland, V. M. Rheinberger, *Int. J. Appl. Glass Sci.* **1**, 104–117 (2010).
6. A. Schmitz, J. Kamiński, B. Maria Scalet, A. Soria, *Energy Policy* **39**, 142–155 (2011).
7. N. Wintour, "The glass industry: Recent trends and changes in working conditions and employment relations" (International Labour Office, Sectoral Policies Department, Working Paper 310, 2015); www.ilo.org/wcmsp5/groups/public/—ed_dialogue/—sector/documents/publication/wcms_442086.pdf.
8. E. A. Olivetti, J. M. Cullen, *Science* **360**, 1396–1398 (2018).
9. A. de Mello, *Lab Chip* **2**, 31N–36N (2002).
10. G. M. Whitesides, *Nature* **442**, 368–373 (2006).
11. S. Bäumer, Ed., *Handbook of Plastic Optics* (Wiley, ed. 2, 2005).
12. R. Pini, A. Symmons, "Molded optics: Precision molded glass challenges plastic optics" (Laser Focus World, 2011); www.laserfocusworld.com/optics/article/16562818/molded-optics-precision-molded-glass-challenges-plastic-optics.
13. R. A. Schaut, K. C. Hoff, S. E. Demartino, W. K. Denson, R. L. Verkleeren, *PDA J. Pharm. Sci. Technol.* **71**, 511–528 (2017).
14. K. L. Wlodarczyk, D. P. Hand, M. M. Maroto-Valer, *Sci. Rep.* **9**, 20215 (2019).
15. A. J. Ikushima, T. Fujiwara, K. Saito, *J. Appl. Phys.* **88**, 1201–1213 (2000).
16. J. H. Butler, P. Hooper, in *Waste: A Handbook for Management*, T. M. Letcher, D. A. Vallero, Eds. (Elsevier, ed. 2, 2019), pp. 307–322.
17. J. D. Mackenzie, *J. Non-Cryst. Solids* **48**, 1–10 (1982).
18. F. Klocke, O. Dambon, G. Liu, J. Dukwen, *Prod. Eng.* **10**, 367–374 (2016).
19. J. Dukwen *et al.*, *Wear* **364–365**, 144–153 (2016).
20. D. Hülsenberg, A. Harnisch, A. Bismarck, *Microstructuring of Glasses*, vol. 87 of *Springer Series in Materials Science* (Springer, 2008).
21. H. Zhu, M. Holl, T. Ray, S. Bhushan, D. R. Meldrum, *J. Micromech. Microeng.* **19**, 065013 (2009).
22. F. Kotz *et al.*, *Adv. Mater.* **28**, 4646–4650 (2016).
23. F. Kotz *et al.*, *Adv. Mater.* **30**, e1707100 (2018).
24. F. Kotz *et al.*, *Nature* **544**, 337–339 (2017).
25. F. Kotz *et al.*, *Nat. Commun.* **10**, 1439 (2019).
26. V. Piotter *et al.*, *Microsyst. Technol.* **17**, 251–263 (2011).
27. L. Nyborg, E. Carlström, A. Warren, H. Bertilsson, *Powder Metall.* **41**, 41–45 (1998).
28. D. Lin, J. Lee, S. J. Park, *J. Korean Powder Metall. Inst.* **23**, 26–32 (2016).
29. D. Lin *et al.*, *Ceram. Int.* **41**, 5057–5065 (2015).
30. T. Moritz *et al.*, *Ceram. Modern Technol.* **1**, 111–119 (2019).
31. J. Hidalgo, J. M. Contreras, D. Berzal, A. Jiménez-Morales, J. M. Torralba, in *World PM2010 Proceedings: Powder Injection Moulding* (European Powder Metallurgy Association, 2010), pp. 256–263.
32. P. Richet, Y. Bottinga, L. Denielou, J. P. Petitet, C. Tequi, *Geochim. Cosmochim. Acta* **46**, 2639–2658 (1982).
33. Materials and methods are available as supplementary materials online.
34. M. R. Kamal, A. I. Isayev, S.-J. Liu, Eds., *Injection Molding: Technology and Fundamentals* (Hanser, 2009).
35. J. M. Park, J. S. Han, J. W. Oh, S. J. Park, *Met. Mater. Int.* 10.1007/s12540-019-00455-4 (2019).
36. E. M. Rabinovich, *J. Mater. Sci.* **20**, 4259–4297 (1985).
37. M. Levant, D. Château, S. Parola, D. Bartolo, *Adv. Mater. Technol.* **3**, 1700267 (2018).
38. F. Zhang *et al.*, *Sci. Rep.* **8**, 2419 (2018).
39. C. Xu, C. Ke, J. Ma, Y. Huang, Z. Zeng, *Sci. Rep.* **8**, 2331 (2018).
40. B. Kumar, N. Fernelius, J. A. Detrio, *J. Am. Ceram. Soc.* **64**, C-178–C-180 (1981).
41. D. M. Dodd, D. B. Fraser, *J. Appl. Phys.* **37**, 3911 (1966).
42. B. Sloots, *Vib. Spectrosc.* **48**, 158–161 (2008).
43. R. Brückner, *J. Non-Cryst. Solids* **5**, 123–175 (1970).
44. I. H. Malitson, *J. Opt. Soc. Am.* **55**, 1205–1209 (1965).
45. R. Clasen, *Glastech. Ber.* **66**, 299–304 (1993).
46. X. Fan, M. Wang, G. Xiong, *Mater. Sci. Eng. B* **21**, 55–58 (1993).
47. C. Weiping, Z. Ye, Z. Lide, *J. Phys. Condens. Matter* **10**, L473–L477 (1998).
48. C. Liu, B. Qian, R. Ni, X. Liu, J. Qiu, *RSC Advances* **8**, 31564–31567 (2018).

ACKNOWLEDGMENTS

We thank K. Steffen for assisting in the fabrication of nickel shim mold inserts and R. Prediger for the measurement of PEG removal rates in the liquid debinding step. We thank Babyplast Christmann for the opportunity to test our material. **Funding:** This work was partially funded by the German Federal Ministry of Education and Research (BMBF), under "Fluoropor" (funding code: 03X5527). This project has received funding from the European Research Council (ERC) under the European Union's Horizon 2020 research and innovation program (grant no. 816006). This work is part of the Research Cluster "Interactive and Programmable Materials (IPROM)" funded by the Carl Zeiss Foundation. B.E.R. and D.H. thank the German Research Foundation (Deutsche Forschungsgemeinschaft, DFG) for funding through the Centre for Excellence livMatS Exec 2193/1 – 390951807. **Author contributions:** F.K. and B.E.R. conceived the idea. M.M. designed the experiments and synthesized the materials. M.M. and O.S. processed the materials. B.H. performed XRD measurements. A.D. performed refractive index measurements. A.W. performed TGA measurements. P.R. and H.Z. performed white light microscopy measurements. M.M., F.K., D.H., and B.E.R. contributed to writing the manuscript. **Competing interests:** The Glassomer GmbH has patented the technology described in this paper (patent application no. EP20195971.5) and is in the process of commercializing it. The authors declare no other competing interests. **Data and materials availability:** All data are available in the main text or the supplementary materials.

SUPPLEMENTARY MATERIALS

science.sciencemag.org/content/372/6538/182/suppl/DC1
Materials and Methods
Figs. S1 to S5
Tables S1 to S3

8 October 2020; accepted 26 January 2021
10.1126/science.abf1537

TIME-DOMAIN ASTRONOMY

Enhanced x-ray emission coinciding with giant radio pulses from the Crab Pulsar

Teruaki Enoto[1]†*, Toshio Terasawa[2,3,4]†*, Shota Kisaka[5,6,7]†*, Chin-Ping Hu[1,8,9]†*, Sebastien Guillot[10], Natalia Lewandowska[11], Christian Malacaria[12,13], Paul S. Ray[13], Wynn C.G. Ho[11,15], Alice K. Harding[16,17], Takashi Okajima[16], Zaven Arzoumanian[16], Keith C. Gendreau[16], Zorawar Wadiasingh[16,18], Craig B. Markwardt[16], Yang Soong[16], Steve Kenyon[16], Slavko Bogdanov[19], Walid A. Majid[20,21], Tolga Güver[22], Gaurava K. Jaisawal[23], Rick Foster[24], Yasuhiro Murata[25,26,27], Hiroshi Takeuchi[25,27], Kazuhiro Takefuji[26,28], Mamoru Sekido[28], Yoshinori Yonekura[29], Hiroaki Misawa[30], Fuminori Tsuchiya[30], Takahiko Aoki[31], Munetoshi Tokumaru[32], Mareki Honma[33,34,35], Osamu Kameya[33,35], Tomoaki Oyama[33], Katsuaki Asano[2], Shinpei Shibata[36], Shuta J. Tanaka[37]

Giant radio pulses (GRPs) are sporadic bursts emitted by some pulsars that last a few microseconds and are hundreds to thousands of times brighter than regular pulses from these sources. The only GRP-associated emission outside of radio wavelengths is from the Crab Pulsar, where optical emission is enhanced by a few percentage points during GRPs. We observed the Crab Pulsar simultaneously at x-ray and radio wavelengths, finding enhancement of the x-ray emission by 3.8 ± 0.7% (a 5.4σ detection) coinciding with GRPs. This implies that the total emitted energy from GRPs is tens to hundreds of times higher than previously known. We discuss the implications for the pulsar emission mechanism and extragalactic fast radio bursts.

Spinning neutron stars emit periodic radio pulses from their magnetospheres, which can be observed as a pulsar. The radio pulses are emitted by a coherent mechanism (*1*). Some pulsars also show optical, x-ray, and gamma-ray pulses, which are usually interpreted using incoherent emission mechanisms. Giant radio pulses (GRPs) are a form of sporadic pulsar emission that have radio fluences at least an order of magnitude higher than those of regular pulses and are of unknown origin (*2*, *3*). GRPs have a power-law intensity distribution, unlike regular pulses, which have log-normal or exponential intensity distributions (*4*).

GRPs are bright, sometimes exceeding a megajansky (MJy, where 1 Jy = 10^{-26} W m^{-2} Hz^{-1}) for a few nanoseconds to microseconds (*5*). This is sufficient to detect each GRP during a single stellar rotation. GRPs from young neutron stars have been proposed as the origin of fast radio bursts (FRBs), short-duration radio transients at cosmological distances (*6*, *7*). A nearby counterpart has provided evidence for this association (*8*, *9*) and for a connection between coherent and incoherent processes in the neutron star magnetosphere (*10*). Although GRPs are not the leading explanation for FRBs, the broadband characteristics of GRPs provide information on coherent radio emission in neutron star magnetospheres that may be relevant to FRBs.

GRPs have been detected from only a small fraction of pulsars (*11*, *12*). The pulsar in the Crab Nebula, known as the Crab Pulsar (PSR B0531+21), was initially discovered by its GRPs (*13*). Regular periodic emission from the Crab Pulsar occurs from low-frequency radio waves to high-energy gamma rays. At 2 GHz (S-band), the GRP emission occurs at two rotational phases: the main pulse (MP) and the interpulse (IP), with a phase separation of 0.4 cycles. Sporadic GRPs occur both at the MP and IP of the average radio pulse, with each individual GRP lasting for a much narrower interval (~3 × 10^{-4} in phase) than the regular pulse.

Previous studies have searched for a correlation between radio giant pulses and higher energy emission [table S1; (*14*)]. The radio flux of GRPs is two to three orders of magnitude higher than regular pulses, and such a large enhancement does not occur at other wavelengths. An enhancement of ~3% (7.8σ significance) is known in the optical band (650 to 700 nm) (*15*) and has been independently confirmed (*16*). X-ray and gamma-ray observations have not detected any statistically significant correlations (*14*).

We searched for enhancement in x-rays during GRPs from the Crab Pulsar using the *Neutron star Interior Composition Explorer* (*NICER*) x-ray observatory mounted on the International Space Station (*17*). *NICER* has an effective collecting area of 1900 cm^2 at 1.5 keV, time resolution <100 ns, and flexible scheduling. Since launch in 2017, we have monitored the Crab Pulsar with *NICER* for calibration and scientific purposes. The total average count rate of the Crab Pulsar and Crab Nebula combined is 1.1 × 10^4 counts s^{-1} in the 0.3- to 10-keV band (~370 counts per spin cycle), which is below *NICER*'s maximum throughput of ~3.8 × 10^4 counts s^{-1}, and thus the data are nearly unaffected by pileup, dead-time, and data-transfer losses. The constant emission from the Crab Nebula (1.03 × 10^4 counts s^{-1}) was subtracted before analyzing the GRPs. We also observed the Crab Pulsar with two radio telescopes in Japan: the 34-m radio telescope of the Kashima Space Technology Center (*18*) and the 64-m radio dish of the Usuda Deep Space Center, both operating at 2 GHz [tables S2 to S5 and figs. S1 to S8; (*14*)]. In 2017–2019, we coordinated 15 *NICER* observations concurrently with either the Usuda or Kashima observatories [tables S2 and S6; (*14*)]. We extracted a total of 126 ks of exposure with simultaneous radio and x-ray coverage (*14*). The arrival time of

[1]Cluster for Pioneering Research, RIKEN, Wako 351-0198, Japan. [2]Institute for Cosmic Ray Research, University of Tokyo, Kashiwa 277-8582, Japan. [3]Mizusawa VLBI Observatory, National Astronomical Observatory of Japan, Mitaka 181-8588, Japan. [4]Interdisciplinary Theoretical Science Research Group, RIKEN, Wako 351-0198, Japan. [5]Frontier Research Institute for Interdisciplinary Sciences, Tohoku University, Sendai 980-8578, Japan. [6]Astronomical Institute, Tohoku University, Sendai 980-8578, Japan. [7]Department of Physical Science, Hiroshima University, Higashi-Hiroshima 739-8526, Japan. [8]Department of Physics, National Changhua University of Education, Changhua 50007, Taiwan. [9]Department of Astronomy, Kyoto University, Kyoto 606-8502, Japan. [10]Institut de Recherche en Astrophysique, Toulouse 31028, France. [11]Department of Physics and Astronomy, Haverford College, Haverford, PA 19041, USA. [12]NASA Marshall Space Flight Center, National Space Science and Technology Center, Huntsville, AL 35805, USA. [13]Universities Space Research Association, Science and Technology Institute, Huntsville, AL 35805, USA. [14]US Naval Research Laboratory, Washington, DC 20375, USA. [15]Mathematical Sciences and STAG Research Centre, University of Southampton, Southampton SO17 1BJ, UK. [16]NASA Goddard Space Flight Center, Greenbelt, MD 20771, USA. [17]Theoretical Division, Los Alamos National Laboratory, Los Alamos, NM 87545, USA. [18]Universities Space Research Association, Columbia, MD 21046, USA. [19]Columbia Astrophysics Laboratory, Columbia University, New York, NY 10027, USA. [20]Jet Propulsion Laboratory, California Institute of Technology, Pasadena, CA 91109, USA. [21]California Institute of Technology, Pasadena, CA 91125, USA. [22]Istanbul University, Science Faculty, Department of Astronomy and Space Sciences, Beyazıt, 34119 Istanbul, Turkey. [23]National Space Institute, Technical University of Denmark, Elektrovej 327-328, Denmark. [24]Massachusetts Institute of Technology Kavli Institute for Astrophysics and Space Research, Cambridge, MA 02139, USA. [25]Institute of Space and Astronautical Science, Japan Aerospace Exploration Agency, Sagamihara 252-5210, Japan. [26]Usuda Deep Space Center, Japan Aerospace Exploration Agency, Saku 384-0306, Japan. [27]Department of Space and Astronautical Science, SOKENDAI (The Graduate University for Advanced Studies), Sagamihara 252-5210, Japan. [28]Kashima Space Technology Center, National Institute of Information and Communications Technology, Kashima 314-8501, Japan. [29]Center for Astronomy, Ibaraki University, Mito 310-8512, Japan. [30]Planetary Plasma and Atmospheric Research Center, Tohoku University, Sendai 980-8578, Japan. [31]The Research Institute for Time Studies, Yamaguchi University, Yamaguchi 753-8511, Japan. [32]Institute for Space-Earth Environmental Research, Nagoya University, Nagoya 464-8601, Japan. [33]Mizusawa VLBI Observatory, National Astronomical Observatory of Japan, Oshu 023-0861, Japan. [34]Department of Astronomy, University of Tokyo, Tokyo 113-0033, Japan. [35]Department of Astronomical Science, SOKENDAI (The Graduate University for Advanced Studies), Mitaka 181-8588, Japan. [36]Department of Physics, Yamagata University, Yamagata 990-8560, Japan. [37]Department of Physics and Mathematics, Aoyama Gakuin University, Sagamihara 252-5258, Japan.

†These authors contributed equally to this work.

*Corresponding author. E-mail: teruaki.enoto@riken.jp (T.E.); terasawa@icrr.u-tokyo.ac.jp (T.T.); kisaka@hiroshima-u.ac.jp (S.K.); cphu0821@cc.ncue.edu.tw (C.-P. H.)

each x-ray photon was converted to barycentric dynamical time. Figure 1A shows the measured x-ray pulse profile in bins of 132 μs. The x-ray MP peak precedes the average radio profile by the rotation phase $\Delta\phi \cong 0.01$ (~300 μs), consistent with previous observations (*19*). Movie S1 shows how this profile accumulated as a function of exposure.

During the concurrent coverage, we detected ~2.49×10^4 and ~1.75×10^3 GRPs at the MP and IP phases of ϕ = 0.9917 to 1.0083 and ϕ = 1.3944 to 1.4111, respectively (hereafter MP-GRPs and IP-GRPs, respectively). The occurrence rates of MP-GRPs and IP-GRPs at the S-band are 0.67% (24,851 cycles) and 0.047% (1,749 cycles), respectively, of the observed 3,731,830 pulsar rotations. Figure 1A shows the phase distribution of the GRPs. We defined our GRP samples as those pulses with signal-to-noise ratio exceeding 5.0σ, which corresponds to a fluence of $\gtrsim 10^3$ Jy μs [fig. S8 (*14*)]. The occurrence phases and fractions of the MP- and IP-GRPs are consistent with past measurements (*20*, *21*).

We combined the x-ray photons in three bins, corresponding to pulsar rotation cycles where MP-GRPs, IP-GRPs, or neither occurred. These are hereafter referred to as MP-GRP-associated, IP-GRP-associated, or non-GRP-associated x-ray events, respectively. Figure 1B compares the MP-GRP-associated x-ray profile with the non-GRP-associated profile. The MP-GRP-associated x-ray profile shows an enhancement around the phase of the MP, with characteristics similar to those of the previously reported optical enhancement (*15*, *16*). Within the pulse phase interval ϕ = 0.985 to 0.997 [the same width as the optical measurement (*16*), taking into account the observed phase shift between the x-ray and optical bands (*22*)], the MP-GRP-associated x-ray profile shows an enhancement by 3.8±0.7% over the non-GRP-associated profile. We performed the same analysis for IP-GRP-associated x-rays, but did not find statistically significant enhancement, deriving a 3σ upper limit of 10% at ϕ = 1.378 to 1.402 rotational phase (*14*). Hereafter, we focus on the MP-GRP-associated case.

To evaluate the statistical significance of this enhancement, we generated synthetic x-ray samples that have no correlation with MP-GRPs, taking into account the look elsewhere effect (*23*). We randomly selected x-ray events with the same number of cycles as the MP-associated ones (24,826 cycles) from the non-GRP-associated sample. We repeatedly generated 1000 synthetic control samples and made a histogram of simulated enhancements (*14*). This histogram has a Gaussian distribution with mean −0.02% and SD 0.70%. Therefore, the significance of our measured enhancement is 3.8%/0.70% = 5.4σ. Figure 2 shows the growth curves of the detection significance and the x-ray enhancement rate as a function of the accumulated numbers of MP-GRP-associated cycles. The curves show the expected monotonic increase in significance, proportional to the square root of the number of the MP-GRP-associated cycles, and a consistent x-ray enhancement rate. We also confirmed this detection with a lag analysis (*14*). We did not detect any spectral changes (at the MP)

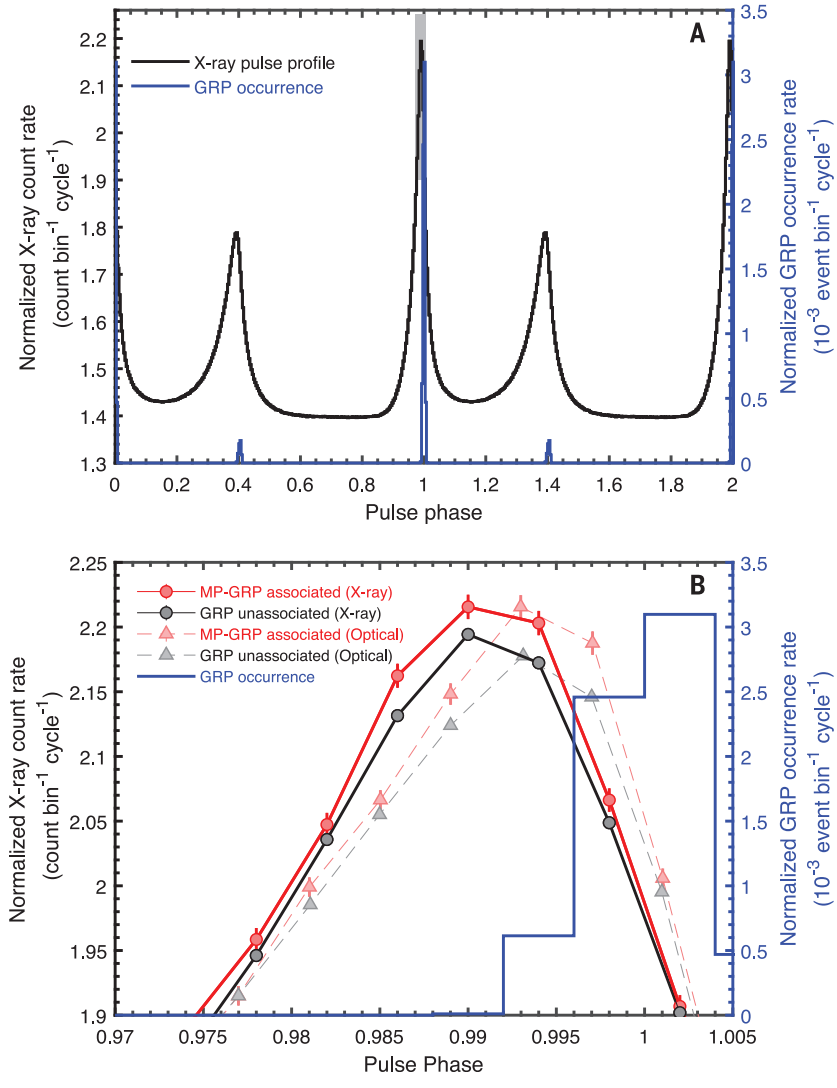

Fig. 1. X-ray and optical pulse profiles of the Crab Pulsar compared with GRPs. (**A**) The 0.3- to 10.0-keV profile (black histogram) observed with *NICER* in 2017–2019 (left axis). The profile was generated with 250 phase bins per spin period, includes the contribution from the Crab Nebula, and is normalized by the total number of pulsar spin cycles. Two pulse cycles are shown for clarity. The phase distribution of GRPs is shown in blue, as measured in our 2.2- to 2.3-GHz radio data from the Usuda and Kashima observatories (right axis). (**B**) A zoomed view of gray-shaded area of (A). Black and red circle symbols connected with solid lines show the x-ray profiles without and with GRP association, respectively, with error bars indicating the 1σ statistical uncertainties (error bars of the black circle and gray triangle points are too small to be visible). The blue histogram shows the GRP occurrence distribution [identical to (A)]. The faint dashed lines (black and red triangle symbols) show the optical profiles without and with GRP association, respectively, normalized by an arbitrary scaling (*16*).

between the GRP-associated and the non-GRP-associated profiles, only an increase in normalization corresponding to the GRP enhancement (*14*).

The total number of x-ray photons concurrent with radio observations in our analysis was 1.4×10^9 counts, about three orders of magnitude higher than previous x-ray studies [e.g., (*3*, *21*)]. Figure 3 compares our detection of the x-ray enhancement of MP-GRPs with previous multiwavelength studies [table S1; (*14*)]. Our detection of a 3.8% x-ray enhancement is consistent with the upper limits of ~10% obtained in previous studies and similar to the measured 3.2 ± 0.5% optical enhancement (*16*). The pulse phase where this x-ray excess appears, $\phi = 0.985$ to 0.997, is also consistent with the reported enhancement phase ($\phi = 0.987$ to 0.999) at optical wavelengths (*16*). This implies that the MP-GRP-associated higher-energy component extends from optical to x-rays without a change in the pulse phase or a spectral cutoff compared with the average regular pulse. The x-ray flux of the regular pulsed emission ($\sim 4.43 \times 10^{-9}$ ergs s^{-1} cm^{-2} in 0.3 to 10 keV) is ~1000 and ~10^7 times higher than those of the optical pulses [$\sim 4.6 \times 10^{-12}$ ergs s^{-1} cm^{-2} at 5500 Å (*24*)] and regular radio pulses [$\sim 1.7 \times 10^{-16}$ ergs s^{-1} cm^{-2} at 2 GHz (*25*)], respectively. Assuming the same enhancement rate (~4%) in both the optical and x-ray bands implies one to two orders of magnitude higher total energy (both flux and fluence) emitted from GRP-associated events than the value derived from the radio and optical data only.

If the x-ray enhancement derived by averaging over ~300 μs (Fig. 1) consists of multiple short pulses similar to GRP pulses (a typical duration of ~15 μs for each GRP, evaluated as fluence divided by the individual peak flux), the peak x-ray flux could be much higher (~20 times) than the averaged enhancement flux.

These results constrain the GRP emission mechanism. The same degree of enhancements (~4%) between the optical and x-rays indicates that the GRP-associated high-energy radiation has the same spectral energy distribution as that of regular pulses. Thus, the energy distribution of GRP-emitting particles is similar to those of particles emitting regular pulses, which result from particle acceleration in the pulsar magnetosphere or a thin corrugated plasma flow at the equatorial plane (a current sheet). The x-ray emission associated with GRPs implies that the radio emission efficiency is ≲1%, consistent with a magnetic reconnection model (*26*).

A previously proposed model of GRP high-energy radiation invokes a temporal increase in particle number density in the emitting region (*27*). The difference in enhancement between the radio (several orders of magnitude) and optical/x-ray bands (~4%) is then attributed to incoherent (x-ray and optical) emissions being proportional to the particle number, whereas coherent (radio) emission is proportional to the particle number squared (see the supplementary text). Other proposed mechanisms are emission from high-energy particles in the plasma blobs (plasmoids) generated by magnetic reconnection (*26*) or from the resonant absorption of radio photons by x-ray emitting particles (*28*) (*14*).

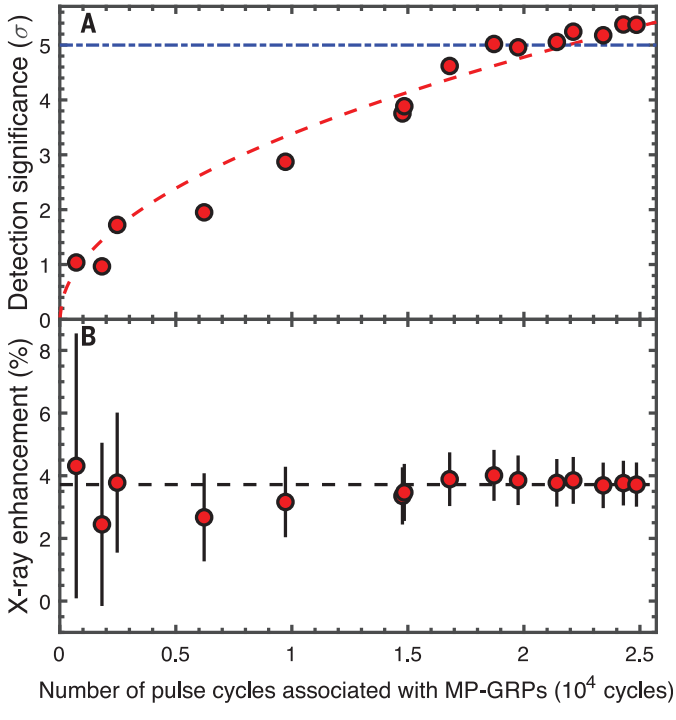

Fig. 2. Growth curves of the detection significance and x-ray enhancement. (**A**) Detection significance as a function of the accumulated number of rotation cycles observed to be associated with MP-GRPs. Data accumulation was performed chronologically, i.e., each data point represents all the *NICER* data up to that epoch. The horizontal blue dot-dashed line is the 5σ detection significance level, and the red dashed curve is the best-fitting model: the square root of the cycle number. (**B**) Same as (A) but for the degree of x-ray enhancement. The horizontal dashed line shows the 3.8% enhancement ratio derived from the entire dataset. Error bars are statistical 1σ uncertainties.

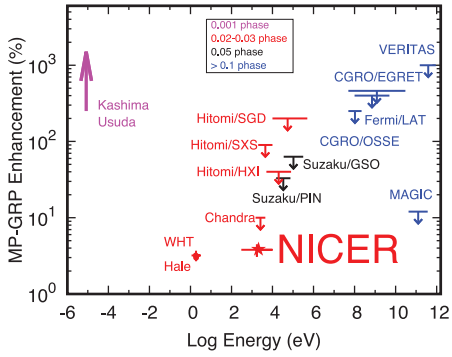

Fig. 3. Enhancement rates with MP-GRPs as a function of photon energy. Optical (WHT and Hale telescopes) and *NICER* data points are detections. All other observations are upper limits in the x-ray and gamma-ray bands indicated by downward arrows [values and references are listed in table S1, and abbreviations are defined in (14)]. Magenta, red, blue, and black colors represent different analyzed phase ranges of 0.001, 0.02 to 0.03, 0.05, and >0.1, respectively. For our observed radio enhancements with Kashima and Usuda, the detection threshold is shown with the magenta upward arrow.

Bright GRPs from young and energetic pulsars or magnetars have been proposed as low-energy analogs of FRBs (*7*), but this proposal has been disputed (*29*). The proposal relies on the unknown GRP radio emission efficiency η relative to the spin-down luminosity. Even in the case of an extremely high efficiency (η ~ 1), the spin-down time scale for FRB sources are shorter than 100 years (*29*, *30*). If FRBs are accompanied by x-ray emission increases similar to Crab GRPs, then the spin-down rate would be enhanced by a factor of 1/η with η << 1. This would cause rapid radio flux decay, which is inconsistent with observations of the repeating FRB 121102 (*31*). Our results therefore disfavor the proposed connection between GRPs and repeating FRBs.

REFERENCES AND NOTES

1. D. B. Melrose, R. Yuen, *J. Plasma Phys.* **82**, 635820202 (2016).
2. H. S. Knight, M. Bailes, R. N. Manchester, S. M. Ord, B. A. Jacoby, *Astrophys. J.* **640**, 941–949 (2006).
3. A. V. Bilous, M. A. McLaughlin, V. I. Kondratiev, S. M. Ransom, *Astrophys. J.* **749**, 24 (2012).
4. W. A. Majid, C. J. Naudet, S. T. Lowe, T. B. H. Kuiper, *Astrophys. J.* **741**, 53 (2011).
5. T. H. Hankins, J. A. Eilek, *Astrophys. J.* **670**, 693–701 (2007).
6. D. R. Lorimer, M. Bailes, M. A. McLaughlin, D. J. Narkevic, F. Crawford, *Science* **318**, 777–780 (2007).
7. J. M. Cordes, I. Wasserman, *Mon. Not. R. Astron. Soc.* **457**, 232–257 (2016).
8. C. D. Bochenek *et al.*, *Nature* **587**, 59–62 (2020).
9. CHIME/FRB Collaboration, *Nature* **587**, 54–58 (2020).

10. W. Lu, P. Kumar, B. Zhang, *Mon. Not. R. Astron. Soc.* **498**, 1397–1405 (2020).
11. R. N. Manchester, G. B. Hobbs, A. Teoh, M. Hobbs, *Astron. J.* **129**, 1993–2006 (2005).
12. T. Enoto, S. Kisaka, S. Shibata, *Rep. Prog. Phys.* **82**, 106901 (2019).
13. D. H. Staelin, E. C. Reifenstein 3rd, *Science* **162**, 1481–1483 (1968).
14. Materials and methods are available as supplementary materials.
15. A. Shearer *et al*., *Science* **301**, 493–495 (2003).
16. M. J. Strader *et al*., *Astrophys. J.* **779**, L12 (2013).
17. K. C. Gendreau *et al*., "The Neutron Star Interior Composition Explorer (NICER): design and development," in *Space Telescopes and Instrumentation 2016: Ultraviolet to Gamma Ray*, J.-W. den Herder, T. Takahashi, M. Bautz, Eds. (SPIE, 2016), vol. 9905 of *Proceedings of SPIE*, p. 99051H.
18. K. Takefuji *et al*., *Publ. Astron. Soc. Pac.* **128**, 084502 (2016).
19. A. Martin-Carrillo *et al*., *Astron. Astrophys.* **545**, A126 (2012).
20. R. Mikami *et al*., *Astrophys. J.* **832**, 212 (2016).
21. Hitomi Collaboration, *Publ Astron Soc Jpn Nihon Tenmon Gakkai* **70**, (2018).
22. R. Bühler, R. Blandford, *Rep. Prog. Phys.* **77**, 066901 (2014).
23. E. Gross, O. Vitells, *Eur. Phys. J. C* **70**, 525–530 (2010).
24. A. A. Abdo *et al*., *Astrophys. J.* **208**, 17 (2013).
25. A. V. Bilous *et al*., *Astron. Astrophys.* **591**, A134 (2016).
26. A. Philippov, D. A. Uzdensky, A. Spitkovsky, B. Cerutti, *Astrophys. J.* **876**, L6 (2019).
27. M. Lyutikov, *Mon. Not. R. Astron. Soc.* **381**, 1190–1196 (2007).
28. A. K. Harding, J. V. Stern, J. Dyks, M. Frackowiak, *Astrophys. J.* **680**, 1378–1393 (2008).
29. M. Lyutikov, *Astrophys. J.* **838**, L13 (2017).
30. S. Kisaka, T. Enoto, S. Shibata, *Publ. Astron. Soc. Jpn.* **69**, L9 (2017).
31. M. Cruces *et al*., *Mon. Not. R. Astron. Soc.* **500**, 448–463 (2021).
32. C. P. Hu, Source code and GRP list for Crab GRP analysis, Version 0.1, Zenodo (2021); https://doi.org/10.5281/zenodo.4586922.

ACKNOWLEDGMENTS

We thank Y. Terada and N. Kawai for suggestions on our analysis and manuscript; the Usuda 64-m antenna operation support team in Space Tracking and Communication Center and ISAS, JAXA for coordinating simultaneous observations with NICER; and E. Kawai and S. Hasegawa of the Space Time Standard Laboratory of the Kashima Space Technology Center of the National Institute of Information and Communications Technology (NICT) for supporting observations with the Kashima 34-m antenna. *NICER* analysis software and data calibration were provided by the NASA *NICER* mission and the Astrophysics Explorers Program. **Funding:** T.E., T.T., H.M., K.A., M.H., S.S., S.J.T., and S.K. are supported by JSPS/MEXT KAKENHI grant nos. 15H00845, 15K05069,16H02198, 17H01116, 17K18270, 17K18776, 18H01245, 18H01246, 18H04584, and 19K14712. T.E. acknowledges Hakubi projects of Kyoto University and RIKEN. W.C.G.H. acknowledges support through grant no. 80NSSC20K0278 from NASA. C.H. was supported as the JSPS International Research Fellow (ID: P18318) and by the Ministry of Science and Technology in Taiwan through grant no. MOST 109-2112-M-018-009-MY3. C.M. is supported by an appointment to the NASA Postdoctoral Program at the Marshall Space Flight Center, administered by Universities Space Research Association under contract with NASA. H.T. was supported by the discretionary expenses of the director of Institute of Space and Astronautical Science (ISAS), JAXA. W.A.M performed research at the Jet Propulsion Laboratory, California Institute of Technology, under a contract with the NASA. **Author contributions:** T.E. and T.T. led this radio-x-ray collaboration. T.T. and C.H. led the radio and x-ray timing analyses, respectively. S.G. performed the x-ray spectral analyses. S.K. led the theoretical discussion. P.S.R., T.O., Z.A., K.C.G., C.B.M., Y.S., S.K., S.B., and R.F. were responsible for *NICER* detector development, timing calibration, and observation planning. C.M., W.C.G.H., A.K.H., Z.W., W.A.M., T.G., G.K.J., K.A., S.S., N.L., and S.J.T. contributed to the theoretical interpretation. Y.M., H.T., K.T., M.S., Y.Y., H.M., F.T., T.A., M.T., M.H., O.K., and T.O. were responsible for the radio observations and associated data analyses. N.L. contributed the summary of previous studies. **Competing interests:** The authors declare no competing interests. **Data and materials availability:** The *NICER* x-ray data are available from the NASA HEASARC archive https://heasarc.gsfc.nasa.gov/ under the observation IDs listed in table S6. The HEASOFT x-ray analysis software is available from https://heasarc.gsfc.nasa.gov/docs/software/heasoft/. The GRP event lists and our analysis source codes are available on Zenodo (*32*).

SUPPLEMENTARY MATERIALS

science.sciencemag.org/content/372/6538/187/suppl/DC1
Materials and Methods
Supplementary Text
Figs. S1 to S20
Tables S1 to S7
References (*33*–*78*)
Movie S1
MDAR Reproducibility Checklist

23 June 2020; accepted 5 March 2021
10.1126/science.abd4659

SUPERCONDUCTIVITY

Gate-controlled BCS-BEC crossover in a two-dimensional superconductor

Yuji Nakagawa[1,2], Yuichi Kasahara[3], Takuya Nomoto[1], Ryotaro Arita[1,4], Tsutomu Nojima[5], Yoshihiro Iwasa[1,2,4]*

Bardeen-Cooper-Schrieffer (BCS) superfluidity and Bose-Einstein condensation (BEC) are the two extreme limits of the ground state of the paired fermion systems. We report crossover behavior from the BCS limit to the BEC limit realized by varying carrier density in a two-dimensional superconductor, electron-doped zirconium nitride chloride. The phase diagram, established by simultaneous measurements of resistivity and tunneling spectra under ionic gating, demonstrates a pseudogap phase in the low-doping regime. The ratio of the superconducting transition temperature and Fermi temperature in the low–carrier density limit is consistent with the theoretical upper bound expected in the BCS-BEC crossover regime. These results indicate that the gate-doped semiconductor provides an ideal platform for the two-dimensional BCS-BEC crossover without added complexities present in other solid-state systems.

The pairing and condensation of fermions are fundamental to a variety of systems including neutron stars, superconductors, and ultracold atomic gases (*1*–*7*). There are two limiting cases for fermion condensation, described by two distinct theories: the Bardeen-Cooper-Schrieffer (BCS) theory and Bose-Einstein condensation (BEC). The former explains superfluidity in the weak-coupling or high-density limit, where individual fermions directly condense to a coherent state of fermion pairs. This type of condensation is typically observed in the superconductivity of electrons. The latter occurs in the strong-coupling, low-density limit. Fermions first form pairs that behave as bosons, and these bosons then undergo the BEC to the superfluid state (*1*). This phenomenon is most clearly seen in fermionic gases (*3*). These two limits are continuously connected through an intermediate regime, exhibiting universal behavior called the BCS-BEC crossover (*2*, *7*).

Ultracold atomic gases and superconductors are favorable experimental settings for the observation of the BCS-BEC crossover because the coupling strength between the constituent fermions can be controlled in a quasi-continuous manner. In ultracold atomic gases, the coupling strength is highly modulated via Feshbach resonances (*7*), sweeping through the crossover regime from the BEC limit (*4*, *6*). In superconductors, the crossover regime can be entered from the BCS limit by controlling the carrier density and, consequently, the coupling strength.

The dimensionless coupling strength in superconductors is determined by Δ/E_F, where Δ is the superconducting gap and E_F is the Fermi energy measured from the bottom of the conduction band. As Δ/E_F is increased by enhanced pairing interaction or reduced carrier density, the system enters the BCS-BEC crossover regime accompanied by the enhancement of T_c/T_F, where T_c and T_F are the superconducting critical temperature and the Fermi temperature, respectively. As represented in the well-known Uemura plot (*8*), conventional metallic superconductors such as Nb and Al reside deep inside the BCS limit ($T_c/T_F << 1$), whereas the "exotic" superconductors, including cuprates, organics, heavy fermions, and iron-based superconductors, are located rather close to the BCS-BEC crossover region with $T_c/T_F \sim 0.05$. However, even in these systems, the coupling strengths are not high enough to reach the BEC limit beyond the crossover regime; additionally, when carrier

[1]Department of Applied Physics, University of Tokyo, Hongo 7-3-1, Bunkyo-ku, Tokyo 113-8656, Japan. [2]Quantum-Phase Electronics Center, University of Tokyo, Hongo 7-3-1, Bunkyo-ku, Tokyo 113-8656, Japan. [3]Department of Physics, Kyoto University, Kitashirakawa Oiwakecho, Sakyo-ku, Kyoto 606-8502, Japan. [4]RIKEN Center for Emergent Matter Science, Hirosawa 2-1, Wako, Saitama 351-0198, Japan. [5]Institute for Materials Research, Tohoku University, Katahira 2-1-1, Aoba-ku, Sendai 980-0812, Japan.
***Corresponding author. Email: iwasa@ap.t.u-tokyo.ac.jp**

density is low, strong electron correlation effects and magnetic ordering (*9*) cloud the crossover phenomena by added complexity. Therefore, the clear demonstration of the BCS-BEC crossover is still a key challenge in the study of superconductivity. Although FeSe systems (*10*–*12*), magic-angle twisted bilayer graphene (*13*, *14*), and layered nitrides (*15*) have been studied in this context, the wide-range control of Δ/E_F needed to go from the BCS regime to the BEC limit has not been realized to date.

Here, we studied the superconductor Li_xZrNCl, a lithium-intercalated layered nitride (*15*, *16*) (Fig. 1A). Lithium supplies electrons to the double-honeycomb ZrN layer, which is a band insulator in the absence of doping. A single conduction band originating from Zr 4d orbitals hybridized with N 2p orbitals exists at each corner of the hexagonal Brillouin zone (K and K′ points). An unusual property reported in polycrystalline bulk samples of Li_xZrNCl is T_c enhancement with decreased doping until superconductivity is quenched by disorder (*17*). A further increase of T_c above 15 K is theoretically proposed to exist in the low–carrier density limit (*18*, *19*), which corresponds to a substantial increase of Δ/E_F and the realization of the BCS-BEC crossover.

Single-crystal measurements of pristine ZrNCl have been performed using ionic-gating methods (*20*, *21*). Interface superconductivity was realized in electrostatic electric double-layer transistors (EDLTs), where the intrinsic two-dimensional (2D) nature of superconductivity has been demonstrated in this 2D material. Recently, we introduced a modified device structure designed for an electrochemical intercalation mode as well as tunneling spectroscopy measurements (*15*). In attempts to approach the low–carrier density limit of both Li_xZrNCl and Li_xHfNCl, the electrical control of the amount of Li in single crystals has been proven to be more effective than the conventional chemical intercalation methods in polycrystalline samples synthesized with *n*-butyllithium. A dimensional crossover from anisotropic 3D to 2D superconductivity was found to occur when the carrier density was decreased (*15*).

Here, we report the superconducting behavior of Li_xZrNCl in a regime of even lower carrier density, down to $x = 0.0038$. With dilution of the carrier density, T_c shows the maximum value of 19.0 K at $x = 0.011$; Δ/E_F increases above 0.3, which is considered to be the border between the weak-coupling BCS limit and the BCS-BEC crossover regime in 2D systems (*22*). The Berezinskii-Kosterlitz-Thouless (BKT) transition temperature T_{BKT} reaches $0.12T_F$, which is close to the maximum value generally predicted in the fermion systems, especially in the BCS-BEC crossover regime (*23*). Tunneling spectroscopy simultaneously performed with the resistivity measurements reveals that the onset temperature of the pseudogap phase at which the fermions form pairs without condensation (*6*, *7*) is higher in the diluted regime. These results are an unambiguous demonstration of a crossover from the BCS to the BEC regime of a 2D superconductor by scanning the doping level across nearly two orders of magnitude from $x = 0.28$ to $x = 0.0038$.

Figure 1B presents a schematic of our ionic-gating device structure. In addition to the Hall bar structure, narrow electrodes for the tunneling spectroscopy were prepared on the channel region between the source and drain electrodes, and the device was then covered with a poly(methyl methacrylate) (PMMA) resist. The cover outside of the channel region was removed such that Li ions in the electrolyte could intercalate from both exposed sides of the flake. During the application of the gate voltage V_G, we traced the intercalation process through the measurement of the source-drain current (Fig. 1C). The forward scan shows a sharp increase of current corresponding to sudden intercalation, possibly because of a change in the stacking pattern (*16*). In contrast, the deintercalation in the reverse scan is rather gradual. This process enabled us to control the intercalation level down to the lowest level of $x = 0.0038$. The Hall effect showed a systematic dependence on V_G (Fig. 1D) and was almost independent of temperature and measurement position on the flake (figs. S2 and S3). To determine the Li concentration x, we used the Hall carrier density at 150 K and assumed that one electron per Li ion is supplied to the ZrNCl conduction layer.

In Fig. 2, A and B, we show the temperature dependence of resistivity at various doping levels. T_c increased from 11.5 K to 19.0 K when the doping level was decreased from 0.28 to 0.011. We defined T_c as the midpoint of the resistive transition. The maximum T_c of 19.0 K is higher than the previously reported value (15.4 K) for the ZrNCl system (*15*, *17*); interestingly, this is realized by reducing the doping level. Below $x = 0.011$, corresponding to a carrier density of $n_{3D} = 2.1 \times 10^{20}$ cm^{-3}, T_c starts to decrease, leading to a peak structure in the phase diagram (Fig. 3E).

The resistive transition in the highly doped regime is sharp, whereas it is substantially broadened in the lightly doped regime (Fig. 2B). As reported previously (*15*), this feature represents a dimensional crossover from anisotropic 3D to 2D superconductivity because of the reduced interlayer hopping, as discussed

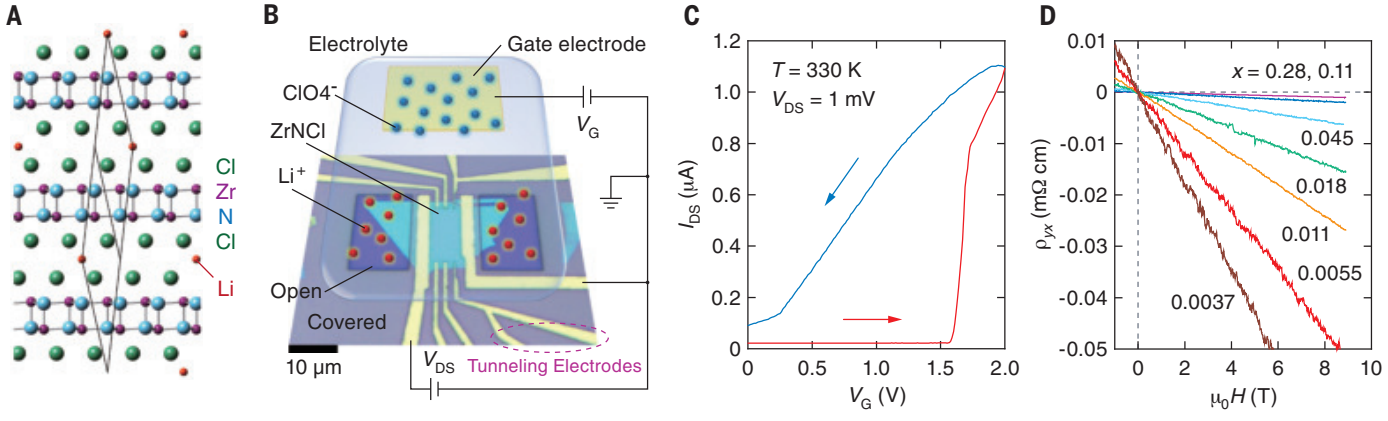

Fig. 1. Gate-controlled intercalation in a ZrNCl device. (**A**) Side view of Li_xZrNCl crystal structure. Solid lines represent the rhombohedral unit cell. (**B**) Schematic illustration of the ionic-gating device based on a real optical micrograph of a ZrNCl single-crystal flake and patterned electrodes. Narrow contacts are prepared for the tunneling spectroscopy measurements. PMMA covers the whole device except for the outer area of the flake and the gate electrode. The electrolyte containing $LiClO_4$ is dropped onto the device. A gate voltage V_G is applied to the electrolyte, and lithium cations and ClO_4 anions move oppositely. Lithium cations intercalate from the sides of the flake. (**C**) Source-drain current I_{DS} of the device in intercalation operation. During the forward sweep of V_G (red), I_{DS} increases steeply, whereas the change of I_{DS} is gradual in the backward scan (blue). V_G is swept at a speed of 10 mV/s. (**D**) Antisymmetrized transverse resistivity at 150 K for various values of the Li content x. The linear slope is used to determine x.

later. In the 2D regime, the superconducting transition is described by the BKT transition, and the temperature dependence of resistivity follows the Halperin-Nelson equation (*24*, *25*):

$$\rho(T) = a\rho_N \exp\left\{-2\left[\frac{b(T_c' - T)}{T - T_{BKT}}\right]^{1/2}\right\} \quad (1)$$

where a, b, and T_c' are fitting parameters, and ρ_N is resistivity in the normal state. According to this formula, $[d(\ln \rho)/dT]^{-2/3}$ is proportional to $(T - T_{BKT})$ around T_{BKT}, from which we determine T_{BKT} as the temperature-axis intercept of the linear extrapolation (Fig. 2C, inset). With this T_{BKT}, Eq. 1 provides a good fit in the transition region for $x = 0.011$ (black line in Fig. 2C, where $T_{BKT} = 17.9$ K, $a\rho_N = 1.59 \times 10^{-3}$ ohm·cm, $b = 1.23$, and $T_c' = 20.1$ K). This resistivity fit to Eq. 1 holds at least up to $x = 0.045$, but not above $x = 0.13$ because of the sharp transition. As reported previously, the two-dimensionality of the superconductivity was also confirmed at $x = 0.06$ by the temperature dependence of the in-plane upper critical field, $H_{c2}^{\parallel}(T) \propto \sqrt{1 - T/T_c}$, which is typical behavior for 2D superconductors explained within the Ginzburg-Landau model [figure 2C of (*15*)]. These results lead us to conclude that the crossover from anisotropic 3D to 2D superconductivity occurs around $x \sim 0.1$.

The dimensional crossover from anisotropic 3D to 2D superconductivity caused by the reduction of carrier density is an unexpected phenomenon, particularly when we recall that the out-of-plane lattice parameter decreases with decreasing Li concentration (*17*). This feature is attributed to the peculiar nature of rhombohedral stacking of ZrNCl layers, where the unit cell is composed of three layers (Fig. 1A). According to symmetry arguments, the interlayer hopping at the K point of the hexagonal Brillouin zone becomes exactly zero up to the second nearest layer in the rhombohedral structure (*26*). Our density functional theory (DFT) calculation with improved energy resolution also confirms the indiscernible K-H dispersion (*27*). When the doping level is reduced, the Fermi surface converges to the K point. Consequently, the interlayer coupling is weakened, and the out-of-plane coherence length is shortened.

Figure 2D shows the temperature dependence of the out-of-plane upper critical field H_{c2} at each doping level (see fig. S4 for the determination of H_{c2}). Based on the Ginzburg-Landau model, $\mu_0 H_{c2}(T) = [\Phi_0/(2\pi\xi^2)][1 - (T/T_c)]$ where Φ_0 is a flux quantum, we derived the in-plane coherence length at zero temperature (ξ) by using the slope of the $\mu_0 H_{c2}$-T line (Fig. 2E). Even after T_c starts to drop below $x = 0.011$, ξ keeps decreasing, indicating that strongly coupled small Cooper pairs are realized in the low–carrier density regime.

During the cooling process for the transport measurements, we were able to perform tunneling spectroscopy because a Schottky barrier, which served as a tunneling barrier (*15*), formed at the electrode interface. Figure 3A displays symmetrized tunneling spectra dI/dV at $T = 2$ K (see fig. S5 for the raw data). We normalized the spectra at 55 K after the subtraction of the channel resistance contribution (*15*). The superconducting gap structure is clearly observed and becomes wider in the low-doping regime. The gap energy Δ is determined by fitting the spectra to the Dynes function (*28*), and its doping dependence is plotted in Fig. 3B. At high doping levels, the present results agree well with the previously reported values determined by specific heat measurements on bulk polycrystalline samples (*29*). The value of $2\Delta/k_B T_c$ is ~3.5 at the highest doping level, indicating that superconductivity in the highly doped state is within the BCS regime. Decreasing carrier

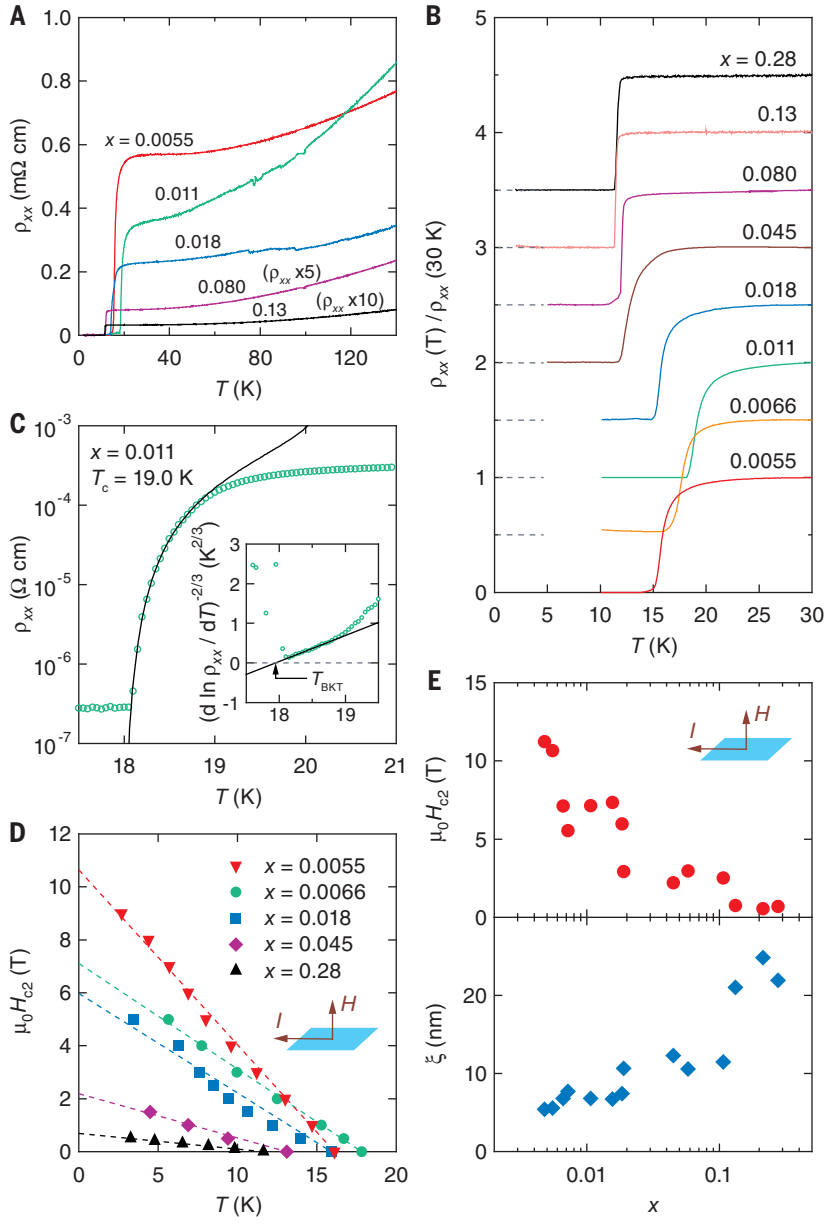

Fig. 2. Transport properties of Li_xZrNCl. (**A**) Temperature dependence of resistivity at different doping levels. The resistivities at $x = 0.080$ and $x = 0.13$ are multiplied by 5 and 10, respectively. (**B**) Resistivity normalized at 30 K. Each curve is shifted by 0.5, and gray dashed lines indicate zero lines. (**C**) Resistivity at $x = 0.011$ showing the BKT transition. The black line is the fit to the Halperin-Nelson formula. Inset: Resistivity plotted on a $[d(\ln \rho)/dT]^{-2/3}$ scale. (**D**) Out-of-plane upper critical field H_{c2} as a function of temperature. Dashed lines are linear extrapolations to 0 K for each doping level. (**E**) Doping dependence of H_{c2} at 0 K in (D) (top) and in-plane coherence length ξ (bottom).

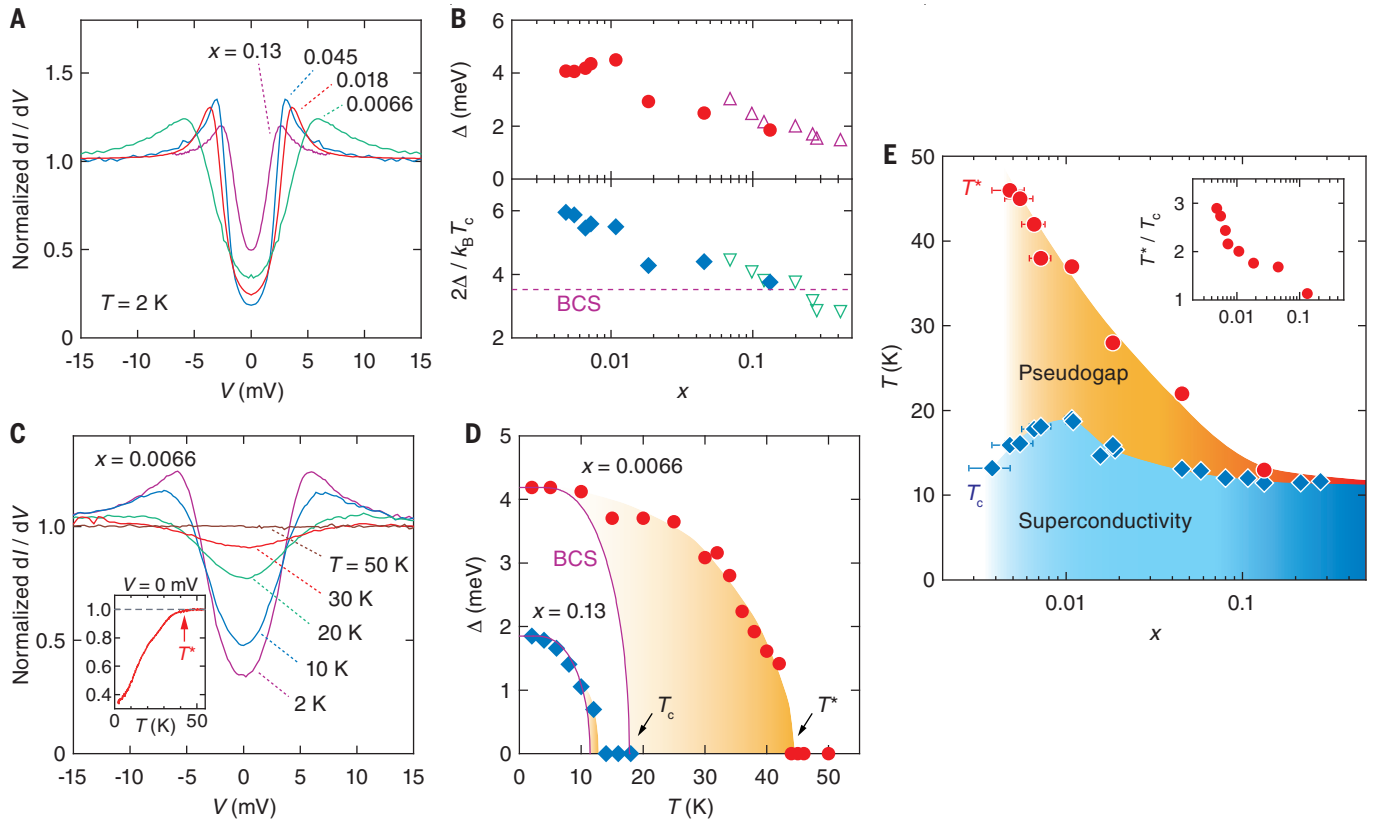

Fig. 3. Tunneling spectroscopy of Li_xZrNCl. (**A**) Symmetrized and normalized tunneling spectra at 2 K. At each doping level, spectra at 55 K are used for the normalization to remove the bias- and x-dependent background after the subtraction of channel resistivity (*15*, *27*). (**B**) Doping dependence of superconducting gap Δ (top) and its ratio to the critical temperature T_c (bottom). The BCS theory predicts $2\Delta/k_BT_c = 3.52$ (dashed line). In both top and bottom panels, open symbols are measured values in polycrystalline samples (*29*). (**C**) Tunneling spectra at $x = 0.0066$ for different temperatures normalized at 55 K without symmetrization. Inset: Temperature scan of zero-bias conductance (ZBC) dI/dV at $V = 0$. The gap-opening temperature T^* is determined by a 1% drop of ZBC. (**D**) Δ at $x = 0.0066$ (circles) and 0.13 (diamonds) as a function of temperature. Solid lines indicate the BCS-type gap function with T_c determined by the resistive transition. (**E**) Phase diagram of Li_xZrNCl. The temperature regime between T_c and T^* represents the pseudogap state. Error bars were estimated by positional dependence measurement with multiple Hall probes (fig. S3). Inset: The ratio between T^* and T_c.

density corresponds to stronger coupling, which is reflected in a rise of $2\Delta/k_BT_c$, reaching 6.0 at the lowest carrier density. We show the temperature evolution of the tunneling spectra at a low doping level in Fig. 3C. The gap smoothly evolves, and it closes only at temperatures higher than T_c.

The inset of Fig. 3C displays the temperature dependence of the zero-bias conductance (ZBC) dI/dV at $V = 0$. We determined the gap-opening temperature T^* by a 1% drop of the ZBC from the value at high temperatures. Figure 3D shows the temperature dependence of Δ at $x = 0.0066$ and 0.13 (see fig. S7 for further information). We set $\Delta = 0$ at temperatures above T^*, and the scaled BCS-type gap function was calculated by using T_c. For $x = 0.0066$, T^* is more than twice as high as T_c, demonstrating the stabilization of the pseudogap state. This is in marked contrast with the case of $x = 0.13$, where T_c and T^* match each other. Such behavior is summarized in the phase diagram (Fig. 3E), which shows that the pseudogap state is developed in the low–carrier density regime.

In Fig. 4A, we show the doping dependence of Δ/E_F and $1/(k_F\xi)$, where k_F is the Fermi wave vector. Δ/E_F can be converted to the dimensionless crossover parameter $\ln(k_Fa_{2D})$, where a_{2D} is the 2D scattering length (*22*). The crossover regime in 2D systems corresponds to $\ln(k_Fa_{2D}) > 2$ and $\Delta/E_F > 0.3$. Larger values of $1/(k_F\xi)$ represent smaller numbers of overlapped pairs because $1/k_F$ represents the interparticle distance. E_F and k_F are estimated by the carrier density and the doping-independent effective mass of ZrNCl, $0.9m_0$, which was extracted from the specific heat measurements (*29*). This effective mass is also supported by the DFT calculation combined with electron-phonon interactions (*27*). The monotonic increase in Δ/E_F and $1/(k_F\xi)$ toward the low doping limit represents the continuous shift from the BCS limit toward the BCS-BEC crossover regime. Note that Δ/E_F becomes larger than 0.3 at $x = 0.005$, corresponding to the BCS-BEC crossover region (*22*). A value of $1/(k_F\xi) \sim 0.36$ means that a few Cooper pairs overlap, contrary to the assumption in the BCS theory.

By taking Δ/E_F or $1/(k_F\xi)$ as a bottom axis, we depict the BCS-BEC crossover phase diagram (Fig. 4B). Both the superconducting and pseudogap phases systematically evolve as predicted by theories (*2*, *7*). Because the 2D superconductivity is realized in the lightly doped regime, it should be compared to the theory developed for 2D systems, where $T_{BKT}/T_F = 0.125$ is derived as the upper bound for the transition in all fermion systems (*23*). The present measurements reached a value of $T_{BKT}/T_F = 0.116$ ($T_c/T_F = 0.121$) at $\Delta/E_F = 0.36$, which is close to the theoretical limit. This agreement demonstrates that superconductors, where charged electron pairs reside in lattice potentials, can reach the general upper bound. Figure 4C shows the Uemura plot of our results together with those for other materials (*11*, *13*, *15*, *30*–*32*). Li_xZrNCl approaches the limit of $T_c/T_F = 0.125$ with decreasing T_F from the BCS limit (lower right side of the plot), providing a strong piece of evidence that the BCS-BEC crossover is indeed realized. The T_c reduction below

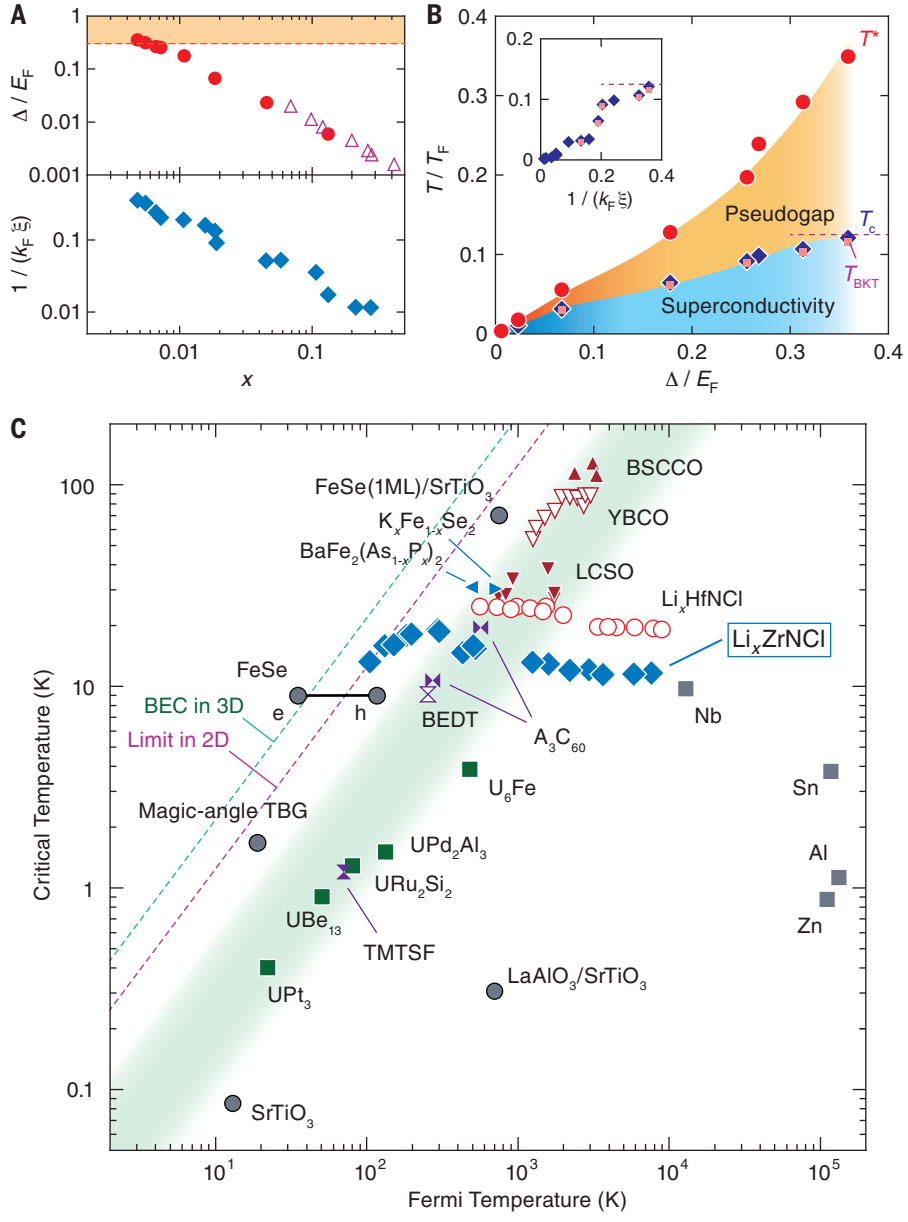

Fig. 4. The BCS-BEC crossover in superconducting Li_xZrNCl. (**A**) Doping dependence of the ratio between superconducting gap and Fermi energy (Δ/E_F) (top) and the ratio between interparticle distance and coherence length ($1/k_F\xi$) (bottom). The orange area represents the BCS-BEC crossover regime (*22*). Open triangles are measured values from specific heat measurement (*29*). (**B**) The phase diagram of the BCS-BEC crossover. Gap opening temperature T^*, critical temperature T_c, and critical temperature of BKT transition T_{BKT} are normalized by Fermi temperature T_F and plotted as functions of Δ/E_F with red spheres, dark blue diamonds, and pink squares, respectively. The dashed line represents the theoretically predicted upper bound, $T_{BKT}/T_F = 0.125$ (*23*). Inset: T_c/T_F and T_{BKT}/T_F as functions of $1/k_F\xi$. (**C**) Uemura plot: Critical temperature versus Fermi temperature is plotted for various superconductors (*11*, *13*, *15*, *30*–*32*). As x is decreased, Li_xZrNCl departs from the BCS limit, arriving at the crossover region having traversed the shaded area, where most of the unconventional superconductors are located (*8*). The dashed line "BEC in 3D" represents the critical temperature in the BEC limit in 3D Fermi gas systems, $T_c = 0.218T_F$ (*2*). The dashed line "Limit in 2D" corresponds to the general upper limit of $T_{BKT} = 0.125T_F$ in all 2D fermionic systems (*23*).

$x = 0.011$ (Fig. 3E) is attributed to the limitation of T_c (T_{BKT}) scaled by T_F in the BCS-BEC crossover regime rather than to other causes, such as a tendency toward electron localization.

It is useful to discuss pseudogap states in several materials and compare them with the present system. In unconventional superconductors, pseudogap states are frequently observed close to insulating phases, but in many cases they tend to be complex because of strong electron correlation effects and magnetic ordering (*9*). In stark contrast, Li_xZrNCl offers a much simpler testbed because the undoped state at $x = 0$ is a band insulator, free from electron correlation effects, magnetic orders, and density waves. Also, unlike magic-angle twisted bilayer graphene, the simple parabolic conduction band does not apply further constraints on T_c (*23*) and makes Li_xZrNCl a model system for the BCS-BEC crossover.

Even in disordered thin films, the pseudogap state originating from localized Cooper pairs is observed (*33*). Such a localized model is unlikely for the present system because resistivity shows metallic behavior. Furthermore, as summarized in table S1, the mean free path in the Li_xZrNCl system is comparable to the Pippard coherence length $\xi_{Pippard} = \hbar v_F/\pi\Delta$, where $\hbar$ and v_F are Dirac's constant and the Fermi velocity, respectively, indicating that the system is far from the dirty limit.

These considerations strongly support the notion that the observed pseudogap state in Li_xZrNCl can be attributed to the preformed pair formation in the BCS-BEC crossover scenario. We note that the pseudogap state is observable in a wide range, even when Δ/E_F is less than 0.3. In a bulk study, a nuclear magnetic resonance measurement on polycrystalline Li_xZrNCl samples reported a pseudogap state on the high-doping side of the superconducting dome (*34*). T^* was reported to be ~25 K when $T_c = 15$ K ($x = 0.08$), which agrees with the present result. The early appearance of pseudogap states below $x \sim 0.1$ may be attributed to two-dimensionality, which prefers the pseudogap formation (*35*). This scenario can be applied to the pseudogap state observed at a $LaAlO_3/SrTiO_3$ interface (*36*). That system is distant from the BCS-BEC crossover regime (Fig. 4C), but its two-dimensionality gives rise to a pseudogap.

We have demonstrated a 2D BCS-BEC crossover through the systematic tuning of the coupling strength of superconductivity in Li_xZrNCl. The 2D BCS-BEC crossover was realized in the present system as a result of the dimensional crossover from anisotropic 3D to 2D superconductivity upon reducing the carrier density. Similar crossover is seen in arrays of 2D clouds of Fermi gases (*37*) where dimensionality is also affected by the coupling strength. Such complementary studies advance our understanding of fermion condensation physics.

REFERENCES AND NOTES

1. D. M. Eagles, *Phys. Rev.* **186**, 456–463 (1969).
2. C. A. R. Sá de Melo, M. Randeria, J. R. Engelbrecht, *Phys. Rev. Lett.* **71**, 3202–3205 (1993).
3. M. Greiner, C. A. Regal, D. S. Jin, *Nature* **426**, 537–540 (2003).
4. C. A. Regal, M. Greiner, D. S. Jin, *Phys. Rev. Lett.* **92**, 040403 (2004).
5. A. Gezerlis, J. Carlson, *Phys. Rev. C* **81**, 025803 (2010).

6. J. P. Gaebler *et al.*, *Nat. Phys.* **6**, 569–573 (2010).
7. M. Randeria, E. Taylor, *Annu. Rev. Condens. Matter Phys.* **5**, 209–232 (2014).
8. Y. J. Uemura *et al.*, *Phys. Rev. Lett.* **66**, 2665–2668 (1991).
9. B. Keimer, S. A. Kivelson, M. R. Norman, S. Uchida, J. Zaanen, *Nature* **518**, 179–186 (2015).
10. S. Rinott *et al.*, *Sci. Adv.* **3**, e1602372 (2017).
11. S. Kasahara *et al.*, *Proc. Natl. Acad. Sci. U.S.A.* **111**, 16309–16313 (2014).
12. T. Hashimoto *et al.*, *Sci. Adv.* **6**, eabb9052 (2020).
13. Y. Cao *et al.*, *Nature* **556**, 43–50 (2018).
14. J. M. Park, Y. Cao, K. Watanabe, T. Taniguchi, P. Jarillo-Herrero, *Nature* **590**, 249–255 (2021).
15. Y. Nakagawa *et al.*, *Phys. Rev. B* **98**, 064512 (2018).
16. Y. Kasahara, K. Kuroki, S. Yamanaka, Y. Taguchi, *Physica C* **514**, 354–367 (2015).
17. Y. Taguchi, A. Kitora, Y. Iwasa, *Phys. Rev. Lett.* **97**, 107001 (2006).
18. K. Kuroki, *Phys. Rev. B* **81**, 104502 (2010).
19. M. Calandra, P. Zoccante, F. Mauri, *Phys. Rev. Lett.* **114**, 077001 (2015).
20. J. T. Ye *et al.*, *Science* **338**, 1193–1196 (2012).
21. Y. Saito, Y. Kasahara, J. Ye, Y. Iwasa, T. Nojima, *Science* **350**, 409–413 (2015).
22. L. He, H. Lü, G. Cao, H. Hu, X.-J. Liu, *Phys. Rev. A* **92**, 023620 (2015).
23. T. Hazra, N. Verma, M. Randeria, *Phys. Rev. X* **9**, 031049 (2019).
24. B. I. Halperin, D. R. Nelson, *J. Low Temp. Phys.* **36**, 599–616 (1979).
25. A. M. Kadin, K. Epstein, A. M. Goldman, *Phys. Rev. B* **27**, 6691–6702 (1983).
26. R. Akashi, Y. Iida, K. Yamamoto, K. Yoshizawa, *Phys. Rev. B* **95**, 245401 (2017).
27. See supplementary materials.
28. R. C. Dynes, V. Narayanamurti, J. P. Garno, *Phys. Rev. Lett.* **41**, 1509–1512 (1978).
29. Y. Kasahara *et al.*, *Phys. Rev. Lett.* **103**, 077004 (2009).
30. Q.-W. Wang *et al.*, *Chin. Phys. Lett.* **29**, 037402 (2012).
31. Y. J. Uemura, *J. Phys. Condens. Matter* **16**, S4515–S4540 (2004).
32. X. Lin, Z. Zhu, B. Fauqué, K. Behnia, *Phys. Rev. X* **3**, 021002 (2013).
33. B. Sacépé *et al.*, *Nat. Phys.* **7**, 239–244 (2011).
34. H. Kotegawa *et al.*, *Phys. Rev. B* **90**, 020503(R) (2014).
35. Q. Chen, I. Kosztin, B. Jankó, K. Levin, *Phys. Rev. B* **59**, 7083–7093 (1999).
36. C. Richter *et al.*, *Nature* **502**, 528–531 (2013).
37. M. G. Ries *et al.*, *Phys. Rev. Lett.* **114**, 230401 (2015).
38. Harvard Dataverse, https://doi.org/10.7910/DVN/MJAMIV.

ACKNOWLEDGMENTS

We thank K. Kanoda, T. Shibauchi, T. Hanaguri, M. Nakano, R. Akashi, M. Hirayama, and F. Qin for fruitful discussions, and M. Heyl for critical reading and correction of the manuscript. **Funding:** Supported by A3 Foresight Program and JSPS KAKENHI grants JP19H05602 and JP17J08941. Y.N. was supported by the Materials Education Program for the Future Leaders in Research, Industry, and Technology (MERIT). **Author contributions:** Y.N., T.N., and Y.I. conceived and designed the experiments; Y.N. fabricated the devices, performed measurements, and analyzed the data; Y.K. grew the single crystal of ZrNCl; T.N. and R.A. conducted the DFT calculations; and all authors discussed the results and wrote the manuscript. **Competing interests:** The authors declare no competing interests. **Data and materials availability:** Data shown in the main text and the supplementary materials and instructions for the calculations are available at (*38*).

SUPPLEMENTARY MATERIALS

science.sciencemag.org/content/372/6538/190/suppl/DC1
Materials and Methods
Supplementary Text
Figs. S1 to S8
Table S1
References (*39*–*54*)

31 March 2020; accepted 5 March 2021
Published online 18 March 2021
10.1126/science.abb9860

NANOMATERIALS

Seeded 2D epitaxy of large-area single-crystal films of the van der Waals semiconductor 2H $MoTe_2$

Xiaolong Xu[1,2], Yu Pan[1], Shuai Liu[1], Bo Han[3,4], Pingfan Gu[1], Siheng Li[4], Wanjin Xu[1], Yuxuan Peng[1], Zheng Han[5,6], Ji Chen[1], Peng Gao[2,3,4], Yu Ye[1,2,7]*

The integration of two-dimensional (2D) van der Waals semiconductors into silicon electronics technology will require the production of large-scale, uniform, and highly crystalline films. We report a route for synthesizing wafer-scale single-crystalline 2H molybdenum ditelluride ($MoTe_2$) semiconductors on an amorphous insulating substrate. In-plane 2D-epitaxy growth by tellurizing was triggered from a deliberately implanted single seed crystal. The resulting single-crystalline film completely covered a 2.5-centimeter wafer with excellent uniformity. The 2H $MoTe_2$ 2D single-crystalline film can use itself as a template for further rapid epitaxy in a vertical manner. Transistor arrays fabricated with the as-prepared 2H $MoTe_2$ single crystals exhibited high electrical performance, with excellent uniformity and 100% device yield.

Two-dimensional (2D) semiconductors, such as MoS_2 (*1*) and black phosphorus (*2*), could compete with silicon technology because of their atomic thickness (*1*, *3*), excellent physical properties (*2*, *4*–*6*), and compatibility with classic complementary metal-oxide semiconductor (CMOS) technologies (*7*, *8*). A prerequisite for achieving large-scale integrated circuits made of 2D semiconductors is the mass production of their raw materials with high quality and uniformity (*9*, *10*). Silicon wafers are obtained by cleaving bulk ingots of Si single crystals, whereas large-area 2D semiconductors are usually obtained through bottom-up deposition methods (*11*–*14*). Flaws such as grain boundaries and crystallographic defects introduced during growth often lead to severe degradation of electronic performance (*15*). Wafer-scale single-crystalline 2D semiconductors on insulating substrates are highly desired, but their growth remains extremely challenging.

Most methods for preparing bulk single crystals cannot be adopted for synthesizing large-sized 2D semiconductor single crystals, because the atomic thickness of 2D materials makes their synthesis strongly dependent on the surface properties of the substrates (*10*, *16*). For example, transforming a polycrystalline 2D thin film into a single crystal only by thermal annealing must overcome the high energy barrier of rotating a 2D crystal domain on a substrate (*17*). Recently, graphene, a single-crystalline 2D semimetal, and hexagonal boron nitride (hBN), an insulator, were grown on single-crystalline metallic substrates or a molten metal surface by ensuring an identical crystal orientation of all the grains to avoid any grain boundaries during coalescence (*18*–*22*). However, for 2D semiconductors grown on a single-crystalline substrate, although the film has essentially one crystallographic orientation, translational grain boundaries still exist because of the presence of imperfectly stitched domains (*23*, *24*).

To mitigate this problem, we devised a seamless epitaxial growth of a 2D-confined single crystal via the solid-to-solid phase transition and recrystallization process. Wafer-scale lateral extension of van der Waals (vdW) 2H molybdenum ditelluride ($MoTe_2$) semiconductor was triggered by a single nucleus deliberately implanted in the center of an amorphous insulating wafer. Single-crystalline 2H $MoTe_2$ with 100% 2D film coverage, excellent uniformity, and large size was grown, which can be further used as a template for rapid epitaxy in a vertical manner. Transistor arrays fabricated with the single-crystalline 2H $MoTe_2$ wafers showed high electrical performance, with excellent uniformity and 100% device yield. Our method opens up possibilities for future industrial implementation of vdW 2D semiconductors for next-generation nanoelectronics.

The synthesis processes of wafer-scale single-crystalline 2H $MoTe_2$ film is shown schematically in Fig. 1A. First, the Mo film (3 nm thick) deposited on the Si/SiO_2 wafer was tellurized with Te vapor to obtain a polycrystalline 1T′ $MoTe_2$ wafer (~10 nm thick) with existence

[1]State Key Laboratory for Mesoscopic Physics and Frontiers Science Center for Nano-Optoelectronics, School of Physics, Peking University, Beijing 100871, China. [2]Collaborative Innovation Center of Quantum Matter, Beijing 100871, China. [3]Electron Microscopy Laboratory, School of Physics, Peking University, Beijing 100871, China. [4]International Center for Quantum Materials, School of Physics, Peking University, Beijing 100871, China. [5]State Key Laboratory of Quantum Optics and Quantum Optics Devices, Institute of Opto-Electronics, Shanxi University, Taiyuan 03006, China. [6]Collaborative Innovation Center of Extreme Optics, Shanxi University, Taiyuan 03006, China. [7]Peking University Yangtze Delta Institute of Optoelectronics, Nantong 226010, Jiangsu, China.
***Corresponding author. Email: ye_yu@pku.edu.cn**

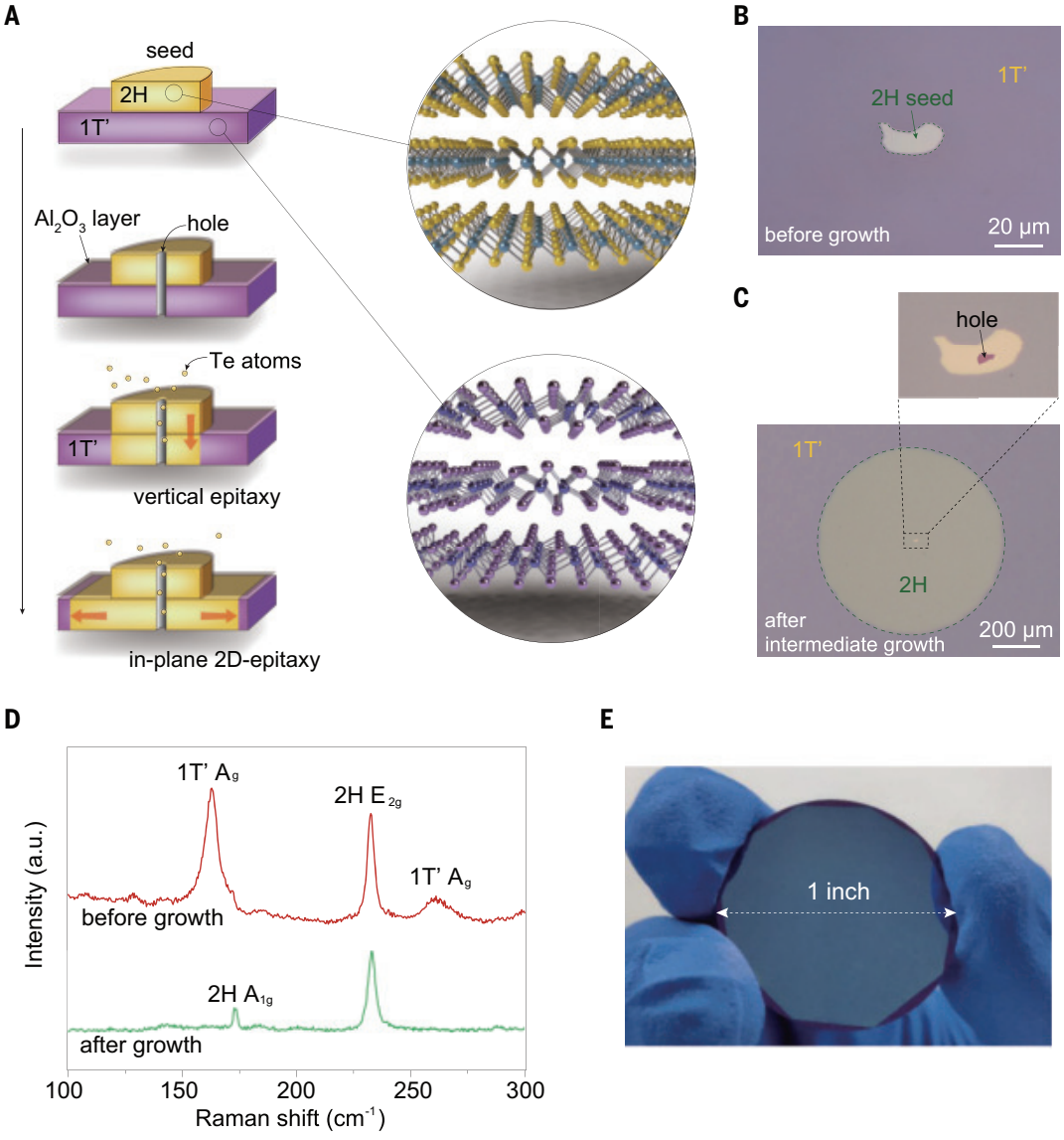

Fig. 1. Seeded growth of the single-crystalline 2H $MoTe_2$ wafers. (**A**) The schematic diagrams for the in-plane 2D-epitaxy synthesis of wafer-scale single-crystalline 2H $MoTe_2$ thin film. (**B**) Optical image of a 2H $MoTe_2$ nanoflake assembled in the center of the 1T′ $MoTe_2$ wafer as a seed to induce the phase transition and recrystallization. (**C**) Optical image of the wafer after intermediate growth at 650°C for 2 hours. Inset shows the seed crystal with a needle probe–punched hole. (**D**) Raman spectra of the seed region before and after growth. a.u., arbitrary units. (**E**) Optical image of a synthesized 2.5-cm (1-inch) single-crystalline 2H $MoTe_2$ wafer.

of Te vacancies (see supplementary materials) (*25*, *26*). The domain size of the 1T′ $MoTe_2$ film was about tens of nanometers (fig. S1). After that, a single-crystalline 2H $MoTe_2$ nanoflake exfoliated from the bulk crystal was assembled to the center of the 1T′ $MoTe_2$ wafer by a dry transfer method (see supplementary materials) and served as a seed crystal to trigger the phase transition and recrystallization (Fig. 1, A and B).

Next, a 30-nm-thick dense Al_2O_3 layer was deposited on the surface of the wafer by atomic layer deposition (ALD) to isolate the 1T′ $MoTe_2$ film from the Te atoms in the environment during growth (Fig. 1A). Given that the supply of Te atoms for 1T′ $MoTe_2$ is a necessary condition for filling the Te vacancies to induce the 1T′ to 2H $MoTe_2$ phase transition (*25*, *27*, *28*), this structure avoided the spontaneous nucleation of 2H $MoTe_2$ with random crystal orientations in the 1T′ $MoTe_2$ film (fig. S2). The phase transition and atom rearrangement started from the seed region and extended outward during the entire growth period, which was crucial for the growth of wafer-scale single-crystalline film. Thus, a small hole was introduced into the seed region as the only channel for the supply of Te atoms (Fig. 1, A and inset of C); the hole was punched by a tungsten probe mounted on a 3D translation stage (fig. S3). The wafer and a 3-g Te lump (prepared by annealing Te powders at 500°C for 30 min) were placed in a closed quartz tube with a removable plug and then loaded into a 5-cm (2-inch) quartz tube in a chemical vapor deposition (CVD) furnace. This closed environment effectively reduced the consumption of Te sources, thereby ensuring the continuous supply of Te during the entire growth process. The wafer-scale single-crystalline 2H $MoTe_2$ film was synthesized at a flow rate of 5 standard cubic centimeters per minute (sccm) of Ar and 4 sccm of H_2 under atmospheric pressure.

The 1T′ $MoTe_2$ layer underneath the seed crystal transformed into a 2H $MoTe_2$ single crystal with the same crystallographic orientation as the seed crystal through the phase transition and recrystallization induced by the vertical 2H/1T′ interface (Fig. 1A). In this way, an in-plane 2H/1T′ $MoTe_2$ interface was formed, and the recrystallization and phase transition occurred at this interface and extended outward. The phase transition process was driven by atom diffusion, thus resulting in a single-crystalline 2H $MoTe_2$ circle centered on the seed region. At an intermediate stage of growth (650°C, 2 hours), we observed a 2H $MoTe_2$ circle with a radius of ~396 μm centered on the seed region (Fig. 1C), indicating that the phase

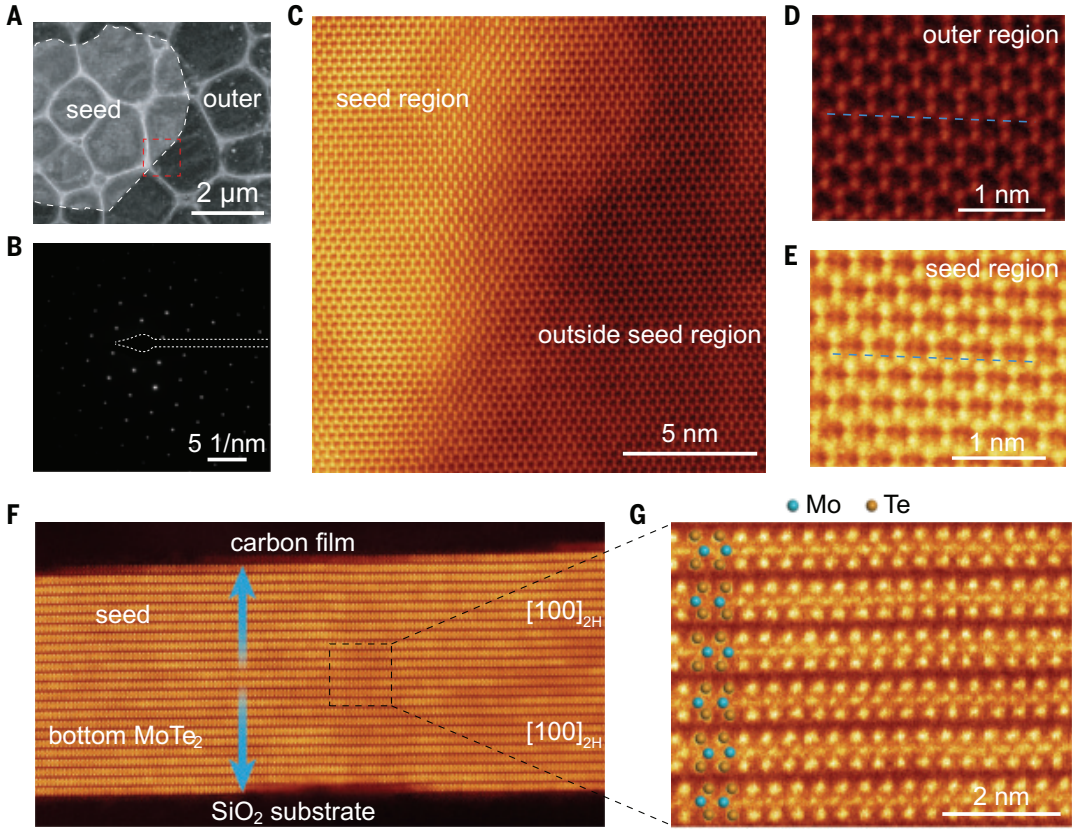

Fig. 2. TEM characterization around the seed region. (**A**) Low-magnification STEM image of the single-crystalline $MoTe_2$ film. The outline of the seed is marked by the dashed white line. (**B**) SAED pattern obtained at an area around the edge of the seed [marked by the dashed red box in (A)], containing only one set of sixfold symmetric 2H phase spots. (**C**) HAADF-STEM image acquired around the edge of the seed. (**D** and **E**) The zoomed-in STEM image of the seed region and the outside seed region, sharing the same crystal structure and orientation. The blue dashed lines indicate the zigzag crystal direction of 2H $MoTe_2$. (**F** and **G**) The cross-sectional HAADF-STEM image and zoomed-in image of the seed region.

transition rate was 3.3 μm/min under these conditions.

Before growth, both the typical Raman peaks of 2H (E_{2g}, 234 cm^{-1}) and 1T′ (A_g, 161 cm^{-1}; and A_g, 256 cm^{-1}) $MoTe_2$ could be observed in the seed region (Fig. 1D) (*29*, *30*). After growth, only the Raman peak of 2H $MoTe_2$ was observed (Fig. 1D), indicating that the implanted seed induced the phase transition of 1T′ $MoTe_2$ at the bottom into 2H $MoTe_2$ (Fig. 1A). The vertical 2H/1T′ $MoTe_2$ interface was the key factor, in that other 2D materials (such as graphene and hBN) could not be used as the seeds to induce the phase transition of the 1T′ $MoTe_2$ at the bottom (fig. S4). Initial 1T′ $MoTe_2$ film of 2 to 3 nm was discontinuous and had a surface roughness, R_a, of ~1.2 nm, while the film of 35.5 nm became very rough with a R_a of ~3.7 nm. The film discontinuity and roughness resulted in a poor interface between the seed and the 1T′ film, which prevented the film under the seed region from phase transition through the vertical interface. Under all other initial 1T′ $MoTe_2$ film thicknesses, the seed-induced phase transitions were observed (figs. S5 and S6). After 3 days of long-term growth, the entire film phase-transformed into the 2H phase to form a wafer-scale semiconducting $MoTe_2$ single crystal with a diameter of 2.5 cm (1 inch) (Fig. 1E). The obtained film was continuous, smooth, and uniform over a large scale, with an R_a in the range of 0.20 to 0.25 nm (figs. S7 and S8). As long as the growth condition remained unchanged, the growth rate was relatively stable over time (fig. S9). At a temperature below 530°C, no phase transition occurred, because such a low temperature could not provide sufficient energy to cross the activation barrier of the phase transition (*25*). At temperatures above 710°C, the film was destroyed. Under all other temperatures, the seed-induced phase transition occurred, with a phase transition rate increasing exponentially with increasing temperature (fig. S10). The first-principle calculation and designed experiments confirmed that the diffusion rate of Te atoms was faster than the recrystallization rate, indicating that the phase transition rate was limited by the recrystallization rate under our growth conditions (figs. S11 and S12).

We used aberration-corrected scanning transmission electron microscopy (AC-STEM) to evaluate the crystallinity of the film around the seed region (Fig. 2A). The high-angle annular dark-field (HAADF) image of the thicker seed region, which appeared brighter owing to the larger sample thickness (*31*), showed a hexagonal lattice structure without any moiré patterns (Fig. 2C). The results showed that the lattice structure, orientation, and stacking order of the bottom $MoTe_2$ were exactly the same as those of the seed crystal. The Te and Mo atoms in the bottom 1T′ $MoTe_2$ rearranged according to the lattice structure of 2H $MoTe_2$ at the vertical 2H/1T′ interface during the phase transition. This recrystallization behavior was confirmed by the cross-sectional STEM characterizations of the seed region. Both the seed and bottom $MoTe_2$ layer maintained a perfect AB stacking order and had exactly the same crystal orientation (Fig. 2F), and there was no obvious gap between the seed and bottom $MoTe_2$ layers (Fig. 2G). The outside seed region also showed the hexagonal lattice structure of the 2H $MoTe_2$ (Fig. 2C), and its crystal orientation was the same as that of the seed region (Fig. 2, D and E), indicating that a similar recrystallization process also occurred during the in-plane phase transition.

During the phase transition, the Te and Mo atoms in the metastable 1T′ $MoTe_2$ migrated and rearranged themselves according to the lattice structure and orientation of the adjacent 2H $MoTe_2$ at the in-plane interface (*32*). Because this phase transition was driven by an atom-diffusion process in which the 2H $MoTe_2$ at the interface served as a template, the process was not substrate-sensitive and could even be performed on an amorphous SiO_2 surface. Thus, subsequent device fabrication could be performed directly on

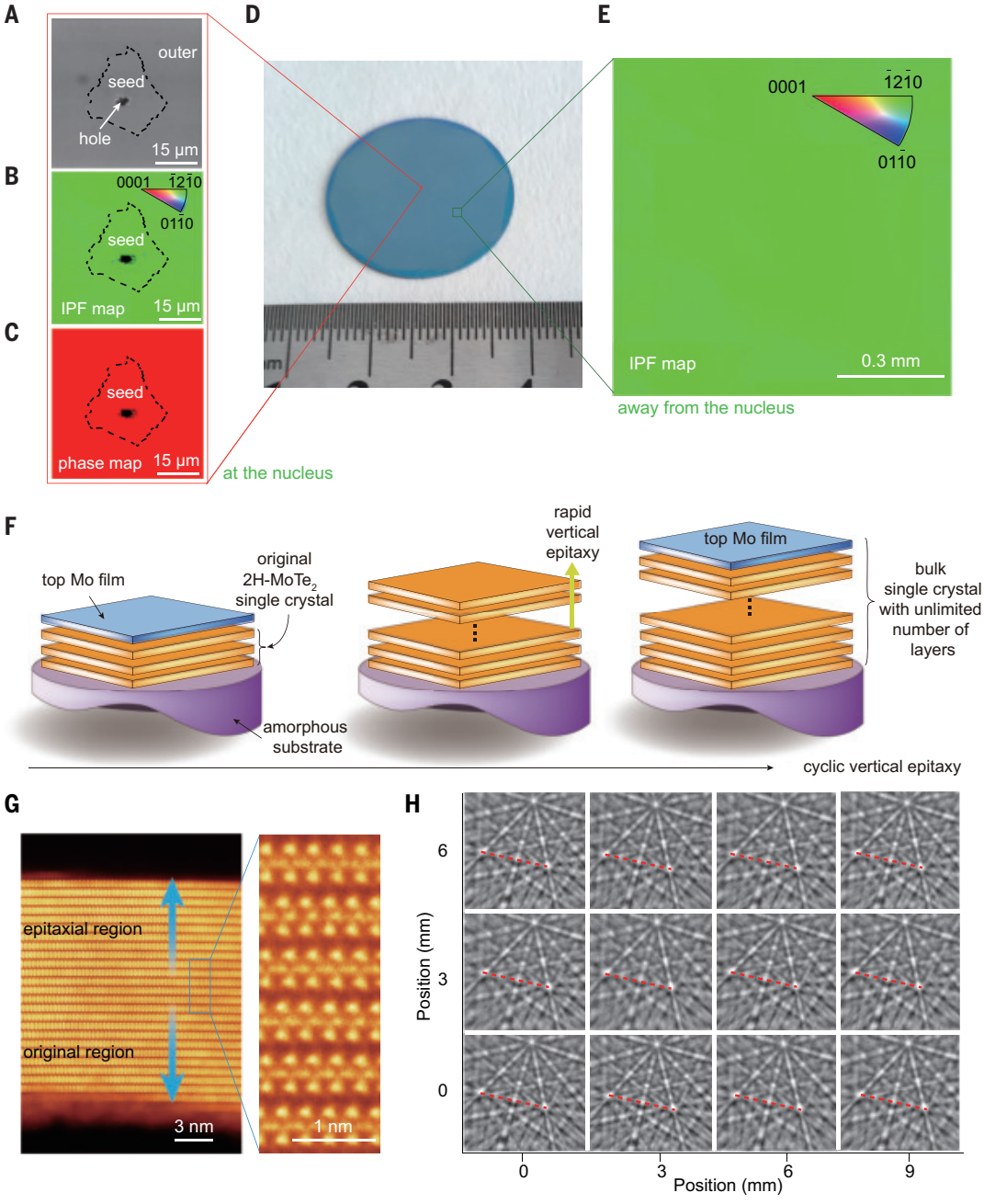

Fig. 3. EBSD characterization of the wafer-scale single-crystalline $MoTe_2$. (**A**) SEM image around the seed region. The outline of the seed with a hole at the center was marked by the dashed black line. (**B**) The in-plane transverse IPF map showed a uniform green color, confirming that the in-plane crystal orientation was identical at the region around the seed. (**C**) The phase distribution map at the same region as that of IPF map. (**D**) Optical image of the 2.5-cm (1-inch) single-crystalline $MoTe_2$ wafer. (**E**) The in-plane transverse IPF map of a large area far away from the seed. (**F**) The schematic diagrams of the cyclic rapid vertical epitaxy of the single crystal into a bulk single crystal with an unlimited number of layers. (**G**) The cross-sectional HAADF-STEM images of the epitaxial film. (**H**) EBSPs at different positions across the wafer.

the substrate without the need to transfer the 2D semiconductor film, thus preserving the material quality and the integrity of the film. Owing to the 2D nature of the as-synthesized film, the intact 2D film wafer could also be transferred to other substrates (fig. S13). Because the as-synthesized films were multilayered, an atomic defect might not be visible in the Z-contrast image, because of the presence of other atoms from all other layers that could obscure the slight changes in the column intensity (fig. S14). In principle, the phase transition occurred from the Te vacancy–related 1T′ $MoTe_2$ phase to the stoichiometric 2H $MoTe_2$ phase, and this phase transition process did not suffer from the difficulty of balancing metal and chalcogen vapor pressures as other transition metal dichalcogenides (TMDCs) during the growth (*33*). From the energy dispersive x-ray spectroscopy (EDX) spectrum of the obtained film with a size of 300 nm by 300 nm (fig. S14), no corresponding peaks related to Si and Al were observed, indicating that Si and Al were not incorporated into the 2H $MoTe_2$ film during the high-temperature growth. The selected area electron diffraction (SAED) pattern obtained around the seed region (marked with the red dashed box in Fig. 2A) contained only one set of sixfold symmetrical 2H phase spots (Fig. 2B), further confirming that bottom and nearby $MoTe_2$ of the seed region inherited the lattice structure and crystal orientation of those of seed 2H $MoTe_2$.

We used electron back-scattered diffraction (EBSD) to further analyze the crystallinity of the film on a large length scale. The scanning electron microscope (SEM) image of a representative seed with a hole is shown in Fig. 3A. In the inverse pole figure (IPF) map along the normal direction of the surface (fig. S15), the uniform red color (related to the [0001] crystal

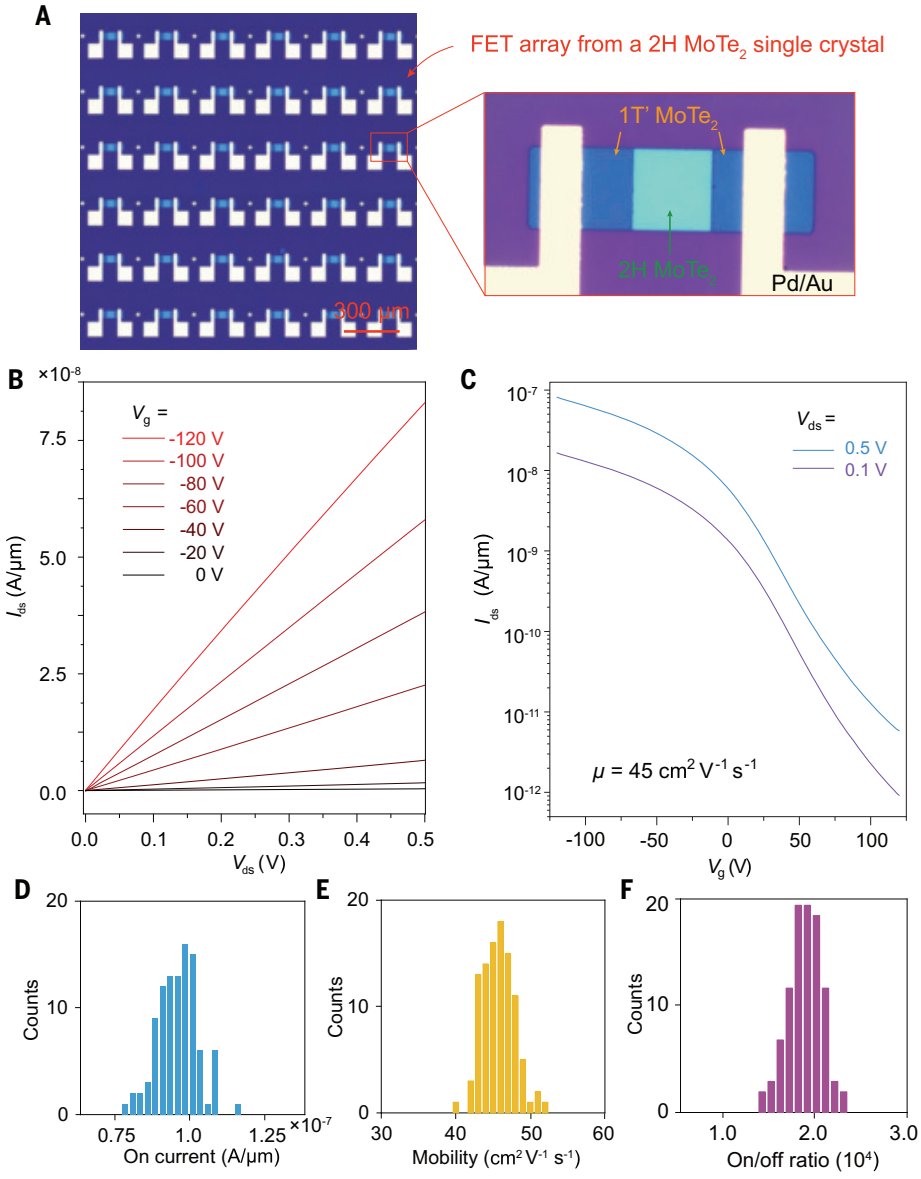

Fig. 4. Electrical characterizations of the FET devices fabricated on the single-crystalline 2H $MoTe_2$ film. (**A**) Optical image of the heterophase 1T′/2H/1T′ $MoTe_2$ FET array fabricated with a phase-engineered method. (**B**) Typical I_{ds}-V_{ds} curves of heterophase FET measured under various gate voltages. (**C**) Typical transfer curves of the heterophase FET. (**D** to **F**) The statistical histograms of the on-current, field-effect mobility, and on/off ratio measured on a 10 by 10 $MoTe_2$ FET array, all showing a narrow distribution.

orientation) indicated that the 2H $MoTe_2$ layers were stacked along the normal direction, which was consistent with cross-sectional STEM results. The in-plane transverse IPF map showed a uniform green color (Fig. 3B), indicating that the in-plane crystal orientation of the film around the seed region was the same, which was again consistent with the STEM results at a larger scale. Because the phase transition gradually advanced outward through the 2H/1T′ interface, the phase transition is thorough on the entire wafer. The obtained 2H phase film was continuous with 100% coverage, as confirmed by the uniform color of the phase-distribution map (Fig. 3C) related to the 2H phase. We also performed EBSD characterization of a larger area (1 mm by 1 mm) far away from the seed (marked by the green box in Fig. 3D). The in-plane IPF map showed not only a single color but also exactly the same color as that of the seed region (Fig. 3E), confirming that after the phase transition, the entire film strictly inherited the crystal lattice and orientation of the seed.

To further verify the single crystallinity, electron back-scattered patterns (EBSPs) were randomly collected at different positions across the 2.5-cm (1-inch) wafer. All EBSPs showed only one set of Kikuchi patterns (related to the 2H $MoTe_2$) and had the same crystal orientation (fig. S16). The EBSP analysis unambiguously demonstrated that the wafer film was a single crystal whose crystal orientation was completely determined by the implanted seed crystal. If the crystal orientation of the seed crystal was deformed, the deformation was inherited throughout the film (fig. S17). This effect could provide a method for controllably preparing grain boundaries with different angles. In some cases, with an imperfect seed, we found that the IPF maps of the obtained $MoTe_2$ films showed small angle deflections (usually less than 1°) radiating from the seeds (fig. S18). These deflections might be caused by the stress generated during the seed-transfer process or stress caused by thermal fluctuations during growth.

Rapid epitaxy in the stacking direction using the single-crystalline 2H $MoTe_2$ 2D semiconductor single-crystal bulk wafer, as shown schematically in Fig. 3F. First, the Al_2O_3 film on the single-crystalline 2H $MoTe_2$ wafer was dissolved using a hot phosphoric acid solution (see materials and methods). A Mo film (3 nm thick) was deposited on the wafer. Then, the wafer was sent back into the furnace for tellurizing at

650°C for 5 min. The Mo film was initially converted into 1T′ $MoTe_2$ and formed a vertical 2H/1T′ $MoTe_2$ interface. Phase transition and recrystallization were induced through the interface. Similar to the seed-induced recrystallization discussed above, in a short period of time, the Te and Mo atoms in the top 1T′ $MoTe_2$ migrated and rearranged according to the lattice structure and orientation of the bottom wafer-scale single-crystalline 2H $MoTe_2$, thereby achieving the rapid epitaxy of the wafer. The thickness of the film increased from 10 to 20 nm after the epitaxy (fig. S19), indicating that both the original and epitaxial films are about 14 layers thick.

The single crystallinity of the film was characterized by STEM and EBSD. The cross-sectional HAADF-STEM image showed that the films in both the original and epitaxial regions maintained a perfect AB stacking order, and there was no observable gap between the original and epitaxial layers (Fig. 3G). The top-view HAADF-STEM image and the SAED pattern (fig. S20) showed a pure hexagonal lattice and a set of sixfold symmetric diffraction spots, respectively, indicating that an atomic-precision epitaxy of the 2H $MoTe_2$ was realized. EBSPs were also collected at different positions across the wafer. All EBSPs showed one set of 2H $MoTe_2$ Kikuchi patterns with the same crystal orientation (Fig. 3H), indicating that the epitaxy was consistent throughout the sample scale. The number of epitaxial layers was determined by the thickness of the deposited Mo film, and the epitaxy speed exceeded 150 layers per hour. This vertical epitaxy process could also be repeated as long as there is a single-crystal template. The rapid epitaxy method could be used in combination with the recently reported wafer-scale single-layer 2D materials peeling technique (*34*) to mass-produce single-layer single-crystalline 2H $MoTe_2$ wafers.

For monolithic integration technology, high device uniformity and reliability are critical, and we expected that the uniformity and reliability of the device could be greatly improved with single-crystalline films. On the basis of the wafer-scale single-crystalline 2H $MoTe_2$ thin film and our previously developed phase-engineered growth technique (see materials and methods for details) (*35*), we fabricated a large-scale coplanar heterophase 1T′/2H/1T′ $MoTe_2$ field-effect transistor (FET) array with optimized contacts directly on the growth substrate (Fig. 4A), with p^+-Si as the global back gate electrode. The typical gate voltage (V_g)–dependent source-drain current-voltage (I_{ds}-V_{ds}) output curves showed a linear response (Fig. 4B), indicative of a low contact barrier between the 1T′ and 2H $MoTe_2$ (fig. S21). The typical I_{ds}-V_g transfer curves at bias voltages of 0.5 and 0.1 V showed p-type transistor characteristics (Fig. 4C). From the transfer characteristics, we extracted a room-temperature field-effect mobility (μ) of ~45 $cm^2\ V^{-1}\ s^{-1}$ and an on/off ratio of ~1.5×10^4 (Fig. 4C), comparable to the reported values of single-crystalline 2H $MoTe_2$ nanoflake transistors with a similar in-plane heterophase structure (*36*, *37*). Moreover, the channel could be fully turned off when measured in vacuum, showing an enhanced on/off ratio of ~2×10^6 (fig. S22), because adsorbed gas molecules (such as oxygen and water) in ambient could induce a conducting channel near the top surface that could not be fully turned off by the back gate (*38*, *39*). The temperature-dependent Hall measurements confirmed that the mobility was limited by the phonon-related scattering, indicating the high electrical performance of the obtained 2H $MoTe_2$ film (fig. S23). The statistical results of the 10 by 10 $MoTe_2$ FET array showed that the on-current, field-effect mobility, and on/off ratio of the device were all highly narrow-distributed, with an average value of $9.38 \pm 0.75 \times 10^{-8}$ A/μm, 45 ± 2 $cm^2\ V^{-1}\ s^{-1}$, and $1.8 \pm 0.3 \times 10^4$, respectively (Fig. 4, D to F), confirming the spatial uniformity of the electrical properties of the devices on a large scale. The single-crystalline nature of the continuous film also ensures a 100% device yield.

Until now, applying this method to other TMDCs required more effort, because the energy differences between the 2H phase and 1T′/1T phase of other TMDCs are much larger than that of $MoTe_2$. But big strides have been achieved in the synthesis of the 1T/1T′ phase of other TMDCs. For example, the stable 1T′ phase of MoS_2 has been synthesized directly using a CVD method by choosing the proper precursor of K_2MoS_4 (*40*). The high phase-purity 1T′ MoS_2 and $MoSe_2$ have also been synthesized by the mixture of K_2MoS_4 with S and Se (*41*). Meanwhile, the transition from the 1T′ phase to the 2H phase is observed by thermal annealing and laser irradiation. With the development of phase-engineering techniques, this method might be applied to other 2D materials. As in silicon manufacturing, the electrical characteristics of the semiconducting 2H $MoTe_2$ wafers can be controlled by adding dopants such as Nb and Re to the Mo film before it is tellurized. The ability to use this method on a variety of substrates might lead to the widespread adoption of 2D semiconductors in conventional CMOS devices.

REFERENCES AND NOTES

1. B. Radisavljevic, A. Radenovic, J. Brivio, V. Giacometti, A. Kis, *Nat. Nanotechnol.* **6**, 147–150 (2011).
2. L. Li *et al*., *Nat. Nanotechnol.* **9**, 372–377 (2014).
3. S. B. Desai *et al*., *Science* **354**, 99–102 (2016).
4. S. Manzeli, D. Ovchinnikov, D. Pasquier, O. V. Yazyev, A. Kis, *Nat. Rev. Mater.* **2**, 17033 (2017).
5. K. F. Mak, J. Shan, *Nat. Photonics* **10**, 216–226 (2016).
6. D. A. Bandurin *et al*., *Nat. Nanotechnol.* **12**, 223–227 (2017).
7. C. Liu *et al*., *Nat. Nanotechnol.* **15**, 545–557 (2020).
8. G. Fiori *et al*., *Nat. Nanotechnol.* **9**, 768–779 (2014).
9. C. Liu, L. Wang, J. Qi, K. Liu, *Adv. Mater.* **32**, e2000046 (2020).
10. J. Dong, L. Zhang, F. Ding, *Adv. Mater.* **31**, e1801583 (2019).
11. C. Zhao *et al*., *Nat. Nanotechnol.* **15**, 53–58 (2020).
12. K. Kang *et al*., *Nature* **550**, 229–233 (2017).
13. K. Kang *et al*., *Nature* **520**, 656–660 (2015).
14. Q. Wang *et al*., *Nano Lett.* **20**, 7193–7199 (2020).
15. D. Rhodes, S. H. Chae, R. Ribeiro-Palau, J. Hone, *Nat. Mater.* **18**, 541–549 (2019).
16. J. Zhou *et al*., *Nature* **556**, 355–359 (2018).
17. H. Lin *et al*., *Nat. Mater.* **18**, 602–607 (2019).
18. T.-A. Chen *et al*., *Nature* **579**, 219–223 (2020).
19. L. Wang *et al*., *Nature* **570**, 91–95 (2019).
20. V. L. Nguyen *et al*., *Nat. Nanotechnol.* **15**, 861–867 (2020).
21. X. Xu *et al*., *Sci. Bull.* **62**, 1074–1080 (2017).
22. J. S. Lee *et al*., *Science* **362**, 817–821 (2018).
23. D. R. Hickey *et al*., arXiv:2006.11668 [cond-mat.mtrl-sci] (20 June 2020).
24. M. Chubarov *et al*., arXiv:2006.10952 [cond-mat.mtrl-sci] (19 June 2020).
25. X. Xu *et al*., *J. Am. Chem. Soc.* **141**, 2128–2134 (2019).
26. L. Zhou *et al*., *J. Am. Chem. Soc.* **137**, 11892–11895 (2015).
27. J. C. Park *et al*., *ACS Nano* **9**, 6548–6554 (2015).
28. X. Zhu *et al*., *J. Mater. Chem. C* **7**, 10598–10604 (2019).
29. M. Yamamoto *et al*., *ACS Nano* **8**, 3895–3903 (2014).
30. R. Beams *et al*., *ACS Nano* **10**, 9626–9636 (2016).
31. O. L. Krivanek *et al*., *Nature* **464**, 571–574 (2010).
32. X. Xu *et al*., *Adv. Mater.* **32**, e2000236 (2020).
33. D. Edelberg *et al*., *Nano Lett.* **19**, 4371–4379 (2019).
34. J. Shim *et al*., *Science* **362**, 665–670 (2018).
35. X. Xu *et al*., *Nano Lett.* **19**, 6845–6852 (2019).
36. S. Cho *et al*., *Science* **349**, 625–628 (2015).
37. J. H. Sung *et al*., *Nat. Nanotechnol.* **12**, 1064–1070 (2017).
38. A. J. Arnold, D. S. Schulman, S. Das, *ACS Nano* **14**, 13557–13568 (2020).
39. N. R. Pradhan *et al*., *ACS Nano* **8**, 5911–5920 (2014).
40. L. Liu *et al*., *Nat. Mater.* **17**, 1108–1114 (2018).
41. Y. Yu *et al*., *Nat. Chem.* **10**, 638–643 (2018).

ACKNOWLEDGMENTS

Funding: This work was supported by the National Key R&D Program of China (grants 2018YFA0306900 and 2017YFA0206301), the Beijing Natural Science Foundation (4182028), the China Postdoctoral Science Foundation (2020TQ0015), the Key Research Program of Frontier Sciences, CAS (grant ZDBS-LY-JSC015), the National Natural Science Foundation of China (grants 61521004 and 11974024), and the Strategic Priority Research Program of the Chinese Academy of Science (grant XDB33000000). We are grateful for computational resources provided by Peking University, the TianHe-1A supercomputer, and the Shanghai Supercomputer Center. **Author contributions:** Y.Y. and X.X. conceived of the project and designed the experiments. X.X. synthesized the film, characterized the film, fabricated the devices, and performed the electrical measurements. Y.Pa. and S.Liu assisted in the synthesis of the thin film and the fabrication of the devices. B.H. conducted the STEM and EDX characterizations under the direction of P.Ga. W.X. performed the magnetron sputtering. P.Gu. performed the temperature-dependent electrical measurements. S.Li conducted the DFT calculations under the direction of J.C. Z.H. and Y.Pe. provided useful discussions. Y.Y. supervised this research. X.X. and Y.Y. wrote the manuscript. All authors contributed to discussions. **Competing interests:** None declared. **Data and materials availability:** All data needed to evaluate the conclusions in this paper are present in the paper or the supplementary materials.

SUPPLEMENTARY MATERIALS

science.sciencemag.org/content/372/6538/195/suppl/DC1
Materials and Methods
Figs. S1 to S23
References (*42*–*47*)

4 November 2020; accepted 4 March 2021
10.1126/science.abf5825

REGENERATION

Krüppel-like factor 1 is a core cardiomyogenic trigger in zebrafish

Masahito Ogawa[1,2], Fan-Suo Geng[3,4], David T. Humphreys[4,5], Esther Kristianto[6], Delicia Z. Sheng[1], Subhra P. Hui[1], Yuxi Zhang[7], Kotaro Sugimoto[1], Maki Nakayama[1], Dawei Zheng[1], Daniel Hesselson[4,7,8,9], Mark P. Hodson[6,10], Ozren Bogdanovic[3,11], Kazu Kikuchi[1,2,4]*

Cardiac regeneration requires dedifferentiation and proliferation of mature cardiomyocytes, but the mechanisms underlying this plasticity remain unclear. Here, we identify a potent cardiomyogenic role for Krüppel-like factor 1 (Klf1/Eklf), which is induced in adult zebrafish myocardium upon injury. Myocardial inhibition of Klf1 function does not affect heart development, but it severely impairs regeneration. Transient Klf1 activation is sufficient to expand mature myocardium in uninjured hearts. Klf1 directs epigenetic reprogramming of the cardiac transcription factor network, permitting coordinated cardiomyocyte dedifferentiation and proliferation. Myocardial expansion is supported by Klf1-induced rewiring of mitochondrial metabolism from oxidative respiration to anabolic pathways. Our findings establish Klf1 as a core transcriptional regulator of cardiomyocyte renewal in adult zebrafish hearts.

Unlike mammals, zebrafish efficiently regenerate damaged hearts. In an earlier study, we observed that fish with ventricular injury displayed increased expression of the retinoic acid–synthesizing enzyme Raldh2/Aldh1a2. Inhibiting this factor prevents cardiomyocyte proliferation (*1*). In an expression-profiling analysis, we noted that *klf1*, a gene that encodes a transcription factor essential for erythropoiesis (*2*, *3*), is induced in injured zebrafish hearts that exhibit reduced cardiomyocyte proliferation because of genetic attenuation of retinoic acid signaling. Injury-induced *klf1* expression peaked by 7 days post-injury (dpi) (fig. S1A), aligning with the maximal cardiomyocyte-proliferative response (*4*). *klf1* expression was restricted to purified cardiomyocytes (fig. S1B), and in situ hybridization of damaged ventricles showed colocalization of *klf1* mRNA with the cytosolic muscle marker troponin C (fig. S1C), confirming the myocardial expression of *klf1* during regeneration.

To investigate Klf1 function in heart regeneration, we generated a conditional *klf1* gene-trap line (fig. S2, A to D). After validating the erythropoietic phenotype of Klf1 by global knockdown (fig. S2, E to I) (*5*, *6*), myocardial-specific *klf1* knockdown was performed with a cardiac Cre-driver line (*7*) (*klf1-mKD*; Fig. 1A and fig. S2J). *klf1-mKD* and *Cre*-negative clutch-mates (*klf1-CTRL*) were subjected to ventricular resection after 4-hydroxytamoxifen (4-HT) induction of Cre activity and analyzed at 7 dpi. *klf1-mKD* ventricles exhibited impaired regeneration with scarring (Fig. 1, B and C). Injured *klf1-mKD* hearts expressed lower levels of the dedifferentiation markers smooth muscle protein 22a (Sm22) (*8*) (Fig. 1, D and E) and Alcam (*9*) (fig. S3, A and B), contributing to a significant reduction in the number of myocyte enhancer factor 2–positive proliferating cell nuclear antigen–positive ($Mef2^+PCNA^+$) proliferating cardiomyocytes (Fig. 1, F and G).

In contrast to the role for Klf1 in regeneration, myocardial *klf1* expression was virtually undetectable by in situ hybridization during development, and cardiac development was normal in *klf1-mKD* embryos (fig. S4, A to D). Similarly, dominant-negative inhibition of Klf1 in the myocardium severely impaired cardiac regeneration (fig. S5, A to G) but not development (fig. S5, H to K). These data indicate a post-developmental and regeneration-specific requirement for Klf1 in cardiomyogenesis.

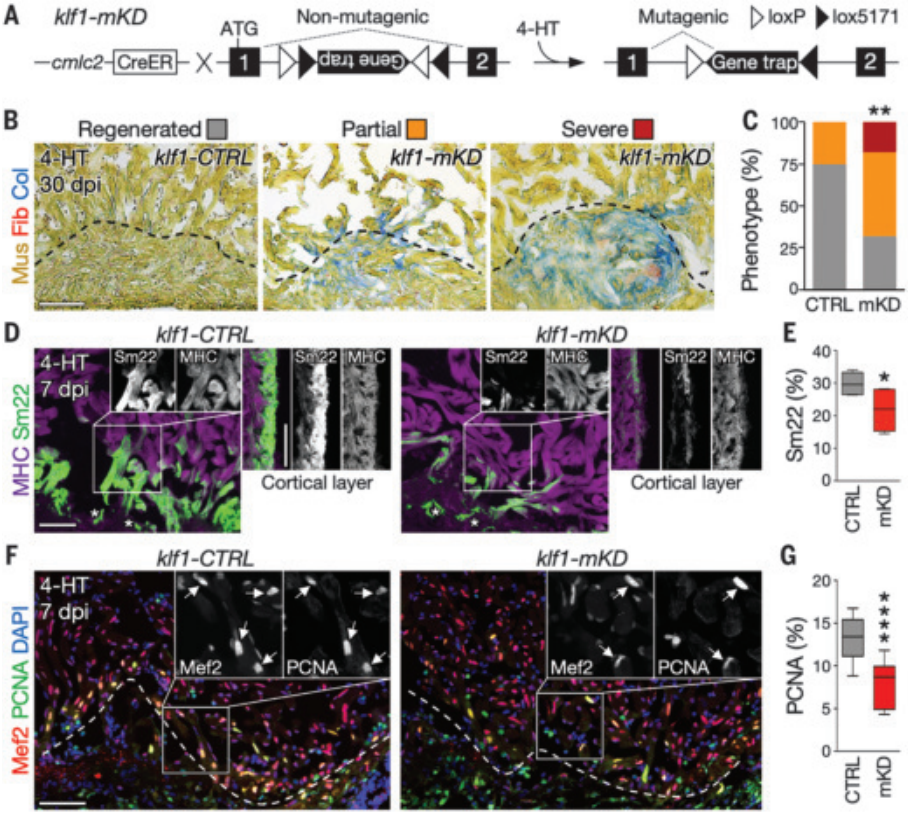

Fig. 1. Myocardial *klf1* is required for heart regeneration in zebrafish. (**A**) Schematic of *klf1-mKD*. (**B**) Picro-Mallory staining. Dotted lines indicate injury border. (**C**) Quantification of B (n = 20 to 22). (**D**) Immunofluorescence of Sm22/Transgelin and myosin heavy chain (MHC). Cortical (subepicardial) myocardium on the right. Asterisks indicate myofibroblast-like cells. (**E**) Quantification of $Sm22^+MHC^+$ areas on the injury border zone of the ventricle (n = 5 to 6). (**F**) Immunofluorescence of the myonuclear marker Mef2 and PCNA. Dotted lines and arrows indicate injury border and colabeled cells, respectively. (**G**) Quantification of $Mef2^+PCNA^+$ cells (n = 7 to 9). Col, Collagen; DAPI, 4′,6-diamidino-2-phenylindole; Fib, fibrin; Mus, muscle. $^*P < 0.05$, $^{**}P < 0.01$, $^{****}P < 0.001$ by Fisher's exact test (C) or unpaired t test (E, G). Scale bars, 50 μm.

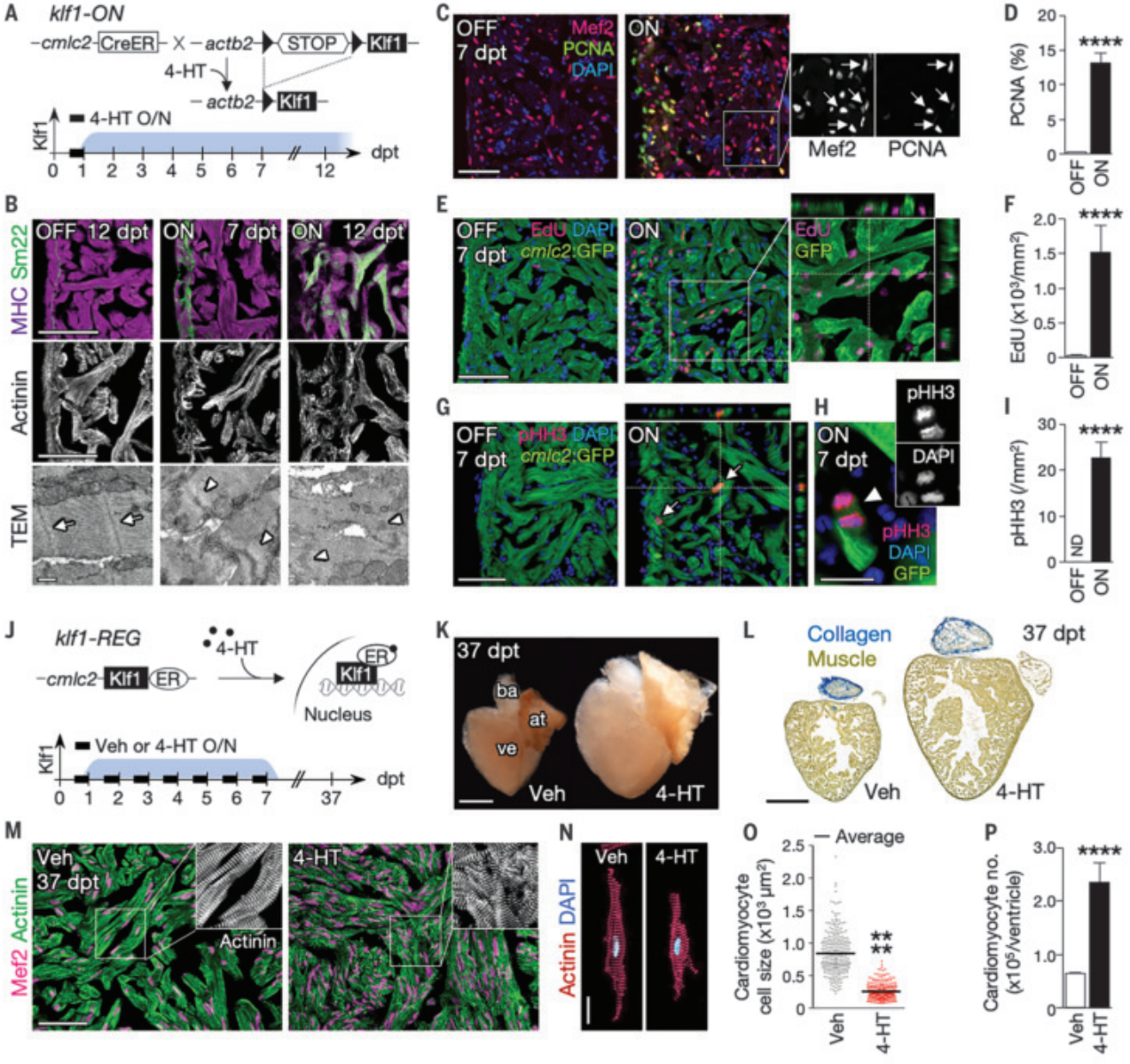

Fig. 2. Klf1 triggers an injury-independent cardiomyogenic response. (**A**) *Tg (actb2:loxP-TagBFP-STOP-loxP-3xHA-klf1)*^{vcc29} fish were crossed with *cmlc2:CreER* fish (*klf1-ON*). *Cre*-negative clutch-mates were used as controls (*klf1-OFF*). The 4-HT treatment regimen is shown below. (**B**) Immunofluorescence of MHC and Sm22 (top), α-actinin (Actinin, middle), and transmission electron microscope (TEM) of sarcomeres (bottom). Arrows and arrowheads indicate normal (left) and diffuse Z-disks (middle and right), respectively. (**C**) Immunofluorescence of Mef2 and PCNA. Arrows indicate colabeled cells. (**D**) Quantification of Mef2$^+$PCNA$^+$ cells (n = 7). (**E**) EdU incorporation into myonuclei. (**F**) Quantification of EdU$^+$ myonuclei (n = 8). (**G**) Immunofluorescence of pHH3. Arrows indicate pHH3$^+$ myonuclei. (**H**) Example of cardiomyocytes in anaphase. (**I**) Quantification of pHH3$^+$ myonuclei (n = 6). *klf1-OFF* and *klf1-ON* fish carrying *cmlc2:GFP* transgene were used in (E) to (I). (**J**) Schematic of *klf1-REG* and 4-HT treatment regimen. (**K**) *klf1-REG* hearts analyzed at 37 dpt. (**L**) Picro-Mallory staining. (**M**) Immunofluorescence of Mef2 and actinin. (**N**) Dissociated ventricular cardiomyocytes. (**O** and **P**) Quantification of cell size [(O); n = 332 Veh, 326 4-HT] and number of cardiomyocytes in ventricles [(P); n = 3]. at, atrium; ba, bulbus arteriosus; O/N, overnight; ND, not detected; ve, ventricle; Veh, vehicle. ****P < 0.001 by Mann–Whitney U test [(D), (F), and (I)] or unpaired t test [(O) and (P)]. Scale bars, 500 nm in (B), 10 µm in (H), 500 µm in (K) and (L), and 50 µm in all other panels.

[1]Developmental and Stem Cell Biology Division, Victor Chang Cardiac Research Institute, Darlinghurst, New South Wales, Australia. [2]Department of Regenerative Medicine and Tissue Engineering, National Cerebral and Cardiovascular Center Research Institute, Suita, Osaka, Japan. [3]Genomics and Epigenetics Division, Garvan Institute of Medical Research, Darlinghurst, New South Wales, Australia. [4]St. Vincent's Clinical School, University of New South Wales Sydney, Kensington, New South Wales, Australia. [5]Molecular, Structural, and Computational Biology Division, Victor Chang Cardiac Research Institute, Darlinghurst, New South Wales, Australia. [6]Freedman Foundation Metabolomics Facility, Victor Chang Cardiac Research Institute, Darlinghurst, New South Wales, Australia. [7]Diabetes and Metabolism Division, Garvan Institute of Medical Research, Darlinghurst, New South Wales, Australia. [8]Centenary Institute, The University of Sydney, Newtown, New South Wales, Australia. [9]Faculty of Medicine and Health, The University of Sydney, Newtown, New South Wales, Australia. [10]School of Pharmacy, University of Queensland, Woolloongabba, Queensland, Australia. [11]School of Biotechnology and Biomolecular Sciences, University of New South Wales Sydney, Kensington, New South Wales, Australia.
***Corresponding author. Email: kikuchi@ncvc.go.jp**

To investigate whether enhanced *klf1* expression is sufficient to induce the regenerative phenotype in uninjured hearts, we conditionally expressed 3xHA-tagged Klf1 in cardiomyocytes (*klf1-ON*; Fig. 2A and S6A). *klf1-ON* fish or *Cre*-negative clutch-mates (*klf1-OFF*) were subjected to 4-HT treatment (Fig. 2A). *klf1-ON* hearts up-regulated myocardial expression of Sm22 (27-fold; Fig. 2B and fig. S3E) and Alcam (118-fold; fig. S3, C and D) by 7 days post-treatment (dpt), and expression increased even more at 12 dpt (41- and 532-fold for Sm22 and Alcam, respectively; Fig. 2B and fig. S3, C to E), accompanied by sarcomere disassembly (Fig. 2B, middle and bottom). The *klf1-ON* ventricles exhibited a large increase of proliferating cardiomyocytes (58-fold; Fig. 2, C and D) and myocardial incorporation of 5-ethynyl-2′-deoxyuridine (EdU) (115-fold; Fig. 2, E and F). Moreover, we detected a marked increase in mitotic phospho-histone $H3^{+}$ ($pHH3^{+}$) cardiomyocytes (Fig. 2,

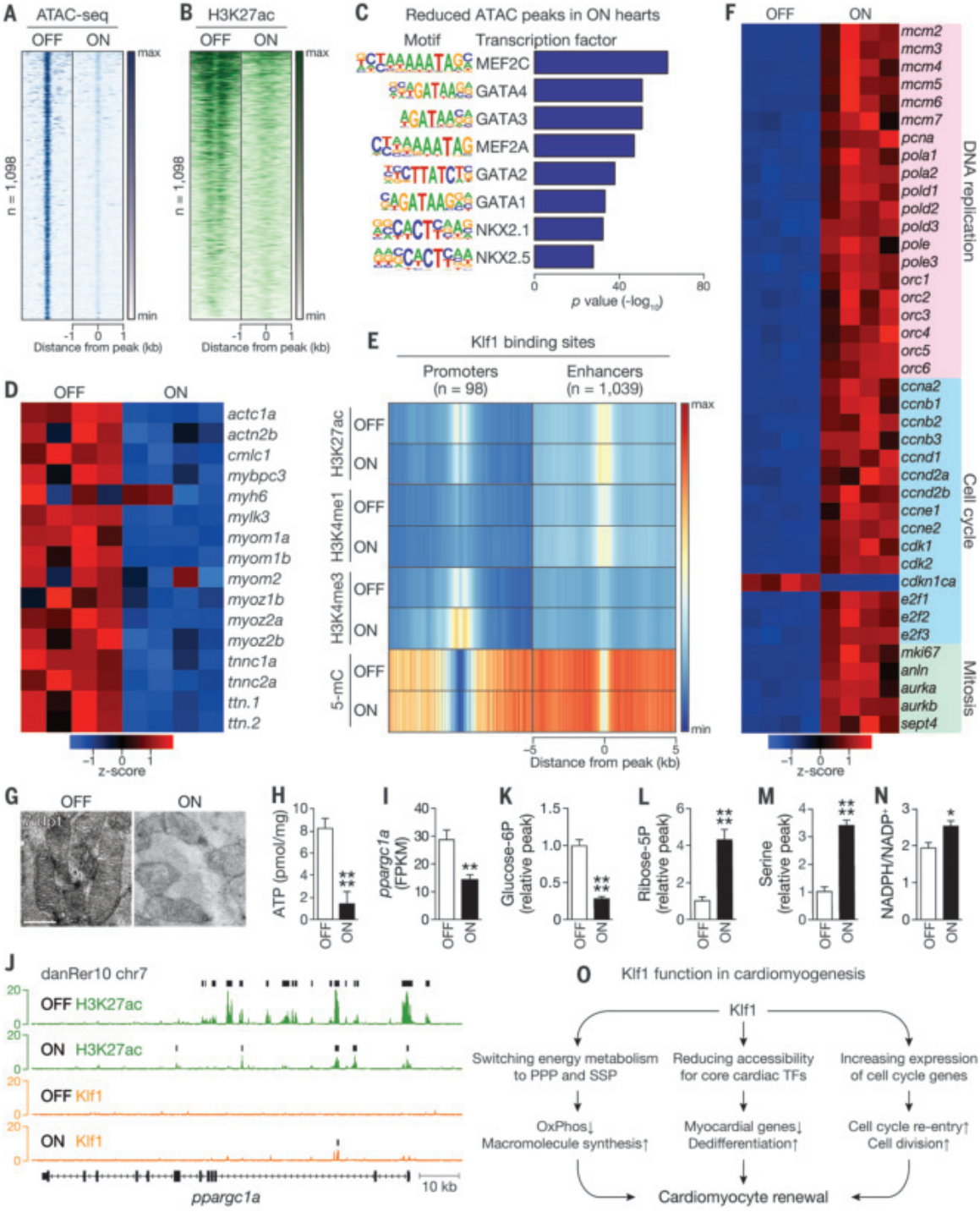

Fig. 3. Klf1 directs epigenetic and metabolic remodeling. (**A**) Heatmaps of ATAC-seq signal in differentially enriched ATAC-seq peaks. (**B**) Heatmaps of H3K27ac ChIP-seq signal centered on differentially enriched ATAC-seq peaks from (A). (**C**) Enriched motifs within ±100 bp of reduced ATAC-seq peak summits in *klf1-ON* hearts. (**D**) Representative myocardial contractile genes [false discovery rate (FDR) < 0.05]. (**E**) Clustered heatmaps of 5-methylcytosine (5-mC) levels and normalized ChIP-seq read densities for H3K27ac, H3K4me1, or H3K4me3 at Klf1-binding sites. K-means clustering (n = 2) was used to separate the data into two categories based on their epigenetic signal corresponding to promoters and enhancers. (**F**) Differentially expressed cell cycle genes (FDR < 0.05). (**G**) Ultrastructure of mitochondria. (**H**) Quantification of ATP (n = 4). (**I**) Expression of *ppargc1a* in FPKM (fragments per kilobase of exon per million mapped reads). (**J**) Klf1 and H3K27ac ChIP-seq signal (normalized reads) in the *ppargc1a* locus. Filled boxes indicate peaks. (**K** to **M**) Quantification of glucose-6-phosphate (K), ribose-5-phosphate (L), and serine (M) (n = 5). Quantified value is shown relative to the control. (**N**) Quantification of NADPH/$NADP^{+}$ (n = 3). (**O**) Model for Klf1 function. PPP, pentose phosphate pathway; SSP, serine synthesis pathway; TF, transcription factor. *P < 0.05, **P < 0.01, ****P < 0.001 by unpaired t test. Scale bar, 1 μm.

G and I), confirming successful progression to anaphase (Fig. 2H). Using genetic fate mapping, we determined that induced cardiomyocytes were derived from the myocardial lineage during the robust proliferative response in *klf1-ON* hearts (fig. S6G). We also investigated whether the KLF1-related orthologs KLF2 and KLF4 (*10*) have cardiomyogenic activity. Zebrafish KLF2 and KLF4 (fig. S6, B to D) exhibited much less mitogenic activity than Klf1 (fig. S6, E and F). These data highlight cardiomyogenic specificity within the Klf1 subclade and demonstrate that Klf1 acts cell autonomously to trigger robust cardiomyocyte dedifferentiation and proliferation in adult hearts.

Consistent with the reduction in contractile structures (Fig. 2B), *klf1-ON* zebrafish exhibited heart failure–like symptoms (fig. S7A and movies S1 and S2) and reduced survival (fig. S7B). To investigate whether Klf1-induced cardiomyocytes could integrate into the preexisting ventricular structure without pathogenic sequelae, we added temporal control by fusing 3xHA-Klf1 with the 4-HT–regulated human estrogen receptor (ER) (*11*) (*klf1-REG*; Fig. 2J). Daily 4-HT treatment (Fig. 2J) induced nuclear 3xHA-Klf1-ER localization (fig. S7C) and proliferative responses in uninjured ventricles by 7 dpt (fig. S7, D and E). However, after cessation of 4-HT treatment, *klf1-REG* fish did not exhibit distress or reduced survival, permitting analysis at later time points (fig. S7, C to E, right panels). Hearts from 4-HT–treated *klf1-REG* fish were enlarged at 37 dpt (Fig. 2K), producing a twofold increase in ventricular area (Fig. 2L and fig. S8J). In contrast to continuous *klf1* overexpression (fig. S8, A to H), transient Klf1 activation induced cardiomegaly without pathological dilation (fig. S8, J to L) or persistent fibrosis (fig. S8M) and permitted cardiomyocyte redifferentiation (fig. S8N) and sarcomeric reassembly (fig. S8, O and P), suggesting a mechanism for the improved survival of *klf1-REG* fish. The number of $Mef2^+$ nuclei was markedly increased in *klf1-REG* ventricles (Fig. 2M), accompanied by well-organized Z-disks (Fig. 2, M and N). Individual cardiomyocytes in the enlarged ventricles were smaller (Fig. 2O), and thus not hypertrophic, and their number was increased fivefold compared with controls (Fig. 2P), demonstrating the cardiomyogenic potency of Klf1.

To investigate the mechanism of Klf1-induced cardiomyogenesis, we performed open chromatin profiling [assay for transposase-accessible chromatin sequencing (ATAC-seq)] and chromatin immunoprecipitation sequencing (ChIP-seq) of H3K27ac, an active chromatin mark, in *klf1-OFF* and *klf1-ON* ventricles at 7 dpt. The majority of differential ATAC-seq peaks in *klf1-ON* hearts were in regions with reduced chromatin accessibility (83.5%; 1098/1315 total peaks; Fig. 3A), which were also associated with reduced H3K27ac (Fig. 3B) and transcription (fig. S9A). Binding motifs for the core cardiomyocyte transcription factors MEF2, GATA4, and NKX2.5 (*12*) were significantly enriched in regions with reduced chromatin accessibility in *klf1-ON* ventricles (Fig. 3C), consistent with the down-regulation of sarcomerogenic and muscle contraction genes (Fig. 3D and figs. S9B and S10A).

To characterize Klf1 target sites, we performed Klf1-HA ChIP-seq on *klf1-OFF* and *klf1-ON* ventricles at 7 dpt (fig. S9, C and D) and integrated the data with histone modification and DNA methylation profiles. The majority of Klf1 peaks were found at active enhancers (91.4%; 1039/1137 total peaks), which were constitutively marked with H3K27ac/H3K4me1 and DNA hypomethylation (Fig. 3E), regardless of Klf1 binding (OFF vs ON; Fig. 3E), and functionally linked to myocardial development (fig. S9E). Integrating datasets of developmental zebrafish enhancers (*13*, *14*), we found that Klf1-targeted enhancers acquired the activated epigenetic profiles as early as 48 hours postfertilization (fig. S9F). These data indicate that Klf1 regulates the myocardial gene network through associations with developmentally activated, preexisting myocardial enhancers in adult hearts.

Consistent with the histological phenotype (Fig. 2, C to I), *klf1-ON* hearts up-regulated cell cycle genes (Fig. 3F and fig. S10, C to H). Specifically, Klf1-binding regions were found upstream of *ccnd1* (fig. S9G) and *ccnd2a* (fig. S9H), which encode D-type cyclins required for G1-S commitment. By contrast, *klf1-ON* hearts down-regulated genes regulating mitochondrial energy production (fig. S10, B and E to H) and oxidative phosphorylation (OxPhos; fig. S11A). *klf1-ON* hearts exhibited mitochondria with reduced cristae and enlarged matrices (Fig. 3G and fig. S11B) and significantly lower ATP levels (Fig. 3H) and mitochondrial DNA content (fig. S11C). The mitochondrial attenuation was not associated with increased autophagic flux in *klf1-ON* hearts (fig. S11D). Rather, *klf1-ON* hearts down-regulated regulatory networks governing mitochondrial biogenesis, maintenance, and function (fig. S11E), including the master regulator PGC-1α/PPARGC1A (*15*) (Fig. 3I). Despite the stability of epigenetic marks at most Klf1-binding sites (Fig. 3E), induced Klf1 was enriched at *ppargc1a* and associated with a reduction of H3K27ac (Fig. 3J), suggesting that Klf1 epigenetically represses the transcription of specific genes, including *ppargc1a*, which contributes to attenuated mitochondrial function.

Switching from OxPhos to aerobic glycolysis, known as the Warburg effect, occurs in cancer (*16*) and has recently been shown to support cardiac morphogenesis and regeneration (*17*, *18*). However, gene-expression profiling (fig. S11F) and metabolomics analysis (fig. S12, A to C) of *klf1-ON* hearts showed down-regulation of the glycolytic (Fig. 3K and figs. S11F and S12D) and tricarboxylic acid pathways (figs. S10F and S11F), which is inconsistent with the Warburg effect. Instead, we observed up-regulation of the pentose phosphate (Fig. 3, L and N, and figs. S11F and S12E) and serine synthesis pathways (Fig. 3M and fig. S11F), which are glycolytic shunts that produce macromolecules (e.g., nucleic acids) and prevent oxidative stress (e.g., NADPH) in highly proliferative cells (*19*, *20*). These data indicate that Klf1 rewires cellular respiration through glycolytic shunts to provide metabolic support for the robust induction of cardiomyocyte proliferation.

This study identifies Klf1 as a transcription factor that stimulates renewal of preexisting cardiomyocytes in adult zebrafish hearts. Klf1 coordinates the repression of transcriptional networks controlling myocardial differentiation and mitochondrial metabolism with up-regulation of cell proliferation genes (Fig. 3O). Klf1 may use context-dependent cofactors to orchestrate different regenerative mechanisms. The elucidation of Klf1-dependent regeneration mechanisms will further extend our control of cardiomyogenesis in adult hearts (*21*, *22*). The identification of Klf1 as a potent cardiomyogenic regulator may offer therapeutic strategies for better repair of poorly regenerative human hearts.

REFERENCES AND NOTES

1. K. Kikuchi *et al*., *Dev. Cell* **20**, 397–404 (2011).
2. M. R. Tallack, A. C. Perkins, *IUBMB Life* **62**, 886–890 (2010).
3. M. Siatecka, J. J. Bieker, *Blood* **118**, 2044–2054 (2011).
4. K. D. Poss, L. G. Wilson, M. T. Keating, *Science* **298**, 2188–2190 (2002).
5. B. Nuez, D. Michalovich, A. Bygrave, R. Ploemacher, F. Grosveld, *Nature* **375**, 316–318 (1995).
6. A. C. Parkins, A. H. Sharpe, S. H. Orkin, *Nature* **375**, 318–322 (1995).
7. K. Kikuchi *et al*., *Nature* **464**, 601–605 (2010).
8. T. Kubin *et al*., *Cell Stem Cell* **9**, 420–432 (2011).
9. T. O. Monroe *et al*., *Dev. Cell* **48**, 765–779.e7 (2019).
10. A. B. Bialkowska, V. W. Yang, S. K. Mallipattu, *Development* **144**, 737–754 (2017).
11. E. Coghill *et al*., *Blood* **97**, 1861–1868 (2001).
12. E. N. Olson, *Science* **313**, 1922–1927 (2006).
13. O. Bogdanovic *et al*., *Genome Res.* **22**, 2043–2053 (2012).
14. O. Bogdanović *et al*., *Nat. Genet.* **48**, 417–426 (2016).
15. J. Lin, C. Handschin, B. M. Spiegelman, *Cell Metab.* **1**, 361–370 (2005).
16. M. G. Vander Heiden, L. C. Cantley, C. B. Thompson, *Science* **324**, 1029–1033 (2009).
17. H. Honkoop *et al*., *eLife* **8**, e50163 (2019).
18. R. Fukuda *et al*., *eLife* **8**, e50161 (2019).
19. K. C. Patra, N. Hay, *Trends Biochem. Sci.* **39**, 347–354 (2014).
20. M. Yang, K. H. Vousden, *Nat. Rev. Cancer* **16**, 650–662 (2016).
21. K. Song *et al*., *Nature* **485**, 599–604 (2012).
22. L. Qian *et al*., *Nature* **485**, 593–598 (2012).

ACKNOWLEDGMENTS

We thank A. Hay, C. Jenkin, and K. Brennan for zebrafish care and shipment to Japan; P. Young for ChIP-seq library preparation; the Kinghorn Centre for Clinical Genomics for sequencing; E. Lam at the Garvan Flow for cell sorting; N. Ariotti and N. Kapoor-Kaushik at the UNSW Sydney Electron Microscope

Unit for TEM analysis; and R. Graham, R. Harvey, N. Mochizuki, E. Wong, S. Iismaa, H. Nakajima, C. Abe, and M. Shirai for comments on the manuscript. **Funding:** This work was supported by funding from the NSW state government to M.P.H. and K.K.; ARC DP190103852 to O.B.; and NHMRC APP1160466 and JSPS KAKENHI JP20H03683 to K.K. **Author contributions:** K.K. conceived the project. M.O. performed all zebrafish experiments. M.O. and K.K. designed the experimental strategy and analyzed data. M.O., D.H., and K.K. prepared the manuscript. D.Z.S., S.P.H., K.S., M.N., and D.Z. generated and characterized genetically modified zebrafish. F.-S.G., D.T.H., and O.B. performed genomics and transcriptomic analysis. E.K. and M.P.H. performed metabolomic analysis. Y.Z. and D.H. performed autophagy assays. **Competing interests:** K.K. and M.O. are inventors on patent/patent application (PCT/AU2020/050775) held/submitted by the Victor Chang Cardiac Research Institute and the National Cerebral and Cardiovascular Center that covers KLF-induced cardiomyogenesis. **Data and materials availability:** Sequencing data are available at NCBI (https://www.ncbi.nlm.nih.gov) under BioProject accession nos. PRJNA551130 and PRJNA677856. Metabolomics data will be available at MetaboLights (https://www.ebi.ac.uk/metabolights/) under the unique identifier MTBLS2348. Information for genetically modified zebrafish lines will be available at ZFIN: The Zebrafish Information Network (https://zfin.org). Zebrafish lines and constructs generated in this study are available from the corresponding author under a material transfer agreement with the Victor Chang Cardiac Research Institute.

SUPPLEMENTARY MATERIALS

science.sciencemag.org/content/372/6538/201/suppl/DC1
Materials and Methods
Figs. S1 to S12
Tables S1 and S2
References (*23*–*43*)
Movies S1 and S2
MDAR Reproducibility Checklist

11 August 2020; accepted 2 March 2021
10.1126/science.abe2762

Controlled-Rate Freezers
In line with the need for pharmaceutical research, cell and gene therapy, vaccine production, and biobanking laboratories for dependable sample protection, Thermo Fisher Scientific's series of controlled-rate freezers provides precise, repeatable freezing capabilities while enhancing data traceability to support Good Manufacturing Practice and 21 CFR Part 11 requirements. Our CryoMed Controlled-Rate Freezers (CRF) safeguard sample safety and integrity using Type T thermocouples for real-time monitoring of chamber and sample temperatures. Precise temperature control, temperature uniformity, and accelerated freezing are enabled via an air-handling system and dual solenoid valves capable of balancing liquid-nitrogen injection volumes. A remote alarm capability prompts corrective action to ensure ideal conditions are always maintained, notifying users of thermocouple failures, heater malfunction, breach of high/low temperature limits, and power failures. The CryoMed CRF systems are available in three capacities, while also offering 6 preset and up to 14 user-defined custom freezing profiles. For maximum ease-of-use, a "run last" feature allows the same profile to be run consecutively at the touch of a button.
Thermo Fisher Scientific
For info: 866-984-3766
ww.thermofisher.com/cold

Organ-on-a-Chip
CN Bio announces its PhysioMimix organ-on-a-chip (OOC) Multi-Organ Microphysiological System (MPS). The company's advanced 3D liver model can be reliably and easily interconnected with other organs (such as gut, lung, or kidney) to provide a human in vitro alternative to animal or in silico first-pass metabolism studies (absorption, distribution, metabolism, and excretion), to elicit a deeper human-specific mechanistic understanding of disease states, and to identify reactive metabolite-driven toxicity or multiorgan toxicity. Furthermore, in vitro to in vivo clinical predictions can be extrapolated using physiologically based pharmacokinetic mathematical models to increase the accuracy and precision of data translation. For existing PhysioMimix users, an upgrade path is available.
CN Bio
For info: +44-(0)-1223-737941
cn-bio.com/sot-2021

Spheroid Culture Plate
Corning Elplasia plates enables researchers to generate a high density of spheroids in a scaffold-free model using microcavity technology. They can generate, culture, and analyze hundreds to thousands of spheroids, all in a standard plate footprint. The plates are available in multiple formats, two well geometry types (round and square bottom), and two surface coatings (ultralow attachment and plasma-treated). Elplasia plates are compatible with many cell types and may be used across many applications, including drug screening, high-throughput screening, cancer/tumor biology, stem cell biology, cell therapy research, and 3D tissue engineering. A high volume of spheroids in each well produces more signals per well without increasing spheroid size. Additionally, more spheroids mean increased data points. Corning Elplasia plates consistently produce high-quality spheroids and reproducible results.
Corning
For info: 800-492-1110
www.corning.com

Patient-Derived Human Primary Cancer Cells
AMSBIO has expanded its range of primary human cancer cells sourced from a wide variety of tissue types that allow the study of cancer in a more in vivo like fashion. Our range of primary human cancer cells are available for specific tumor types, both primary and metastatic. All exhibit heterogeneous cell populations with diverse genetic backgrounds. Provided with the original pathological diagnoses and analyzed for key mutations, these cells present the real characteristics of their in vivo state and remain heterogeneous for several passages, thus enhancing pharmacogenetic and molecular diagnostic testing abilities. Typical applications include drug discovery and development, drug testing, drug screening, and basic research as well as functional and cytotoxicity analyses.
AMS Biotechnology
For info: 617-945-5033
www.amsbio.com/human-primary-cancer-cells

3D Cell-Culture Slide
ibidi's µ-Slide I Luer 3D is an innovative slide with one channel and three wells for 3D cell culture under flow. Sample preparation is easy: Fill each of the three wells with a gel (e.g., collagen, Matrigel, or fibrinogen). Then, simply seed the cells into the channel, where they will adhere to the gel. For applying defined shear stress, the slide is connected to a pump (e.g., to the ibidi Pump System). Thanks to the ibidi Polymer Coverslip on the slide's top and bottom, the cells can be imaged using high-resolution microscopy. The µ-Slide I Luer 3D is a versatile channel slide designed for a huge variety of 3D cell-culture experiments under flow. Scientists can create a cell monolayer on the gel matrix for polarization assays or transendothelial migration studies. Researchers who would like to test the I Luer 3D with their own experiments can request free samples at ibidi.com.
ibidi
For info: +49-(0) 89-520-46-17-0
ibidi.com

Single-Cell Isolation
iBiochips' 1CellPlate provides easy, simple, and fast isolation of single cells. It does not require equipment/instrument or expertise to isolate single cells. All operations are completed only by a common pipette. With a simple press of the thumb on a pipette, single-cell isolation is immediately performed with high viability and integrity. 1CellPlate is also versatile, since it is compatible with large and small cells, even below 80 µm in diameter. These features make it a convenient tool to boost single-cell analysis, including single-cell PCR and sequencing, single-cell cloning, and target-cell isolation from gene-edited cells and clinical samples.
iBiochips
For info: 832-538-1925
ibiochips.com

Electronically submit your new product description or product literature information! Go to www.sciencemag.org/about/new-products-section for more information.

Newly offered instrumentation, apparatus, and laboratory materials of interest to researchers in all disciplines in academic, industrial, and governmental organizations are featured in this space. Emphasis is given to purpose, chief characteristics, and availability of products and materials. Endorsement by *Science* or AAAS of any products or materials mentioned is not implied. Additional information may be obtained from the manufacturer or supplier.

THE UNIVERSITY OF TENNESSEE KNOXVILLE

The **Department of Earth and Planetary Sciences** invites applications for the position of **Professor and Department Head**. The position is at the tenured, full Professor level and preferably starts **August 1, 2021**.

The requirements for this position are: **(i)** a Ph.D. in a relevant Earth Science discipline; **(ii)** a strong service record with demonstrated administrative experience and financial management skills; **(iii)** an established track record of obtaining external research funding; **(iv)** teaching and research experience in any area of Environmental Earth Science, Geology, and/or Planetary Geoscience. The successful candidate should be an inspiring, energetic, and well-organized leader who can interact effectively with all faculty, staff, and students within the department. The candidate should also have excellent interpersonal communication skills, high ethical standards, and be able to foster a collegial environment. They will be expected to build collaborative relationships with other programs and departments, advocate on behalf of the department with administrative units throughout the University, and to interact with external organizations. We are particularly interested in candidates who can increase the participation of underrepresented students and/or faculty within the department and who will contribute to the diversity and intercultural goals of the Knoxville campus.

Please submit **(i)** a cover letter, **(ii)** Curriculum Vitae, **(iii)** vision statement incorporating administration, teaching, research, and diversity approaches, and **(iv)** contact information for three academic references via **http://apply.interfolio.com/85122**. Only electronic applications will be considered and acceptable file formats are .pdf or .docx. We will start reviewing applications by **May 1, 2021**, until the position is filled.

The University of Tennessee is an Equal Opportunity/Affirmative Action/Title VI/Title IX/Section 504/ADA/ADEA institution in the provision of its education and employment programs and services. All qualified applicants will receive equal consideration for employment and admission without regard to race, color, national origin, religion, sex, pregnancy, marital status, sexual orientation, gender identity, age, physical or mental disability, genetic information, veteran status, and parental status.

Features in myIDP include:

- Exercises to help you examine your skills, interests, and values.
- A list of 20 scientific career paths with a prediction of which ones best fit your skills and interests.

myIDP

Visit the website and start planning today!
myIDP.sciencecareers.org

ScienceCareers | AAAS In partnership with:

FASEB Federation of American Societies for Experimental Biology
University of Massachusetts Medical School
UMASS
UCSF University of California San Francisco
UIC
BURROUGHS WELLCOME FUND

ScienceCareers online @sciencecareers.org

Science Careers online @sciencecareers.org

Science Careers helps you advance your career. Learn how !

- Register for a free online account on **ScienceCareers.org**.
- Search hundreds of job postings and find your perfect job.
- Sign up to receive e-mail alerts about job postings that match your criteria.
- Upload your resume into our database and connect with employers.
- Watch one of our many webinars on different career topics such as job searching, networking, and more.
- Download our career booklets, including Career Basics, Careers Beyond the Bench, and Developing Your Skills.
- Complete an interactive, personalized career plan at "my IDP."
- Visit our Employer Profiles to learn more about prospective employers.
- Read relevant career advice articles from our library of thousands.

Visit **ScienceCareers.org** today — all resources are free

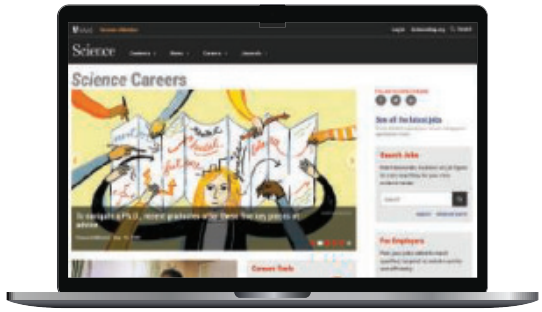

SCIENCECAREERS.ORG

ScienceCareers
FROM THE JOURNAL SCIENCE AAAS

YOU'D SMILE TOO IF YOU JUST ADVANCED YOUR CAREER.

Find your next job at ScienceCareers.org

There's scientific proof that when you're happy with what you do, you're better at what you do. Access career opportunities, see who's hiring and take advantage of our proprietary career-search tools. Get tailored job alerts, post your resume and manage your applications all in one place: sciencecareers.org

ScienceCareers

FROM THE JOURNAL SCIENCE AAAS

By **Virginia Zarulli**

A risk worth taking

The question was simple, clear, and brutal. A few days earlier, I had announced my third pregnancy during a department meeting. My female colleague—more senior than I am, with two young children—congratulated me. Then, apologizing for her bluntness, she asked a question that had been nagging at me for months: "How do you feel about having another child and your career? Aren't you afraid of not making it this time?" Hearing it from someone else sharpened my fears. My answer was also simple, clear, and brutal: "Yes, I know this could potentially wipe me out of academia."

Maybe I have been too daring. I already have a 7-year-old boy and a 5-and-a-half-year-old girl; why do I want more? Here I am, a young associate professor, having one more child when I should be focusing on establishing myself in my department and in the scientific community, and building up my CV and publication record to support my career progression and hopeful promotion to full professor. Will I make it? Will the experience I've gained with my other children help carry me through?

"Having this third child comes with trade-offs [but] I've tried to plant as many seeds as possible."

My husband and I have always wanted three children. I got pregnant with our first during my first year as a postdoc. My supervisor was very supportive but didn't give me much guidance about planning for my leave. I spent most of that first postdoc year publishing work from my dissertation, so I had done very little to plan research directions for after my return. As a result, coming back was like starting from scratch. I felt aimless and lost. As a sleep-deprived, overwhelmed new mother, I had to reinvent myself and my position.

The second time around, still a postdoc, I was a bit more prepared. I returned to the lab with some research ideas, and my supervisor assigned me to a well-defined project. With little time and energy to spare, being able to focus on a specific plan made things easier. When my husband and I finally regained some hours of uninterrupted sleep, our motivation to have a third child faded—until it recently re-emerged.

And now? I know how hard it will be. And I know that no matter what I do, having this third child comes with trade-offs that may diminish my scholarly output and career progress. But by proactively planning for my leave, I hope to minimize the negative impact and ease the transition at least a little bit. My university allows staff on parental leave to maintain contact, if they desire, so they can keep up to date, and it offers a teaching-free period to parents returning after leave, which I think will help. For my part, I've tried to plant as many seeds as possible: starting collaborations; authoring manuscripts, hoping that some will be published during my leave; and taking responsibility for various projects that I will be able to pick back up once I return to work, with collaborators running them while I'm out. In fact, I worry I've gone too far, overloading my plate for these last weeks leading up to my leave and perhaps upon my return. Still, I hope I've done enough to set myself up for success.

I realize now how unprepared I was to navigate such an immense personal and professional transition, especially on my first leave. As any parent knows, it's impossible to truly understand what having a child is like until it happens—which makes it awfully difficult to prepare for. I wish my institution had offered more resources and structured support, rather than leaving me to my own devices to plan for something so life-changing.

So, to the expectant and future parents, do your best to strategically plan for your leave to make your re-entry as smooth as possible. And to supervisors, department chairs, and administrators: It shouldn't be the sole responsibility of expectant parents to lay all the groundwork. Help us find and set up opportunities that can be easily picked up once we're back to work. Invite us to be involved in projects with timelines that match our planned leaves. Consider creating formal mechanisms to guide us in developing plans and strategies for before, during, and after leave. Perhaps if a culture like this becomes the norm, future researchers will be able to worry a little less that having the children they desire could cost them their careers. ■

Virginia Zarulli is an associate professor at the University of Southern Denmark. Send your career story to SciCareerEditor@aaas.org.

ILLUSTRATION: ROBERT NEUBECKER

ScienceSignaling.org

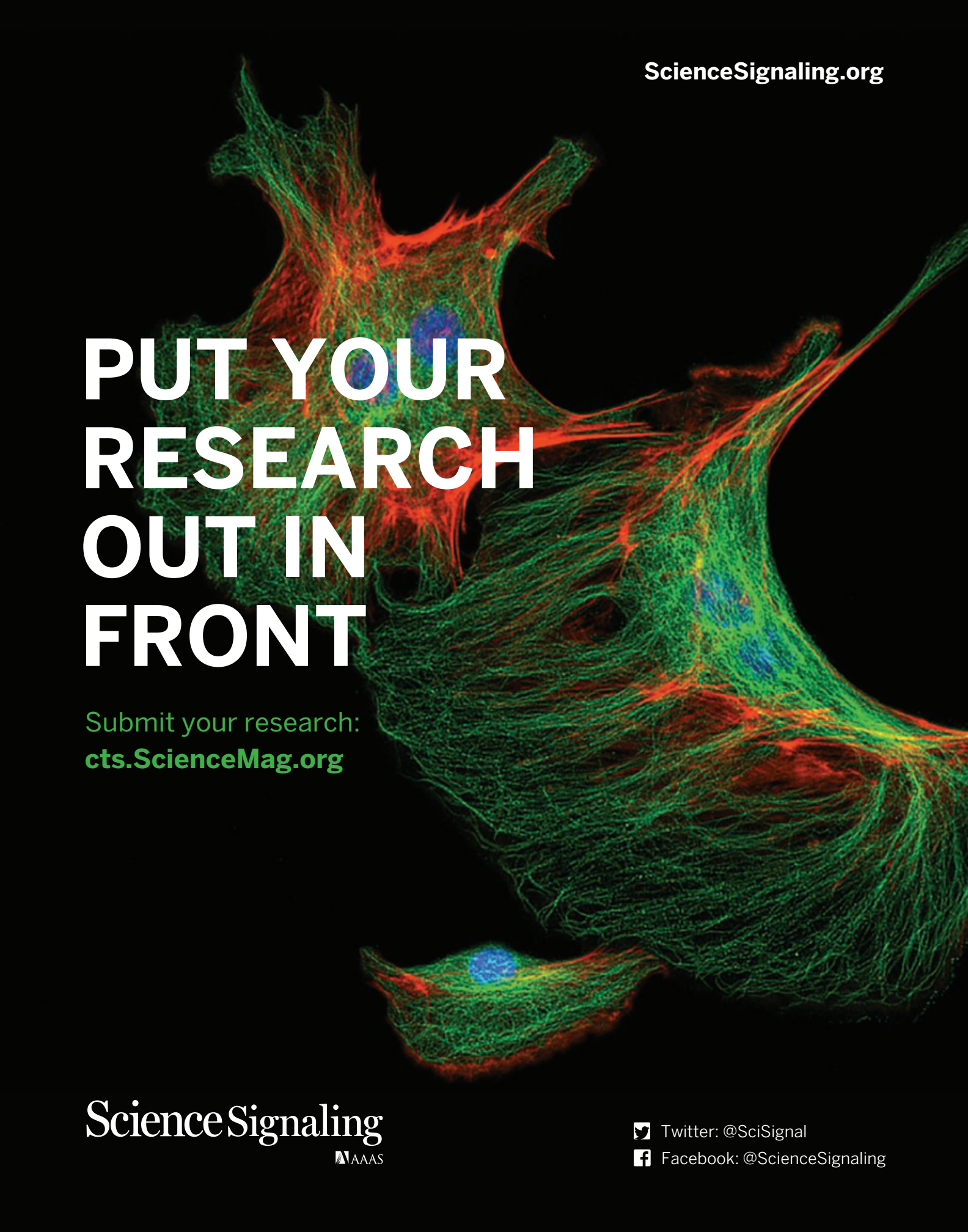

PUT YOUR RESEARCH OUT IN FRONT

Submit your research:
cts.ScienceMag.org

Science Signaling
AAAS

Twitter: @SciSignal
Facebook: @ScienceSignaling

Custom Lentivirus Generation

One-Stop-CRO for CAR-T Research

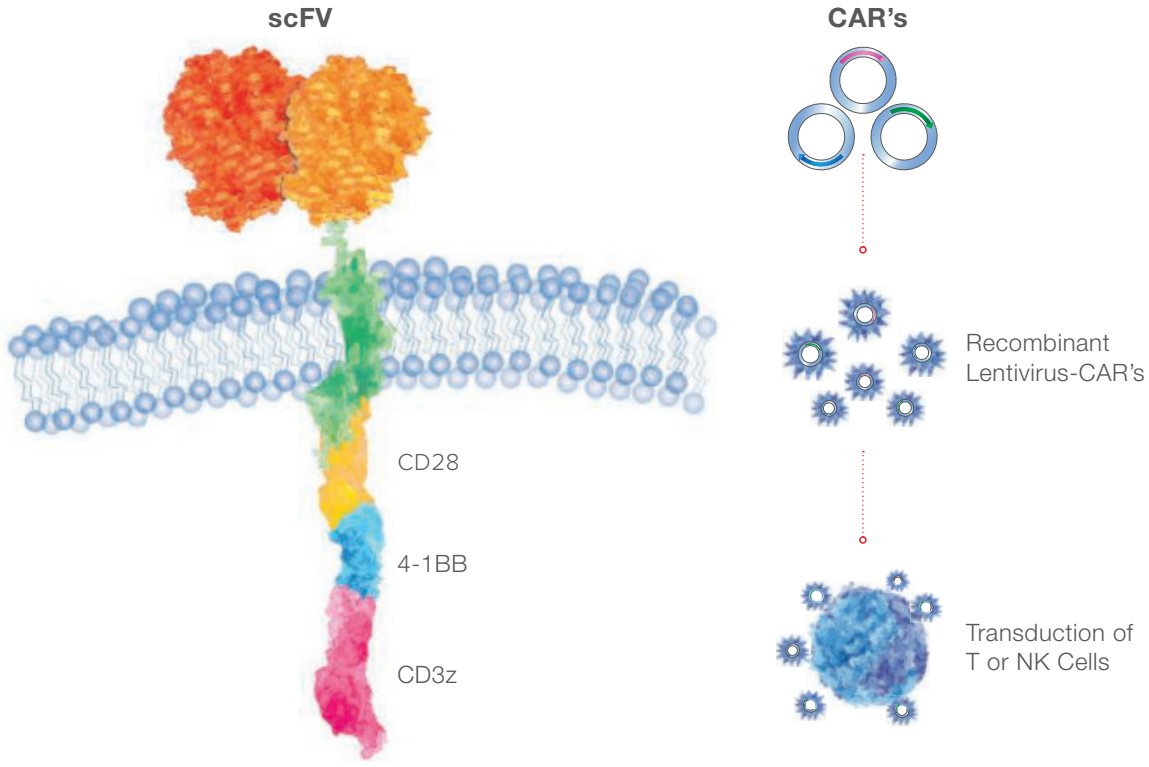

ProMab Biotechnologies commits to stay at the forefront of CAR-T technologies by providing an all-inclusive pre-clinical research program for CAR-T development. Our CAR-T platform utilizes lentivirus as it has become widely used as a vector to deliver specific genes of interest and to compliment gene and cell therapy applications.

Our standardized and highly optimized platform enables ProMab to produce recombinant lentivirus with many benefits:

- Custom vector engineering from gene synthesis to plasmid production
- High titer: 10^8 to 10^10 particles/ml
- Fast turnaround time: 2 to 3 weeks
- Variety of analytical options
- Ready to use CAR-T lentivirus
- Downstream to CAR-T or stable cell line development services

All products are for research only

Discover more | www.promab.com

ProMab Biotechnologies, Inc.
2600 Hilltop Dr, Building B, Richmond, CA 94806
1.866.339.0871 | info@promab.com